ISTANBUL TECHNICAL UNIVERSITY ★ GRADUATE SCHOOL

VIBRATION ANALYSIS OF ROTATING BEAM STRUCTURES MADE OF FUNCTIONALLY GRADED MATERIALS IN A THERMAL ENVIRONMENT BY GENERALIZED DIFFERENTIAL QUADRATURE METHOD

Ph.D. THESIS

Mustafa Tolga YAVUZ

Department of Aeronautics and Astronautics Engineering

Aeronautics and Astronautics Engineering Programme

OCTOBER 2024

ISTANBUL TECHNICAL UNIVERSITY ★ GRADUATE SCHOOL

VIBRATION ANALYSIS OF ROTATING BEAM STRUCTURES MADE OF FUNCTIONALLY GRADED MATERIALS IN A THERMAL ENVIRONMENT BY GENERALIZED DIFFERENTIAL QUADRATURE METHOD

Ph.D. THESIS

Mustafa Tolga YAVUZ
(511152116)

Department of Aeronautics and Astronautics Engineering

Aeronautics and Astronautics Engineering Programme

Thesis Advisor: Prof. Dr. Ibrahim OZKOL

OCTOBER 2024

ISTANBUL TEKNİK ÜNİVERSİTESİ ★ LİSANSÜSTÜ EĞİTİM ENSTİTÜSÜ

FONKSİYONEL DERECELENDİRİLMİŞ DÖNEN KİRİŞ YAPILARIN ISIL ORTAMDA GENELLEŞTİRİLMİŞ DİFERANSİYEL KARELEME YÖNTEMİ İLE TİTREŞİM ANALİZİ

DOKTORA TEZİ

Mustafa Tolga YAVUZ
(511152116)

Uçak ve Uzay Mühendisliği Anabilim Dalı

Uçak ve Uzay Mühendisliği Programı

Tez Danışmanı: Prof. Dr. İbrahim ÖZKOL

EKİM 2024

Mustafa Tolga YAVUZ, a Ph.D. student of ITU Graduate School student ID 511152116, successfully defended the thesis entitled “VIBRATION ANALYSIS OF ROTATING BEAM STRUCTURES MADE OF FUNCTIONALLY GRADED MATERIALS IN A THERMAL ENVIRONMENT BY GENERALIZED DIFFERENTIAL QUADRATURE METHOD”, which he prepared after fulfilling the requirements specified in the associated legislations, before the jury whose signatures are below.

Thesis Advisor :	**Prof. Dr. Ibrahim OZKOL** İstanbul Technical University	.....
Jury Members :	**Prof. Dr. Metin Orhan KAYA** Istanbul Technical University	.....
	Prof. Dr. Ahmet KIRIŞ Istanbul Technical University	.....
	Prof. Dr. Osman Ergüven VATANDAŞ Istanbul Gelisim University	.....
	Prof. Dr. Erol UZAL Istanbul University	.....

Date of Submission : 23 August 2024
Date of Defense : 18 October 2024

Dedicated to my altruistic family and all my distinguished teachers, who have always supported and guided me in my pursuit of knowledge and truth,

A Humble Servant of Mathematics.

FOREWORD

I want to begin by expressing my gratitude to my thesis advisor Professor Ibrahim Ozkol for his invaluable guidance and support throughout completing this study and writing process. I would also like to thank the members of my thesis committee Professors Erol UZAL, and Metin Orhan KAYA for their valuable contributions and constructive feedback on my thesis study, and my hidden supporters Professors Ahmet KIRIS, Aytac ARIKOGLU, Guven KOMURGOZ, and Hayri ACAR.

Finally, I would like to thank my family and my dear friends Dr. Ahmet Gokay OZTURK, and Dr. Caglar UYULAN for their endless support throughout my thesis study. Without their encouragement and patience, this work would not have been completed.

I hope that this study will attract the interest of researchers working on thermal structures, and will provide a useful foundation for future studies on structural analysis of rotating beam structures in a thermal environment.

May 2024

Mustafa Tolga YAVUZ
Structural Analysis Engineer

TABLE OF CONTENTS

Page

FOREWORD ..... **ix**
TABLE OF CONTENTS ..... **xi**
ABBREVIATIONS ..... **xiii**
SYMBOLS ..... **xv**
LIST OF TABLES ..... **xix**
LIST OF FIGURES ..... **xxi**
SUMMARY ..... **xxvii**
ÖZET ..... **xxix**
1. INTRODUCTION **1**
1.1 Literature Review 3
1.2 Purpose of the Thesis 8
1.3 Structure of the Thesis 9
2. THERMOSTRUCTURAL DESIGN ASPECTS **11**
2.1 Fighter Aircraft Generations 11
2.2 High-Temperature Effects in Aircraft Structures 16
2.3 Materials for High-Speed Flight 19
2.4 Airframe Construction 24
2.5 Thermal Structural Tests 26
2.6 Closing Remarks 30
3. FUNDAMENTALS OF THERMOELASTICITY **31**
3.1 Definitions 31
3.2 Theory of Elasticity 35
3.3 Heat Transfer in Aircraft Structures 37
3.4 Thermal Stresses in Airframe 39
3.5 Basic Equations of Thermoelasticity 45
3.6 Closing Remarks 50
4. NUMERICAL APPROACHES IN COMPUTATIONAL MECHANICS **51**
4.1 Differential Transform Method 51
4.1.1 Application of differential transform method to beam element 53
4.1.2 Application of differential transform method to plate element 61
4.2 Differential Quadrature Method 75
4.2.1 Application of differential quadrature method to beam element 78
4.2.2 Application of differential quadrature method to plate element 83
4.3 Finite Difference Method 89
4.3.1 Application of finite difference method to beam element 94
4.3.2 Application of finite difference method to plate element 96
4.4 Closing Remarks 100
5. VIBRATION ANALYSIS OF ROTATING BEAMS **101**
5.1 Structural Dynamics of Double Tapered Rotating Beams 101
5.1.1 Equation of motion for beam vibration 102
5.1.2 Numerical solution by generalized differential quadrature method 108
5.1.3 Numerical results and discussion 112

5.2 Thermal Influences on Dynamic Characteristics 122
5.2.1 Equation of motion for fgm beam vibration thermal environment 127
5.2.2 Numerical results and discussion 138
5.3 Closing Remarks 146
6. CONCLUSION 147
REFERENCES 149
APPENDICES 167
APPENDIX A 168
APPENDIX B 173
APPENDIX C 176
APPENDIX D 181
APPENDIX E 183
APPENDIX F 185
APPENDIX G 187
APPENDIX H 188
CURRICULUM VITAE 189

ABBREVIATIONS

ADM : Adomian Decomposition Method
AESA : Active Electronically Scanned Array
AFRP : Aramid Fiber Reinforced Polymers
APU : Auxiliary Power Unit
ATS : Advanced Tactical Fighter
AVFEM : Air Vehicle Finite Element Model
BMI : Bismaleimides
BVR : Beyond Visual Range
CFC : Carbon Fibre Composites
CFRP : Carbon-Fiber-Reinforced Polymers
CMC : Ceramic Matrix Composites
DQM : Differential Quadrature Method
DSM : Dynamic Stiffness Method
DTM : Differential Transform Method
EEB : Euler Bernoulli Beam
FEM : Finite Element Method
FGM : Functionally Graded Material
FRP : Fiber Reinforced Polymer
GFRP : Glass Fiber Reinforced Polymers
IOC : Initial Operational Capability
JAST : Joint Advanced Strike Technology
LPD : Low Probability Detection
LPI : Low Probability Intercept
MMC : Metal Matrix Composites
MTI : Moving Target Indication
PSM : Power Series Method
RAM : Radar Absorbing Materials
RAP : Radar Absorbing Paint
RCS : Radar Cross Section
RMS : Reliability, Maintainability, and Supportability
RRM : Rayleigh-Ritz method

SAM **:** Surface to Air Missile

SAR **:** Synthetic Aperture Radar

TBC **:** Thermal Barrier Coating

TCC **:** Thermal Contact Conductance

TMM **:** Transfer Matrix Method

TVC **:** Thrust Vector Control

SYMBOLS

f_s	: Factor of safety
$S_{ultimate}$	: Ultimate strength
S_{yield}	: Yield strength
σ_{max}	: Maximum applied stress
α	: Thermal expansion coefficient under zero applied stress
β_t	: Volume thermal expansion coefficient for isotropic materials
B	: Volume modulus of elasticity
λ_L	: Lame elastic constant
e_v	: Volumetric dilatation
γ_G	: Grüneisen constant
L	: Length
V	: Volume
E	: Elasticity modulus
σ_m	: Mechanical stress
σ_t	: Thermal stress
ε_m	: Mechanical strain
ε_t	: Thermal strain
ε_x	: Mechanical strain in the x-direction (extensional strain)
ε_y	: Mechanical strain in the y-direction
ε_z	: Mechanical strain in the z-direction
ν	: Poisson's ratio
κ	: Thermal diffusivity
k or k_t	: Thermal conductivity
ρ	: Material density
c	: Specific heat at constant strain
T	: Temperature
T_0	: Stress-free temperature
q_{tot}	: Total heat transfer rate
q_{cond}	: Heat transfer rate by conduction
q_{conv}	: Heat transfer rate by convection

q_{rad} : Heat transfer rate by radiation

q_{gen} : Generated heat transfer rate

$\dot{E}_g$: Generated energy rate per unit volume

$\dot{E}_{st}$: Stored energy rate per unit volume

$\dot{E}_{work}$: Work transfer rate per unit volume

A : Cross-sectional area perpendicular to the heat flow

h : Convective heat transfer coefficient

T_s : Surface temperature

T_f : Fluid temperature

σ : Stefan-boltzmann constant

ε : Emissivity of the surface

P_e : External load

δ : Gap width

k_{sp} : Spring constant coefficient

R : Radius of curvature

Ψ : Small rotation angle

ε_0 : Extensional strain

ε_b : Bending strain

M_T : Thermal moment

F_T : Thermal force

I : Area moment of inertia

ω : Angle of a beam rotation

u : Axial displacement

v : Transverse displacement

w : Spanwise displacement

V : Transverse shear force

M : Mechanical bending moment

q : The transverse distributed load

Δ : The forward difference operator

∇ : The backward difference operator

∂ : Partial derivative operator

L : Beam length

Ω : Nondimensional natural frequency

ω : Natural frequency

w : Nondimensional deflection function

A : Cross-sectional area

λ : Length ratio

x : Non-dimensional coordinate along the x-axis of the beam

y : Non-dimensional coordinate along the y-axis of the Beam

p, q : Boundary condition constants, $p = \nu\left(\frac{\sigma\pi}{\lambda}\right)^2$, $q = (2-\nu)\left(\frac{\sigma\pi}{\lambda}\right)^2$

υ : Poisson ratio

N, M : Number of grid points in x and y directions

$A_{ik}^{(r)}, B_{jl}^{(s)}$: Weighting coefficients of r^{th} and s^{th} order derivatives.

c : Taper ratio

b, h : Tip breadth and height

Ω : Rotational speed

β : Setting angle between the hub axis and beam axis

I : Second moment of area

ω : Circular frequency

θ : Rotation angle due to bending

u, w : Axial and bending displacements

R : Hub radius

F : Force

$U, \Im$: Potential and kinetic energy

X, W : Dimensionless length transverse displacement parameter

ξ : The dimensionless hub radius parameter

λ : Dimensionless rotational speed parameter

μ, η : Rotary inertia parameter to a frequency and rotational speed

ψ : Dimensionless natural frequency parameter

α : The dimensionless setting angle parameter

x, y, z : Spanwise, transverse, and vertical distance

N : Number of grid points

γ : Frequency parameter

K : Spring coefficient

b, h : Breadth and height values

$cent$: Centrifugal

LIST OF TABLES

Page

Table 4.1 : Fundamental function transforms. **52**
Table 4.2 : The boundary conditions for a uniform beam. **54**
Table 4.3 : The transformed boundary conditions for a uniform beam. **54**
Table 4.4 : The first nine nondimensional natural frequency of the beam. **58**
Table 4.5 : Boundary conditions of the plate along *y=0*, and *y=1* edges. **63**
Table 4.6 : Transformed boundary conditions for the reduced plate. **64**
Table 4.7 : The first nine dimensionless frequencies of Kirchhoff-Love plate via DTM. **72**
Table 4.8 : Discretized boundary conditions for Euler-Bernoulli beam. **79**
Table 4.9 : The first ten dimensionless frequencies of Euler-Bernoulli beam. **82**
Table 4.10 : Boundary conditions at the edges of rectangular plate. **84**
Table 4.11 : Transformed boundary conditions at the edges of rectangular plate. **84**
Table 4.12 : The first nine dimensionless frequencies of Kirchoff-Love plate via DQM. **85**
Table 4.13 : The first ten dimensionless frequencies of Euler-Bernoulli beam. **95**
Table 4.14 : The first nine dimensionless frequencies of Kirchoff-Love plate via FDM. **97**
Table 5.1 : Equations for classical and non-classical supports. **107**
Table 5.2 : Equations of discretized boundary conditions **111**
Table 5.3 : Variations of the first four natural frequencies of the rotating beam structure to hub radius, rotational speed, and boundary conditions ($c_b=c_h=0$, $\mu=\eta=0$, $\alpha=0$, $EI/K_{rot}=0.1$, $EI/K_{tran}=0.0092$). **119**
Table 5.4 : Variations of the first four natural frequencies of the rotating beam structure to hub radius, taper ratios, and boundary conditions ($\lambda=8$, $\mu=\eta=0$, $\alpha=0$, $EI/K_{rot}=0.1$, $EI/K_{tran}=0.0092$). **120**
Table 5.5 : Comparison of the first three dimensionless natural frequencies of the rotating beam. **121**
Table 5.6 : Temperature-dependent coefficients of material properties for functionally graded material constituents. **123**
Table 5.7 : Thermophysical properties of ceramic and metal constituent of functionally graded materials. **127**
Table 5.8 : Variations of the fundamental frequencies of rotating FGM beams to rotation speed, and material distribution ($L/h=5$, $c_b=c_h=0$, $\mu=0$, $\xi=0$, $T=300^oK$) **139**
Table C.1 : Variations of the fundamental frequencies of rotating FGM beams to rotation speed, and material distribution ($L/h=5$, $c_b=c_h=0$, $\mu=0$, $\xi=0$, $T=1500^oK$) **176**
Table C.2 : Variations of the fundamental frequencies of rotating FGM beams to rotation speed, and material distribution ($L/h=20$, $c_b=c_h=0$, $\mu=0$, $\xi=0$, $T=300^oK$) **177**

Table C.3 : Variations of the fundamental frequencies of rotating FGM beams to rotation speed, and material distribution (*L/h=20, c_b=c_h=0, μ=0, ξ=0, T=900ºK*).....**178**
Table C.4 : Variations of the fundamental frequencies of rotating FGM beams to rotation speed, and material distribution (*L/h=20, c_b=c_h=0, μ=0, ξ=0, T=1500ºK*).....**179**
Table C.5 : Variations of the fundamental frequencies of rotating FGM beams to rotation speed, and material distribution (*L/h=5, c_b=c_h=0, μ=0, ξ=0, T=900ºK*).....**180**

LIST OF FIGURES

Page

Figure 1.1 : Boeing structural design criteria chart. **2**
Figure 1.2 : A comparison of thermal barriers used in thermal structures. **3**
Figure 1.3 : Functionally graded materials in the aerospace industry: (a) Turbine blades, (b) Jet engine nozzle, (c) Turbofan combustion chamber, (d) Rocket nozzle, (e) Space shuttle nose cone, (f) Hubble telescope empennages. **4**
Figure 1.4 : Examples of rotating aerospace structures (a) Gas turbine blades, (b) Tilt-rotor propellers, (c) Wind turbine blades, (d) Helicopter rotary wings. **6**
Figure 2.1 : A look at key fighter aircraft generations. **13**
Figure 2.2 : A look at key fighter aircraft generations from top view. **14**
Figure 2.3 : Evolution of fighter aircraft performance by generation. **15**
Figure 2.4 : Probable sources of thermal structural problems in aircraft components. **16**
Figure 2.5 : Composite material usage percentage in military aircraft structures over time. **21**
Figure 2.6 : Material distribution on F/A-18E/F and F-22. ..... **21**
Figure 2.7 : Classification scheme of composite materials **23**
Figure 2.8 : General overview of aerospace alloys **23**
Figure 2.9 : Corrugated flexibility in aircraft structures. **25**
Figure 2.10 : Schematic overview of active cooling of aircraft structures via flow patterns. **25**
Figure 2.11 : External insulation of aircraft structures **25**
Figure 2.12 : Flight test scenario. **27**
Figure 2.13 : Thermal contact conductance test setup. **27**
Figure 2.14 : Experimental setup for infrared radiant thermal testing with quartz lamp: a) Thermal shock testing platform, b) Schematic diagram. **27**
Figure 2.15 : Aircraft components placement within a test chamber. **29**
Figure 2.16 : Diagram of the creep testing machine. **29**
Figure 2.17 : Thermal buckling test setup. **29**
Figure 3.1 : Thermal stresses on the aircraft structures due to temperature difference and different material usage: a) Material distribution on the aircraft frame, b) Skin temperature due to aerodynamic heating, c) Low-temperature kerosene. **32**
Figure 3.2 : Coupled thermal mechanical design. **33**
Figure 3.3 : Thermal shock parameters of some materials as a function of temperature. **34**
Figure 3.4 : Thermal stress ratio of some materials as a function of temperature. **34**

Figure 3.5 : a) Collar's aeroelastic triangle, b) Thermal triangle, c) Garrick's aerothermoelastic tetrahedron, d) Aeroservoelastic tetrahedron, e) Aerothermoservoelastic hexahedron. **35**
Figure 3.6 : Strain compatibility of elastic solid elements: (a) Discretized elastic solid, (b) Undeformed configuration of solid elements, (c) Deformed configuration of solid elements with continuous displacements, (d) Deformed configuration of solid elements with discontinuous displacements. **36**
Figure 3.7 : Aerodynamic heating as heat source in modern aircraft. **38**
Figure 3.8 : Electrical power system as heat source in modern fighter aircraft. **38**
Figure 3.9 : The F-35 hybrid composite-metallic structure. **40**
Figure 3.10 : The F-22 wing composite-metallic substructure. **40**
Figure 3.11 : Equivalent bar structures for hybrid metal-composite structures: a) Bars in parallel, b) Bars with expansion gap, c) Bars with spring element. **41**
Figure 3.12 : Bending deflection of beams due to thermal loads. **44**
Figure 3.13 : Bending of beams due to thermal effects and transverse loads: a) Differential element of a beam, b) Load distribution on beam. **44**
Figure 3.14 : Components of stress within an element: a) Three-dimensional stress with nine scalar components in cartesian coordinates, b) Differential element with body forces and plane stresses in cartesian coordinates **49**
Figure 3.15 : Heat conduction for a differential control volume in cartesian coordinates. **49**
Figure 4.1 : DTM solution algorithm's flowchart. **59**
Figure 4.2 : Mode shapes of different beam types. **60**
Figure 4.3 : Convergence analysis of the natural frequencies for the 9^{th} mode. **61**
Figure 4.4 : Convergence of the natural frequencies for the 9^{th} mode with a/b: 2/5. **65**
Figure 4.5 : Convergence of the natural frequencies for the 9^{th} mode with a/b:2/3.. **65**
Figure 4.6 : Convergence of the natural frequencies for the 9^{th} mode with a/b:1. ..... **66**
Figure 4.7 : Convergence of the natural frequencies for the 9^{th} mode with a/b:3/2.. **66**
Figure 4.8 : Convergence of the natural frequencies for the 9^{th} mode with a/b:5/2.. **67**
Figure 4.9 : Algorithm flowchart of the Differential Quadrature Method. **77**
Figure 4.10 : Discretization process of the Euler-Bernoulli beam. **79**
Figure 4.11 : Convergence analysis of the natural frequencies for CGL grid distribution. **81**
Figure 4.12 : Discretization of a rectangular plate using CGL grid distribution. **83**
Figure 4.13 : Kirchhoff-Love plate mode shapes for SSSS BCs. **88**
Figure 4.14 : Finite difference approximation. **90**
Figure 4.15 : Stencil points for some finite difference operators. **92**
Figure 4.16 : FDM algorithm's flowchart. **93**
Figure 4.17 : Convergence analysis of the natural frequencies for the 9^{th} mode. **94**
Figure 4.18 : A finite difference mesh and nodal points. **96**
Figure 5.1 : Rotating structures: a) Turbine blades, b) Helicopter rotary wings, c) Wind turbine blades, d) Tilt-rotor propellers. **102**
Figure 5.2 : Dimensions and axis system of the rotating double tapered beam with flexible root and setting angle: a) Top view, b) Front view, c) Isometric view, d) Side view. **103**
Figure 5.3 : Defined displacements for the deformed rotating euler-bernoulli beam: a) Longitudinal view, b) Cross-sectional view. **104**

Figure 5.4 : The boundary conditions for the rotating tapered beam: a) Clamped, b) Elastically clamped, c) Simply-supported, d) Elastically pinned-free. **108**
Figure 5.5 : CGL grid distribution on the beam with elastically clamped and pinned–free boundaries. **109**
Figure 5.6 : Convergence analysis for clamped-free (C-F), simply supported-free (S-F), elastically clamped-free (EC-F), elastically pinned-free, elastically clamped and pinned-free (ECP-f) boundary conditions ($\lambda=0$, $c_b=c_h=0$, $\alpha=0$, $EI/K_{rot}=0.035$, $EI/K_{tran}=0.0001$)..... **112**
Figure 5.7 : Variation of the first natural frequency to the setting angle, hub radius, and the rotational speed for clamped-free boundaries ($c_b=c_h=0$, $K_{rot}=K_{tran}=0$). **113**
Figure 5.8 : Variation of the first natural frequency to the setting angle, hub radius, and the rotational speed for clamped-free boundaries ($c_b=c_h=0$, $K_{rot}=K_{tran}=0$). **113**
Figure 5.9 : Variation of the first four natural frequencies to rotational speed and taper ratios for clamped-free boundaries ($\xi=0$, $\alpha=0$, $K_{rot}=K_{tran}=0$). .. **114**
Figure 5.10 : Variation of the first four natural frequencies to breadth and height taper ratio for clamped-free boundaries ($\alpha = 0$, $\lambda=8$, $K_{rot}=K_{tran}=0$)... **115**
Figure 5.11 : Variation of the first four natural frequencies to rotational speed and taper ratios for clamped-free boundaries ($c_b=c_h=0$, $\mu=\eta=2$, $\xi=0$, $\alpha=0$, $K_{rot}=K_{tran}=0$). **115**
Figure 5.12 : Variation of the first four natural frequencies to dimensionless length for C-F ($K_{rot}=K_{tran}=0$), EC-F ($EI/K_{rot}=0.1$), S-F($K_{rot}=K_{tran}=0$), EP-F ($EI/K_{tran}= 0.0092$), ECP-F ($EI/K_{rot}=0.1$, $EI/K_{tran}=0.0092$) boundaries ($c=0$, $\mu=2$, $\lambda=8$). **116**
Figure 5.13 : Variation of the first four natural frequencies to spring coefficients for elastically clamped and pinned-free boundaries ($c_b=c_h=0$, $\mu=\eta=0$, $\xi=\alpha=0$, $\lambda = 0$) **117**
Figure 5.14 : Variation of the first four natural frequencies to spring coefficients for elastically clamped and pinned-free boundaries ($c_b=c_h=0.4$, $\mu=0$, $\xi=1$, $\alpha=0$, $\lambda =8$). **117**
Figure 5.15 : Material gradation through cross section of the beam made of FGM. **122**
Figure 5.16 : Influence of temperature and volume fraction index on the Young's modulus in the thickness direction (CMSX-4 and Zirconia)..... **125**
Figure 5.17 : Influence of temperature and volume fraction index on the Young modulus in the thickness direction (CMSX-4 and Zirconia)..... **125**
Figure 5.18 : Effect of temperature on material properties of functionally graded material constituents. **126**
Figure 5.25 : Material and temperature distribution on the turbofan engine. **128**
Figure 5.26 : Simplified View of a Rotating Blade in a Turbofan Engine. **128**
Figure 5.27 : Dimensions and axis system of the rotating pre-twisted functionally graded beam structure: a) Top view, b) Front view, c) Isometric view, d) Side view. **130**
Figure 5.28 : Kinematics of the deformed rotating beam structures: a) Longitudinal view, b) Cross-sectional view. **131**
Figure 5.23 : Variation of first four NNF of Timoshenko beam with slenderness ratio L/h ($\lambda = 0$, $c_b=c_h=0$, $\mu=0$, $\xi=0$, $T=300^oK$). **140**

Figure 5.24 : Variation of first four NNF of Timoshenko beam with slenderness ratio *L/h (λ = 10, c_b=c_h=0, μ=0, ξ=0, T=300ºK).* **140**
Figure 5.25 : Variation of first four nondimensional natural frequency with gradiation index k (*L/h* = 5, λ = 0, c_b=c_h=0, μ=0, ξ=0, T=300ºK) . **141**
Figure 5.26 : Variation of first four nondimensional natural frequency with gradiation index k (*L/h* = 5, λ = 10, *c=0, μ=0, ξ=0, T=300ºK*) **141**
Figure 5.27 : Variation of first four nondimensional natural frequencies of FGM beam with rotation speed λ (*L/h* = 5, c_b=c_h=0, μ=0, ξ=0, T=300ºK) **143**
Figure 5.28 : Variation of first four nondimensional natural frequencies of FGM beam with rotation speed λ (*L/h* = 20, c_b=c_h=0, μ=0, ξ=0, T=300ºK) **143**
Figure 5.29 : Variation of first four nondimensional natural frequencies of FGM beam with temperature (*λ = 0, L/h* = 5, c_b=c_h=0, μ=0, ξ=0) **144**
Figure 5.30 : Variation of first four nondimensional natural frequencies of FGM beam with temperature (*λ = 0, L/h* = 20, c_b=c_h=0, μ=0, ξ=0) **144**
Figure 5.31 : Variation of first nondimensional natural frequency of FGM beam with respect to temperature and rotation speed (*L/h* = 20, c_b=c_h=0, μ=0, ξ=0) **145**
Figure 5.32 : Variation of second nondimensional natural frequency of FGM beam with respect to temperature and rotation speed *(L/h = 20, c_b=c_h=0, μ=0, ξ=0)* **145**
Figure A.1 : Kirchhoff-Love plate mode shapes for SSSF BCs. **168**
Figure A.2 : Kirchhoff-Love plate mode shapes for SCSS BCs. **169**
Figure A.3 : Kirchhoff –Love plate mode shapes for SCSC BCs. **170**
Figure A.4 : Kirchhoff –Love plate mode shapes for SCSF BCs. **171**
Figure A.5 : Kirchhoff-Love plate mode shapes for SFSF BCs. **172**
Figure B.1 : Influence of temperature and volume fraction index on the thermal expansion coefficient in the thickness direction (CMSX-4 and Zirconia) **173**
Figure B.2 : Influence of temperature and volume fraction index on the thermal expansion coefficient in the thickness direction (CMSX-4 and Zirconia) **173**
Figure B.3 : Influence of temperature and volume fraction index on the Poisson ratio in the thickness direction (CMSX-4 and Zirconia) **174**
Figure B.4 : Influence of temperature and volume fraction index on the Poisson ratio in the thickness direction (CMSX-4 and Zirconia) **174**
Figure B.5 : Influence of temperature and volume fraction index on the density in the thickness direction (CMSX-4 and Zirconia) **175**
Figure B.6 : Influence of temperature and volume fraction index on the density in the thickness direction (CMSX-4 and Zirconia) **175**
Figure D.1 : Variation of first four NNF of Timoshenko beam with slenderness ratio *L/h (λ = 0, c_b=c_h=0, μ=0, ξ=0, T=900ºK).* **181**
Figure D.2 : Variation of first four NNF of Timoshenko beam with slenderness ratio *L/h (λ = 10, c_b=c_h=0, μ=0, ξ=0, T=900ºK).* **181**
Figure D.3 : Variation of first four NNF of Timoshenko beam with slenderness ratio *L/h (λ = 0, c_b=c_h=0, μ=0, ξ=0, T=1500ºK).* **182**
Figure D.4 : Variation of first four NNF of Timoshenko beam with slenderness ratio *L/h (λ = 10, c_b=c_h=0, μ=0, ξ=0, T=1500ºK).* **182**

Figure E.1 : Variation of first four nondimensional natural frequency with gradiation index k (L/h = 5, λ = 0, c_b=c_h=0, μ=0, ξ=0, T=900ºK)..... **183**
Figure E.2 : Variation of first four nondimensional natural frequency with gradiation index k (L/h = 5, λ = 10, c_b=c_h=0, μ=0, ξ=0, T=900ºK)..... **183**
Figure E.3 : Variation of first four nondimensional natural frequency with gradiation index k (L/h = 5, λ = 0, c_b=c_h=0, μ=0, ξ=0, T=1500ºK)..... **184**
Figure E.4 : Variation of first four nondimensional natural frequency with gradiation index k (L/h = 5, λ = 10, c_b=c_h=0, μ=0, ξ=0, T=1500ºK)..... **184**
Figure F.1 : Variation of first four nondimensional natural frequencies of FGM beam with rotation speed λ (L/h = 5, c_b=c_h=0, μ=0, ξ=0, T=900ºK) **185**
Figure F.2 : Variation of first four nondimensional natural frequencies of FGM beam with rotation speed λ (L/h = 20, c_b=c_h=0, μ=0, ξ=0, T=900ºK) **185**
Figure F.3 : Variation of first four nondimensional natural frequencies of FGM beam with rotation speed λ (L/h = 5, c_b=c_h=0, μ=0, ξ=0, T=1500ºK) **186**
Figure F.4 : Variation of first four nondimensional natural frequencies of FGM beam with rotation speed λ (L/h = 20, c_b=c_h=0, μ=0, ξ=0, T=1500ºK) **186**
Figure G.1 : Variation of first four nondimensional natural frequencies of FGM beam with temperature (λ = 10, L/h = 5, c_b=c_h=0, μ=0, ξ=0) **187**
Figure G.2 : Variation of first four nondimensional natural frequencies of FGM beam with temperature (λ = 10, L/h = 20, c_b=c_h=0, μ=0, ξ=0) **187**
Figure H.1 : Variation of third nondimensional natural frequency of FGM beam with respect to temperature and rotation speed (L/h = 20, c_b=c_h=0, μ=0, ξ=0) **188**
Figure H.2 : Variation of fourth nondimensional natural frequency of FGM beam with respect to temperature and rotation speed (L/h = 20, c_b=c_h=0, μ=0, ξ=0) **188**

VIBRATION ANALYSIS OF ROTATING BEAM STRUCTURES MADE OF FUNCTIONALLY GRADED MATERIALS IN A THERMAL ENVIRONMENT BY GENERALIZED DIFFERENTIAL QUADRATURE METHOD

SUMMARY

In recent years, there has been increasing curiosity in rotating aerospace structures such as gas turbine blades, helicopter rotary wings, wind turbine blades, tilt-rotor propellers, and flexible appendages of space vehicles due to various problems up to the chosen material type, boundary conditions, rotational speed, geometric properties, and environmental effects that have been studied for the best solution. To overcome these problems and prevent possible catastrophic failures, various analyses like vibration, buckling, static of structures, fatigue, and thermal are performed through engineering analysis software, user-written scripts based on numerical and semi-analytical methods, or specific test equipment. Then, the structure is improved by changing design parameters and operating conditions at the beginning of the design process if any unwanted cases occur. In specific design problems, user-written scripts are generally preferred as engineering analysis tools to obtain more accurate and precise results in a short time. The existence of this wide research field causes many researchers to turn their attention to the topics related to such types of rotating structures able to be modeled as beam elements.

One of the extensively studied topics realized under free vibration analysis is the computation of dynamic characteristics, which is a critical design and performance evaluation criteria designating the life of a structure, operating limits, and stability. Therefore, many numerical methods have been attempted to analyze and avoid possible resonance cases by calculating the dynamic characteristics of rotating beam structures accurately. Of these numerical approaches, DQM is first introduced by Bellman et al. to solve nonlinear partial differential equations accurately by expressing them as a set of algebraic equations. This technique uses weighting coefficients to approximate the derivatives of a function at a point and employs a weighted linear sum of the function values at all discrete points. In many areas of engineering problems, it presents satisfactory results for the well-optimized spacing of grid points and well-determined weighting coefficients by using suitable functions. Being computationally less expensive, easy implementation of non-classical boundary conditions, less memory requirements, simple algorithm building, derivation of new numerical methods by combining element-based methods to solve complex geometries, etc. are some reasons why preferred by many researchers.

The first objective of this study is to develop a mathematical model for a rotating double-tapered beam with a flexible root i.e. elastic restraints on the root of the beam attached to a rigid hub and present a numerical solution algorithm based on DQM to compute the dynamic characteristics of the beam. As a beam model, the Euler-Bernoulli beam theory is employed to model the system easily with a reasonable result in the first part of free vibration analysis. Using DQM, the governing differential equations of beam and boundary conditions are transformed into a set of linear

algebraic equations written in the matrix form. Both of them are defined in different matrices, and boundary conditions are entered by updating corresponding rows of the system matrix created for the governing differential equations, which gives great flexibility to use various nonclassical support types defined as mixed-type partial or ordinary differential equations. Differently from previous studies based on DQM, the effect of rotary inertia, setting angle, and linear changes in taper ratios on dynamic characteristics are investigated. Also, the effect of hub radius and rotational speed are presented akin to previous research findings. To validate the solution method, the obtained results are compared with other studies in the open literature.

The second objective is to investigate the elevated temperature and material effects on the mechanical behavior of the beam structures made of functionally graded materials, including shear deformations. Under a uniform temperature distribution, the variations in natural frequencies and mode shapes are investigated for temperature-dependent material properties. The findings of the second part of the solution present that the gradational composition of material, thermal loads, and shear deformation have a significant effect on the dynamic characteristics of the beam structures exposed to elevated temperatures. To overcome the softening effect of high temperatures, the composition of the ceramic-metal mixtures must be determined accurately by employing meshless numerical approaches such as DQM.

To sum up, a comprehensive study about free vibration analysis of beam structures used in the aerospace industry has been presented through the thesis, providing assessments of their vibration behavior. Understanding the structural dynamics of these structures is vital in sectors like aerospace, energy, and manufacturing.

FONKSİYONEL DERECELENDİRİLMİŞ DÖNEN KİRİŞ YAPILARIN ISIL ORTAMDA GENELLEŞTİRİLMİŞ DİFERANSİYEL KARELEME YÖNTEMİ İLE TİTREŞİM ANALİZİ

ÖZET

Son yıllarda, havacılık sektöründe artan talepler doğrultusunda, dönen kiriş yapıların detaylı analizine duyulan ihtiyaç daha belirgin hale gelmiştir. Bu yapılar, özellikle yüksek dönme hızlarında ve yükler altında çalışan turbofan motor kanatları, helikopter rotor kanatları, rüzgar türbini kanatları ve uzay araçlarının esnek uzantıları gibi kritik unsurların bir parçasıdır. Dönen kirişler, bu tür yapıların bir boyutlu elemanlara indirgenerek, yapısal analizlerinin hızlı ve etkili bir şekilde yapılmasını ve istenilen yapısal dayanıklılığı sağlayacak boyutların belirlenmesi sağlar. Bu tür sistemlerde yüksek hız ve sıcaklık gibi dış etkenler nedeniyle karmaşık termal ve mekanik yüklenmeler meydana gelir. Bu nedenle, dönen kiriş yapıların dinamik davranışlarını anlamak, yalnızca yapısal bütünlüğün korunması için değil, aynı zamanda uzun ömür ve güvenilir işleyiş açısından da büyük önem taşır.

Dönen kirişlerin serbest titreşim analizleri, bu tür yapıların yüksek hızlarda rezonans durumuna girme riskini ve buna bağlı titreşim kaynaklı hasar potansiyelini önceden tahmin etmeyi amaçlar. Rezonans durumuna giren bir yapı, doğal frekanslarında titreşir ve bu durum, genellikle yapının dayanıklılığı üzerinde olumsuz etkilere yol açar. Bu tür bir titreşimle karşılaşıldığında, yapının hasar görme olasılığı yüksek olur ve uzun vadede performans kayıpları yaşanabilir. Bu bağlamda, dönen kirişlerin titreşim analizleri, yapının tasarım optimizasyonunda, malzeme seçiminde ve bakım planlarının oluşturulmasında önemli bir mühendislik aracıdır. Dinamik analiz sonuçları, tasarım süreçlerinde karar verme sürecine doğrudan katkı sağlar. Yapıların uzun süreli dayanıklılığı, mühendisler tarafından yapılan bu analizlerle artırılır.

Dönen kiriş yapılarının tasarımında dikkate alınması gereken parametreler, yalnızca dönme hızı veya geometrik boyutlarla sınırlı değildir; yapıların çalışma ortamında maruz kaldığı yüksek sıcaklık ve sıcaklığa bağlı olarak değişen malzeme özellikleri de önemli birer faktördür. Havacılık yapıları gibi zorlayıcı koşullar altında çalışan yapıların yüksek sıcaklıklara maruz kalması, malzemede çeşitli termal gerilmelere yol açar. Yüksek sıcaklıkların etkisi altında yapı malzemelerinde oluşan termal gerilmeler, malzemenin elastik modülü, yoğunluk ve sönüm oranı gibi özelliklerde değişikliklere neden olur. Bu tür değişiklikler, dönen kirişlerin titreşim özelliklerini doğrudan etkiler. Örneğin, sıcaklık arttıkça malzemenin elastikiyeti azalabilir veya genlik büyük oranda artabilir, bu da kirişin titreşim karakteristiklerini değiştirir.

Özellikle motor parçaları gibi uçak yapılarında sıcaklığın artması, yapısal elemanların bütünlüğünü ve işlevselliğini doğrudan etkiler. Bu yapısal elemanlar yüksek sıcaklık altında çalıştıklarında, dayanıklılığın ve ömrün korunabilmesi için malzeme özelliklerinde meydana gelen değişimlerin de modellenmesi gerekir. Termal etkiler, malzeme özelliklerinde zamana bağlı değişimlere yol açarak yapının doğal frekanslarını ve mod şekillerini değiştirir. Bu nedenle, sıcaklık etkilerinin titizlikle

dikkate alınması, dönen kiriş yapılarında doğru titreşim analizleri yapılmasını sağlar ve güvenilir sonuçlar elde edilmesine katkıda bulunur.

Serbest titreşim analizleri, dönen kiriş yapılarının yüksek hızlarda güvenli bir şekilde çalışabilmesi için kritik öneme sahiptir. Bu analiz, yapının rezonansa girebileceği frekansları ve mod şekillerini belirleyerek, titreşim kaynaklı hasarları önceden öngörme olanağı sunar. Rezonans, yapının doğal frekanslarında titreşmeye başlaması anlamına gelir ve bu durum, yüksek genlikli titreşimlere ve yapısal hasara yol açabilir. Bu analizler sayesinde, dönen yapının dinamik davranışının en iyi şekilde anlaşılarak, mühendislere malzeme seçiminden geometrik tasarım optimizasyonuna kadar geniş bir yelpazede karar alma olanağını sağlar. Ayrıca, titreşim analizlerinin sonuçlarına dayanarak bakım aralıkları ve periyotları belirlenir; bu sayede yapının uzun vadede güvenli çalışması sağlanır. Serbest titreşim analizleri, hem güvenlik hem de maliyet açısından önemli faydalar sağlayarak dönen yapıların dayanıklılığını ve uzun ömürlülüğünü artırır. Örneğin, bir rotor kanadının rezonans frekansının hesaplanması, kanat yapısının hangi hızda çalışması gerektiği hakkında bilgi verir ve böylece çalışma aralıkları optimize edilirek yapının ömrü ve bakım aralıkları uzatılabilir. Bundan ötürü, havacılık veya enerji sektöründe, dönen yapıların uzun ömürlü ve dayanıklı olabilmesi için serbest titreşim analizlerinin sonuçları dikkate alınarak çeşitli tasarım optimizasyonlarına ihtiyaç vardır.

Dönen kiriş yapılarının serbest titreşim analizindeki yönetici denklemleri ayrıklaştırmak için kullanılan sayısal yöntemlerden biri olan Genelleştirilmiş Diferansiyel Kareleme Yöntemi (GDKY), mühendislik problemlerinde etkin bir çözüm yöntemidir. GDKY, düşük hesaplama maliyeti, sınır koşullarının kolay bir şekilde uygulanabilmesi, düşük bellek gereksinimleri ve basit algoritma yapısı gibi avantajlarından ötürü katı cisim mekaniği ve çeşitli araştırma alanlarındaki denklemlerin çözülmesinde tercih edilmektedir. Bu yöntem, dönen yapıların karmaşık yapısal analizlerinin doğruluğunu artırarak daha doğru ve güvenilir sonuçlar elde edilmesine yardımcı olduğu için diğer nümerik ve yarı analitik çözüm yöntemlerine tercih edilmiştir. Benzer şekilde, diğer mühendislik problemleri de GDKY'nin sahip olduğu özelliklerden ötürü kullanmaya elverişlidir. Örneğin, GDKY'nin sağladığı çözüm esnekliği sayesinde farklı sınır koşullarına ve malzeme özelliklerine sahip yapıların titreşim analizleri kolaylıkla yapılabilmektedir.

Dönen kiriş yapılarının üretiminde kullanılan malzemeler arasında Fonksiyonel Derecelendirilmiş Malzemeler (FGM) son yıllarda dikkat çekmektedir. FGM'ler, mekanik ve termal özelliklerin konum bazında, yapının kalınlığı veya boyu doğrultusunda, kademeli olarak değiştiği metal seramik karışımı özel malzemelerdir. Bu özellik, malzemelerin sıcaklık ve mekanik yük altındaki davranışlarını optimize etmelerini ve ısıl gerilmeleri kalınlık boyunca değişen malzeme bileşimine göre yumuşak geçişini sağlar. Bu özelliklerinden ötürü, FGM'ler, dönen kiriş yapılarının sıcaklık ve yük altında daha dayanıklı olmasına katkı sağladığı için özellikle havacılık ve enerji sektöründe yüksek sıcaklığa maruz kalan yapılarda tercih edilir. Örneğin, bir motor kanadı FGM kullanılarak üretildiğinde, kanatçığın yüksek sıcaklık ve dönme hızları altında daha iyi dinamik ve statik performans gösterdiği görünmektedir. Ayrıca, FGM'lerin malzeme özelliklerinin yapı boyunca dağılımının sürekli olması, yapının verimliliğini artırır ve ömrünü uzatır.

Anlatılanlar doğrultusunda bu çalışmada, dönen kiriş yapıların yüksek sıcaklık altında maruz kaldığı termal ve merkezkaç yüklerinin titreşim davranışı üzerindeki etkilerin de dikkate alınarak dinamik modelin çıkarılması ve GDKY kullanılarak yapılan

analizler ile farklı malzeme ve tasarım parametreleri için yapının doğal frekansları ve mod şekillerinin hassas bir şekilde belirlenmesi hedeflenmektedir. Böylece, titreşim analizlerinin sunduğu bilgiler ışığında yapının dayanıklılığı artırılabilir ve kritik öneme sahip parçaların daha güvenli bir şekilde çalışması sağlanabilir. Ayrıca, dönen yapılarda yüksek performans ve uzun ömürlü bir yapısal bütünlük sağlanarak ilgili sektörlerde maliyet ve zaman tasarrufu sağlanabilir.

Havacılık, enerji ve imalat gibi sektörlerde, bu tür yapıların sıcaklık etkisine bağlı olarak dinamik özelliklerinde meydana gelebilecek değişikliklerin öngörülmesi büyük bir avantaj sağlar. Örneğin, havacılık sektöründe yüksek hızlı motor parçalarının rezonans frekanslarının doğru bir şekilde belirlenmesi, uçak güvenliği için kritik öneme sahiptir. Benzer şekilde, enerji sektöründe rüzgar türbinleri gibi yapılar da sürekli döner durumda olduğundan, yapısal bileşenlerin titreşim analizleri ile güvenilirliğinin sağlanması büyük ölçüde önem taşır. Sıcaklık ve malzeme etkilerinin de hesaba katıldığı bu tür analizler, yapının tasarımının optimizasyonu ve bakım periyotlarının belirlenmesi için de yol gösterici bir rol oynar.

Özetlemek gerekirse, bu çalışma, dönen kiriş yapıların sıcaklık etkisi altında titreşim analizine yönelik önemli bir katkı sunmaktadır. Diferansiyel Kareleme Yöntemi (DKY) kullanılarak yapılan analizler, dönen kiriş yapıların doğal frekansları ve mod şekillerini doğru bir şekilde belirleyebilmekte, bu da mühendislik kararlarının güvenilirliğini artırmaktadır. Özellikle yüksek sıcaklık altında çalışan dönen yapılar için güvenli çalışma aralıklarının belirlenmesi ve rezonans risklerinin önceden tespit edilmesi, yapısal hasarların önlenmesine katkıda bulunur. Çalışmanın sonuçları, dönen yapıların güvenilirliğini ve dayanıklılığını artırarak mühendislik uygulamalarında daha güvenilir kararlar alınmasına olanak tanır.

1. INTRODUCTION

In the design cycle of aircraft, structural analysis plays a vital role in ensuring the safety, durability, and longevity of the aircraft. By means of the structural analyses in Figure 1.1, we can assess the strength of the aircraft components to determine the potential weak points in the structure, optimize material distribution, and guide the structural design [1-3]. Of these analyses, vibration analysis helps in identifying the natural frequencies and mode shapes of structural components, which is essential for avoiding probable resonance conditions and fatigue that can lead to catastrophic failure in aerospace structures [4].

Except for vibration analysis, other analyses are also conducted in the design steps of aircraft to understand whether they meet safety standards and structural design criteria. For instance, fatigue analysis focuses on how materials handle repetitive loading, while static analysis computes stresses and strains for applied loads [5]. Aeroelasticity analysis investigates the interaction between aerodynamic forces, elasticity, and inertial forces to evaluate structural stability [6], like buckling analysis. Damage and tolerance analysis is used to detect probable cracks and the post-damage behavior of the structure [7, 8].

In recent decades, the use of functionally graded material (FGM) has become increasingly popular in aircraft components exposed to elevated temperatures. Therefore, their vibration characteristics must be investigated like other components, including their composition and gradual properties so that we can understand how temperature-dependent properties influence natural frequencies, mode shapes, and dynamic responses.

Unlike conventional materials with uniform characteristics, FGMs feature a continuous variation in composition. This property is highly effective in alleviating thermal stresses in thermal structures due to their unique gradation [9-11]. The resistance to thermal shocks due to sudden temperature changes is another significant reason why it is preferred in rotating thermal structures so that thermal stress distributes more uniformly through the thickness of the structure. Additionally, the

customizability of its composition during the manufacturing process allows engineers to make precise gradations, enabling the creation of optimized structures for the unique thermal stress challenges. These advantages of FGM can also be seen in Figure 1.2, which makes it clear why it is used in rotating structures. Traditional shielding might fail due to thermal mismatches and sharp thermal stresses that induce cracking and spalling. Conversely, the structures made of FGM present a smooth transition in a stress diagram.

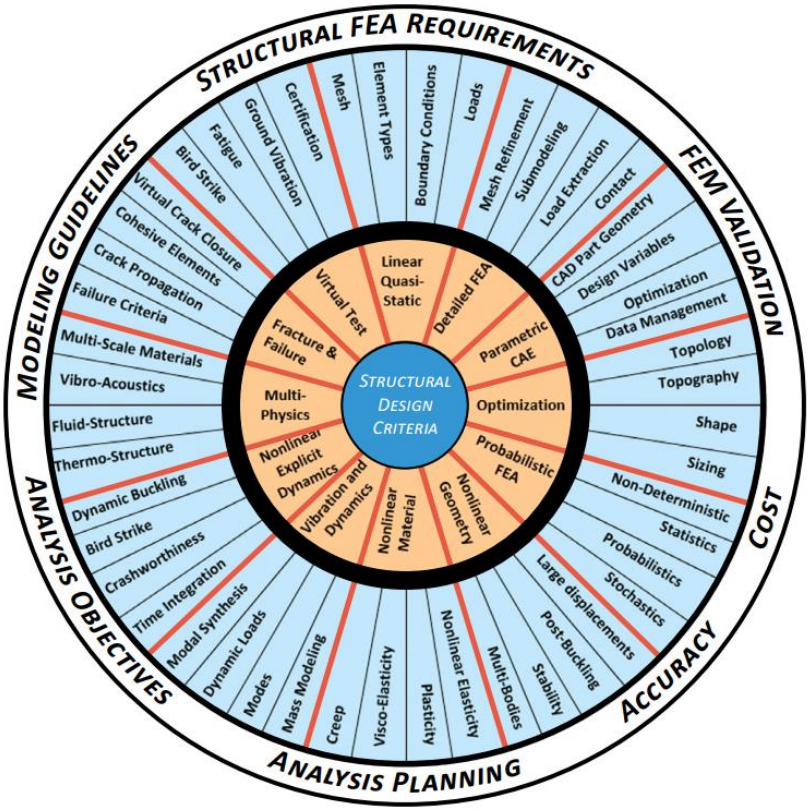

Figure 1.1 : Boeing structural design criteria chart [1].

Except for turbine blades, jet engine nozzles, rocket engines, space shuttle noses, and satellite empennages are other applications of FGM within the aerospace industry, as can be seen in the Figure 1.3 [12-15]. Beyond these examples, it might be applied to gear structures, reflectors, solar panels, leading edge of hypersonic vehicles, and so on.

The following literature review about vibration analysis of rotating structures in thermal environment summarizes recent studies in the literature and employed numerical techniques, and parameters affecting the dynamic characteristic of the beam.

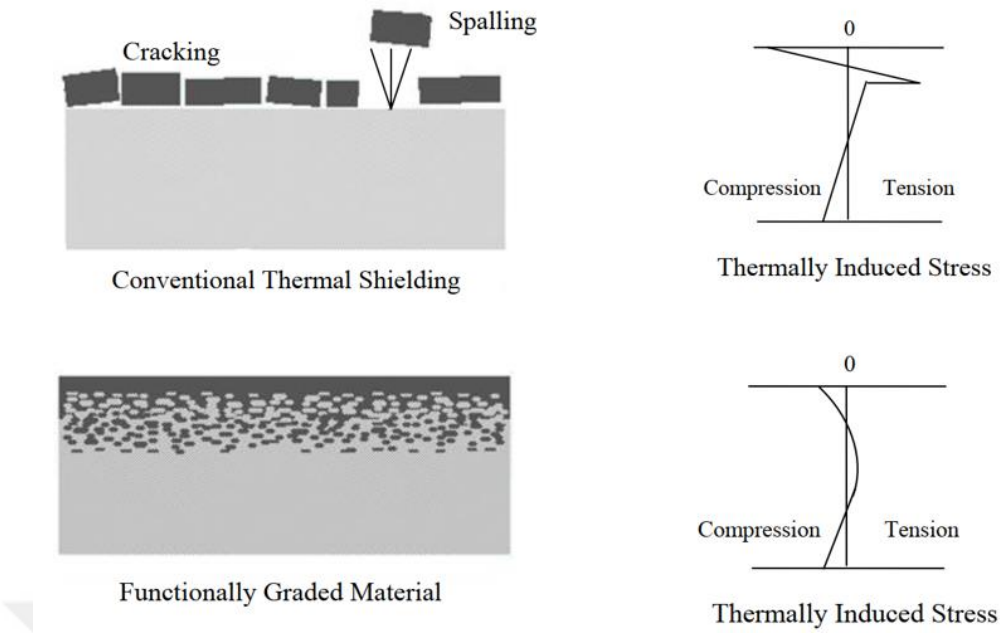

Figure 1.2 : A comparison of thermal barriers used in thermal structures [9].

1.1 Literature Review

The dynamic analysis of rotating structures, especially in the context of free vibration behavior, is one of the important research topics in various engineering applications such as aerospace, mechanical, and structural, as illustrated in the Figure 1.4. In the open literature, there are numerous studies on understanding the parameters affecting vibration characteristics, solutions employing various methods, and more accurate modeling techniques for these structures.

In the first part of this literature review, the recent advancements in their vibration analysis are presented, assuming these structures are modeled with beam elements. The effects of high temperatures and variable material properties through the thickness direction are meticulously investigated in the second part of this review.

Numerous papers in the literature have focused on the vibration analysis of rotating beams employing various numerical methods. For instance, Lee and Lee [26] used a transfer matrix method (TMM) to compute the free vibration characteristics of a rotating height tapered Euler-Bernoulli beam (EBB) in the case of bending vibration and investigated the effects of variations in taper ratio and rotation speed on the dynamics characteristics. In their next paper [27], they examined the same effects for a double-tapered beam. Similarly, Rui et al. [28] applied TMM to the helicopter rotor fuselage system to analyze the flapwise vibration of hingeless rotor blades modeled as

a uniform EBB. Huang et al. [29] studied the power series method (PSM) to determine the natural frequency of rotating EBB in the case of flapwise bending and coupled lagwise-axial vibrations and investigated the effects of Coriolis force at a high angular velocity. Adair and Jaeger [30] used PSM for the dynamic response of a rotating nonuniform EBB with an elastic restraint root. Adair [31] also studied vibration analysis by using the Adomian decomposition method (ADM) for a uniform pre-twisted case. Mao [32] solved a similar problem with arbitrary boundary conditions by the modified version of ADM.

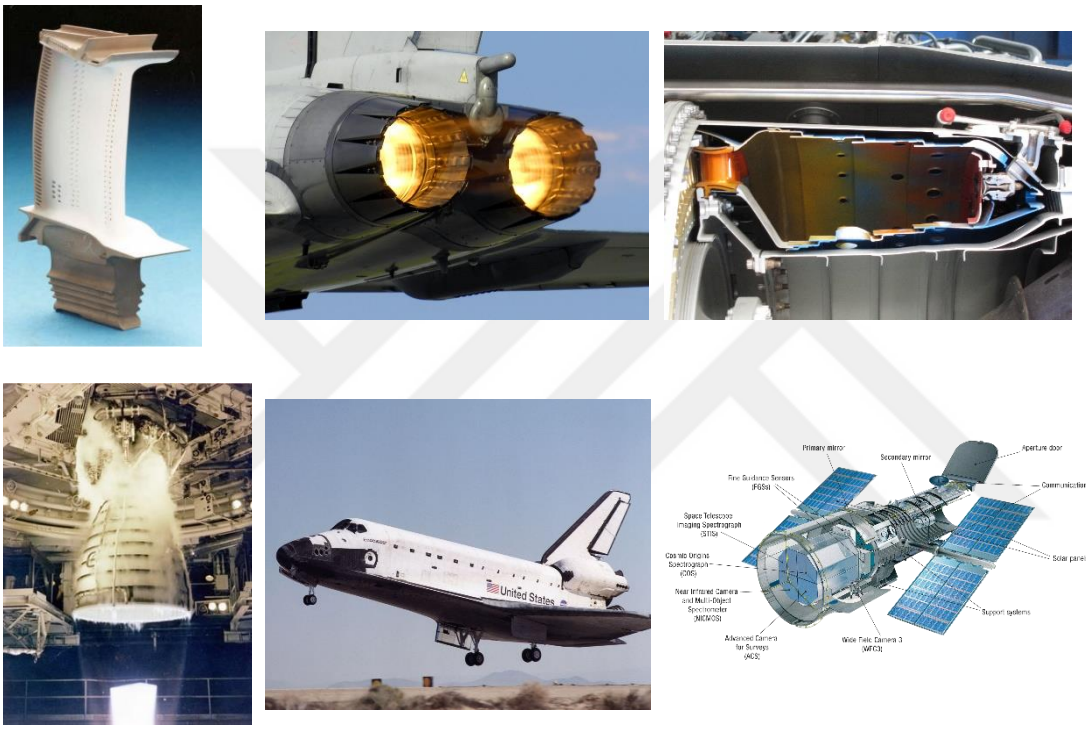

Figure 1.3 : Functionally graded materials in the aerospace industry: (a) Turbine blades, (b) Jet engine nozzle, (c) Turbofan combustion chamber, (d) Rocket nozzle, (e) Space shuttle nose cone, (f) Hubble telescope empennages [16-25].

Aksencer and Aydogdu [33] investigated the effect of a point mass attached to anywhere on the flapwise vibration of a rotating composite beam by using the Ritz method. Ramesh and Rao [34] studied the Rayleigh-Ritz method (RRM) to investigate the effect of the hub radius, power-law index, and angular speed on the natural frequencies for a rotating homogenous uniform beam made from FGM. In a similar vein, Oh and Yoo [35] used RRM to determine vibration characteristics of rotating cantilever beam orienting inward with a setting angle and point mass. Roy and Meguid [36] solved the governing differential equations of a rotating blade structure in a gas turbine engine by using RRM and investigated the effects of coupled lateral and axial

displacements due to Coriolis force, rotary inertia, shear deformation, and nonlinear thickness variations on the natural frequencies.

Panchore et al. [37] studied the meshfree Galerkin technique for the free vibration analysis of a rotating uniform EBB. Banerjee [38] used the dynamic stiffness method (DSM) to compute the vibration characteristics of a rotating uniform and tapered EBB for various classical boundary conditions. Banerjee et al. [39] did a similar study to see the limitations of the theory, the effects of design parameters. Expanding on this, Banerjee and Kennedy [40] studied the Coriolis effect between the axial and lagwise bending deformations by using DSM. Wang and Werely [41] used a spectral finite element technique for the determination of modal characteristics of rotating uniform tapered blades.

Kaya [42] studied the differential transform method (DTM) for flapwise bending vibration analysis of a rotating Timoshenko beam. Ozdemir and Kaya [43] employed DTM for tapered and double tapered EBB cases to determine vibration characteristics. Mei [44] applied DTM to a centrifugally stiffened rotating uniform EBB to analyze free lateral vibrations. Nourifar et al. [45] did the vibration analysis of rotating EBB having an exponentially decaying circular cross-section by the mean of DTM. Kumar et al. [46] used DTM to investigate the height taper ratio effect on free vibration of a rotating beam covered with functionally graded material.

Choi et al. [47] studied the differential quadrature method (DQM) to compute the dynamic characteristics of a spinning Timoshenko beam for classical and elastic boundary conditions. Bambill et al. [48] used DQM to calculate the natural frequencies of free vibration for a rotating cantilever Timoshenko beam. Rajasekaran [49] used both DQM and DTM to analyze the free bending vibration of rotating EBB made from FGM. Chen et al. [50] analyzed the flapwise bending vibration of a rotating tapered beam by using a variational iteration method. Chen and Du [51] solved the transverse vibration of a rotating beam with elastic boundaries employing a Fourier series. Hodges and Rutkowski [52] studied a variable order finite element method to analyze the free vibration of uniform and nonuniform rotating beams with respect to dimensionless rotation speed. Hoa [53] investigated the effect of tip mass, setting angle, etc. on the vibration frequency of a rotating beam using the finite element method (FEM). Abbas [54] employed FEM to investigate the dynamic stability of a rotating beam with a flexible root. Chung and Yoo [55] used a finite element analysis

for a cantilever beam to determine time responses and the natural frequencies of chordwise and flapwise motion.

Figure 1.4 : Examples of rotating aerospace structures (a) Gas turbine blades, (b) Tilt-rotor propellers, (c) Wind turbine blades, (d) Helicopter rotary wings [16-25].

Until now, the numerical approaches employed in the free vibration analysis of rotating beams have been discussed. Another critical design aspect of these structures is the effect of high temperatures and variable material properties. Therefore, our attention now shifts to the vibration analysis of rotating beam structures made of FGM in a thermal environment. To express these effects on the structural dynamics, gas turbine or turbofan engine blades can help us to understand the thermal structural problems encountered.

The probable problems in rotating structures exposed to high temperatures encompass a wide range of issues such as aerothermoelastic instabilities, material degradation, thermal buckling, and so on. The importance of these problems is highlighted in a vast number of studies like the study of Van Nimwegen [56] in 1961, and investigated how to prevent them. With this aim, Men et al. (2022) [57] investigated the effects of thermal buckling on thin-walled blades in high-speed aircraft engines. Padture (2019) [58] addressed the challenges in protecting ceramic-matrix composites in gas-turbine engines from high-temperature degradation. Complementing this study, Guo et al.

(2019) [59] explored the microstructural degradation of a failed gas turbine blade. The degradation of protective coatings used in turbine components was discussed by Blachnio et al. (2021) and Szczepankowski and Przysowa (2022) [60,61]. Additionally, engine instabilities and blade failures resulting from thermal loads are investigated in the studies of Reddy (2004), Sharma (2020), Wang (2021), and Mourad (2023) [62-65].

To overcome these thermal-structural challenges in rotating structures, thermal barrier coatings made of functionally graded materials can be a solution in addition to cooling strategies and the use of flexible structures. The success of FGM at alleviating thermal stress and other detrimental effects of temperature on the structure is highlighted in the studies of Sankar (2002), Huda (2013), and Hu (2020) [66-68]. Therefore, the utilization of Functionally Graded Materials (FGMs) in rotating beams used to model rotating structures has been the subject of extensive investigation.

In addition to studies discussing numerical techniques [69-76], a vast number of studies have been devoted to the vibration of rotating FGM beams. To emphasize the crucial role of material properties on natural frequencies, Kumar and Rao (2017) conducted the flapwise vibration analysis of rotating FGM beams [77]. A similar study was done, including taper ratios, by Maganti and Nalluri (2015) [78]. Oh and Yoo (2016) examined the effect of pretwist angle on the vibration characteristics of gas turbine blades [79]. Amoozgar and Gelman (2022) explored the free vibration in porous FGM rotating blades [80]. Rathore and Sanjay (2022) concentrated on the modal analysis of functionally graded sandwich blades [81]. Ramesh and Mohan (2013) studied the natural frequencies of pre-twisted rotating FGM beams [82]. Zhang and Zhu (2014) developed a dynamic model for a rotating hub-FGM beam system [83]. Tian, Zhang, and Hua (2019) introduced a semi-analytical model to analyze the free vibration in rotating FGM beams with porosities and complex cross-sections [84].

In the case of the temperature effect included, the dynamic behavior of FGM beam structures is changed, which has been discussed by many researchers. Oh et al. (2003) [85] focused on the vibration analysis of thermoelastic thin-walled rotating blades made of FGM. Oh, and Librescu (2003) [86] analyzed the vibration of rotating turbomachinery blades made of FGMs under temperature gradients. Concurrently, Librescu et al. (2005,2008) [87,88] investigated the vibration and stability of thin-walled beams in high-temperature environments. Fazelzadeh et al. (2007) [89] studied

the effect of aerodynamic heating on the vibrational characteristics of rotating thin-walled FGM blades. In a related vein, Fazelzadeh and Hosseini (2007) [90] conducted the aerothermoelastic behavior of rotating FGM beams in turbomachinery. Further contributing to this field, the studies [91-101] can be found exploring the effect of geometric nonlinearities, used shear deformation theories, and thermomechanical behavior of the materials.

1.2 Purpose of the Thesis

The primary objectives of the thesis can be outlined as follows:

1. The first objective of this study is to accurately model the dynamic behavior of rotating beam structures commonly found in mechanical systems like turbines, aircraft wings, and rotor blades. Therefore, vibration analyses are conducted to understand the dynamics of the structure, which are also crucial for ensuring that these structures maintain their structural integrity and safety while they are effectively withstanding various operational stresses to prevent catastrophic failures.
2. The second objective is to investigate the effect of temperatures on the dynamic characteristics. Elevated temperatures can significantly change the stiffness and damping properties of the components as a result of the temperature dependent material properties, especially when exposed to high temperatures. In the vibration analysis of the structures made of metals or composites, the softening effect of thermal loads must be included to assess their structural performance and stability, precisely.
3. In many practical applications, the root or base of a rotating structures such as in turbine blades, rotor blades, or machinery components are not perfectly rigid. From this aspect, the effects of flexible constraints must be included into the mathematical model of the beam to reflect the boundary conditions more accurately.
4. Components operating at high temperatures are covered with thermal barriers made of ceramic materials to prevent the detrimental effects of the temperature. One of the such materials is functionally graded materials, which are characterized by their graded properties that vary across the thickness of the beam. In such cases, the effect of material gradations on the vibration

characteristic of the structure must be investigated. With this aim, this research also utilizes free vibration analysis of the beam structures made of FGM when subjected to thermal loads. In these analyses, the assessment of changes in stiffness, strength, and damping properties provides a comprehensive understanding of their behavior.

5. Pretwist and variation in material properties through thickness cause damping effects on the structures, which decrease the frequencies of the beam. The effects of damping must also be determined by conducting parametric analyses to minimize them.
6. The development of a numerical tool to perform vibration analysis in turbo machinery for discussed design parameters is another outcome of this study.

1.3 Structure of the Thesis

This thesis is organized across six comprehensive chapters. The introductory chapter begins with an overview of the current advancements in the field of vibration analysis of rotating beam structures and numerical methodologies used in computational mechanics. Additionally, this chapter highlights the paramount of the conducted study.

Chapter two presents a brief overview of the thermal structural design aspects of supersonic aircraft. Historical development of supersonic aircraft, particularly in military aviation, the effects of high temperatures on airframes, advanced engineering materials, airframe construction, and thermal-structural tests are discussed throughout the chapter.

In chapter three, the focus of the thesis shifts to the essentials of thermoelasticity. Fundamental definitions are given, and elasticity theory and heat transfer mechanisms in aircraft structures are summarized to understand the concept of thermal stress. Basic expressions for thermoelasticity are provided.

The numerical methods used in computational mechanics are discussed in chapter four. Specifically, the Differential Quadrature, Differential Transform, and Finite Difference Methods are conducted for one and two-dimensional vibration problems. Solution methodology for the beam and plate vibrations, algorithm scheme, and comparison of these methods are presented.

According to the foundation built in the first four chapters, Chapter Five presents the numerical solution to the vibration problem in rotating beam structures by employing the Differential Quadrature Method. The effects of design parameters such as rotation speed, material properties, and high temperature are examined to minimize probable thermal problems and mitigate the detrimental effects of elevated temperatures.

Ultimately, the general overview of the conducted thesis study, significant outcomes, and future study suggestions are carried out in the conclusion section. As future studies, this study can be expanded to aerothermoelastic and vibration analysis of rotating functionally graded structures, or structural optimization.

2. THERMOSTRUCTURAL DESIGN ASPECTS

The development of supersonic aircraft has been a remarkable journey, originating from the pioneering planes like the Bell X-1 and the Soviet MiG-15 introduced in the 1950s to today's sophisticated engineering marvels. In this process, meticulous attention is dedicated to the construction and materials employed in these aircraft, ensuring they can withstand harsh operating conditions during high-speed flight. To understand the thermal-structural challenges we face in these vehicles, it is essential to investigate the evolution of the supersonic aircraft must be investigated, particularly the development of supersonic fighter planes. With this aim, this chapter is dedicated to advancement in supersonic aircraft, thermal-structural problems in aircraft structures, materials for high-speed flight, airframe construction, and thermostructural testing procedures.

2.1 Fighter Aircraft Generations

From the early days of flight to modern aircraft, the attempt at supersonic flight has shaped the course of aviation history, redefining the limits of speed, agility, and combat capability [102-103], which can be seen in Figures 2.1 and 2.2. In these figures, the evolution of fighters across generations with key features is illustrated [105-107].

As seen, first-generation fighters specialized in basic air-to-air combat and had minimal maneuverability. Second-generation fighters improved their air-to-air capability by incorporating radar and guided missiles. Third-generation aircraft had enhanced radar, guided missiles, and ground attack capabilities. Fourth-generation fighters featured improved avionics and partial stealth. However, fifth-generation fighters usher in a new era in aviation by seamlessly integrating superior stealth, multi-role adaptability, integrated sensors, and unparalleled situational awareness. Also, these fighters, capable of striking first, excelling in fundamental roles, and redefining air warfare, represent the pinnacle of modern combat airpower [104].

Designing fifth-generation stealthy fighter aircraft necessitates a sophisticated integration of signature reduction across the electromagnetic spectrum, hence increasing both survival potential and weapon efficacy. Achieving radar invisibility is critical, but low observability across several spectral domains is also important. This trade-off approach applies to stability and control, requiring minimal control surfaces while maintaining balance for stealth. Tailless variants expand the function of flight control systems, potentially incorporating thrust vector control to remove vertical tails. Weight issues resulting from fuel scarcity and internal weapon limits make fighter aircraft design difficult. Substantial interior weapon bays have an impact on structural integrity, stealth, and weapon release dynamics, increasing uncertainty. Fuel and supplies demand a larger fuselage, which adds weight. Within this complex design context, including Radar Absorbing Materials (RAM) tiles and applying Radar Absorbing Paint (RAP) to leading edges emerge as critical techniques. Carbon fiber composites (CFC) offset weight surges caused by signature control, hence strengthening structural integrity [112-114].

The evolution of fighter aircraft performance [108-111] by generation in terms of climb rate, max takeoff weight, service ceiling, thrust-to-weight ratio, max range, max speed, and max thrust is depicted in Figure 2.3. This provides a comprehensive overview of how these critical metrics have advanced across the various eras of fighter aircraft development. As seen from this figure, the climb rate has continuously improved over generations, indicating increased engine power and aerodynamic efficiency. Maximum takeoff weight has consistently increased, owing to stronger airframes and superior materials. The service ceiling, or operational altitude, has risen dramatically as a result of advances in propulsion and flight control systems in developed modern aircraft. The thrust-to-weight ratio, a vital measure of maneuverability and acceleration, is steadily increasing, demonstrating the ongoing pursuit of greater agility. Max range, max speed, and max thrust have all seen significant increases, demonstrating the constant pursuit of greater operating reach and velocities.

First Gen	Second Gen	Third Gen	Fourth Gen	Fifth Gen
1940s to 1950s	*1950s to 1960s*	*1960s to 1970s*	*1970s to 1990s*	*1990s to date*
Features: ▪ *Basic Avionics* ▪ *Unguided Bombs/Rockets* ▪ *Visual Air Combat* ▪ *Turbojet Engines*	***Features:*** ▪ *Radar Warning Receivers* ▪ *Advanced Aerodynamic Design and Engines* ▪ *BVR Engagement* ▪ *Infrared Missile*	***Features:*** ▪ *Improved Maneuverability* ▪ *Guided RF Missiles* ▪ *Multirole Fighters* ▪ *BVR Air Combat*	***Features:*** ▪ *Head-up displays*	***Features:*** ▪ *Low Observable* ▪ *Increased SA* ▪ *LPI/LPD* ▪ *High Range Precise Weapons*
F-86 Sabre	*F-104 Starfighter*	*F-4 Phantom II*	*F-16*	*F-22 Raptor*
F-84 Thunderjet	*F-106 Delta Dart*	*Mirage F-1*	*Eurofighter-Typhoon*	*F-35A Lightning II*
MIG-15	*MIG-21*	*MIG-23*	*Dassault Rafale*	*T-50 PAK FA*
MIG-17	*Chengdu J-7*	*Shenyang J-8*	*MIG-29*	*Chengdu J-20 Black Eagle*
	MIG-19, F-105 Thunderchief	*SU-17, MIG-27, IAI Kfir, Saab 37 Viggen Thunderbolt, Northrop F-5 A/B*	*F/A-18 Super Hornet, PAC JF-17 Thunder, Tornado, Chengdu J-9/10, Mirage 2000, MIG-31, F-15 Eagle, SU-27/30/33/35, JAS-39 Gripen, F-14 Tomcat* ***Features:*** ▪ *SAR, AESA, Higher SA* ▪ *TVC Engines*	*YF-23 Black Widow II, KF-21 Boramae, Mitsubishi X-2 Shinshin, Shenyang FC-31, TAI TF-X, Sukhoi SU-75 Checkmate, HAL AMCA*

Figure 2.1 : A look at key fighter aircraft generations [105-107].

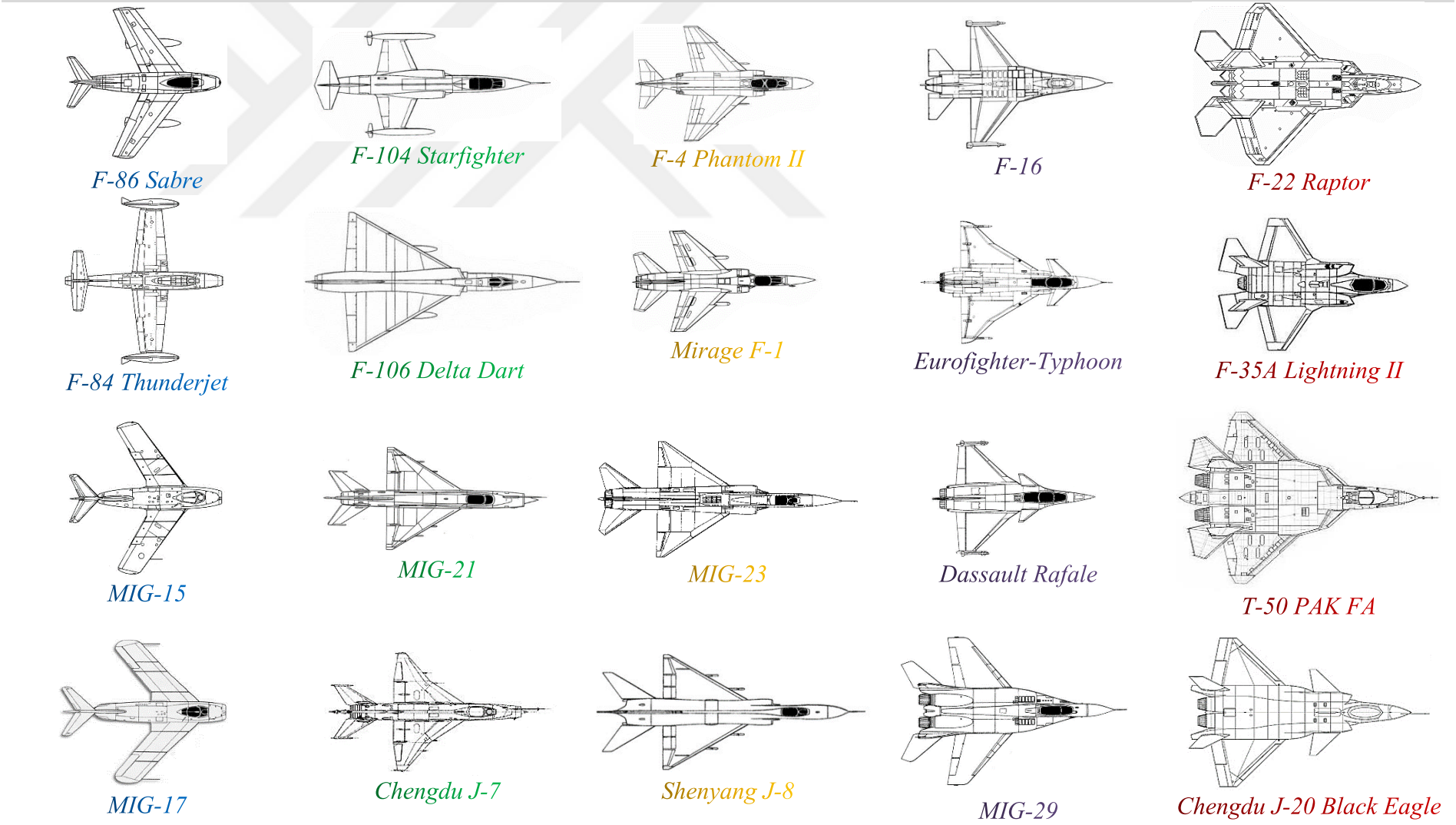

Figure 2.2 : A look at key fighter aircraft generations from top view.

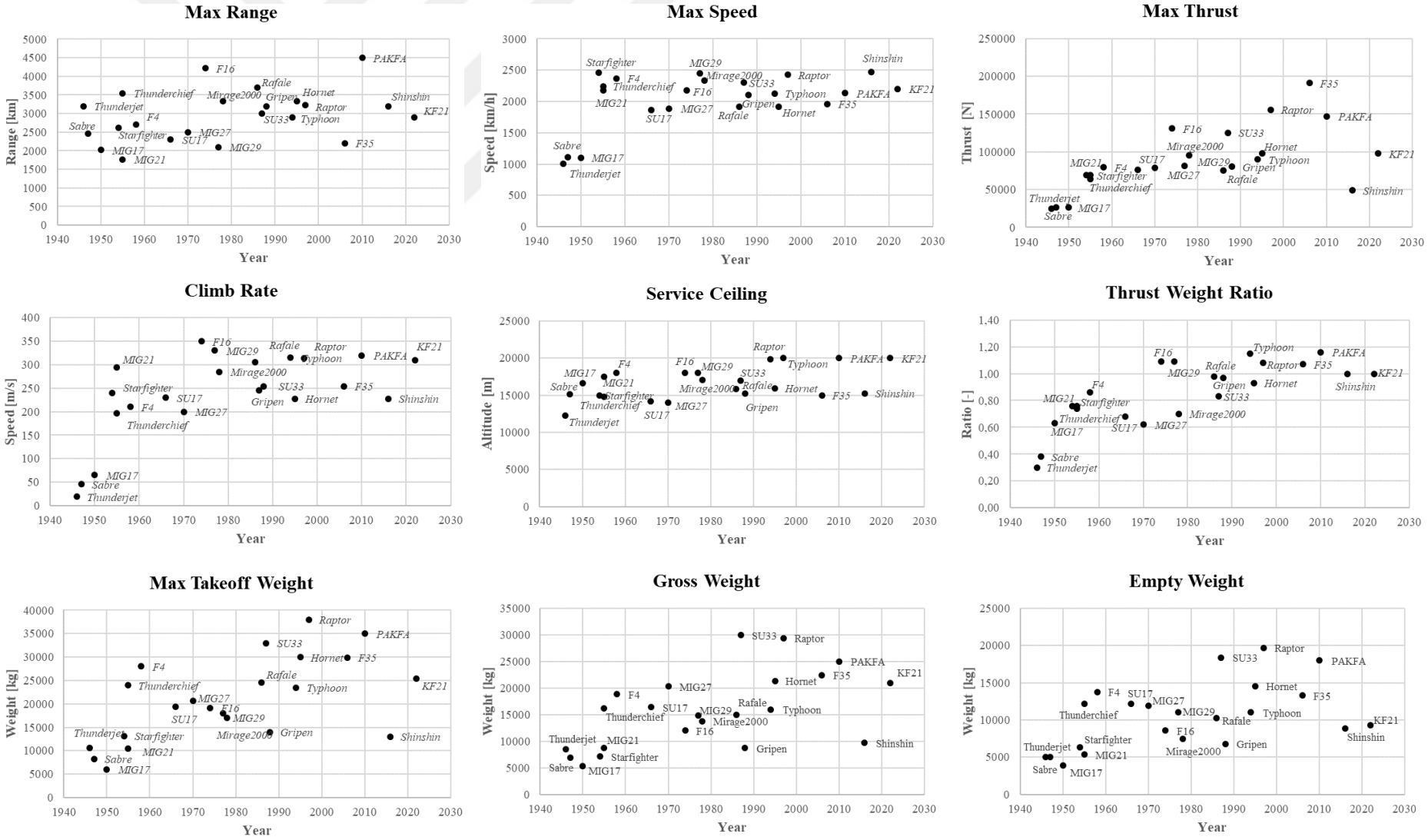

Figure 2.3 : Evolution of fighter aircraft performance by generation [108-111].

2.2 High-Temperature Effects in Aircraft Structures

Thermal-structural issues like thermal buckling, material degradation, thermal fatigue, and aerothermoelastic instabilities have been extensively researched by the aerospace community since the beginning of flying. To address these issues, they are focusing their efforts on the development of novel materials and optimized structures that can endure the severe temperature extremes encountered during flight. Figure 2.4 depicts the potential thermostructural problems seen in supersonic aircraft. The dynamic interaction of temperature distribution, material behavior, and mechanical response, are primary reasons for these issues.

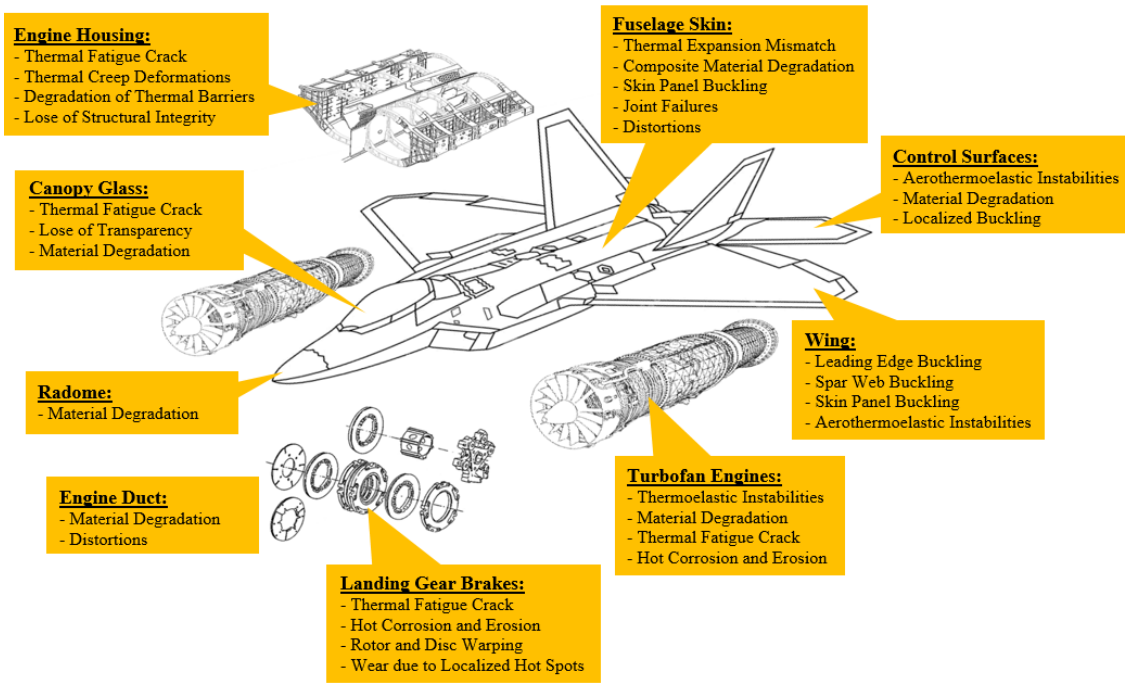

Figure 2.4 : Probable sources of thermal structural problems in aircraft components.

Understanding of these thermal problems in aircraft structures has grown via a series of pioneering research conducted at the beginning of the supersonic aircraft era, with substantial contributions made between 1940 and 1965. Each of these investigations has contributed significantly to our understanding of how temperature changes affect materials and aircraft structural integrity. A brief examination of these basic papers demonstrates the progressive nature of research throughout this key period.

Studies of thermal stresses caused by high temperatures in airplane structures have proven essential. Tendeland and Schlaff's 1948 flight experiments concentrated on temperature gradients in a high-speed fighter aircraft's wing structure during fast dives

[115]. In this study, the complexities of assessing thermal stresses caused in wing structure by temperature gradients during high-altitude dives is emphasized. O'Sullivan's 1951 research investigated elements influencing aerodynamic heating, whereas Parkes' 1953 study looked at transient thermal stresses in a cellular wing structure [116,117]. Loveless and Boswell's 1954 research addressed thermal strains caused by materials expanding with temperature, while Rendel's 1954 study emphasized growing thermal difficulties in high-performance aircraft [118, 119]. Pohle and Oliver's 1954 work sought to address temperature distribution and thermal stress difficulties in a supersonic wing model [120]. Walker's 1955 research addressed structural issues caused by kinetic heating, whereas Schuh's 1955 study computed temperature distributions and thermal stresses in a skin-shear web structure [121,122]. Mahlmeister, Ishimoto, and Ambrosio's 1955 work examined the influence of transitory external heating, whereas Chauvin's 1956 publication revealed aerodynamic heat transfer data at supersonic speeds [123, 124]. Hoff's 1956 work investigated thermal problems in aircraft structures during supersonic flight, while O'Sullivan's 1957 paper provided a theoretical examination of structural models under transient aerodynamic heating and external stresses [125, 126]. Brooks et al.'s 1957 study examined joint conductivity and internal radiation as influences on temperature distributions and thermal stresses [127]. Vosteen, McWithey, and Thomson's 1957 research looked at the effect of transitory heating on the vibration frequencies of basic wing structures [128]. Hoff's 1958 research investigated the effects of aerodynamic heating on airplane structures, including heat transport and appropriate materials [129]. Kitchenside's 1958 research classified the effects of kinetic heating in supersonic flight, while Kordes' 1961 study shed information on the structural heating experiences of the X-15 [130, 131]. Capey's 1965 research classified thermal stress mitigation approaches in aircraft structures into three categories: cooling, external insulation, and structural design, with an emphasis on material selection and design considerations against thermal stresses to meet kinetic heating difficulties [132].

Several important papers have considerably improved our knowledge of buckling caused by aerodynamic heating. Gossard and Roberts' 1951 study investigates the thermal buckling of flat plates in supersonic aircraft under nonuniform heating, providing insights into temperature distributions and buckle patterns that are critical for understanding thermal buckling in such aircraft [133]. Heldenfels and Roberts

(1951) discuss structural design issues associated with aerodynamic heating, focusing on creep and thermal buckling, highlighting the latter's importance in structural design for high-speed aircraft [134]. Hoff's 1956 study focuses on the thermal buckling of supersonic wing panels, providing important insights into temperature and thermal stress distributions in multicellular wing structures and establishing a buckling criterion for cover plates subjected to thermal stresses during supersonic flight [135]. Pride, Hall Jr., and Anderson's 1957 study investigates the impact of rapid heating on airframe component strength, finding that thermal stresses reduce bending loads at buckling for multi-web beams and ring-stiffened cylinders, emphasizing the potential for severe thermal stresses in airplane primary structures due to aerodynamic heating rates [136]. Mansfield's 1960 study focuses on leading-edge buckling in wings caused by aerodynamic heating, resulting in a formula for forecasting onset and examining post-buckling behavior [137]. Webber and Houghton's 1963 study examines the buckling of a simply supported rectangular plate under various in-plane stresses and presents a determinantal equation for estimating critical thermal stress magnitude while accounting for aerodynamic and inertia forces, as well as kinetic heating effects [138]. McKenzie's 1962 research of leading-edge buckling caused by aerodynamic heating in a thin built-up wing provides insights into spanwise thermal stress effects, calculated buckling load values, and criteria for leading-edge buckling in various dimensions [139].

Some research has focused on the complicated interplay between heat effects, aeroelastic behavior, and torsional stiffness. Budiansky and Mayers' 1956 work analyzes how aerodynamic heating affects the effective torsional stiffness of narrow wings, providing theoretical conclusions for solid wings at supersonic speeds and showing considerable potential losses [140]. Kochanski and Argyris' 1957 study undertakes a preliminary investigation into the effects of kinetic heating on the torsional and flexural stiffness of thin solid wings, broadening the research to include substantial deformations and offering insights into the stiffness of thin wings at supersonic speeds [141]. Biot's 1957 work investigates the effect of thermal stresses on the aeroelastic stability of supersonic wings, taking into account effects on effective torsional stiffness and anticlastic effects, and predicts a considerable impact on both [142]. Houbolt's 1958 thesis investigates aerothermoelastic problems during high-speed flight, focusing on dynamic aeroelastic effects and addressing changes in

strength properties and stiffness caused by elevated temperatures and thermal stresses, thereby contributing to our understanding of aerothermoelasticity [143]. Several seminal studies have made significant contributions to our understanding of thermal fatigue. Heath-Smith and Kiddle's 1975 study examined the effects of kinetic heating on fatigue in aluminum alloy airplane structures [144]. The study demonstrated how heating causes softening in strain-hardened materials, transferring local stress through creep. The study underscored the need to understand how frequent heating affects the gradual accumulation of fatigue damage at ambient temperature. Kroll's 1959 paper expanded this investigation to the relationship between aerodynamic heating and fatigue in airplane structures [145]. Reviewing expected physical conditions for future airplanes highlighted the need to include fatigue issues in design procedures. Specific research initiatives have focused on understanding the intricate relationship between thermal effects and creep. Libove and Heimerl's 1951 research investigates airplane structural difficulties caused by creep at temperatures seen in supersonic flight [146]. The study emphasizes the need to consider allowed deformation and intended service lifespan when designing airplane structures at high temperatures. Pope's 1961 paper provides a continuous solution for stress distribution in a basic wing surface under uniform temperature rise [147]. Taking into account the bending, shear, and direct stiffness of edge components, the analysis sheds light on stress distribution in the presence of creep, as well as the effect of aerodynamic heating.

In light of these pioneering studies [115-148], engineers must rigorously design, test, and apply new heat-resistant materials and active/passive cooling systems to preserve the structural integrity and lifetime of aircraft components while pushing the limits of flight in an age of ever-changing technological possibilities.

2.3 Materials for High-Speed Flight

The unique challenges faced by supersonic aircraft necessitate the use of materials with exceptional strength, heat resistance, and durability to ensure structural integrity and survivability. To provide these properties, a complex mixture of modern alloys and advanced composites is utilized to the thermal and mechanical load requirements. For example, modern aerospace alloys such as titanium and nickel-based superalloys are preferred at aft fuselage airframes and engine parts to provide strength and resistance to high temperatures while advanced composites such as carbon-fiber-

reinforced polymers (CFRP) and Bismaleimides (BMI) are used in fuselage skin exposed to aerodynamic heating or other thermal loads to provide compromising strength-to-weight ratio, suitability for higher-temperature applications, increased toughness, and resilience in challenging operational environments.

The use of composites in military aircraft from the first generation to the fifth generation has evolved dramatically, as seen in Figure 2.5. In the early days of aviation, composites were rarely used due to fabrication capabilities, high cost, and their unknown mechanical properties while conventional materials like aluminum and steel have dominated the building of military aircraft. However, as technology advanced in the aerospace industry, the second and third generations of military aircraft saw a steady increase in composite use, particularly in non-structural components. By the fourth generation, composites had established themselves as a vital component in aircraft construction. Composites serve a critical part in the present period of fifth-generation military aircraft, such as the F-35 Lightning II and F-22 Raptor, accounting for a considerable portion of the airframe, as shown in Figure 2.5. The gradual growth in composite utilization across generations represents a strategic reaction to the needs of contemporary warfare.

The main reasons for the use of composites in supersonic aircraft components can be ordered as weight reduction, excellent resistance to fatigue and corrosion, and stealth benefit in military applications. Furthermore, their design flexibility is another important advantage, which enables the fabrication of complicated forms and structures [153-156]. As previously stated, the materials used in airframes have evolved significantly between the Wright brothers' first powered-flight airplane and the present. This progress has resulted in the predominant usage of modern aerospace alloys, mostly aluminum, as well as the introduction of carbon-fiber-reinforced polymer (CFRP) composites [157]. The increased use and experience with CFRP composites have resulted in breakthroughs in both fibers and matrix materials, including thermosets and thermoplastics [158]. These advancements have resulted in CFRP composites with improved mechanical properties, allowing them to replace more traditional materials like aluminum and titanium alloys for primary structures in a variety of applications, including flaps, vertical and horizontal stabilizers, fuselages, avionics access, and landing gear doors [159-161].

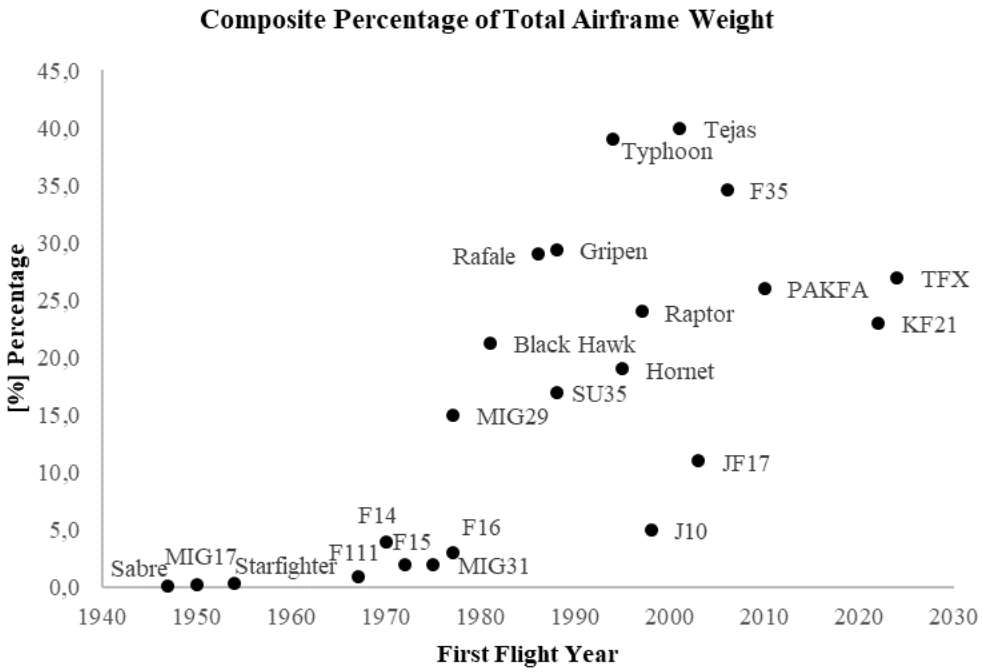

Figure 2.5 : Composite material usage percentage in military aircraft structures over time [149,150].

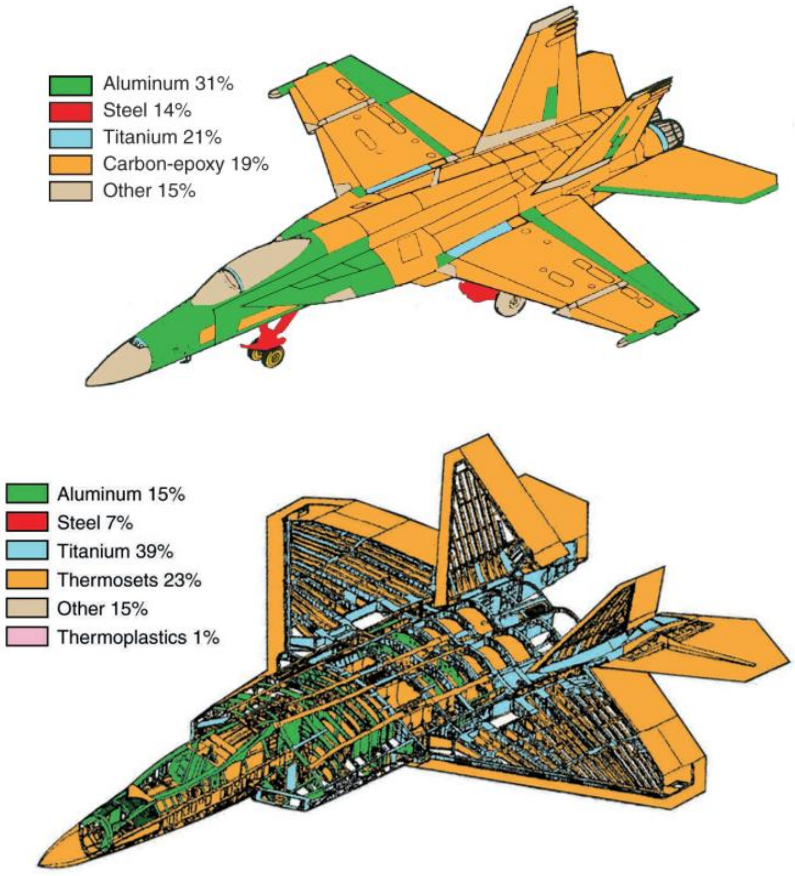

Figure 2.6 : Material distribution on F/A-18E/F and F-22 [151, 152].

Figure 2.6 illustrates the use of composite and alloy materials in various components of sample aircraft. CFRPs are commonly used in wings because of their high strength-to-weight ratio, which contributes to better performance. Glass Fiber Reinforced Polymers (GFRPs) and Aramid Fiber Reinforced Polymers (AFRPs) are often used in radomes since they require radiofrequency transparency and impact resistance. CFRPs are commonly used for structural components in the central fuselage, however, Metal Matrix Composites (MMCs) may be used in high-temperature locations. CFRPs benefit the aft fuselage because of their strength and weight advantages, and hybrid composites are adapted to specific requirements. Tails, which include vertical and horizontal stabilizers, frequently use CFRPs for their high strength and stiffness, which contributes to stability, while essential portions may use MMCs for increased temperature resistance. Figure 2.7 provides a broad overview of composite materials utilized in airplane construction.

Several reasons contribute to the fact that composites have not completely replaced metal components. To begin, composites are still being developed, with the introduction of novel fibers and matrices whose characteristics are not as well understood as those of metals. Second, some metals, such as titanium and steel, have mechanical and thermal qualities that are required for certain applications and that existing composites cannot entirely reproduce. Third, composites continue to have challenges in producing some complicated designs at a reasonable cost. Finally, this study found that composites had a greater production cost per kg than metals, notably aluminum [151].

The most prevalent alloys used in airplane constructions are aluminum alloys, titanium alloys, and high-strength steel alloys, as shown in Figure 2.8. Aluminum alloys are the most often used alloys in aircraft structural applications because of their well-known performance properties, low fabrication costs, vast design knowledge, and the availability of established production processes and facilities [162,163]. 2000 series aluminum alloys are specifically chosen for airframe structural applications due to their damage tolerance, whereas 7000 series alloys are used in the construction of upper wing skins, stringers, and horizontal/vertical stabilizers due to their higher strength when compared to other aluminum alloy classes [164].

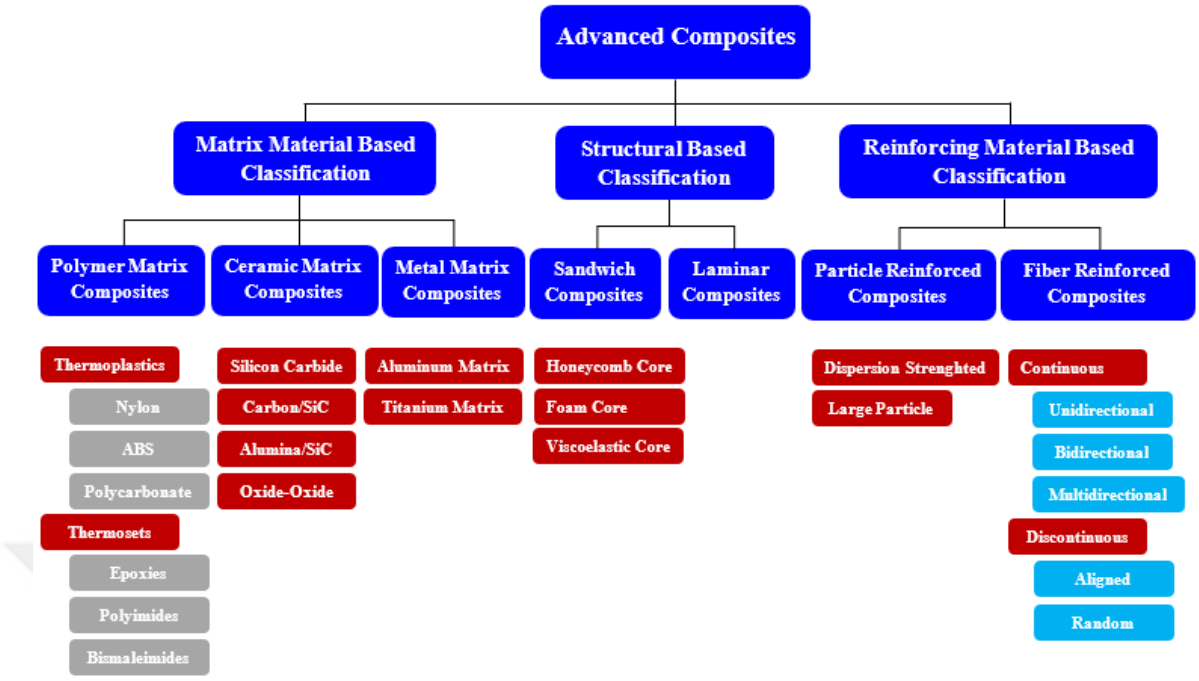

Figure 2.7 : Classification scheme of composite materials

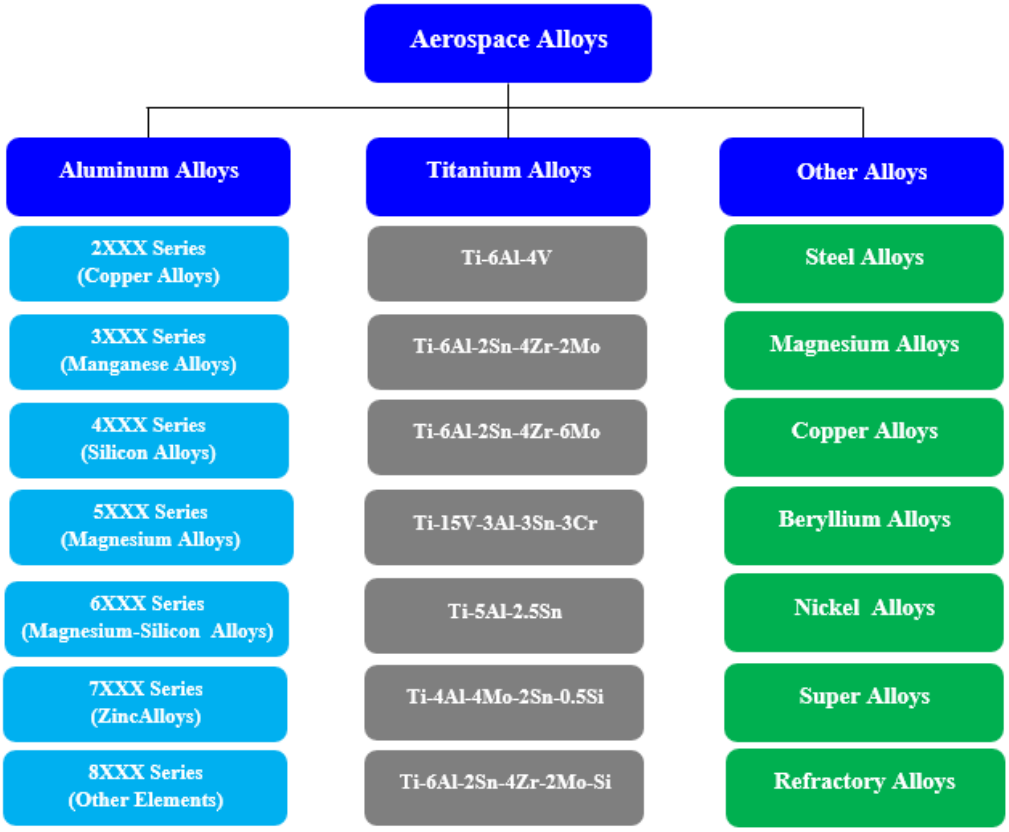

Figure 2.8 : General overview of aerospace alloys

As seen in Figure 2.5, titanium alloys are also highly preferred in aircraft structures exposed to high temperatures due to their high strength-to-weight ratio, corrosion resistance, and ability to tolerate extreme temperatures. Of the titanium alloy family, Ti-6A1-4V (Ti-6-4) is commonly used in engine components, and aft fuselage, while Ti-6A1-2Sn-2Zr-2Cr-2Mo-0.2Si (Ti-6-22-22), Ti-6A1-2Sn-4Zr-2Mo-0.2Si (Ti-6242), and Ti-10V-2Fe-3A1 (Ti-10-2-3) are employed in applications requiring elevated temperatures [165].

In addition to these materials, sandwich composites, functionally graded materials, and advanced steel alloys also are used in the various aircraft components. For instance, high strength-to-weight ratios are the reason why it is preferred in the fuselage skin of the vehicle while functionally graded materials are used in the components operating in high temperatures.

2.4 Airframe Construction

The airframe of supersonic aircraft exposes rapid temperature fluctuations and mechanical loads due to the dynamic nature of flight and operating environment, which necessitates airframes capable of withstanding intense coupled thermal and mechanical stresses. Therefore, design issues become crucial, including appropriate material selection, structural integrity, and aerodynamic efficiency. To alleviate the effects of thermal stresses, the use of thermal insulation, flexible corrugated structures, and advanced cooling systems are essential safeguards in critical areas exposed to elevated temperatures such as surrounding turbofan engines, heat exchangers, or the auxiliary power unit. Additionally, structural recoveries such as the integration of expansion joints can also be an alternative solution to tolerate thermal expansion without compromising structural integrity. These probable precautions and structural solutions to thermal stress are illustrated in Figures 2.9-2.11 [132,168-170].

In addition to these diverse techniques, the use of light alloy bulkheads [171], the application of a truss framework, curved structural elements, expansion cutouts in the webs [172], the application of a paint layer on the surface of the aircraft as an insulator [173], strain relievers in the intersection of aircraft components [174], and webs with expansion joints [132] are other techniques employed to effectively reduce thermal stresses in aircraft structures.

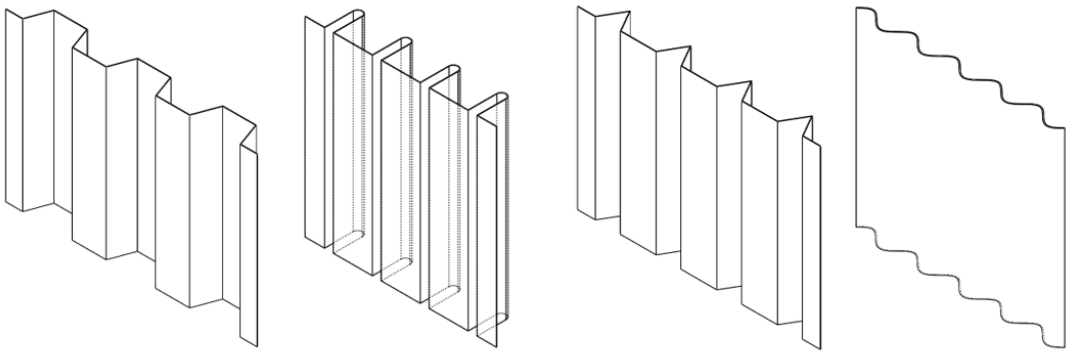

Figure 2.9 : Corrugated flexibility in aircraft structures [132,166].

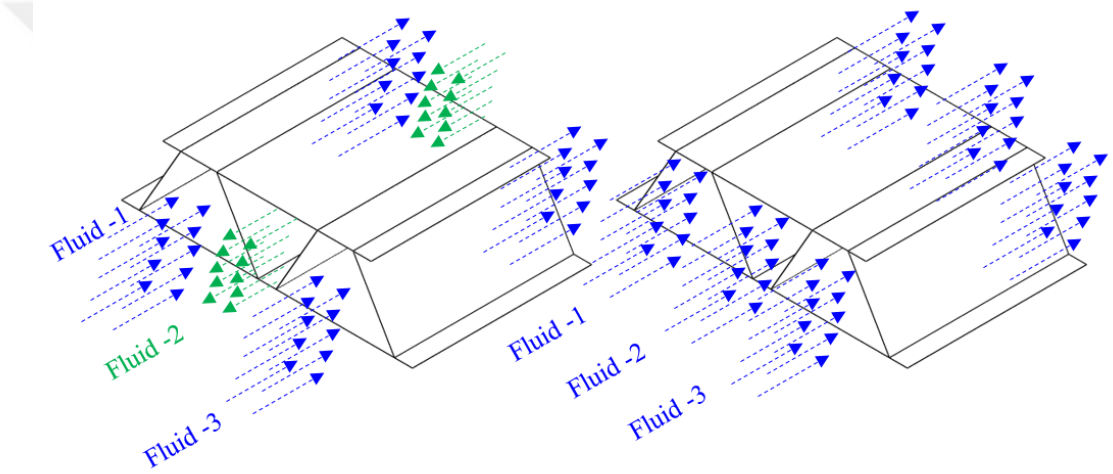

Figure 2.10 : Schematic overview of active cooling of aircraft structures via flow patterns [167].

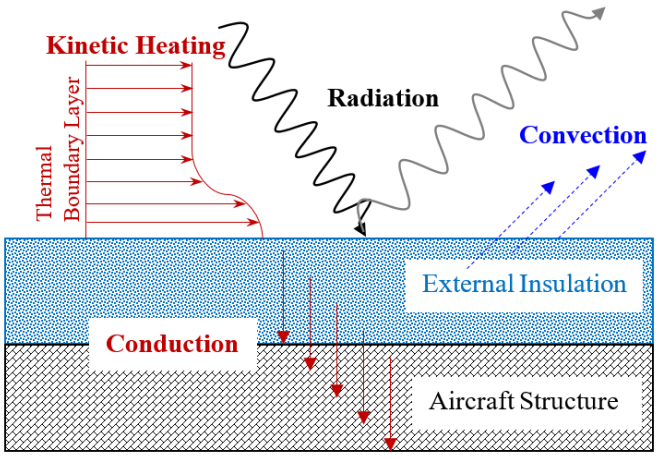

Figure 2.11 : External insulation of aircraft structures

2.5 Thermal Structural Tests

During the aircraft design cycle, a few of the key problems are selecting appropriate materials minimizing thermal stresses, and designing structures capable of withstanding the detrimental effects of high temperatures. To overcome these problems and find probable risky zones in the airframe, how different materials and structural components withstand the harsh thermal conditions aircraft face must be simulated by conducting thermal structural tests. With this aim, numerous thermal structural testing methods were developed in the post-World War II era after their importance was understood [175].

To certify the aircraft to specified safety standards such as MIL-STD 810 [176], provide empirical data for validation of computational models, and safety assurance, conducted thermal-structural tests can be classified into two groups structural tests and material property measurement tests. One of the structural tests is flight testing visualized in Figure 2.12, in which strain and temperature data are measured via strain gauges and thermocouples replaced to specific locations in the airframe by generating high-temperature gradients [177]. On the other hand, thermal contact conductance tests depicted in Figure 2.13 are realized to assess the efficiency of heat transfer between two objects in direct contact [178] as a material property measurement. The success of these tests is a function of applied pressure, temperature, interstitial medium, the thermal conductivity of the contacting materials, surface roughness, flatness deviation, asperity slope, gap thickness, hardness, yield strength, modulus of elasticity, and thermal expansion [179]. Another test that can be evaluated under the structural test is thermal shock testing. It helps identify potential weaknesses, such as cracks or deformations, and vulnerabilities in structures by applying different transient heating rates ranging from 5˚C/s to 30˚C/s [183] such as a test setup in Figure 2.14. Meanwhile, a virtual flight environment can be simulated by using environmentally conditioned chambers depicted in Figure 2.15 to test the aircraft components such as the wing or front fuselage. Within this chamber, engineers can observe the effects of extremely cold or hot temperatures on materials and assess the structural of components integrity by measuring thermal stress levels. Also, finite element model validation can be made in the aircraft design and development phase by subjecting the structure to a controlled temperature range from -60 °C to 150 °C for cold and hot day conditions [185, 186].

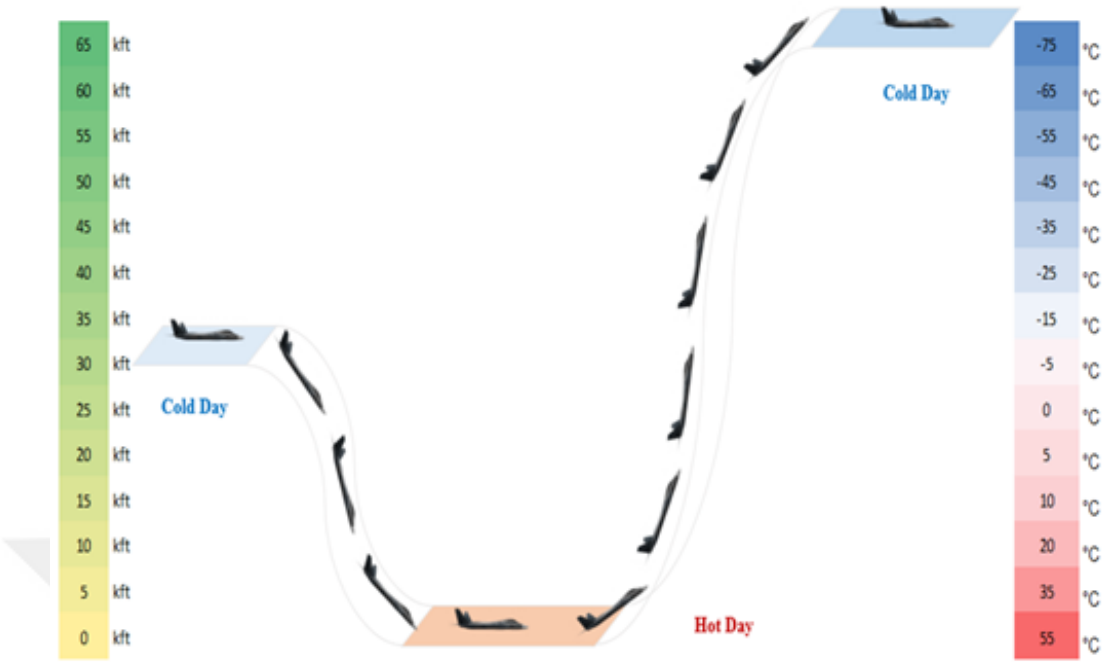

Figure 2.12 : Flight test scenario.

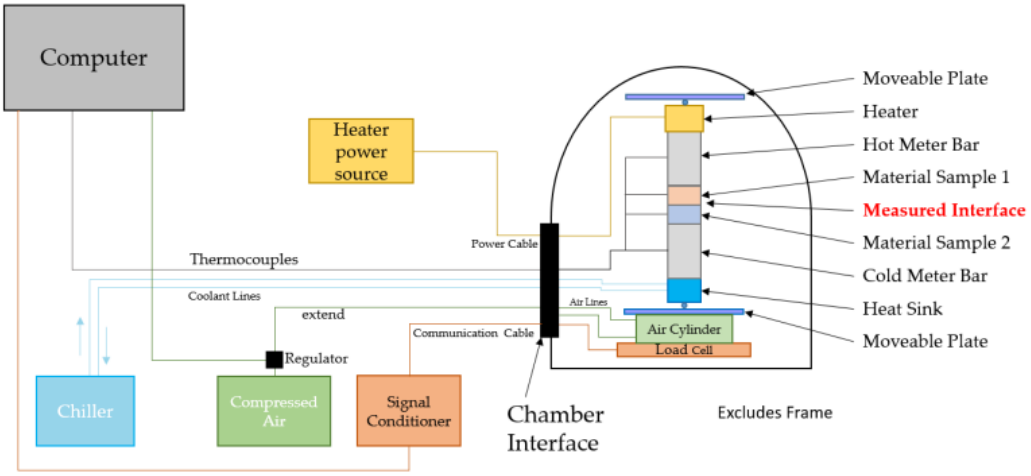

Figure 2.13 : Thermal contact conductance test setup [180].

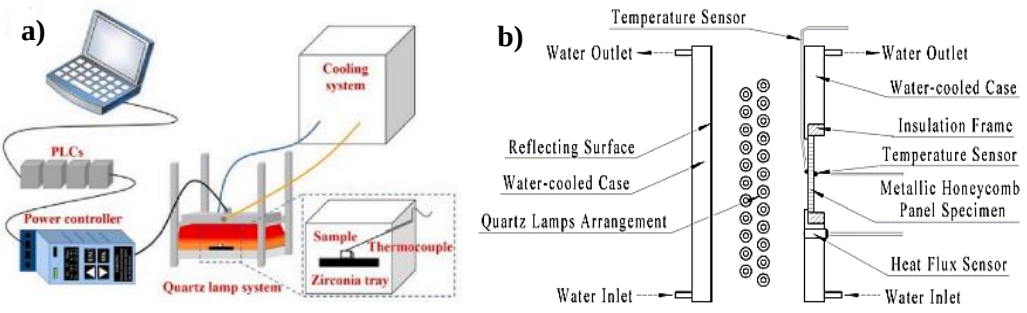

Figure 2.14 : Experimental setup for infrared radiant thermal testing with quartz lamp: a) Thermal shock testing platform [181], b) Schematic diagram [182].

The repeated temperature fluctuations experienced by the airframe cause thermal fatigue in the structural components of the vehicle. To assess their resistance to thermal fatigue, thermal cyclic testing is conducted by applying repetitive cycles of heating and cooling aircraft faces during the flight [187, 188]. The effect of thermal cycles on the structure is also investigated in various academic studies to show the effects of thermal fatigue and express the methodology of measuring the long-term durability of materials and detecting any potential degradation over time. For instance, Mueller's study on fiber metal laminates in wing skins and leading edges reveals changes in interlaminar shear strength after thermal cycling, highlighting the material's response to thermal fatigue [189] while adhesively bonded joints in hybrid structures are investigated under thermal and mechanical cycling conditions in another study [190].

As aforementioned in this section, it is essential to ensure the integrity and longevity of the structure. With this aim, another widely applied thermal-structural testing procedure is thermal creep testing [191], which is based on understanding the time-dependent deformation of materials exposed to prolonged elevated temperatures. The thermal creep test setup used for aircraft components such as engine parts or rivets [192] is shown in Figure 2.16. Meanwhile, structural stability must also be checked due to nonuniform thermal stress distribution in the airframe. To evaluate the behavior of structural elements, thermal buckling testing is employed. The schematic of the test setups used for basic structural elements is illustrated in Figure 2.17, where a test plate is heated along its centerline by the quartz lamp or electrical heater, or the parallel edges are maintained at constant temperature through chilled water flow in tubes.

In addition to these tests, the aircraft design process also involves fire resistance testing, hot gas testing, and thermal expansion testing, which ensure a comprehensive assessment of materials and structures. Among them, fire resistance testing is especially important due to the increasing use of composite materials in the aviation industry. In this test, artificial fire is generated by utilizing electric heating sources to simulate heat flux conditions in real-world fire scenarios so that the flammability of fiber-reinforced polymer or carbon/epoxy composites can be compared to safety standards as well as metals [195,196].

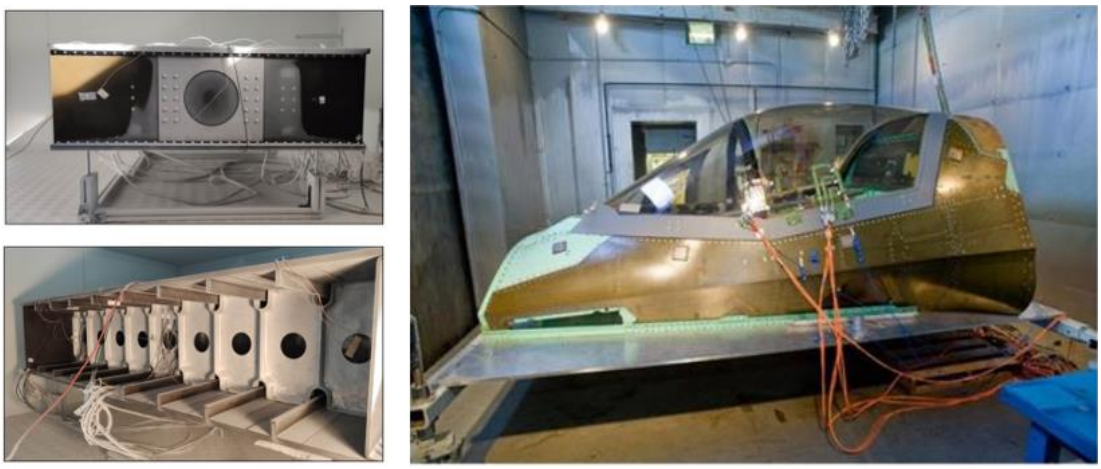

Figure 2.15 : Aircraft components placement within a test chamber [184, 185].

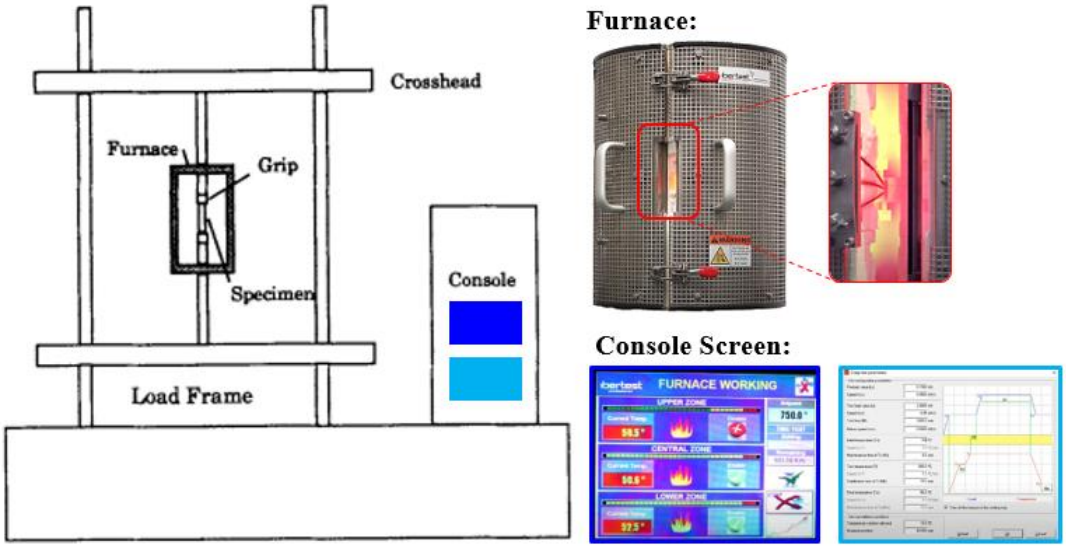

Figure 2.16 : Diagram of the creep testing machine [175, 193].

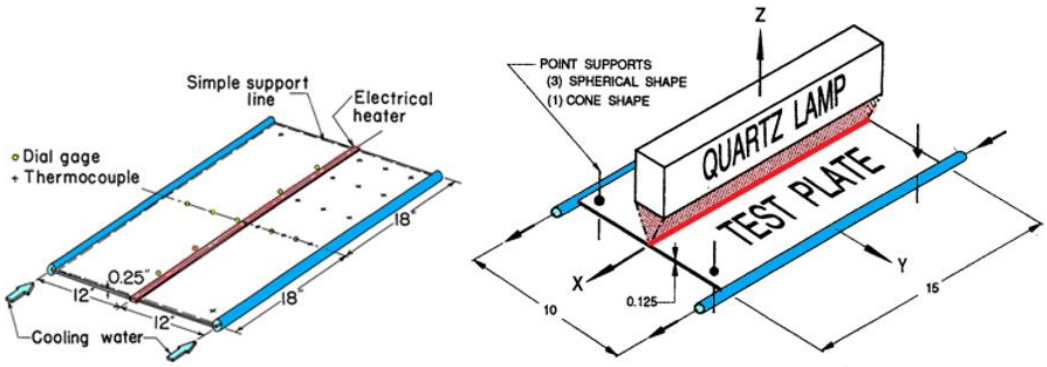

Figure 2.17 : Thermal buckling test setup [175,194].

2.6 Closing Remarks

The evolution of supersonic aircraft has been a remarkable journey that has seen tremendous advancements in engineering, materials science, and structural design. The development of these engineering marvels has not only pushed the boundaries of human ingenuity but has also posed unique challenges in managing the high-temperature effects experienced during high-speed flight. Throughout this chapter, thermal structural design aspects of supersonic aircraft are explored by starting the evolution of military aircraft in particular. Then, high-temperature effects in aircraft structures are investigated to determine the position of the problem discussed in Chapter 5 among the numerous challenges aircraft face in the development process. Based on this foundation, the exploration of suitable materials for elevated temperatures and structural precautions was discussed, which enhance overall structural integrity and withstand the detrimental effects of thermal loads. Ultimately, the importance of the testing procedures is highlighted at the end of this chapter.

3. FUNDAMENTALS OF THERMOELASTICITY

Thermoelasticity is a field of study that concerned with the effect of temperature on the mechanical behavior of the structure. To understand the fundamentals of this sub branch of elasticity theory, this chapter aims to give a brief overview of the essential definitions and equations of thermoelasticity, with a focus on its application to aircraft structures. In the beginning, the definitions, including the concepts of thermal stress, strain, bending, and so on, are provided. Then, the principles of elasticity are reviewed to understand the fundamental equations of thermoelasticty such as equilibrium, compatibility, and energy balance. Following this section, heat transfer mechanisms in aircraft structures are expressed, which are crucial to describing the thermal loads on the structure. In the light of these sections, the fundamental equations of thermoelasticity are given to provide a solid foundation for the vibration analysis of FGM beams in a thermal environment.

3.1 Definitions

To express the behavior of structures in a thermal environment, it is necessary to know several key terms that describe mechanical and thermal behavior of a structure. Thus, we will define the essential terms such as thermal stress, thermal-mechanical design, the factor of safety, thermal expansion, thermal shock, and thermal diffusivity in this section.

In aircraft structures, thermal stresses arise from temperature variations within operating environment and the interactions between the components made of different materials. When the structure undergoes expansion or contraction in response to temperature changes, internal forces induce thermal stress in the presence of internal or external constraints on the structure [197-199]. In Figure 3.1, a comprehensive example of thermal stresses in aircraft structures is depicted, demonstrating the reasons of thermal stresses [200, 201].

In thermal mechanical design steps, the effects of thermal loads can be alleviated by choosing thermal compatible material, limiting temperature changes, relaxing

structural constraints [197]. In Figure 3.2, the cycle of thermal-structural design is described for coupled structural analyses. The overall aim of this design process is to optimize the structural performance and ensure structural integrity for the required safety factor. To encompass uncertainties associated with material properties, maximum applied loading, environmental conditions, model simplifications, and initial stresses, a safety factor must be defined, which is given as:

$$f_s = S_{yield} / \sigma_{\max} \quad \text{or} \quad f_s = S_{ultimate} / \sigma_{\max} \tag{3.1}$$

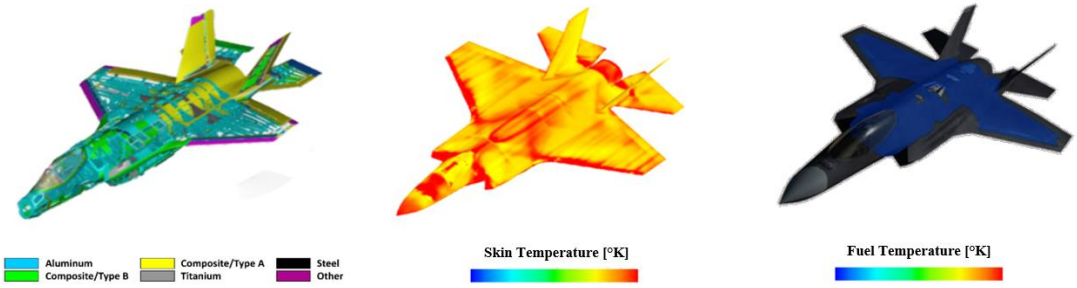

Figure 3.1 : Thermal stresses on the aircraft structures due to temperature difference and different material usage: a) Material distribution on the aircraft frame, b) Skin temperature due to aerodynamic heating, c) Low-temperature kerosene [200, 201].

In these analyses, the thermal expansion coefficient quantifies the extent to which a material expands or contracts in response to changes in temperature. The linear thermal expansion coefficient and volumetric thermal expansion coefficients are defined as:

$$\alpha = \frac{1}{L}\left(\frac{\partial L}{\partial T}\right)\Big|_{\sigma=0} \quad \text{and} \quad \beta_t = 3\alpha = \frac{1}{V}\left(\frac{\partial V}{\partial T}\right)\Big|_{p} \quad \text{for isotropic materials} \tag{3.2}$$

The magnitude of thermal stresses is directly influenced by the modulus of elasticity, which is the resistance of a material to deformation under an applied load. The mathematical formula of it is given by the following equation:

$$E = \left(\frac{\partial \sigma}{\partial \varepsilon}\right)\Big|_{T=const} \tag{3.3}$$

Expansion or contraction in one direction results in changes in other directions, which is described by the Poisson's ratio. It can be given as:

$$\upsilon = -\frac{\varepsilon_y}{\varepsilon_x} \leq \frac{1}{2} \quad \text{for isotropic homogenous materials} \tag{3.4}$$

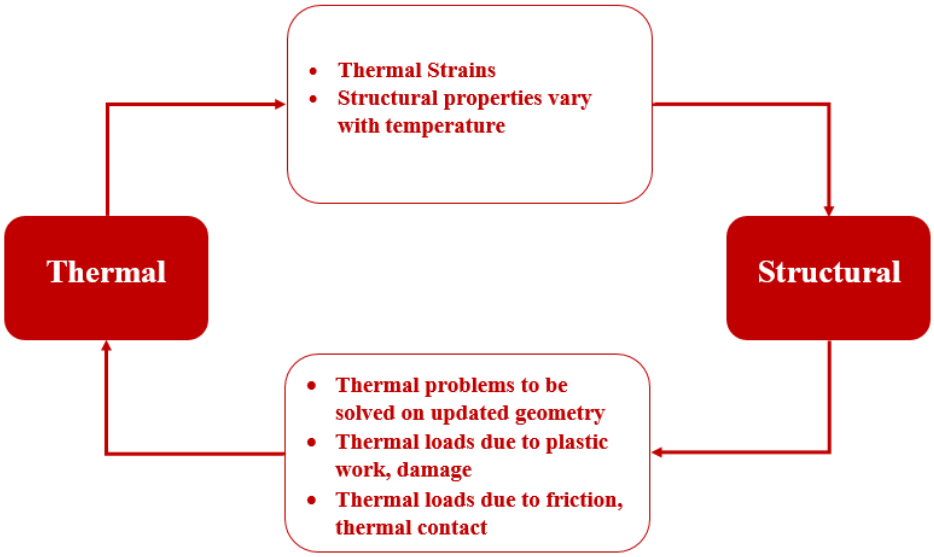

Figure 3.2 : Coupled thermal mechanical design [202].

The conducted energy rate through a solid material contributes to the thermal stress in the structure, which is defined by the thermal diffusivity. It quantifies how quickly heat can propagate within the structure. By considering the thermal diffusivity of materials, engineers can manage the thermal stresses. The mathematical definition of the thermal diffusivity is given as follows:

$$\kappa = \frac{k_t}{\rho c} \tag{3.5}$$

The rapid temperature changes in the structure are defined by the thermal shock parameter (TSP) as in Equation (3.6), which leads to structural failures such as micro-cracks.

$$TSP = \frac{S_u \sqrt{\kappa}}{\alpha E} \quad \text{for transient case} \tag{3.6}$$

A measure of the material's ability to withstand thermal stresses is given by the thermal stress ratio (TSR) for steady-state thermal conditions. A material with a higher TSR value generally exhibits better resistance to thermal stresses.

$$TSR = \frac{S_u}{\alpha E} \quad \text{for steady-state case} \tag{3.7}$$

In Figures 3.3 and 3.4, the relations for TSR and TSP are given for the changes in temperatures, which helps to evaluate the material performance under steady-state and transient conditions.

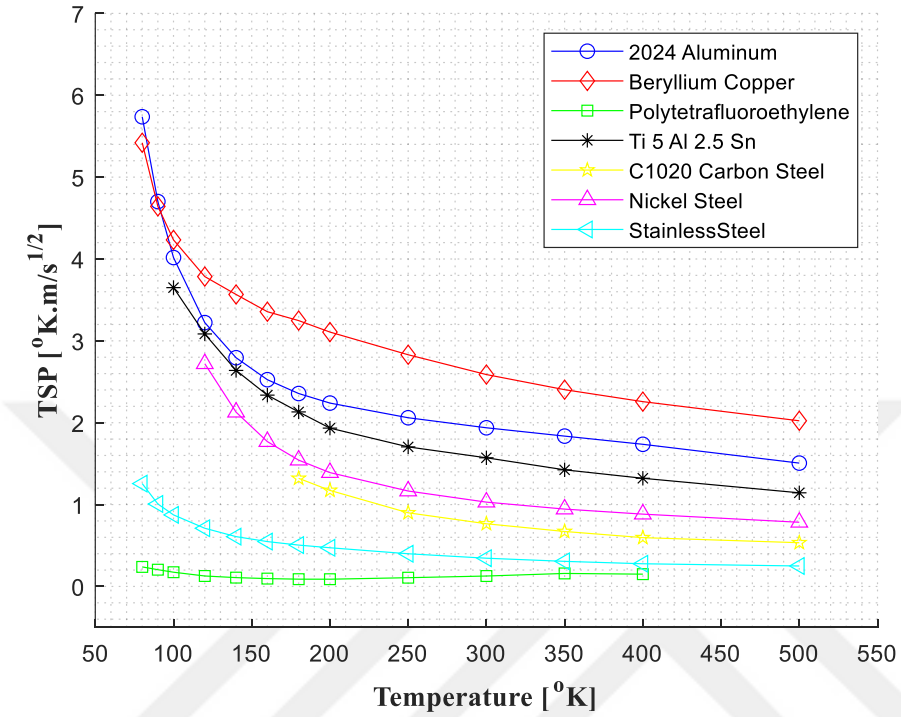

Figure 3.3 : Thermal shock parameters of some materials as a function of temperature.

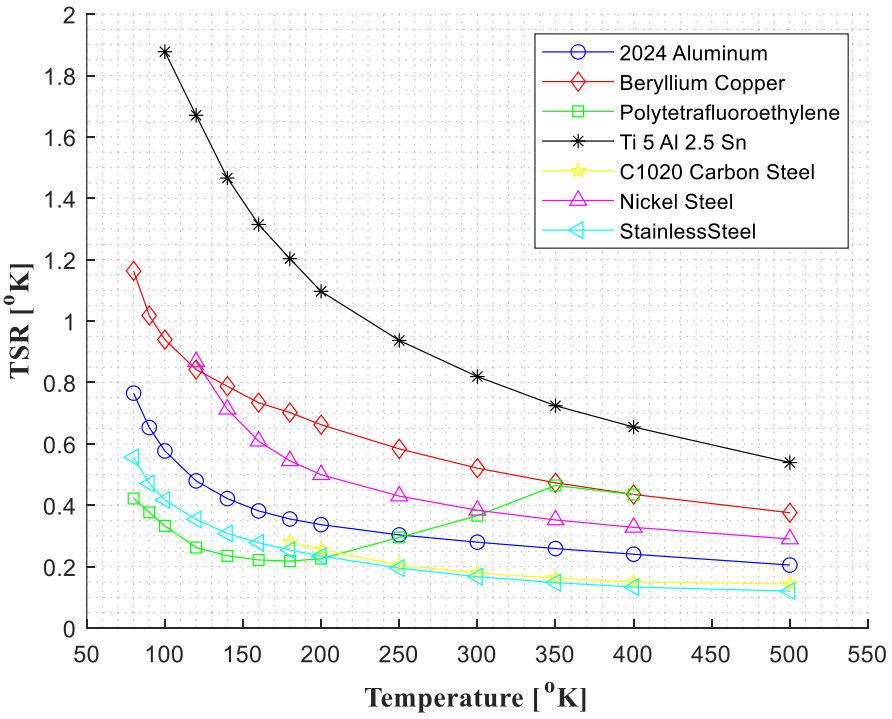

Figure 3.4 : Thermal stress ratio of some materials as a function of temperature.

3.2 Theory of Elasticity

Elasticity theory provides a mathematical model describing the deformation of solid structures under applied thermal and mechanical loads [203-205]. Up to the type of load, it can be divided into subbranches shown in Figure 3.5: aeroelasticity, thermoelasticity, aerothermoelasticity, and aeroservoelasticity. In the structural analysis of aircraft structures, the behavior of materials under thermal and mechanical loading conditions is of paramount importance. Therefore, we can obtain a close-approximate solution to actual stress, strain, and displacement by using elasticity theory. This theory relies on linearity, homogeneity, isotropy, continuum behavior, small deformations, and negligible damping assumptions.

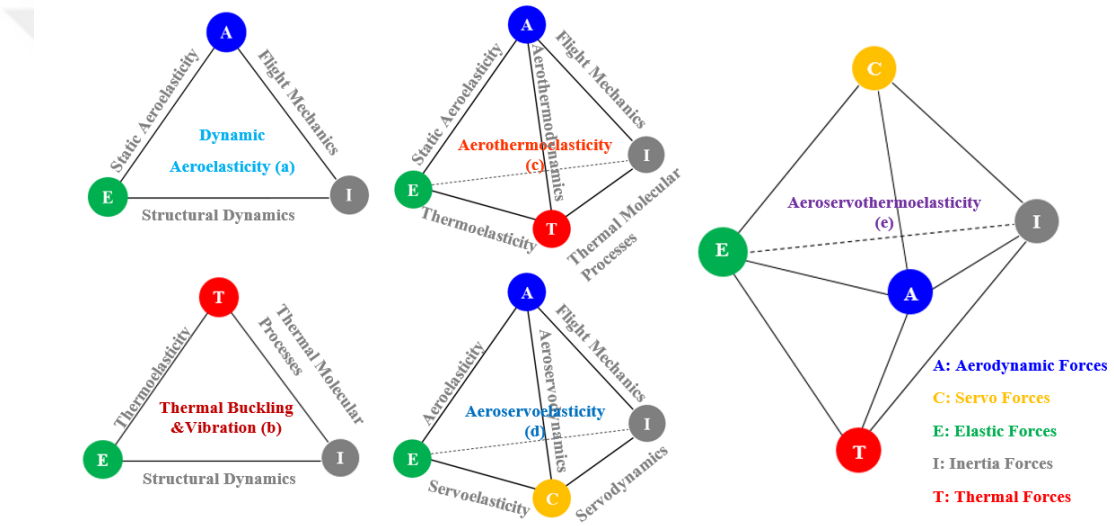

Figure 3.5 : a) Collar's aeroelastic triangle, b) Thermal triangle, c) Garrick's aerothermoelastic tetrahedron, d) Aeroservoelastic tetrahedron, e) Aerothermoservoelastic hexahedron [206-208].

The following elasticity equations can be derived from the principles of conservation of mass and balance of linear momentum, which express the balance of forces acting on a deformable body, stress-strain relations, and the continuity of displacement, respectively.Equilibrium Equations given in Equation (3.8) states the sum of forces acting on a small element of a body in equilibrium is zero.

$$\frac{\partial \sigma_{xx}}{\partial x}+\frac{\partial \sigma_{xy}}{\partial y}+\frac{\partial \sigma_{xz}}{\partial z}+F_x=0,\ \frac{\partial \sigma_{yx}}{\partial x}+\frac{\partial \sigma_{yy}}{\partial y}+\frac{\partial \sigma_{yz}}{\partial z}+F_y=0,$$
$$\frac{\partial \sigma_{zx}}{\partial x}+\frac{\partial \sigma_{zy}}{\partial y}+\frac{\partial \sigma_{zz}}{\partial z}+F_z=0 \tag{3.8}$$

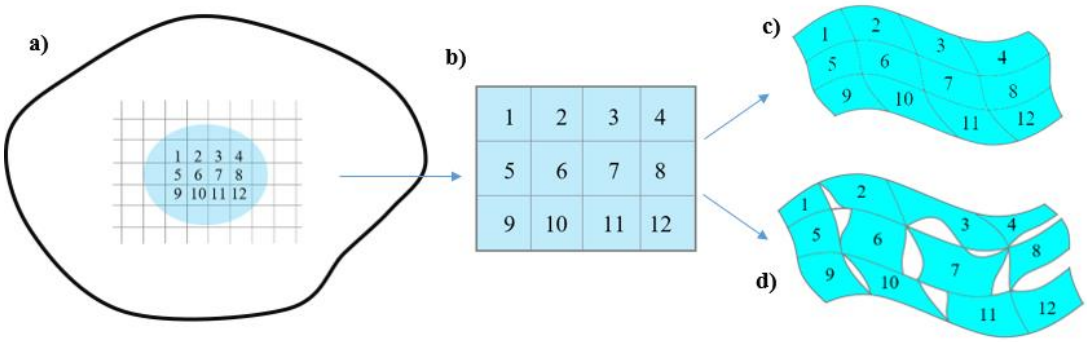

Figure 3.6 : Strain compatibility of elastic solid elements: (a) Discretized elastic solid, (b) Undeformed configuration of solid elements, (c) Deformed configuration of solid elements with continuous displacements, (d) Deformed configuration of solid elements with discontinuous displacements [205, 209].

The constitutive equations (stress-strain relationship) in Equation (3.9) represent the material's response to applied forces.

$$\begin{aligned}
\sigma_{xx} &= \frac{E}{(1+\nu)(1-2\nu)}\left[(1-\nu)\varepsilon_x + \nu(\varepsilon_y + \varepsilon_z)\right] \\
\sigma_{yy} &= \frac{E}{(1+\nu)(1-2\nu)}\left[(1-\nu)\varepsilon_y + \nu(\varepsilon_x + \varepsilon_z)\right] \\
\sigma_{zz} &= \frac{E}{(1+\nu)(1-2\nu)}\left[(1-\nu)\varepsilon_z + \nu(\varepsilon_x + \varepsilon_y)\right] \\
\sigma_{xy} &= \frac{E}{2(1+\nu)}\gamma_{xy},\ \ \sigma_{yz} = \frac{E}{2(1+\nu)}\gamma_{yz},\ \ \sigma_{xz} = \frac{E}{2(1+\nu)}\gamma_{xz}
\end{aligned} \tag{3.9}$$

Compatibility equations express the continuity of displacement and strain throughout a deformable body, like in Figure 3.6.

$$\begin{aligned}
&\frac{\partial^2\varepsilon_x}{\partial y^2} + \frac{\partial^2\varepsilon_y}{\partial x^2} = \frac{\partial^2\gamma_{xy}}{\partial x\partial y},\quad \frac{\partial^2\varepsilon_y}{\partial z^2} + \frac{\partial^2\varepsilon_z}{\partial y^2} = \frac{\partial^2\gamma_{yz}}{\partial y\partial z},\quad \frac{\partial^2\varepsilon_z}{\partial x^2} + \frac{\partial^2\varepsilon_x}{\partial z^2} = \frac{\partial^2\gamma_{zx}}{\partial z\partial x} \\
&2\frac{\partial^2\varepsilon_x}{\partial y\partial z} = \frac{\partial}{\partial x}\left(-\frac{\partial\gamma_{yz}}{\partial x} + \frac{\partial\gamma_{xz}}{\partial y} + \frac{\partial\gamma_{xy}}{\partial z}\right) \\
&2\frac{\partial^2\varepsilon_y}{\partial z\partial x} = \frac{\partial}{\partial y}\left(\frac{\partial\gamma_{yz}}{\partial x} - \frac{\partial\gamma_{xz}}{\partial y} + \frac{\partial\gamma_{xy}}{\partial z}\right) \\
&2\frac{\partial^2\varepsilon_z}{\partial x\partial y} = \frac{\partial}{\partial z}\left(\frac{\partial\gamma_{yz}}{\partial x} + \frac{\partial\gamma_{xz}}{\partial y} - \frac{\partial\gamma_{xy}}{\partial z}\right)
\end{aligned} \tag{3.10}$$

These equations form the basis of elasticity theory, which is used to provide accurate and reliable predictions of structural behavior. To solve these 15 equations with 15

unknowns (6 stress, 6 strain, and 3 displacement), are employed [209]. The choice of a suitable solution technique depends on the problem's complexity, available resources, and desired accuracy.

3.3 Heat Transfer in Aircraft Structures

The heat sources in supersonic aircraft can be listed as aerodynamic heating, engines, plume radiation, solar radiation, and various onboard equipment such as auxiliary power units, avionics systems, and electrical systems [210], which are shown in Figures 3.7, and 3.8. The efficient management of these thermal loads might help prevent the detrimental effect of temperature on aircraft components. Thus, understanding the primary heat transfer mechanisms is vital for minimizing thermal stresses on the structure.

Heat transfer in structures occurs through three primary mechanisms: conduction, convection, and radiation [211-214]. Thermal energy is transferred through direct molecular interactions between adjacent particles by conduction heat transfer. In convection, heat is transferred through the movement of a fluid medium, such as air or liquid, that comes into contact with the aircraft structure. In radiation, the heat is transferred through electromagnetic waves without the need for a material medium.

These heat transfer modes can be expressed by Fourier's Law of Conduction, Newton's Law of Convective Heat Transfer, and Stefan-Boltzman's Law of Radiation [213] as follows:

$$q_{cond} = -k\,A\frac{\partial T}{\partial x} \tag{3.11}$$

$$q_{conv} = h\,A\left(T_s - T_f\right) \tag{3.12}$$

$$q_{rad} = \varepsilon\,\sigma A\left(T_s^{\,4} - T_f^{\,4}\right) \tag{3.13}$$

To conduct heat transfer analysis in aircraft structures, it is it is often necessary to consider all three modes, together. The overall heat transfer rate can be determined using the principle of energy conservation:

$$q = q_{cond} + q_{conv} + q_{rad} \tag{3.14}$$

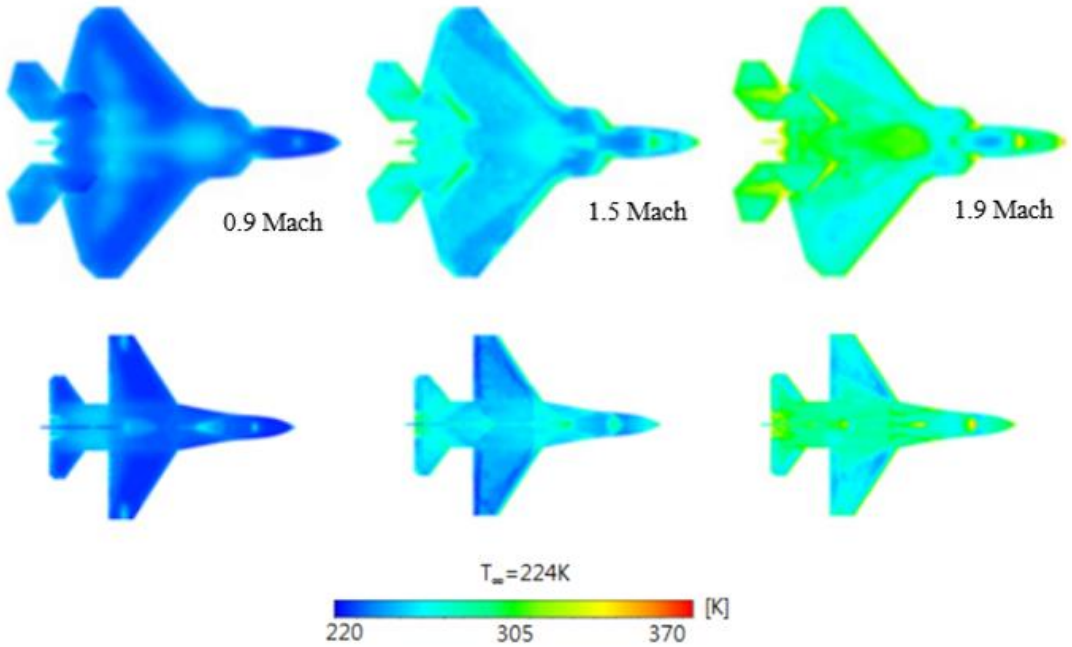

Figure 3.7 : Aerodynamic heating as heat source in modern aircraft: Temperature contour of 5th and 4th generation fighter aircraft for 33 kft, standard day flight [215].

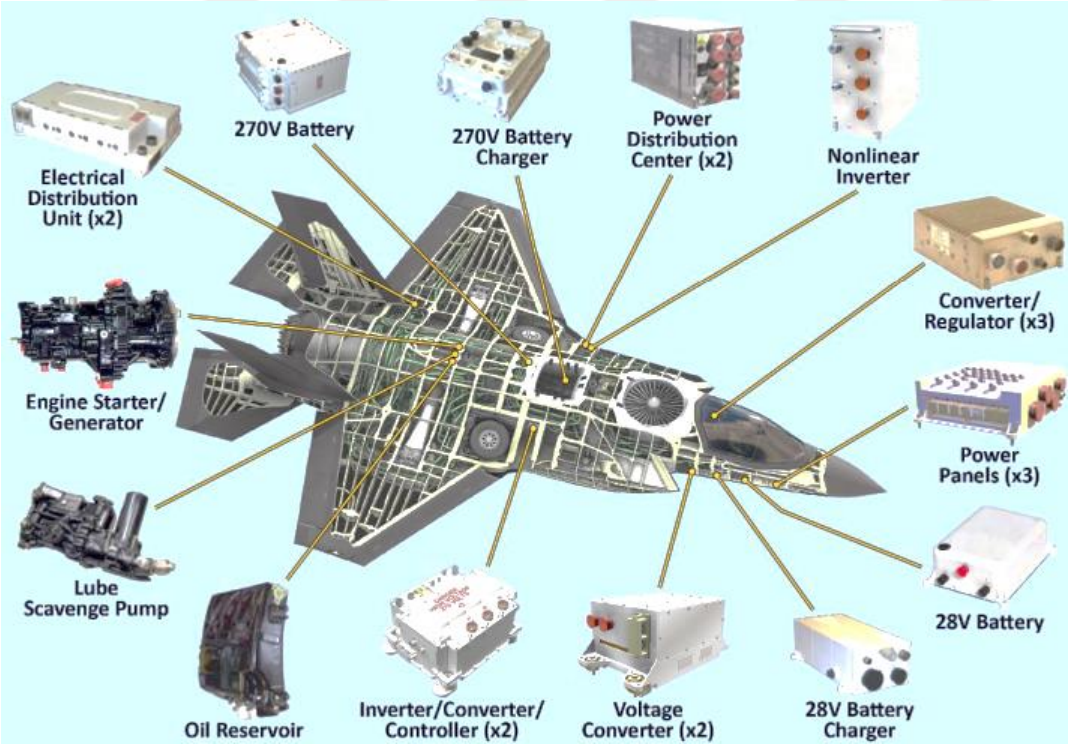

Figure 3.8 : Electrical power system as heat source in modern fighter aircraft [216].

3.4 Thermal Stresses in Airframe

Thermal stresses arise due to limitations on the free expansion or contraction of structural elements within a continuous body. Except for these external structural constraints, non-uniform temperature distribution and the use of dissimilar materials in a structure can cause thermal stresses due to internal constraints [197-199, 217]. In hybrid composite metallic structures exposed to an operational temperature range of -53°C through 162°C [218], thermal stresses due to dissimilar material usage and non-uniform temperature variation are illustrated in Figures 3.9 and 3.10. Understanding these stresses in aircraft structures is of utmost importance to meet the structural design criteria while ensuring the structural integrity of aircraft components exposed to fluctuating temperatures and mechanical loads. In this section, preliminary remarks on thermal stress and thermal bending will be provided, elucidating their application to aircraft components reduced to equivalent bar structures.

To express stress in the presence of temperature variations, the differential of direct strain expression must first be written in terms of temperature and stress. This relationship can be given as:

$$d\varepsilon = \left(\frac{\partial \varepsilon}{\partial \sigma}\right)\Big|_T d\sigma + \left(\frac{\partial \varepsilon}{\partial T}\right)\Big|_\sigma dT \tag{3.15}$$

By employing the expressions in 3.2 and 3.3, the differential of direct strain can be expressed in the following form:

$$d\varepsilon = \frac{d\sigma}{E} + \alpha\, dT \quad \textit{where } \alpha = \frac{1}{L}\frac{\partial L}{\partial T} = \frac{\partial \varepsilon}{\partial T} \tag{3.16}$$

By integrating equation 3.16 from a stress-free temperature state to any desired temperature value, the direct strain relationship for one-dimensional structures, such as bars, trusses and beams, can be derived in terms of stress and temperature as follows:

$$\varepsilon = \varepsilon_m + \varepsilon_t = \frac{\sigma}{E} + \int_{T_0}^{T} \alpha\, dT = \frac{\sigma}{E} + \alpha \Delta T \quad \textit{where } \Delta T = T - T_0 \tag{3.17}$$

From equation 3.17, the stress-strain-temperature relationship is obtained as:

$$\sigma = \sigma_m + \sigma_t = \varepsilon E - \alpha \Delta T\, E \tag{3.18}$$

Figure 3.9 : The F-35 hybrid composite-metallic structure [218].

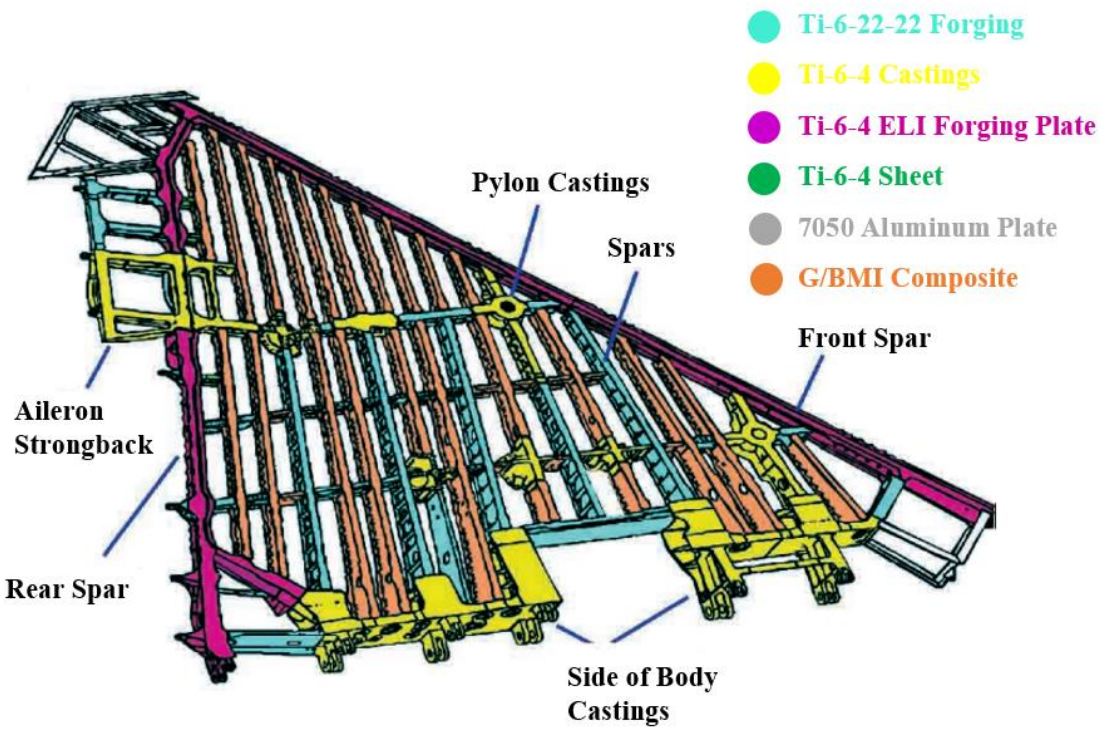

Figure 3.10 : The F-22 wing composite-metallic substructure [165, 219].

Utilizing these expressions allows for the determination of thermal stresses in the composite-metallic structures. To find thermal stresses in these structures, composite skin, and metallic web can be reduced to one-dimensional structural elements, which are demonstrated with equivalent bar elements like in Figure 3.11. This reduction enables a more manageable structural analysis in the selection of proper material pairs, alleviating thermal stresses.

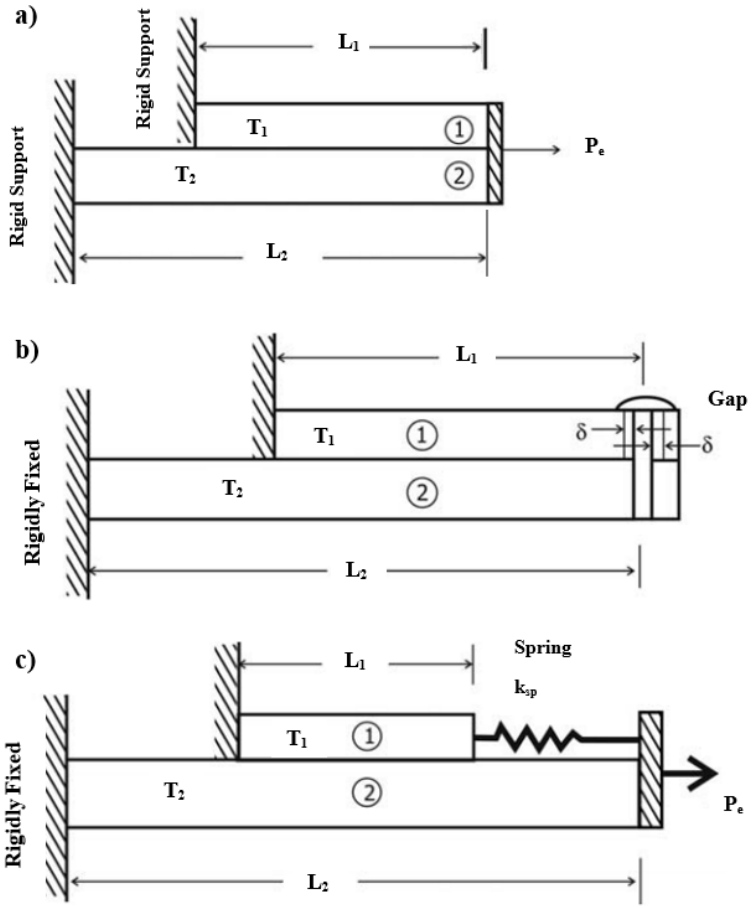

Figure 3.11 : Equivalent bar structures for hybrid metal-composite structures: a) Bars in parallel, b) Bars with expansion gap, c) Bars with spring element [197].

In the phases of flight, these bar systems demonstrating different connection types in hybrid aircraft structures are exposed to different temperature changes while being restrained to have the same change in length. For these structures, thermal stress expressions can be obtained from the force balance as follows:

a) Parallel Bars Configuration

$$\sigma_1 = \frac{A_2E_1E_2\left(\alpha_2L_2\Delta T_2 - \alpha_1L_1\Delta T\right) + P_eE_1L_{21}}{A_1E_1L_2 + A_2E_2L_1}$$
$$\sigma_2 = \frac{A_1E_1E_2\left(\alpha_1L_1\Delta T_1 - \alpha_2L_2\Delta T_2\right) + P_eE_2L_1}{A_1E_1L_2 + A_2E_2L_1} \quad (3.19)$$

b) Bars with Gap Configuration

$$\sigma_1 = \frac{A_2E_1E_2\left(\alpha_2L_2\Delta T_2 - \alpha_1\Delta T_1L_1 \pm \delta\right) \pm 2A_1E_1^2\delta L_2/L_1}{A_1E_1L_2 + A_2E_2L_1}$$
$$\sigma_2 = \frac{A_1E_1E_2\left(\alpha_1L_1\Delta T_1 - \alpha_2L_2\Delta T_2\right) \pm A_1E_1E_2\delta}{A_1E_1L_2 + A_2E_2L_1} \quad (3.20)$$

c) Bars with Spring Configuration

$$\sigma_1 = \frac{k_{sp}E_1\left\{A_2E_2\left(\alpha_2L_2\Delta T_2 - \alpha_1L_1\Delta T_1\right) + P_eL_2\right\}}{\left(A_1E_1L_2 + A_2E_2L_1\right)k_{sp} + A_1A_2E_1E_2}$$

$$\sigma_2 = \frac{A_1E_1E_2k_{sp}\left(\alpha_1L_1\Delta T_1 - \alpha_2L_2\Delta T_2\right) + \left(L_1 + A_1^2E_1^2E_2\right)k_{sp}P_eE_2}{\left(A_1E_1L_2 + A_2E_2L_1\right)k_{sp} + A_1A_2E_1E_2} \quad (3.21)$$

where P_e is the external force, $\Delta T_1 = T_1 - T_0$ and $\Delta T_2 = T_2 - T_0$.

In practical engineering applications, the use of bars with spring configurations [185, 186] is common to predict airframe thermal loads, accurately. Therefore, the use of spring elements allows for the consideration of fastener stiffness, enhancing the accuracy of the analysis while validating the air vehicle finite element model or the mathematical model. Moreover, employing corrugated structures can help reduce thermal stress in inner airframe components.

According to the Euler-Bernoulli beam theory assumptions, the total strain is the sum of a uniform extensional strain and a bending strain, which can be found from equation 3.18 as follows:

$$\varepsilon = \varepsilon_0 + \varepsilon_b = \frac{\sigma}{E} + \alpha\,\Delta T \quad (3.19)$$

where the bending strain component is determined by employing the small deformation assumption, with the tangent of the rotation angle approximately equal to the angle itself, as depicted in Figure 3.12.

$$\tan\Psi \cong \Psi = \varepsilon_b\frac{L}{y} \quad (3.20)$$

The rotation angle can be expressed in terms of the beam length and the radius of curvature as:

$$\tan\Psi/2 \cong \Psi/2 = \frac{L}{2R} \quad (3.21)$$

Then, the expression for the bending strain is obtained by equating equations 3.20 and 3.21 in terms of the radius of curvature:

$$\varepsilon_b = \Psi\frac{y}{L} = \frac{y}{R} \quad (3.22)$$

and the stress expression including thermal loads may be written as:

$$\sigma = E\left(\varepsilon_0 + \frac{y}{R} - \alpha \Delta T \right) \tag{3.23}$$

If an axial force is applied on the centroid of the cross-section, the stress expression can be derived from the force and moment balance relations as follows:

$$\sigma = \frac{P_e + F_T}{A} + y\left(\frac{M + M_{Ty}}{I_{zz}} \right) - \alpha E \Delta T \tag{3.24}$$

where the thermal force and thermal moment (transverse) terms are:

$$F_T = \alpha E \int \Delta T \, dA \quad \text{and} \quad M_{Ty} = \alpha E \int \Delta T \, y \, dA$$

If the temperature varies in *y* and *z* directions or the beam cross-section is not uniform, the stress expression may be given as:

$$\sigma = \frac{P_e + F_T}{A} + \frac{M + \Omega_y}{I_{zz}} y + \frac{\Omega_z}{I_{zz}} - \alpha E \Delta T \tag{3.25}$$

where the quantities in terms of inertia moments and spanwise and transverse thermal moments are:

$$\Omega_y = \frac{I_{yy} M_{Ty} - I_{yz} M_{Tz}}{I_{yy} - I_{yy}^2 / I_{zz}} \quad \text{and} \quad \Omega_z = \frac{I_{zz} M_{Tz} - I_{yz} M_{Tz}}{I_{yy} - I_{yy}^2 / I_{zz}}$$

The displacement relation due to thermal bending shown in Figure 3.13 (a) is essential in understanding the deflection of a beam subjected to bending loads. By utilizing the definition of bending strain, the relation between thermal moment, mechanical moment, and displacement can be determined as follows:

$$\frac{d^2 v}{dx^2} = -\frac{M + M_{Ty}}{E I_{zz}} \tag{3.26}$$

The bending relations play a crucial role when a beam is subjected to the combined action of transverse loads and thermal effects, as depicted in Figure 3.13 (b). By establishing force and moment balance in the y-direction, we can derive the relation between transverse displacement, transverse load, and thermal moment as follows:

$$\frac{d^4v}{dx^4} = \frac{1}{E\,I_{zz}}\left(q - \frac{d^2M_{Ty}}{dx^2}\right) \tag{3.27}$$

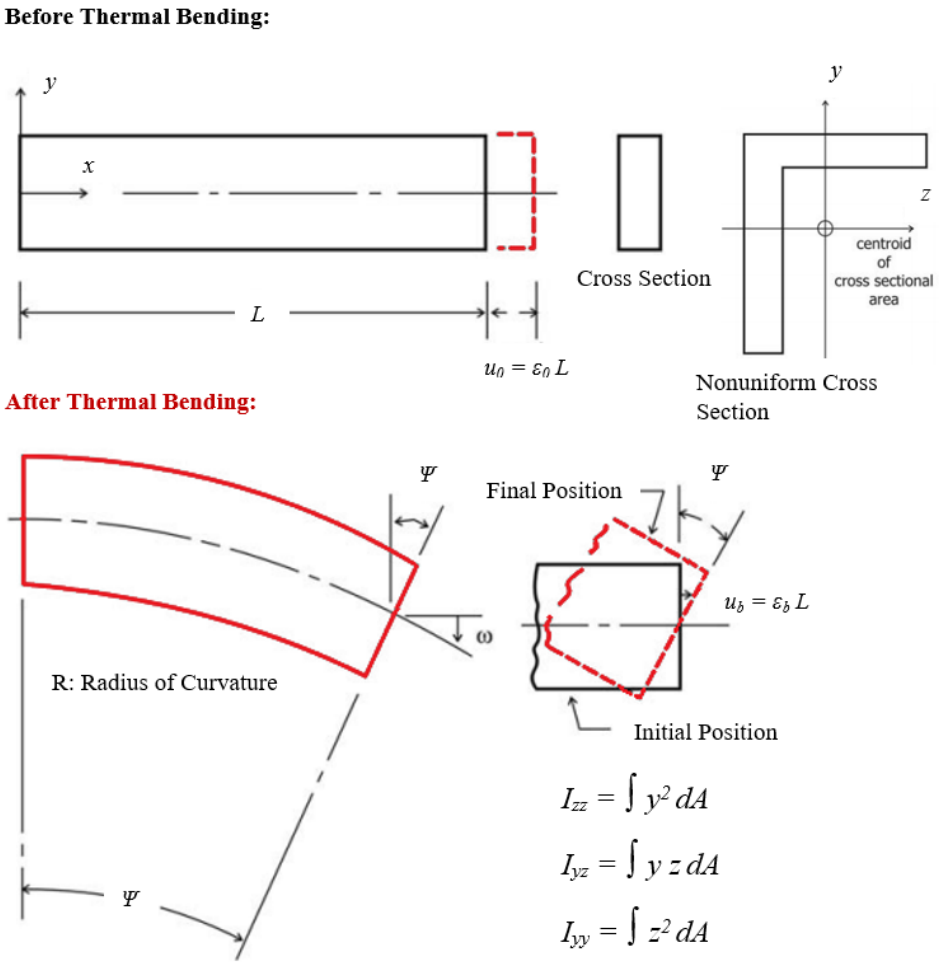

Figure 3.12 : Bending deflection of beams due to thermal loads [197].

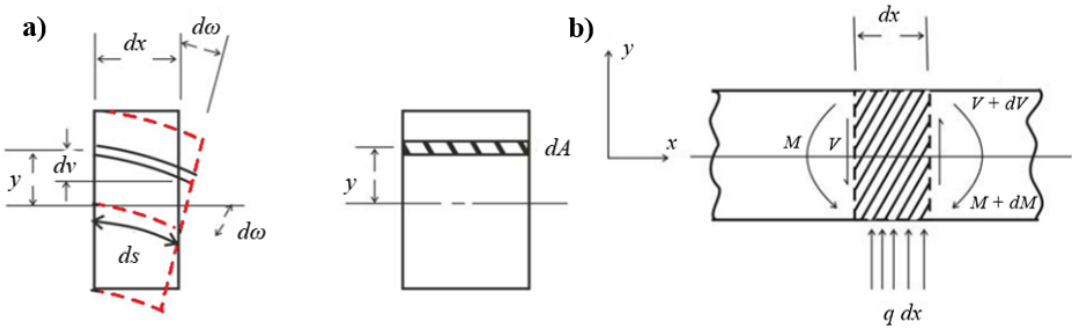

Figure 3.13 : Bending of beams due to thermal effects and transverse loads: a) Differential element of a beam, b) Load distribution on beam [197].

3.5 Basic Equations of Thermoelasticity

Thermoelasticity investigates the mechanical behavior of materials exposed to thermal loads, which has its roots in Duhamel and Neuman's research in the nineteenth century. Unlike elasticity theory, it includes temperature fields and temperature-dependent constitutive equations to establish the link between material properties and temperature [220-222]. It has advanced significantly over time thanks to the contributions of notable researchers such as Timoshenko, Goodier, Wang, Sokolnikoff, Fung, Gatewood, Boley, Weiner, Nowacki, Johns, Parkus, Burgreen, and Nowinski, who have presented novel formulations and solutions to classical thermoelasticity problems [199, 223]. Based on their research, the following stress equilibrium, strain displacement, compatibility, constitutive, and temperature field equations serve as the foundation for thermoelasticity [197, 199, 217, 220, 223, 224].

1. *Stress Equilibrium Equations:* The force balances within the differential solid element depicted in Figure 3.14 can be determined by applying Newton's laws in the x, y, and z directions as follows:

$$\begin{aligned}
&\frac{\partial \sigma_x}{\partial x}+\frac{\partial \tau_{xy}}{\partial y}+\frac{\partial \tau_{xz}}{\partial z}+F_x=\rho\frac{\partial^2 u}{\partial t^2}\\
&\frac{\partial \tau_{yx}}{\partial x}+\frac{\partial \sigma_y}{\partial y}+\frac{\partial \tau_{yz}}{\partial z}+F_y=\rho\frac{\partial^2 v}{\partial t^2}\\
&\frac{\partial \tau_{zx}}{\partial x}+\frac{\partial \tau_{zy}}{\partial y}+\frac{\partial \sigma_z}{\partial z}+F_z=\rho\frac{\partial^2 w}{\partial t^2}
\end{aligned} \tag{3.28}$$

   where σ represents the stress tensor and *F* represents any external forces acting on the structure.

2. *Strain Displacement Equations:* The relationship between the deformation and the displacement field is expressed as:

$$\begin{aligned}
&\varepsilon_x=\frac{\partial u}{\partial x}, \qquad \varepsilon_y=\frac{\partial v}{\partial y}, \qquad \varepsilon_z=\frac{\partial w}{\partial z}\\
&\gamma_{xy}=\frac{\partial u}{\partial y}+\frac{\partial v}{\partial x}, \quad \gamma_{xz}=\frac{\partial u}{\partial z}+\frac{\partial w}{\partial x}, \quad \gamma_{yz}=\frac{\partial v}{\partial z}+\frac{\partial w}{\partial y}
\end{aligned} \tag{3.29}$$

3. *Strain Compatibility Equations:* The strain tensor components must be compatible with the displacement field.

$$\begin{aligned}
&\frac{\partial^2 \varepsilon_x}{\partial y^2}+\frac{\partial^2 \varepsilon_y}{\partial x^2}=\frac{\partial^2 \gamma_{xy}}{\partial x \partial y}\\
&\frac{\partial^2 \varepsilon_y}{\partial z^2}+\frac{\partial^2 \varepsilon_z}{\partial y^2}=\frac{\partial^2 \gamma_{yz}}{\partial y \partial z}\\
&\frac{\partial^2 \varepsilon_z}{\partial x^2}+\frac{\partial^2 \varepsilon_x}{\partial z^2}=\frac{\partial^2 \gamma_{xz}}{\partial x \partial z}\\
&2\frac{\partial^2 \varepsilon_x}{\partial y \partial z}=\frac{\partial^2 \gamma_{xz}}{\partial x \partial y}+\frac{\partial^2 \gamma_{xy}}{\partial x \partial z}-\frac{\partial^2 \gamma_{yz}}{\partial x^2}\\
&2\frac{\partial^2 \varepsilon_y}{\partial x \partial z}=\frac{\partial^2 \gamma_{yz}}{\partial x \partial y}+\frac{\partial^2 \gamma_{xy}}{\partial y \partial z}-\frac{\partial^2 \gamma_{xz}}{\partial y^2}\\
&2\frac{\partial^2 \varepsilon_z}{\partial x \partial y}=\frac{\partial^2 \gamma_{yz}}{\partial x \partial z}+\frac{\partial^2 \gamma_{xz}}{\partial y \partial z}-\frac{\partial^2 \gamma_{xy}}{\partial z^2}
\end{aligned} \tag{3.30}$$

where the normal and shear strain terms are

$$\begin{aligned}
&\varepsilon_x=\frac{1}{E}\left(\sigma_x-\mu\left(\sigma_y+\sigma_z\right)\right)+\alpha\,\Delta T\\
&\varepsilon_y=\frac{1}{E}\left(\sigma_y-\mu\left(\sigma_x+\sigma_z\right)\right)+\alpha\,\Delta T\\
&\varepsilon_z=\frac{1}{E}\left(\sigma_z-\mu\left(\sigma_x+\sigma_y\right)\right)+\alpha\,\Delta T\\
&\gamma_{xy}=\frac{\tau_{xy}}{G},\qquad \gamma_{xz}=\frac{\tau_{xz}}{G},\qquad \gamma_{yz}=\frac{\tau_{yz}}{G}
\end{aligned}$$

4. *Constitutive Equation (Stress-Strain Relations by Generalized Hooke's Law):* The temperature dependency of material properties and coefficient of thermal expansion is considered to provide how stress varies with temperature-induced deformations.

$$\begin{aligned}
&\sigma_x=\left(\lambda_L+2G\right)\varepsilon_x+\lambda_L\left(\varepsilon_y+\varepsilon_z\right)-\beta_t B\,\Delta T\\
&\sigma_y=\left(\lambda_L+2G\right)\varepsilon_y+\lambda_L\left(\varepsilon_x+\varepsilon_z\right)-\beta_t B\,\Delta T\\
&\sigma_z=\left(\lambda_L+2G\right)\varepsilon_z+\lambda_L\left(\varepsilon_x+\varepsilon_y\right)-\beta_t B\,\Delta T\\
&\tau_{xy}=\gamma_{xy}G,\qquad \tau_{xz}=\gamma_{xz}G,\qquad \tau_{yz}=\gamma_{yz}G
\end{aligned} \tag{3.31}$$

where the constants are

$$\lambda_L=\frac{\mu E}{(1+\mu)(1-2\mu)},\qquad B=\frac{E}{3(1-2\mu)},\quad \beta_t=3\alpha\ .$$

5. *Temperature Field Equations:* Heat transfer for a differential control volume in Figure 3.15 is described in these equations by employing Fourier's Law of Conduction and the first law of thermodynamics. The heat transfer rate into the differential control volume in the x-direction [197, 212] can be expressed as follows:

$$\dot{q}_{x,\,in} = -k_t\, dy\, dz \frac{\partial T}{\partial x} \tag{3.32}$$

The heat transfer rate from the differential control volume can be expressed as:

$$\dot{q}_{x,\,out} = \dot{q}_{x,\,in} + \frac{\partial \dot{q}_{x,\,in}}{\partial x} dx = \dot{q}_{x,\,in} - \frac{\partial}{\partial x}\left(k_t \frac{\partial T}{\partial x} \right) dx\, dy\, dz \tag{3.33}$$

The net heat conduction rate in the x-direction is given by:

$$\dot{q}_{x,\,net} = \dot{q}_{x,\,in} - \dot{q}_{x,\,out} = \frac{\partial}{\partial x}\left(k_t \frac{\partial T}{\partial x} \right) dx\, dy\, dz \tag{3.34}$$

Then, the net heat conducted into the differential volume depicted in Figure 3.15 can be expressed as the sum of these three contributions:

$$\dot{q}_{cond,\,net} = \left\{ \frac{\partial}{\partial x}\left(k_t \frac{\partial T}{\partial x} \right) + \frac{\partial}{\partial y}\left(k_t \frac{\partial T}{\partial y} \right) + \frac{\partial}{\partial z}\left(k_t \frac{\partial T}{\partial z} \right) \right\} dx\, dy\, dz \tag{3.35}$$

According to the first law of thermodynamics, mechanical work leads to changes in the internal energy of the material due to a change in the volume of the material, which can be expressed as:

$$\dot{E}_{work} = -\left(\sigma_x \frac{\partial \varepsilon_x}{\partial t} + \sigma_y \frac{\partial \varepsilon_y}{\partial t} + \sigma_z \frac{\partial \varepsilon_z}{\partial t} \right) dx\, dy\, dz \tag{3.36}$$

The other work rates associated with electrical, magnetic, etc., can be taken into account by including the energy dissipation per unit volume as:

$$\dot{E}_{gen} = -\dot{q}_{gen}\, dx\, dy\, dz \tag{3.37}$$

The rate of change of energy stored in the differential control volume [197] is a combination of thermal energy and strain energy, and can be expressed as follows:

$$\dot{E}_{store} = \left(\sigma_x \frac{\partial \varepsilon_x}{\partial t} + \sigma_y \frac{\partial \varepsilon_y}{\partial t} + \sigma_z \frac{\partial \varepsilon_z}{\partial t} \right) dx\,dy\,dz + c_\varepsilon \frac{\partial T}{\partial t} dx\,dy\,dz + \beta_t B \Delta T \left(\frac{\partial \varepsilon_x}{\partial t} + \frac{\partial \varepsilon_y}{\partial t} + \frac{\partial \varepsilon_z}{\partial t} \right) dx\,dy\,dz \tag{3.38}$$

This expression in Equation (3.38) states that changes in temperature and deformation contribute to the overall energy storage within the differential volume in Figure 3.15.

According to the conservation of energy principle, the temperature field equation can be written from these expressions as follows:

$$\dot{E}_{in} - \dot{E}_{out} + \dot{E}_{gen} + \dot{E}_{work} = \dot{E}_{st} \quad where \ \dot{q}_{x,\,net} = \dot{E}_{in} - \dot{E}_{out} \tag{3.39}$$

Equation 3.39 (Barron,2012) can be formulated to describe the temperature distribution as:

$$\left\{ \frac{\partial}{\partial x}\left(k_t \frac{\partial T}{\partial x} \right) + \frac{\partial}{\partial y}\left(k_t \frac{\partial T}{\partial y} \right) + \frac{\partial}{\partial z}\left(k_t \frac{\partial T}{\partial z} \right) \right\} = \rho c_\varepsilon \frac{\partial T}{\partial t} + \beta_t B T_0 \left(\frac{\partial \varepsilon_x}{\partial t} + \frac{\partial \varepsilon_y}{\partial t} + \frac{\partial \varepsilon_z}{\partial t} \right) \tag{3.40}$$

This equation allows for the calculation of temperature distributions, thermal strains, and their interaction with mechanical behavior within a material or structure and captures the relationship between temperature, heat transfer, and other energy-related factors, providing a comprehensive understanding of the thermal behavior of the structure. By using the Grüneisen constant and dilatation expression, Equation (3.40) can be rewritten as:

$$\left\{ \frac{\partial}{\partial x}\left(k_t \frac{\partial T}{\partial x} \right) + \frac{\partial}{\partial y}\left(k_t \frac{\partial T}{\partial y} \right) + \frac{\partial}{\partial z}\left(k_t \frac{\partial T}{\partial z} \right) \right\} = \rho c_\varepsilon \frac{\partial T}{\partial t} + \rho c_v \gamma_G T_0 \frac{\partial e_v}{\partial t} \tag{3.41}$$

where the coupling effects between thermal and structural behaviors can be negligible when the volumetric dilatation rate is significantly smaller than the rate of temperature

change. In such cases, the thermoelasticity equation can be solved independently to obtain the temperature distribution, decoupled from the stress problem. Consequently, the 15 governing equations with 15 unknowns can be simplified to either Beltrami-Michell Thermoelasticity equations or Navier Thermoelasticity equations, which are given in Equations (3.42) and (3.43), respectively.

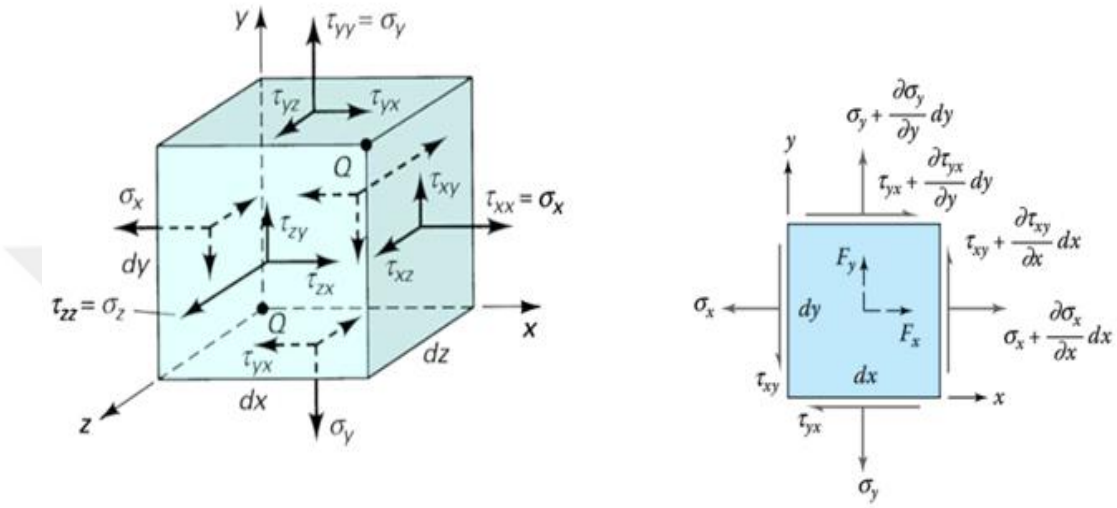

Figure 3.14 : Components of stress within an element: a) Three-dimensional stress with nine scalar components in cartesian coordinates, b) Differential element with body forces and plane stresses in cartesian coordinates [203]

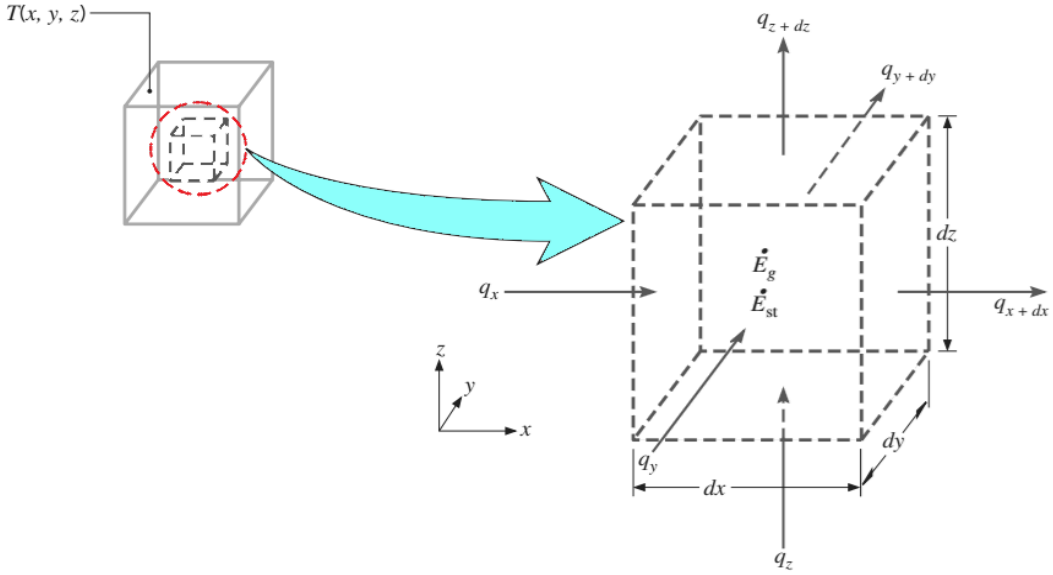

Figure 3.15 : Heat conduction for a differential control volume in cartesian coordinates [213].

$$
\begin{aligned}
&(1+\mu)\nabla^2\sigma_x+\frac{\partial^2}{\partial x^2}(\sigma_x+\sigma_y+\sigma_z)+\alpha E\left(\frac{1+\mu}{1-\mu}\nabla^2\Delta T+\frac{\partial^2\Delta T}{\partial x^2}\right)\\
&\qquad+(1+\mu)\left(\frac{\mu}{1-\mu}\left(\frac{\partial F_x}{\partial x}+\frac{\partial F_y}{\partial y}+\frac{\partial F_z}{\partial z}\right)+2\frac{\partial F_x}{\partial x}\right)=0\\
&(1+\mu)\nabla^2\sigma_y+\frac{\partial^2}{\partial y^2}(\sigma_x+\sigma_y+\sigma_z)+\alpha E\left(\frac{1+\mu}{1-\mu}\nabla^2\Delta T+\frac{\partial^2\Delta T}{\partial y^2}\right)\\
&\qquad+(1+\mu)\left(\frac{\mu}{1-\mu}\left(\frac{\partial F_x}{\partial x}+\frac{\partial F_y}{\partial y}+\frac{\partial F_z}{\partial z}\right)+2\frac{\partial F_y}{\partial y}\right)=0\\
&(1+\mu)\nabla^2\sigma_z+\frac{\partial^2}{\partial z^2}(\sigma_x+\sigma_y+\sigma_z)+\alpha E\left(\frac{1+\mu}{1-\mu}\nabla^2\Delta T+\frac{\partial^2\Delta T}{\partial z^2}\right)\\
&\qquad+(1+\mu)\left(\frac{\mu}{1-\mu}\left(\frac{\partial F_x}{\partial x}+\frac{\partial F_y}{\partial y}+\frac{\partial F_z}{\partial z}\right)+2\frac{\partial F_z}{\partial z}\right)=0\\
&(1+\mu)\nabla^2\tau_{xy}+\frac{\partial^2}{\partial x\partial y}(\sigma_x+\sigma_y+\sigma_z)+\alpha E\frac{\partial^2\Delta T}{\partial x\partial y}+(1+\mu)\left(\frac{\partial F_x}{\partial y}+\frac{\partial F_y}{\partial x}\right)=0\\
&(1+\mu)\nabla^2\tau_{yz}+\frac{\partial^2}{\partial y\partial z}(\sigma_x+\sigma_y+\sigma_z)+\alpha E\frac{\partial^2\Delta T}{\partial y\partial z}+(1+\mu)\left(\frac{\partial F_y}{\partial z}+\frac{\partial F_z}{\partial y}\right)=0\\
&(1+\mu)\nabla^2\tau_{zx}+\frac{\partial^2}{\partial z\partial x}(\sigma_x+\sigma_y+\sigma_z)+\alpha E\frac{\partial^2\Delta T}{\partial z\partial x}+(1+\mu)\left(\frac{\partial F_z}{\partial x}+\frac{\partial F_x}{\partial z}\right)=0
\end{aligned}
\tag{3.42}
$$

$$
\begin{aligned}
&G\nabla^2u+(\lambda_L+G)\frac{\partial e_v}{\partial x}-\beta_t B\frac{\partial\Delta T}{\partial x}+F_x=0\\
&G\nabla^2v+(\lambda_L+G)\frac{\partial e_v}{\partial y}-\beta_t B\frac{\partial\Delta T}{\partial y}+F_y=0\\
&G\nabla^2w+(\lambda_L+G)\frac{\partial e_v}{\partial z}-\beta_t B\frac{\partial\Delta T}{\partial z}+F_z=0
\end{aligned}
\tag{3.43}
$$

3.6 Closing Remarks

Thermoelasticity provides a mathematical framework to investigate the coupled effects between thermal and mechanical behaviors in deformable bodies. By using relations between heat transfer and solid body mechanics, assumptions and calculations can be understood, clearly. Therefore, the fundamentals of thermoelasticity have been summarized after giving a brief review of elasticity theory and heat transfer in aircraft structures in this chapter.

4. NUMERICAL APPROACHES IN COMPUTATIONAL MECHANICS

Solving partial and ordinary differential equations with satisfactory accuracy in structural mechanics or other fields of engineering is always a challenge for engineers in the last few decades. Analytical solutions of these equations often prove impractical due to the intricate nature of the equations and the complexities inherent. Numerical methods step to the forefront, offering practical and effective approaches to approximate solutions of differential equations. Therefore, numerous global and local numerical methods such as Adomian Decomposition, Differential Quadrature, Differential Transform, Finite Difference, Mesh Free Galerkin, Dynamic Stiffness, Transfer Matrix, Discrete Singular Convolution, Fourier Series, Rayleigh-Ritz, and Chebyshev-Wavelet, etc. have been developed to solve a variety of complicated engineering problems in computational mechanics [225, 226].

Within the context of this chapter, the primary focus is to benchmark three specific numerical methods: the Differential Transform Method (DTM), the Differential Quadrature Method (DQM), and the Finite Difference Method (FDM). The strengths and weaknesses of these methods are assessed on beam and plate vibration analysis samples conducted in one and two dimensional domains. A brief overview of these methods, algorithm schemes, implementation strategy, and numerical results of vibration analysis are also discussed in the subsequent sections of this chapter.

4.1 Differential Transform Method

The Differential Transform Method (DTM) is a semi-numerical and analytical technique based on Taylor series expansion, first introduced by Zhou in the field of electrical circuit analysis [227]. Its success in solving a wide range of equations expressed as integral, fractional, difference, and differential equations made it gain recognition and has been extensively applied in the solution of engineering problems, physical phenomena, biological events, and economic systems [228-230].

Unlike traditional high-order Taylor series methods based on symbolic computation, the DTM employs an iterative procedure to solve the equation by defining it as a

polynomial series. Then, applying specific transformation rules outlined in Table 4.1, the governing differential equations and boundary conditions of any system are converted into a set of algebraic equations. The exact or approximate solution to the problem is obtained by solving these algebraic equations.

Table 4.1 : Fundamental function transforms.

Original Function	Transformed Function
$f(x)=g(x)\pm h(x)$	$F(k)=G(k)\pm H(k)$
$f(x)=c\,g(x)$	$F(k)=cG(k)$
$f(x)=x^n$	$F(k)=\delta(k-n)=\begin{cases}1, k=n\\0, k\neq n\end{cases}$
$f(x)=\sin(ax+b)$	$F(k)=\frac{a^k}{k!}\sin\left(\frac{\pi}{2}k+b\right)$
$f(x)=\frac{d^n g(x)}{dx^n}$	$F(k)=\frac{(k+n)!}{k!}G(k)$
$f(x)=g(x)h(x)$	$F(k)=\sum_{l=0}^{k}G(l)H(k-l)$

In order to grasp the practical implementation of the DTM, it is crucial to familiarize oneself with the definitions provided in Equations (4.1), (4.2), and (4.3). These transforms form the foundation of the theoretical background of this method. Function transform rules summarized in Table 4.1 can also be proved from these definitions.

The differential transform of the k^{th} derivative of a function *f(x)* in a one-dimensional case is defined as follows:

$$F(k)=\frac{1}{k!}\left[\frac{d^k f(x)}{dx^k}\right]_{x=x_0} \tag{4.1}$$

where *F(k)* represents the transformed function of the original function *f(x)*, and the inverse differential transform of the *F(k)* function is defined by:

$$f(x)=\sum_{k=0}^{\infty}(x-x_0)^k F(k) \tag{4.2}$$

Any function that can be expressed in the following series expansion form using Equations 4.1 and 4.2 as:

$$f(x)=\sum_{k=0}^{\infty}\frac{(x-x_0)^k}{k!}\left[\frac{d^k f(x)}{dx^k}\right]_{x=x_0} \tag{4.3}$$

A flowchart in Figure 4.1 provides a visual representation of the algorithm of the DTM. By following these steps, promising results in diverse applications, including eigenvalue problems can be obtained. To illustrate its practical application, vibration analyses for beam and plate elements are conducted in the following sections.

4.1.1 Application of differential transform method to beam element

The usage of DTM on one-dimensional structural problems can be understood by eigenvalue problems. With this aim, the expressions in the study of Malik (1998) about the vibration analysis of the Bernoulli-Euler beam are rewritten explicitly to make its application clear [231].

The following expression represents the mathematical model governing the beam's free vibration:

$$\rho A\frac{\partial^2 w(x,t)}{\partial t^2}+EI\frac{\partial^4 w(x,t)}{\partial x^4}=0 \tag{4.4}$$

In a non-dimensional form, the governing differential equation for free harmonic vibration of a Bernoulli-Euler beam with uniform cross-section and length L can be obtained by separating Equation (4.4) into two ordinary differential equations (ODEs). Then, non-dimensional steady equation of the vibration motion is given as follows:

$$\frac{d^4 w(x)}{dx^4}-\Omega^2 w(x)=0 \tag{4.5}$$

where x is the non-dimensional coordinate along the longitudinal axis of the beam. The boundary conditions of a uniform beam at the edges *x=0 and x=1* are tabulated in Table 4.2. Each geometric and natural boundary imposes different constraints on the displacement and rotation of the beam at its ends.

Table 4.2 : The boundary conditions for a uniform beam.

Boundary Type	***Expression***	
Clamped	$w=0,$	$\dfrac{dw}{dx}=0$
Simply-supported	$w=0,$	$\dfrac{d^2w}{dx^2}=0$
Free	$\dfrac{d^2w}{dx^2}=0,$	$\dfrac{d^3w}{dx^3}=0$

Using the transformation rules provided in Table 4.1, the equation of motion in Equation (4.5) for the Bernoulli-Euler beam can be transformed into the following equation:

$$\frac{(k+4)!}{k!}W(k+4)-\Omega^2W(k)=0 \tag{4.6}$$

and the recurrence relation is obtained from Equation (4.6) as follows:

$$W(k+4)=\frac{\Omega^2}{(k+4)(k+3)(k+2)(k+1)}W(k) \tag{4.7}$$

The boundary conditions in Table 4.2 are transformed into algebraic equations at the ends of the beam using the transformation technique in Equations (4.2) and (4.3), which are given in Table 4.3.

Table 4.3 : The transformed boundary conditions for a uniform beam.

Boundary Conditions	$x=0$	$x=1$
Clamped	$W(0)=0, \quad W(1)=0$	$\sum_{k=0}^{N}W(k)=0, \quad \sum_{k=0}^{N}kW(k)=0$
Simply-supported	$W(0)=0, \quad W(2)=0$	$\sum_{k=0}^{N}W(k)=0, \quad \sum_{k=0}^{N}k(k-1)W(k)=0$
Free	$W(2)=0, \quad W(3)=0$	$\sum_{k=0}^{N}k(k-1)W(k)=0, \quad \sum_{k=0}^{N}k(k-1)(k-2)W(k)=0$

By substituting these algebraic equations defined for the boundary conditions into the recurrence relation given in Equation (4.7), the following mode functions and frequency equations in Malik's study (Malik, 1998) can be derived for different combinations of boundary conditions [231]. In structural dynamics, mode shapes provide a visual representation of the spatial deflections, while the frequency values indicate the critical frequencies at which resonance occurs.

According to DTM rules in Table 4.1 and fundamental definitions, the detailed proof of the transformed vibration equations for the clamped-free, clamped-clamped, and clamped-simply supported boundary conditions can be given in Equations 4.8 and 4.9. For the clamped-free beam, the boundary conditions at the clamped edge simplify the recurrence equation as follows:

$$
\begin{aligned}
&k=0\ :\ W_0=0, && W_4=\frac{0!}{4!}\Omega^2 W_0=0 && \rightarrow W_{4k}=0\\
&k=1\ :\ W_1=0, && W_5=\frac{1!}{5!}\Omega^2 W_1=0 && \rightarrow W_{4k+1}=0\\
&k=2\ :\ W_2\neq 0, && W_6=\frac{2!}{6!}\Omega^2 W_2 && \rightarrow W_{4k+2}=\frac{2!}{(4k+2)!}\Omega^{2k} W_2\\
&k=3\ :\ W_3\neq 0, && W_7=\frac{3!}{7!}\Omega^2 W_3 && \rightarrow W_{4k+3}=\frac{3!}{(4k+3)!}\Omega^{2k} W_3
\end{aligned}
\tag{4.8}
$$

where the subscript notation is used to represent *W(k)* instead of W_k. Using the simplified recurrence relations and the boundary conditions at the *x=0*, the following relations can be derived for the free end at the free edge:

$$
\begin{aligned}
\sum_{k=0}^{N} k(k-1)W_k=0:\ & 2.1.W_2+3.2.W_3+6.5.W_6+7.6.W_7\\
&+(4k+2)(4k+1)W_{4k+2}+(4k+3)(4k+2)W_{4k+3}+\ldots=0,\\
&\Rightarrow \sum_{k=0}^{N}\frac{\Omega^{2k}}{(4k)!}W_2+3\sum_{k=0}^{N}\frac{\Omega^{2k}}{(4k+1)!}W_3=0
\end{aligned}
\tag{4.9}
$$

$$
\begin{aligned}
\sum_{k=0}^{N} k(k-1)(k-2)W_k=0:\ & 3.2.1.W_3+6.5.4.W_6+7.6.5.W_7+(4k+2)(4k+1)4k\\
&W_{4k+2}+(4k+3)(4k+2)(4k+1)W_{4k+3}+\ldots=0,\\
&\Rightarrow \sum_{k=0}^{N}\frac{\Omega^{2k}}{(4k-1)!}W_2+3\sum_{k=0}^{N}\frac{\Omega^{2k}}{(4k)!}W_3=0
\end{aligned}
$$

Equations (4.9) can be grouped and rewritten as follows:

$$A_{11}(\Omega).W_2 + A_{12}(\Omega).W_3 = 0$$
$$A_{21}(\Omega).W_2 + A_{22}(\Omega).W_3 = 0 \tag{4.10}$$

where $A_{ij}(\Omega)$ s are closed form polynomials of Ω and given as following expressions

$$A_{11}(\Omega)=\sum_{k=0}^{N}\frac{\Omega^{2k}}{(4k)!},\quad A_{12}(\Omega)=3\sum_{k=0}^{N}\frac{\Omega^{2k}}{(4k+1)!},\quad A_{21}(\Omega)=\sum_{k=0}^{N}\frac{\Omega^{2k}}{(4k-1)!},\quad A_{22}(\Omega)=3\sum_{k=0}^{N}\frac{\Omega^{2k}}{(4k)!}$$

In matrix form, these algebraic equations can be rewritten as:

$$\begin{bmatrix} A_{11}(\Omega) & A_{12}(\Omega) \\ A_{21}(\Omega) & A_{22}(\Omega) \end{bmatrix}\begin{Bmatrix} W_2 \\ W_3 \end{Bmatrix} = 0 \tag{4.11}$$

The frequency equation of the beam is obtained by equating the determinant of the coefficient matrix in Equation (4.11) to zero, and the mode function for the C-F beam can be obtained by from Equations (4.8) and (4.9) as follows:

$$w(x)=\sum_{k=0}^{N}x^k W_k=\sum_{k=0}^{N}\frac{\Omega^{2k}}{(4k+2)!}\,x^{4k+2}-\frac{\sum_{k=0}^{N}\frac{\Omega^{2k}}{(4k)!}}{\sum_{k=0}^{N}\frac{\Omega^{2k}}{(4k+1)!}}\sum_{k=0}^{N}\frac{\Omega^{2k}}{(4k+3)!}\,x^{4k+3} \tag{4.12}$$

The frequency equation for the C-F beam can be expressed as:

$$\sum_{k=0}^{N}\frac{\Omega^{2k}}{(4k)!}\sum_{k=0}^{N}\frac{\Omega^{2k}}{(4k)!}-\sum_{k=0}^{N}\frac{\Omega^{2k}}{(4k+1)!}\sum_{k=0}^{N}\frac{\Omega^{2k}}{(4k-1)!}=0 \tag{4.13}$$

For the clamped-clamped beam, the following recurrence relations can be derived for the both edges at $x = 0$ and $x = 1$.

$$\sum_{k=0}^{N}W_k=0: W_2+W_3+W_6+W_7+\ldots+W_{4k+2}+W_{4k+3}+\ldots=0,$$
$$\Rightarrow\ \sum_{k=0}^{N}\frac{\Omega^{2k}}{(4k+2)!}W_2+3\sum_{k=0}^{N}\frac{\Omega^{2k}}{(4k+3)!}W_3=0$$
$$\sum_{k=0}^{N}kW_k=0: 2W_2+3W_3+6W_6+7W_7+\ldots+(4k+2)W_{4k+2} \tag{4.14}$$
$$+(4k+3)W_{4k+3}+\ldots=0\ \Rightarrow\ \sum_{k=0}^{N}\frac{\Omega^{2k}}{(4k+1)!}W_2+3\sum_{k=0}^{N}\frac{\Omega^{2k}}{(4k+2)!}W_3=0$$

From the Equation (4.14), $A_{ij}(\Omega)$ closed form polynomials for the beam are given as:

$$A_{11}(\Omega)=\sum_{k=0}^{N}\frac{\Omega^{2k}}{(4k+2)!},A_{12}(\Omega)=3\sum_{k=0}^{N}\frac{\Omega^{2k}}{(4k+3)!},A_{21}(\Omega)=\sum_{k=0}^{N}\frac{\Omega^{2k}}{(4k+1)!},A_{22}(\Omega)=3\sum_{k=0}^{N}\frac{\Omega^{2k}}{(4k+2)!}$$

The frequency equation and mode function for the beam can be given in Equations (4.15) and (4.16), respectively.

$$\sum_{k=0}^{N}\frac{\Omega^{2k}}{(4k+2)!}\sum_{k=0}^{N}\frac{\Omega^{2k}}{(4k+2)!}-\sum_{k=0}^{N}\frac{\Omega^{2k}}{(4k+3)!}\sum_{k=0}^{N}\frac{\Omega^{2k}}{(4k+1)!}=0 \tag{4.15}$$

$$w(x)=\sum_{k=0}^{N}x^{k}W_{k}=\sum_{k=0}^{N}\frac{\Omega^{2k}}{(4k+2)!}x^{4k+2}-\frac{\sum_{k=0}^{N}\frac{\Omega^{2k}}{(4k+2)!}}{\sum_{k=0}^{N}\frac{\Omega^{2k}}{(4k+3)!}}\sum_{k=0}^{N}\frac{\Omega^{2k}}{(4k+3)!}x^{4k+3} \tag{4.16}$$

For the clamped-simply supported beam, the recurrence relations can be written for the simply-supported edge at *x =1* by employing DTM theorems as:

$$\begin{aligned}\sum_{k=0}^{N}W(k)=0:{}&W_2+W_3+W_6+W_7+\ldots+W_{4k+2}+W_{4k+3}+\ldots=0,\\ &\Rightarrow\sum_{k=0}^{N}\frac{\Omega^{2k}}{(4k+2)!}W_2+3\sum_{k=0}^{N}\frac{\Omega^{2k}}{(4k+3)!}W_3=0\\ \sum_{k=0}^{N}k(k-1)W(k)=0:{}&2.1.W_2+3.2.W_3+6.5.W_6+7.6.W_7+\ldots\\ &+(4k+2)(4k+1)W_{4k+2}+(4k+3)(4k+2)W_{4k+3}+\ldots=0,\\ &\Rightarrow\sum_{k=0}^{N}\frac{\Omega^{2k}}{(4k)!}W_2+3\sum_{k=0}^{N}\frac{\Omega^{2k}}{(4k+1)!}W_3=0\end{aligned} \tag{4.17}$$

In this case, $A_{ij}(\Omega)$ closed-form polynomials for the beam are given as:

$$A_{11}(\Omega)=\sum_{k=0}^{N}\frac{\Omega^{2k}}{(4k+2)!},\quad A_{12}(\Omega)=3\sum_{k=0}^{N}\frac{\Omega^{2k}}{(4k+3)!},\quad A_{21}(\Omega)=\sum_{k=0}^{N}\frac{\Omega^{2k}}{(4k)!},\quad A_{22}(\Omega)=3\sum_{k=0}^{N}\frac{\Omega^{2k}}{(4k+1)!}$$

The frequency equation and mode function for the beam with clamped-clamped boundary conditions can be given in Equations (4.18) and (4.19), respectively.

$$\sum_{k=0}^{N}\frac{\Omega^{2k}}{(4k+2)!}\sum_{k=0}^{N}\frac{\Omega^{2k}}{(4k+1)!}-\sum_{k=0}^{N}\frac{\Omega^{2k}}{(4k+3)!}\sum_{k=0}^{N}\frac{\Omega^{2k}}{(4k)!}=0 \tag{4.18}$$

$$w(x)=\sum_{k=0}^{N} x^k W_k=\sum_{k=0}^{N}\frac{\Omega^{2k}}{(4k+2)!}\,x^{4k+2}-\frac{\sum_{k=0}^{N}\dfrac{\Omega^{2k}}{(4k+2)!}}{\sum_{k=0}^{N}\dfrac{\Omega^{2k}}{(4k+3)!}}\sum_{k=0}^{N}\frac{\Omega^{2k}}{(4k+3)!}\,x^{4k+3} \tag{4.19}$$

The frequency equation and mode function relations for Simply Supported-Simply Supported Beam, Simply Supported-Free Beam, and Free-Free Beam can be obtained by following the same steps discussed above; hence, they are not reiterated here. By solving these recurrence relations, the dimensionless natural frequencies are tabulated in Table 4.4, and mode shapes are shown in Figure 4.2. The numerical results for the first nine natural frequencies are also compared to the exact analytic results in the study of Blevins (2001) to assess the accuracy and reliability of the DTM [232]. The findings show that the DTM is a powerful numerical tool for one-dimensional problems.

Table 4.4 : The first nine nondimensional natural frequency of the beam.

Boundary Conditions		**C-C**	**C-S**	**C-F**	**S-S**	**S-F**	**F-F**
Mode							
1st	DTM	22,3732	15,4182	3,5172	9,8696	15,4233	22,3882
	Exact	22,3733	15,4182	3,5160	9,8696	15,4182	22,3733
2nd	DTM	61,6723	49,9646	22,0418	39,4783	49,9814	61,7138
	Exact	61,6728	49,9648	22,0345	39,4784	49,9649	61,6728
3rd	DTM	120,9015	104,2465	61,7174	88,8258	104,2817	120,9833
	Exact	120,9034	104,2477	61,6972	88,8264	104,2477	120,9034
4th	DTM	199,8547	178,2665	120,9409	157,9116	178,3269	199,9903
	Exact	199,8594	178,2697	120,9019	157,9137	178,2697	199,8594
5th	DTM	298,5455	272,0237	199,9226	246,7350	272,1162	298,7489
	Exact	298,5555	272,0310	199,8595	246,7401	272,0310	298,5555
6th	DTM	416,9720	385,5171	298,6472	355,2952	385,6487	417,2570
	Exact	416,9908	385,5314	298,5555	355,3058	385,5314	416,9908
7th	DTM	555,1330	518,7456	417,1145	483,5911	518,9234	555,5138
	Exact	555,1652	518,7711	416,9908	483,6106	518,7711	555,1652
8th	DTM	713,0269	671,7079	555,3233	631,6214	671,9389	713,5178
	Exact	713,0789	671,7499	555,1652	631,6547	671,7499	713,0789
9th	DTM	890,6522	844,4023	713,2723	799,3846	844,6937	891,2676
	Exact	890,7318	844,4680	713,0789	799,4380	844,4680	890,7318
10th	DTM	1088,0070	1036,8272	890,9598	986,8791	1037,1862	1088,7614
	Exact	1088,1239	1036,9253	890,7318	986,9604	1036,9253	1088,1239

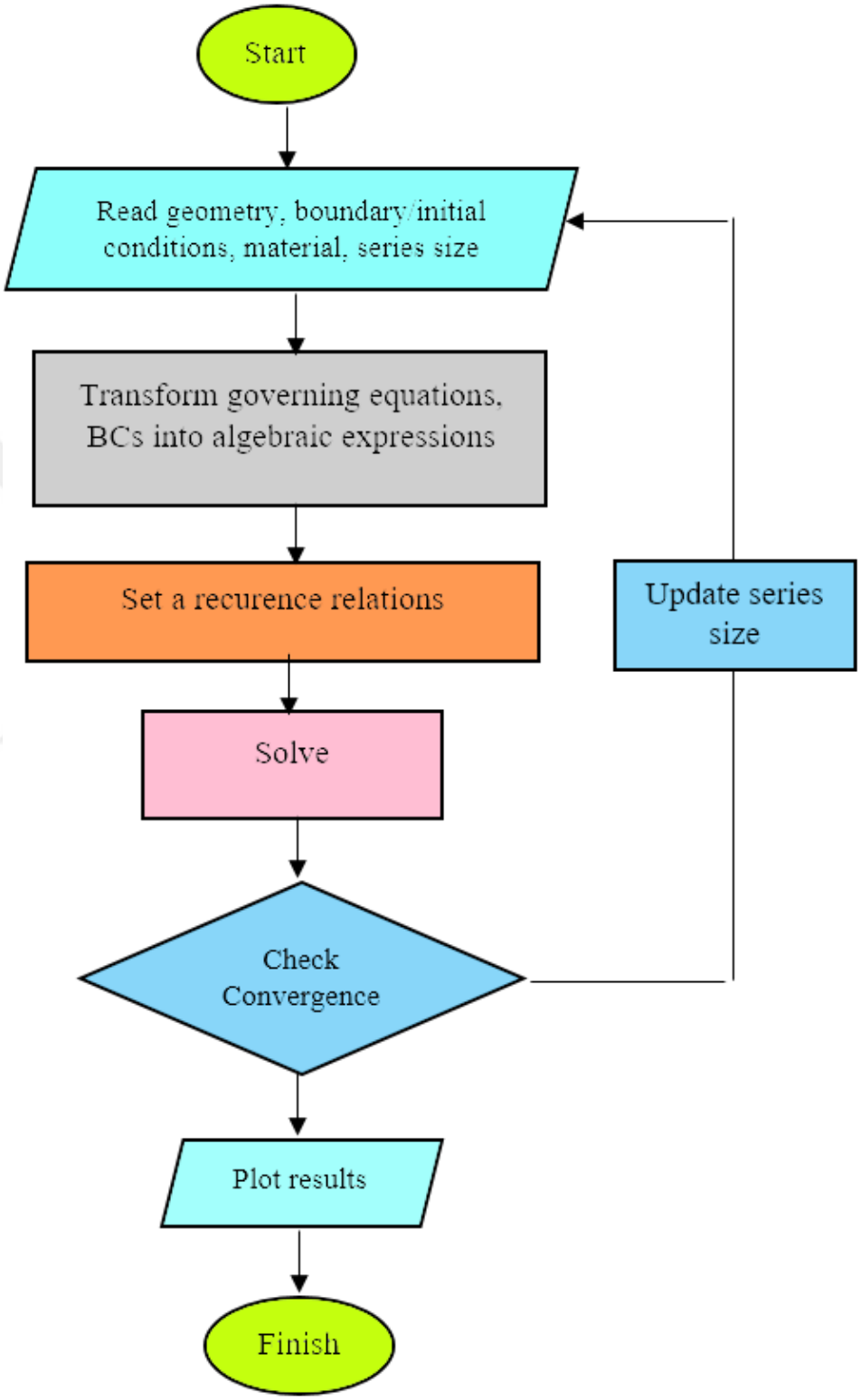

Figure 4.1 : DTM solution algorithm's flowchart.

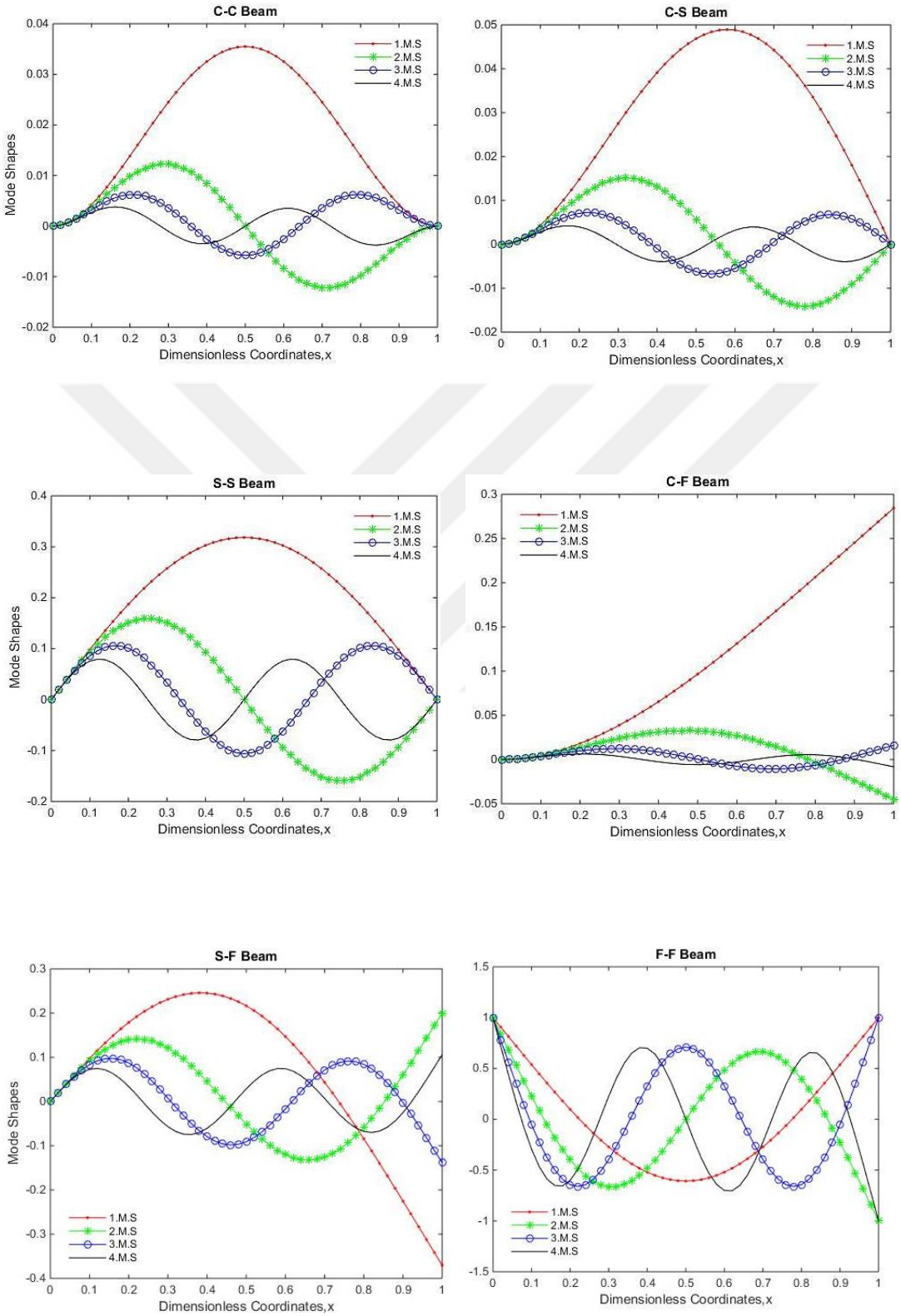

Figure 4.2 : Mode shapes of different beam types.

To achieve computational efficiency and obtain good agreement with the exact analytical results, determining the optimal term number in the series is crucial. By conducting the convergence analysis, the optimal series size can be determined for the recurrence relations. Based on the convergence analysis in Figure 4.3, an appropriate number of series sizes is determined as $N = 22$ for the efficient vibration analysis. For this size, the numerical results converge to the analytical results, which are given in Table 4.4 for different BCs.

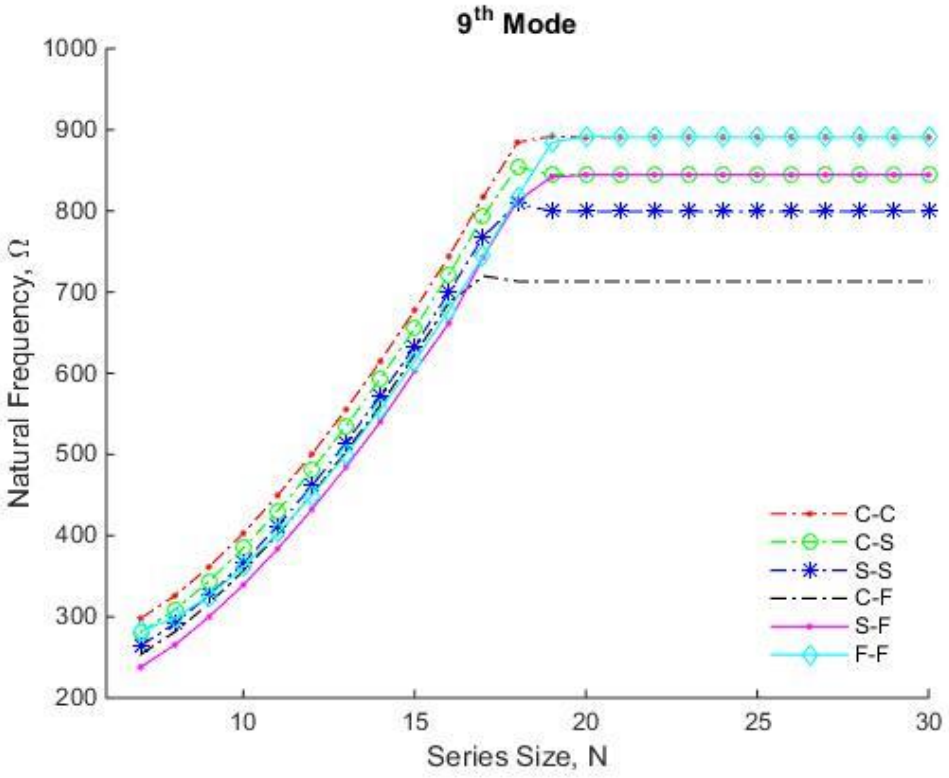

Figure 4.3 : Convergence analysis of the natural frequencies for the 9th mode.

4.1.2 Application of differential transform method to plate element

To illustrate the two-dimensional application of DTM, free vibration analysis of the thin rectangular plate under Kirchhoff's assumptions is considered. Differently from the one-dimensional case, obtaining simplified recurrence relations between boundary conditions and the equation of motion or governing differential equations for two-dimensional DTM applications is challenging, except for some well-arranged problems. By employing the DTM, the mode shapes and natural frequencies of the plate can be determined for the reduced plate model.

For the free vibration analysis of a thin rectangular plate, the mathematical model can be described with the following governing equation:

$$\rho h \frac{\partial^2 w(x,y,t)}{\partial t^2} + D\nabla^4 w(x,y,t) = 0 \tag{4.20}$$

By employing the separation of variables method, the governing differential equation of the plate in Equation (4.20) can be written in a non-dimensional form as follows:

$$\frac{\partial^4 w(x,y)}{\partial x^4} + 2\lambda^2 \frac{\partial^4 w(x,y)}{\partial x^2 \partial y^2} + \lambda^4 \frac{\partial^4 w(x,y)}{\partial y^4} - \Omega^2 w(x,y) = 0 \tag{4.21}$$

By applying the transformation rules provided in Table 4.1, the equation of motion in Equation (4.21) can be converted into the following expression:

$$\begin{aligned} &\frac{(k+4)!}{k!} W(k+4,h) + 2\lambda^2 \frac{(k+2)!(h+2)!}{k!h!} W(k+2,h+2)... \\ &\qquad + \lambda^4 \frac{(h+4)!}{h!} W(k,h+4) - \Omega^2 W(k,h) = 0 \end{aligned} \tag{4.22}$$

From the Equation (4.22), the recurrence relation can be derived as:

$$\begin{aligned} W(k+4,h) = &\frac{\Omega^2}{(k+4)(k+3)(k+2)(k+1)} W(k,h) - 2\lambda^2 \frac{(h+2)(h+1)}{(k+4)(k+3)} \\ &W(k+2,h+2) - \lambda^4 \frac{(h+4)(h+3)(h+2)(h+1)}{(k+4)(k+3)(k+2)(k+1)} W(k,h+4) \end{aligned} \tag{4.23}$$

Unlike the example given for one dimensional case in previous section, the boundary conditions cannot be implemented into this relation, which is necessary to obtain the numerical solution. Therefore, in two-dimensional problems, the order of governing equations sometimes needs to be reduced by using specific functions that satisfy boundary and regularity conditions. This reduction allows for a more manageable and efficient analysis, especially in cases where obtaining simplified recurrence relations directly between the boundary conditions and the governing differential equations in two-dimensional DTM applications.

By the help of the deflection function of the beam for the simply supported case, two dimensional vibration problem can be reduced to one dimensional vibration problem for the plate so that expressions for the mode functions and natural frequencies are obtained.

The following trigonometric deflection equation allows for reducing the size of the plate:

$$w(x,y) = f(y).\sin(\sigma\pi x), \qquad \sigma \in Z^{+} \tag{4.24}$$

Assuming the plate to be simply-supported along the sides *x=0* and *x=1*, the plate deflection equation in non-dimensional coordinates can be written as:

$$\frac{\partial^4 f}{\partial y^4} - 2\varphi\frac{\partial^2 f}{\partial y^2} - \psi f(y) = 0, \text{ where } \varphi = \left(\frac{\sigma\pi}{\lambda}\right)^2, \ \psi = \frac{\Omega^2}{\lambda^4} - \left(\frac{\sigma\pi}{\lambda}\right)^4 \tag{4.25}$$

Using the transformation rules provided in Table 4.1, the equation of motion given in Equation (4.25) can be transformed into the following equation for the simply-supported boundaries along the edges *x = 0* and *x = 1*.

$$\frac{(h+4)!}{h!}F(h+4) - 2\varphi\frac{(h+2)!}{h!}F(h+2) - \psi F(h) = 0 \tag{4.26}$$

For the new plate equation in Equation (4.25), the expressions for the boundaries of the plate must be updated, which are given in Table 4.5. These expressions are essential in defining the dynamic behavior of the structure. Like the transformed equation of motion in Equation (4.26), these conditions are transformed into algebraic equations like the transformed equation of motion in Equation (4.26), which are presented in Table 4.6.

Table 4.5 : Boundary conditions of the plate along *y=0*, and *y=1* edges.

Boundary Type	**Rewritten Boundary Expressions**	
Clamped	$f(y) = 0,$	$\frac{df(y)}{dy} = 0$
Simply-supported	$f(y) = 0,$	$\frac{d^2 f(y)}{dy^2} = 0$
Free	$\frac{d^2 f(y)}{dy^2} - p\, f(y) = 0,$	$\frac{d^3 f(y)}{dy^3} - q\frac{df(y)}{dy} = 0$

Table 4.6 : Transformed boundary conditions for the reduced plate.

Boundary Conditions	$y = 0$	$y = 1$
Clamped	$F(0) = 0,\ F(1) = 0$	$\sum_{h=0}^{M} F(h) = 0, \quad \sum_{h=0}^{M} hF(h) = 0,$
Simply Supported	$F(0) = 0,\ F(2) = 0$	$\sum_{h=0}^{M} F(h) = 0, \quad \sum_{h=0}^{M} h(h-1)F(h) = 0,$
Free	$2F(2) - pF(0) = 0,$ $6F(3) - qF(1) = 0$	$\sum_{h=0}^{M} \{h(h-1) - p\}F(h) = 0,$ $\sum_{h=0}^{M} \{h(h-1)(h-2) - q\}F(h) = 0,$

To simplify the aforementioned algebraic equation, it can be written in 4th order polynomial form by using the fundamental DTM definition $F(h) = d^h/h!$ [233]. Then, Equation (4.26) can be given as:

$$d^4 - 2\varphi d^2 - \psi = 0 \tag{4.27}$$

This simplification enables us to find the roots of the polynomial equation, which correspond to the values of the transformed function at specific points. The roots of Equation (4.27) are obtained as $d_1^2 = \left((\sigma\pi)^2 + \Omega\right)/\lambda^2$, $d_2^2 = \left((\sigma\pi)^2 - \Omega\right)/\lambda^2$, and the transformed general solution can be written easily according to these roots as:

$$F(h) = \frac{1}{h!}\left(C_1 d_1^h + C_2 d_2^h\right), \qquad h = 0,1,2...\infty \tag{4.28}$$

where C_i is the constant. The general solution of the transformed equation of motion (EOM) is expressed in terms of even and odd differential transforms, and hence, it can be written as:

$$\begin{aligned} F_{2h} &= \frac{1}{(2h)!}\left(E_1 d_1^{2h} + E_2 d_2^{2h}\right), \\ F_{2h+1} &= \frac{1}{(2h+1)!}\left(O_1 d_1^{2h+1} + O_2 d_2^{2h+1}\right), \qquad h = 0,1,2...\infty \end{aligned} \tag{4.29}$$

In Equation (4.29), the superscript indicates the power of the parameter *d*, and the subscript shows the root number.

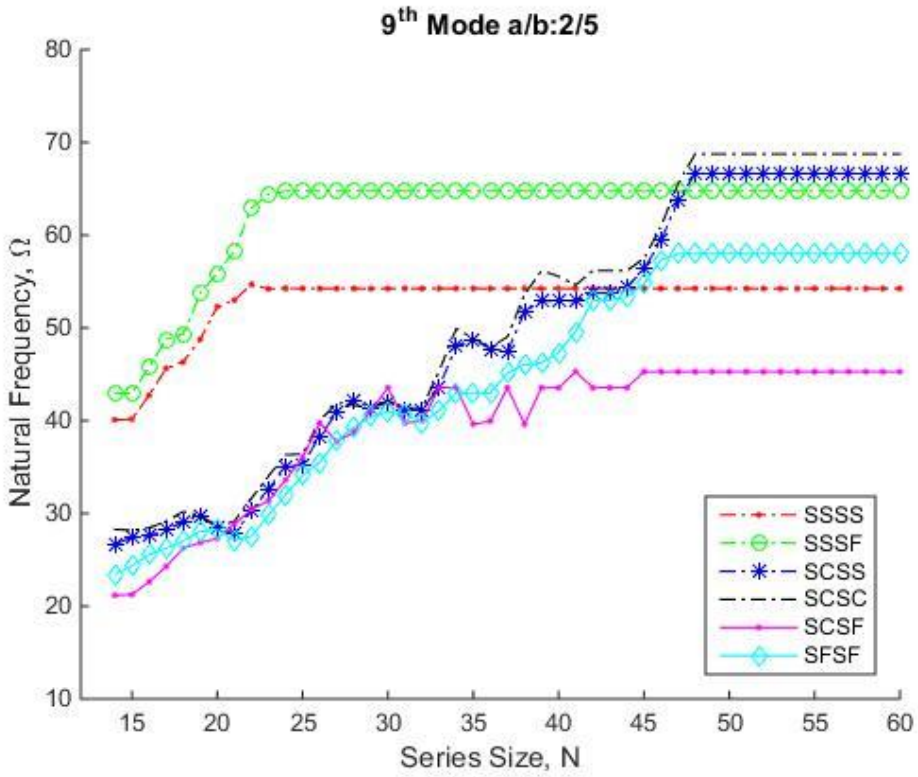

Figure 4.4 : Convergence of the natural frequencies for the 9th mode with a/b: 2/5.

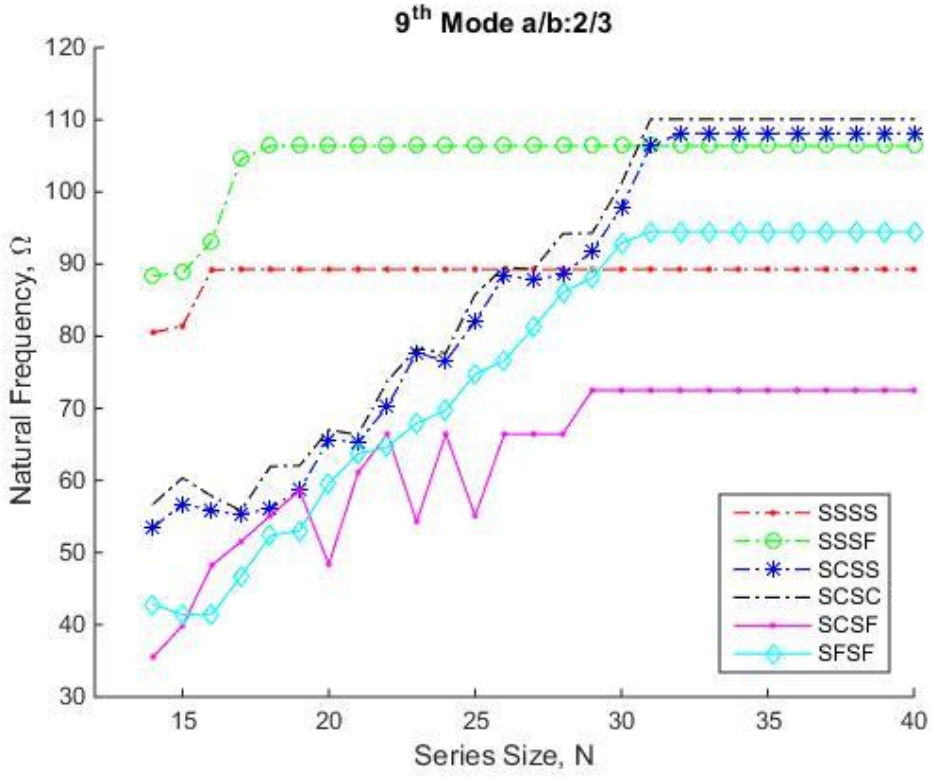

Figure 4.5 : Convergence of the natural frequencies for the 9th mode with a/b:2/3.

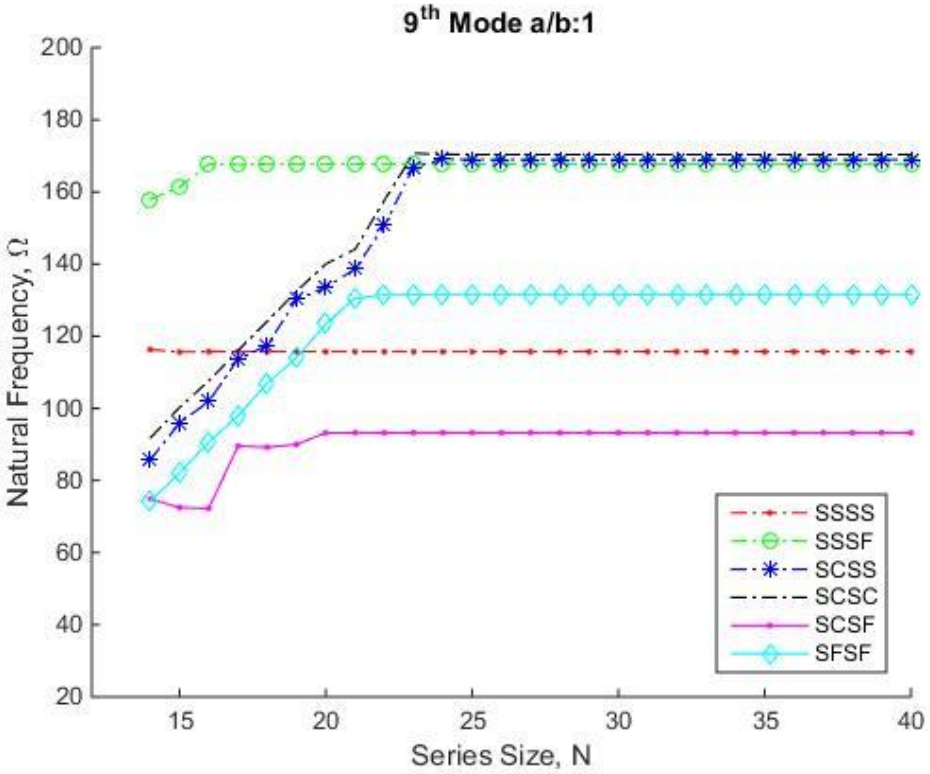

Figure 4.6 : Convergence of the natural frequencies for the 9th mode with a/b:1.

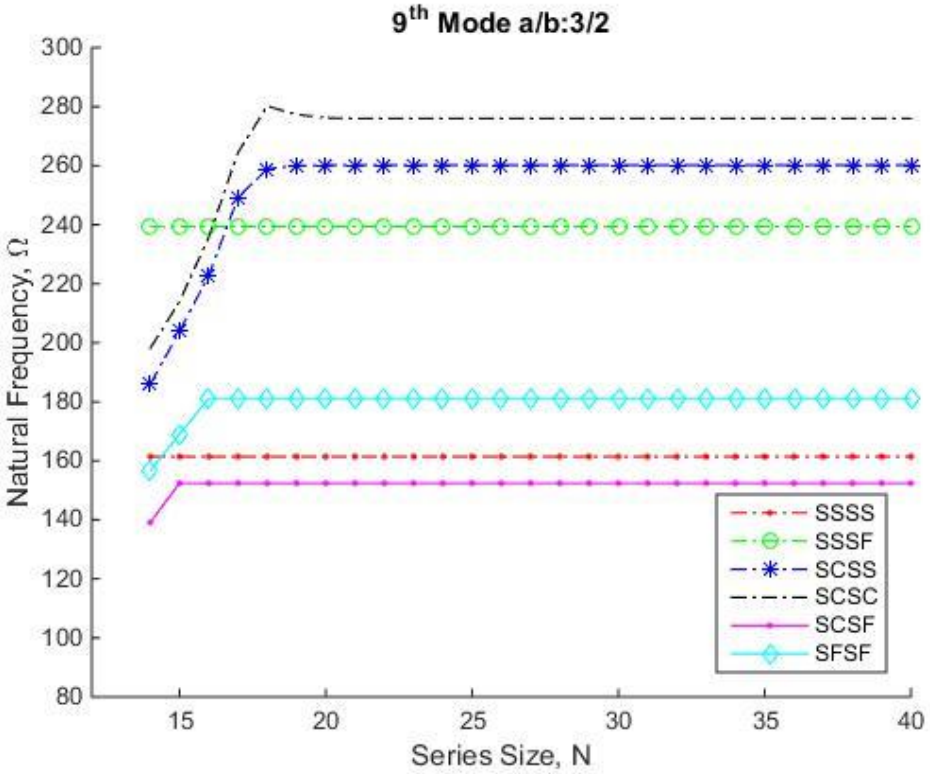

Figure 4.7 : Convergence of the natural frequencies for the 9th mode with a/b:3/2.

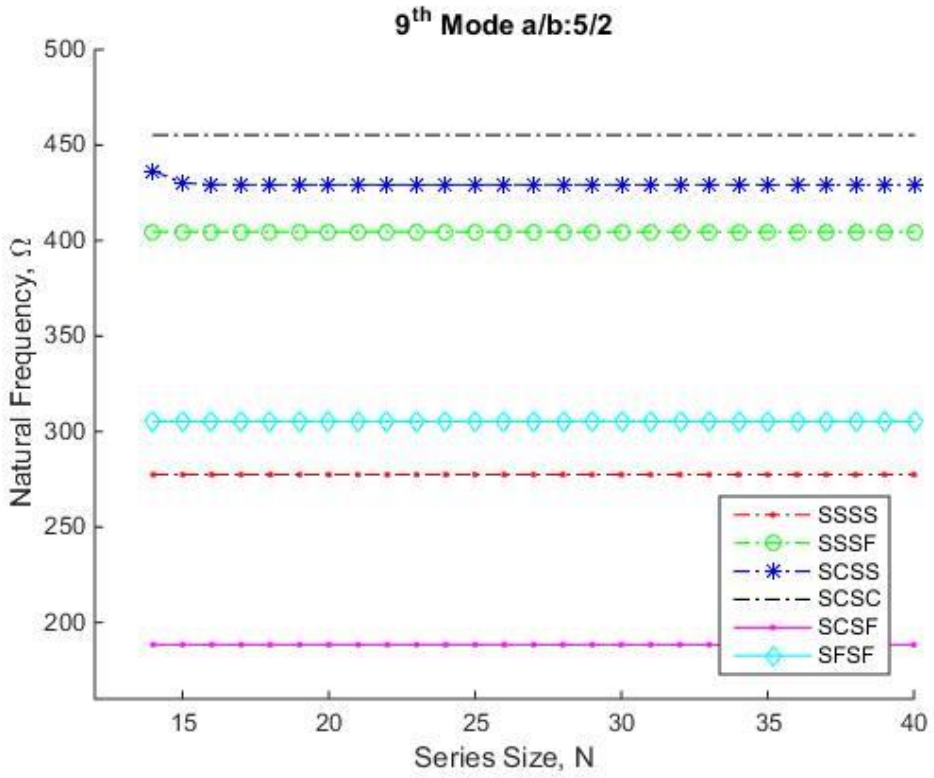

Figure 4.8 : Convergence of the natural frequencies for the 9th mode with a/b:5/2.

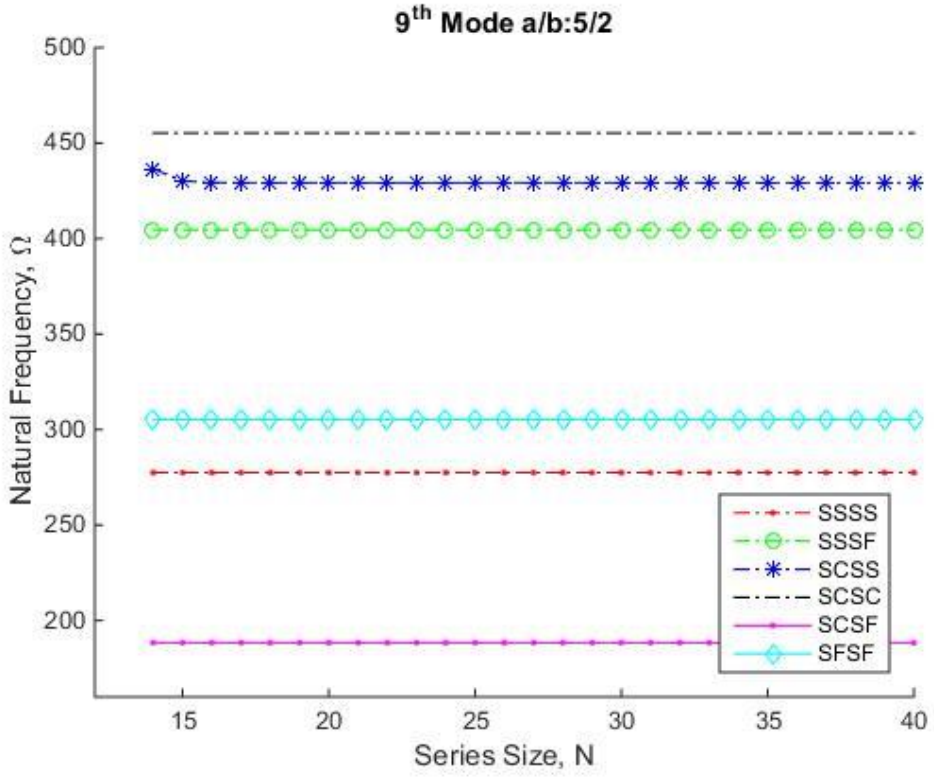

Figure 4.8 : Convergence of the natural frequencies for the 9th mode with a/b:5/2.

By taking the inverse transform of the EOM of the plate in Equation (4.28), the general solution can be obtained as:

$$f(y)=\sum_{h=0}^{M} y^{2h}.F(2h)+\sum_{h=0}^{M} y^{2h+1}.F(2h+1) \tag{4.30}$$

Here, the use of even and odd differential transforms in the general solution allows for a more versatile representation of the reduced deflection function *F(x,y)* during free vibration analysis. In the light of the relations in Table 4.6 and Equation (4.30), the mode functions and natural frequency expressions can be found for the plate with simply supported-free (SSSF) and simply supported-simply supported (SSSS) as:

1. Plate with Simply Supported- Free along y sides (SSSF):

By substituting the algebraic equations defined for the simply supported boundary conditions at *y = 0* into the general solution, the specific relations for the Simply Supported-Free Plate (SSSF) configuration can be obtain for even and odd terms in the solution as:

Even Terms:

$$\left.\begin{aligned} &h=0:\ F_0=0\rightarrow F_0=\frac{1}{0!}\left(E_1d_1^0+E_2d_2^0\right)\\ &h=1:\ F_2=0\rightarrow F_2=\frac{1}{2!}\left(E_1d_1^2+E_2d_2^2\right)\end{aligned}\right\}F_{2h}=0$$

Odd Terms (4.31)

$$\left.\begin{aligned} &h=0:\ F_1\neq 0\rightarrow F_1=\frac{1}{1!}\left(O_1d_1^1+O_2d_2^1\right)\\ &h=1:\ F_3\neq 0\rightarrow F_3=\frac{1}{3!}\left(O_1d_1^3+O_2d_2^3\right)\end{aligned}\right\}F_{2h+1}=\frac{\xi}{(2h+1)!}\left\{\left(\varepsilon_1\varepsilon_2^h-\varepsilon_2\varepsilon_1^h\right)F_1+6\left(\varepsilon_1^h-\varepsilon_2^h\right)F_3\right\}$$

where $\xi=\lambda^2/2\Omega$, $\varepsilon_1=d_1^2$, and $\varepsilon_2=d_2^2$. On the other hand, the boundary conditions at *y=1* edge can be rewritten up to Equation (4.21) as follows:

$$\begin{aligned}&\sum_{h=0}^{M}\left\{(2h+1)(2h)-p\right\}F(2h+1)=0,\\ &\sum_{h=0}^{M}(2h+1)\left\{(2h)(2h-1)-q\right\}F(2h+1)=0\end{aligned} \tag{4.32}$$

By utilizing the simplified relations in Equation (4.31) and the boundary conditions in Equation (4.32) for the free edge at y=1 side, we can derive the following relations for a rectangular plate with two opposite sides simply supported and the other two sides simply supported-free.

$$\begin{aligned}
&\sum_{h=0}^{M}\left\{\frac{(2h+1)(2h)-p}{(2h+1)!}\right\}\left(\varepsilon_1\varepsilon_2^h-\varepsilon_2\varepsilon_1^h\right)F_1+6\sum_{h=0}^{M}\left\{\frac{(2h+1)(2h)-p}{(2h+1)!}\right\}\left(\varepsilon_1^h-\varepsilon_2^h\right)F_3=0\\
&\sum_{h=0}^{M}\left\{\frac{(2h)(2h-1)-q}{(2h)!}\right\}\left(\varepsilon_1\varepsilon_2^h-\varepsilon_2\varepsilon_1^h\right)F_1+6\sum_{h=0}^{M}\left\{\frac{(2h)(2h-1)-q}{(2h)!}\right\}\left(\varepsilon_1^h-\varepsilon_2^h\right)F_3=0
\end{aligned} \tag{4.33}$$

Then, Equation (4.33) can be grouped and rewritten as follows:

$$\begin{aligned}
P_{11}(\Omega).F_1+P_{12}(\Omega).F_3&=0\\
P_{21}(\Omega).F_1+P_{22}(\Omega).F_3&=0
\end{aligned} \tag{4.34}$$

where $P_{ij}(\Omega)$ is closed form polynomials of Ω and given as following expressions

$$\begin{aligned}
P_{11}(\Omega)&=\sum_{h=0}^{M}\left\{\frac{(2h+1)(2h)-p}{(2h+1)!}\right\}\left(\varepsilon_1\varepsilon_2^h-\varepsilon_2\varepsilon_1^h\right),\quad P_{12}(\Omega)=6\sum_{h=0}^{M}\left\{\frac{(2h+1)(2h)-p}{(2h+1)!}\right\}\left(\varepsilon_1^h-\varepsilon_2^h\right)\\
P_{21}(\Omega)&=\sum_{h=0}^{M}\left\{\frac{(2h)(2h-1)-q}{(2h)!}\right\}\left(\varepsilon_1\varepsilon_2^h-\varepsilon_2\varepsilon_1^h\right),\quad P_{22}(\Omega)=6\sum_{h=0}^{M}\left\{\frac{(2h)(2h-1)-q}{(2h)!}\right\}\left(\varepsilon_1^h-\varepsilon_2^h\right)
\end{aligned}$$

In matrix form, these algebraic equations can be written as:

$$\begin{bmatrix} P_{11}(\Omega) & P_{12}(\Omega) \\ P_{21}(\Omega) & P_{22}(\Omega) \end{bmatrix}\begin{Bmatrix} F_1 \\ F_3 \end{Bmatrix}=0 \tag{4.35}$$

The characteristic equation or frequency equation of the plate is obtained by equaling the determinant of the coefficient matrix in Equation (4.35) to zero. Meanwhile, non-dimensional natural frequency equation can be given for SSSF plate as:

$$\begin{aligned}
&\sum_{h=0}^{M}\left\{\frac{(2h+1)(2h)-p}{(2h+1)!}\right\}\left(\varepsilon_1\varepsilon_2^h-\varepsilon_2\varepsilon_1^h\right)\sum_{h=0}^{M}\left\{\frac{(2h)(2h-1)-q}{(2h)!}\right\}\left(\varepsilon_1^h-\varepsilon_2^h\right)\\
&\quad-\sum_{h=0}^{M}\left\{\frac{(2h+1)(2h)-p}{(2h+1)!}\right\}\left(\varepsilon_1^h-\varepsilon_2^h\right)\sum_{h=0}^{M}\left\{\frac{(2h)(2h-1)-q}{(2h)!}\right\}\left(\varepsilon_1\varepsilon_2^h-\varepsilon_2\varepsilon_1^h\right)=0
\end{aligned} \tag{4.36}$$

Moreover, the mode function for the Simply SSSF plate case can be written as follows:

$$f(y)=\sum_{h=0}^{M} y^{2h+1} F_{2h+1}=\sum_{h=0}^{M}\frac{y^{2h+1}}{(2h+1)!}\left(\varepsilon_1\varepsilon_2^h-\varepsilon_2\varepsilon_1^h\right)$$
$$-\frac{\sum_{h=0}^{M}\left\{\frac{(2h+1)(2h)-p}{(2h+1)!}\right\}\left(\varepsilon_1\varepsilon_2^h-\varepsilon_2\varepsilon_1^h\right)}{\sum_{h=0}^{M}\left\{\frac{(2h+1)(2h)-p}{(2h+1)!}\right\}\left(\varepsilon_1^h-\varepsilon_2^h\right)}\sum_{h=0}^{M}\frac{y^{2h+1}}{(2h+1)!}\left(\varepsilon_1^h-\varepsilon_2^h\right) \tag{4.37}$$

Following a similar procedure discussed above, the frequency equations and mode functions can be derived for other types of boundary conditions of the plate. As a second example, an SSSS plate can be given to make the application of DTM in a two-dimensional domain clear.

2. Plate with Simply Supported- Simply Supported along y sides (SSSS):

The boundary conditions at *y=0* were previously given in Equation (4.31), and by utilizing these conditions along with the boundary conditions at y=1 side, the following relations can be derived for the simply supported edge.

$$\sum_{h=0}^{M} F(2h+1)=0,$$
$$\sum_{h=0}^{M}(2h+1)(2h)\,F(2h+1)=0 \tag{4.38}$$

By applying the simplified relations given in Equation (4.31) and utilizing the boundary conditions presented in Equation (4.38) for the simply supported edge at *y=1* side, the following relations for a rectangular plate with two opposite sides being simply supported, and the other two sides being simply supported - simply supported can be derived.

$$\sum_{h=0}^{M}\frac{\left(\varepsilon_1\varepsilon_2^h-\varepsilon_2\varepsilon_1^h\right)}{(2h+1)!}F_1+6\sum_{h=0}^{M}\frac{\left(\varepsilon_1^h-\varepsilon_2^h\right)}{(2h+1)!}F_3=0$$
$$\sum_{h=0}^{M}\frac{\left(\varepsilon_1\varepsilon_2^h-\varepsilon_2\varepsilon_1^h\right)}{(2h-1)!}F_1+6\sum_{h=0}^{M}\frac{\left(\varepsilon_1^h-\varepsilon_2^h\right)}{(2h-1)!}F_3=0 \tag{4.39}$$

Equation (4.39) can be written in a polynomial form. In this case, closed form polynomials $P_{ij}(\Omega)$ can be given for a SSSS plate as:

$$P_{11}(\Omega)=\sum_{h=0}^{M}\frac{\varepsilon_1\varepsilon_2^h-\varepsilon_2\varepsilon_1^h}{(2h+1)!},\ P_{12}(\Omega)=6\sum_{h=0}^{M}\frac{\varepsilon_1^h-\varepsilon_2^h}{(2h+1)!},P_{21}(\Omega)=\sum_{h=0}^{M}\frac{\varepsilon_1\varepsilon_2^h-\varepsilon_2\varepsilon_1^h}{(2h-1)!},$$

$$P_{22}(\Omega)=6\sum_{h=0}^{M}\frac{\varepsilon_1^h-\varepsilon_2^h}{(2h-1)!}$$

By using polynomial expressions, the frequency equation and mode function for the SSSS rectangular plate can be expressed in Equations (4.40) and (4.41), respectively.

$$\sum_{h=0}^{M}\frac{\left(\varepsilon_1\varepsilon_2^h-\varepsilon_2\varepsilon_1^h\right)}{(2h+1)!}\sum_{h=0}^{M}\frac{\left(\varepsilon_1^h-\varepsilon_2^h\right)}{(2h-1)!}-\sum_{h=0}^{M}\frac{\left(\varepsilon_1^h-\varepsilon_2^h\right)}{(2h+1)!}\sum_{h=0}^{M}\frac{\left(\varepsilon_1\varepsilon_2^h-\varepsilon_2\varepsilon_1^h\right)}{(2h-1)!}=0 \tag{4.40}$$

$$f(y)=\sum_{h=0}^{M}\frac{y^{2h+1}}{(2h+1)!}\left(\varepsilon_1\varepsilon_2^h-\varepsilon_2\varepsilon_1^h\right)-\frac{\sum_{h=0}^{M}\frac{\left(\varepsilon_1\varepsilon_2^h-\varepsilon_2\varepsilon_1^h\right)}{(2h+1)!}}{\sum_{h=0}^{M}\frac{\left(\varepsilon_1^h-\varepsilon_2^h\right)}{(2h+1)!}}\sum_{h=0}^{M}\frac{y^{2h+1}}{(2h+1)!}\left(\varepsilon_1^h-\varepsilon_2^h\right) \tag{4.41}$$

The non-dimensional natural frequencies and mode functions for different boundary conditions of the rectangular plate: Clamped - Simply Supported Plate (SCSS), Clamped - Free Plate (SCSF), Free - Free Plate (SFSF), and Clamped - Clamped Plate (SCSC) can be found following the steps in the solution of these examples and algorithm chart in Figure 4.1. In numerical solutions of differential equations, expressions defining the physical phenomena or engineering problem are typically solved iteratively using discrete approximations, and the computed results are dependent on various parameters such as the grid size, time step, or series size. Therefore, convergence analysis is a vital part of the numerical solutions to obtain an accurate solution and determine the optimal series size. With this aim, convergence analysis is performed for the different aspect ratios of the plate, as shown in Figures 4.4 to 4.8. Once, the optimal series size is determined for each case, the non-dimensional natural frequencies in Table 4.7 can be computed, and compared to the exact analytical results in the study of Leissa (1973) to assess the efficiency of DTM [234].

Table 4.7 : The first nine dimensionless frequencies of Kirchhoff-Love plate via DTM.

Boundary Conditions		S-S-S-S					S-S-S-F				
Aspect Ratio		a/b					a/b				
Mode		2/5	2/3	1.0	3/2	5/2	2/5	2/3	1.0	3/2	5/2
1st	Exact	11,4487	14,2561	19,7392	32,0762	71,5564	10,1259	10,6712	11,6845	13,7111	18,8009
	DTM	11,4487	14,2561	19,7392	32,0762	71,5546	10,1259	10,6712	11,6845	13,7111	18,8009
2nd	Exact	16,1862	27,4156	49,3480	61,6850	101,1634	13,0570	18,2995	27,7563	43,5723	50,5405
	DTM	16,1862	27,4156	49,3480	61,6850	101,1634	13,0570	18,2995	27,7563	43,5723	50,5405
3rd	Exact	24,0818	43,8649	49,3480	98,6960	150,5115	18,8390	33,6974	41,1967	47,8571	100,2321
	DTM	24,0818	43,8649	49,3480	98,6960	150,5115	18,8390	33,6974	41,1967	47,8571	100,2321
4th	Exact	35,1358	49,3480	78,9568	111,0330	219,5987	27,5580	40,1307	59,0655	81,4789	110,2259
	DTM	35,1358	49,3480	78,9568	111,0330	219,5987	27,5580	40,1307	59,0655	81,4789	110,2259
5th	Exact	41,0576	57,0244	98,6960	128,3049	256,6097	39,3377	48,4082	61,8606	92,6925	147,6317
	DTM	41,0576	57,0244	98,6960	128,3049	256,6097	39,3377	48,4082	61,8606	92,6925	147,6317
6th	Exact	45,7950	78,9568	98,6960	177,6529	286,2185	39,6118	57,5929	90,2941	124,5635	169,1026
	DTM	45,7950	78,9568	98,6960	177,6529	286,2185	39,6118	57,5929	90,2941	124,5635	169,1026
7th	Exact	49,3480	80,0535	128,3049	180,1203	308,4251	42,6964	64,7281	94,4837	132,8974	203,7304
	DTM	49,3480	80,0535	128,3049	180,1203	308,4251	42,6964	64,7281	94,4837	132,8974	203,7304
8th	Exact	53,6906	93,2129	128,3049	209,7291	335,5665	48,7745	89,1859	108,9185	158,9180	257,4791
	DTM	53,6906	93,2129	128,3049	209,7291	335,5665	48,7745	89,1859	108,9185	158,9180	257,4791
9th	Exact	66,7185	106,3724	167,7833	239,3379	416,9908	54,2497	89,2725	115,6857	161,4205	277,4280
	DTM	64,7446	106,3724	167,7833	239,3379	404,6538	54,2497	89,2725	115,6857	161,4205	277,4280

Table 4.7: The first nine dimensionless frequencies of Kirchhoff-Love plate via DTM (Cont').

Boundary Conditions		S-C-S-S					S-C-S-C				
Aspect Ratio		a/b					a/b				
Mode		2/5	2/3	1.0	3/2	5/2	2/5	2/3	1.0	3/2	5/2
1st	Exact	11,7502	15,5783	23,6463	42,5278	103,9227	12,1347	17,3730	28,9509	56,3481	145,4839
	DTM	11,7502	15,5783	23,6463	42,5278	103,9227	12,1347	17,3730	28,9509	56,3481	145,4839
2nd	Exact	17,1872	31,0724	51,6743	69,0031	128,3382	18,3647	35,3445	54,7431	78,9836	164,7387
	DTM	17,1872	31,0724	51,6743	69,0031	128,3382	18,3647	35,3445	54,7431	78,9836	164,7387
3rd	Exact	25,9171	44,5644	58,6464	116,2671	172,3804	27,9657	45,4294	69,3270	123,1719	202,2271
	DTM	25,9171	44,5644	58,6464	116,2671	172,3804	27,9657	45,4294	69,3270	123,1719	202,2271
4th	Exact	37,8317	55,3926	86,1345	120,9956	237,2502	40,7500	62,0544	94,5853	146,2677	261,1053
	DTM	37,8317	55,3926	86,1345	120,9956	237,2502	40,7500	62,0544	94,5853	146,2677	261,1053
5th	Exact	41,2070	59,4627	100,2698	147,6353	320,7921	41,3782	62,3131	102,2162	170,1112	342,1442
	DTM	41,2070	59,4627	100,2698	147,6353	320,7921	41,3782	62,3131	102,2162	170,1112	342,1442
6th	Exact	46,3620	83,6060	113,2281	184,1006	322,9642	47,0009	88,8047	129,0955	189,1219	392,8746
	DTM	46,3620	83,6060	113,2281	184,1006	322,9642	47,0009	88,8047	129,0955	189,1219	392,8746
7th	Exact	52,9007	88,4384	133,7910	193,8025	346,7382	56,1782	94,2131	140,2045	212,8169	415,6906
	DTM	52,9007	88,4384	133,7910	193,8025	346,7382	56,1782	94,2131	140,2045	212,8169	415,6906
8th	Exact	54,8720	93,6758	140,8456	243,4964	391,0659	56,6756	97,4254	154,7757	276,0012	444,9682
	DTM	54,8720	93,6758	140,8456	243,4964	391,0659	56,6756	97,4254	154,7757	276,0012	444,9682
9th	Exact	66,6637	108,1069	168,9585	260,2020	429,2420	68,7486	101,0788	170,3465	276,0125	455,3054
	DTM	66,6637	108,1069	168,9585	260,2020	429,2420	68,7487	110,0788	170,3465	276,0125	455,3054

Table 4.7: The first nine dimensionless frequencies of Kirchhoff-Love plate via DTM (Cont').

Boundary Conditions		S-C-S-F					S-F-S-F				
Aspect Ratio		a/b					a/b				
		2/5	2/3	1.0	3/2	5/2	2/5	2/3	1.0	3/2	5/2
Mode											
1st	Exact	10,1888	10,9752	12,6874	16,8225	30,6277	9,7600	9,6983	9,6314	9,5582	9,4841
	DTM	10,1888	10,9752	12,6874	16,8225	30,6277	10,0378	10,3469	10,8348	11,4830	10,9887
2nd	Exact	13,6036	20,3355	33,0651	45,3024	58,0804	11,0368	12,9813	16,1348	21,6192	33,6228
	DTM	13,6036	20,3355	33,0651	45,3024	58,0804	10,6142	12,0355	14,5397	19,4336	32,3814
3rd	Exact	20,0971	37,9552	41,7019	61,0178	105,5470	15,0626	22,9535	36,7256	38,7214	38,3629
	DTM	20,0971	37,9552	41,7019	61,0178	105,5470	15,3365	23,4742	37,4453	41,8528	44,7725
4th	Exact	29,6219	40,2717	63,0148	92,3073	149,4569	21,7064	39,1052	38,9450	54,8443	75,2037
	DTM	29,6219	40,2717	63,0148	92,3073	149,4569	21,4860	39,9276	40,5583	50,3758	67,3425
5th	Exact	39,6382	49,7317	72,3976	93,8293	173,1060	31,1771	40,3560	46,7381	65,7922	86,9684
	DTM	39,6382	49,7317	72,3976	93,8293	173,1060	31,3384	40,0161	44,3050	66,5788	95,2636
6th	Exact	42,2425	64,1889	90,6114	141,7834	182,8110	39,2387	42,6847	70,7401	87,6262	130,3576
	DTM	42,2425	64,1889	90,6114	141,7834	182,8110	39,6252	41,4367	72,2323	91,2562	118,7962
7th	Exact	42,9993	67,8993	103,1617	149,6055	235,0155	40,5035	54,2400	75,2834	103,9665	155,3211
	DTM	42,9993	67,8993	103,1617	149,6055	235,0155	39,9495	55,0678	74,8941	99,6863	156,4589
8th	Exact	49,5740	89,3571	111,8964	162,2413	260,6371	43,6698	66,2301	87,9867	105,1608	156,1248
	DTM	49,5740	89,3571	111,8964	162,2413	260,6371	43,5495	66,4417	89,8370	106,2987	164,6628
9th	Exact	58,0019	94,5150	131,4287	181,1868	305,2218	44,9416	73,1982	96,0405	152,7784	199,8452
	DTM	58,0019	94,5150	131,4287	181,1868	305,2218	45,2838	72,4930	93,2327	152,4177	188,4029

4.2 Differential Quadrature Method

The origins of the Differential Quadrature Method (DQM) can be traced back to the study of Bellman and his colleagues in 1972 [235]. In their study about rapid solution of nonlinear partial differential equations, they have proposed a novel numerical method by converting them into a set of algebraic equation. In the following years, many researchers [236-241] contributed to the development of this method, establishing its applicability in distinct engineering fields.The Differential Quadrature Method (DQM) is based on approximating the derivatives of a differential function at specific grid locations. The derivatives are calculated by assigning weighting coefficients to each term and then summing these coefficients to create a linear combination of the function values over the discretized domain. Primary advantages like ease of implementation of linear/nonlinear boundary conditions, less expensive computation methodology, low memory requests, simple algorithm scheme, solvability of complex geometries makes the DQM it an attractive numerical tool for various engineering and scientific applications such as vibration analysis [242-245], stability analysis, heat transfer problems [246], fluid dynamics simulations, structural mechanics, and electromagnetic field analysis.

The mathematical representation of the approximate derivative of any function can be expressed using the weighting coefficients as a linear combination of functional values at discrete grid points within the solution domain as follows:

$$\left.\frac{\partial^n f(x,y)}{\partial x^n}\right|_{\substack{x=x_i,\\ y=y_j}} = \sum_{k=1}^{N_x} A_{ik}^{(n)}\, f(x_k, y_j), \qquad i = 1,2,3...,N_x$$

$$\left.\frac{\partial^m f(x,y)}{\partial y^m}\right|_{\substack{x=x_i,\\ y=y_j}} = \sum_{l=1}^{N_y} B_{jl}^{(m)}\, f(x_i, y_l), \qquad j = 1,2,3...,N_y \tag{4.42}$$

$$\left.\frac{\partial^{n+m} f(x,y)}{\partial x^n \partial y^m}\right|_{\substack{x=x_i,\\ y=y_j}} = \sum_{k=1}^{N_x} A_{ik}^{(n)} \sum_{l=1}^{N_y} B_{jl}^{(m)}\, f(x_k, y_l), \quad i = 1,2,3...,N_x, \;\; j = 1,2,3...,N_y$$

where the grid points are distributed as

$$x_i = \frac{1}{2}\left(1-\cos\left(\frac{i-1}{N_x-1}\pi\right)\right)a, \; y_j = \frac{1}{2}\left(1-\cos\left(\frac{j-1}{N_y-1}\pi\right)\right)b, \; \begin{matrix} i = 1,2,\ldots,N_x \\ j = 1,2,\ldots,N_y \end{matrix} \tag{4.43}$$

To compute the weighting coefficients of first-order derivatives, Shu's approach [247] is employed, which can be given for a two-dimensional solution domain as follows:

$$A_{ik}^{(1)} = \begin{cases} \dfrac{\prod_{h=1,h\neq i}^{N_x}(x_i - x_h)}{(x_i - x_k)\prod_{h=1,h\neq k}^{N_x}(x_k - x_h)}, & i \neq k \\ -\sum_{k=1,k\neq i}^{N_x} A_{ik}^{(n)}, & i = k \end{cases} \qquad B_{jl}^{(1)} = \begin{cases} \dfrac{\prod_{h=1,h\neq j}^{N_y}(y_j - y_h)}{(y_j - y_l)\prod_{h=1,h\neq l}^{N_y}(y_l - y_h)}, & j \neq l \\ -\sum_{l=1,l\neq i}^{N_y} B_{jl}^{(n)}, & j = l \end{cases} \tag{4.44}$$

As seen from the Equation (4.44), these terms are elements of matrices. By substituting these matrix elements into the Equation (4.42), the derivative terms of the differential equations transform into a set of algebraic relations.

The matrix multiplication can be applied to compute the weighting coefficients of higher-order and coupled derivatives in the differential equations as follows:

$$\begin{aligned} A^{(n)} &= A^{(p)}A^{(q)}, & n &= p+q, \quad p,q \in Z^+ \\ B^{(m)} &= B^{(r)}B^{(t)}, & m &= r+t, \quad r,t \in Z^+ \\ C^{(n+m)} &= A^{(n)}B^{(m)}, & & \quad n,m \in Z^+ \end{aligned} \tag{4.45}$$

where the matrices are

$$A^{(n)} = \begin{bmatrix} A_{11}^{(n)} & A_{12}^{(n)} & \cdots & A_{1N_x}^{(n)} \\ A_{21}^{(n)} & A_{22}^{(n)} & \cdots & A_{2N_x}^{n} \\ & & \cdot & \\ & & \cdot & \\ & & \cdot & \\ A_{N_x1}^{(n)} & A_{N_x1}^{(n)} & \cdots & A_{N_xN_x}^{(n)} \end{bmatrix}, \quad B^{(m)} = \begin{bmatrix} B_{11}^{(m)} & B_{12}^{(m)} & \cdots & B_{1N_y}^{(m)} \\ B_{21}^{(m)} & B_{22}^{(m)} & \cdots & B_{2N_y}^{(m)} \\ & & \cdot & \\ & & \cdot & \\ & & \cdot & \\ B_{N_y1}^{(m)} & B_{N_y2}^{(m)} & \cdots & B_{N_yN_y}^{(m)} \end{bmatrix}$$

The reliability of the solution when using the differential quadrature method (DQM) to solve differential equations is greatly influenced by the choice of grid distribution. Regarding this matter, the Chebyshev-Gauss-Lobatto (CGL) grid distribution in Equation (4.43) offers the benefit of having denser grid points near the boundaries so that more accurate solutions can be obtained [246]. Therefore, it is crucial to carefully consider the desired grid distribution in order to achieve dependable and effective solutions when utilizing the differential quadrature method.

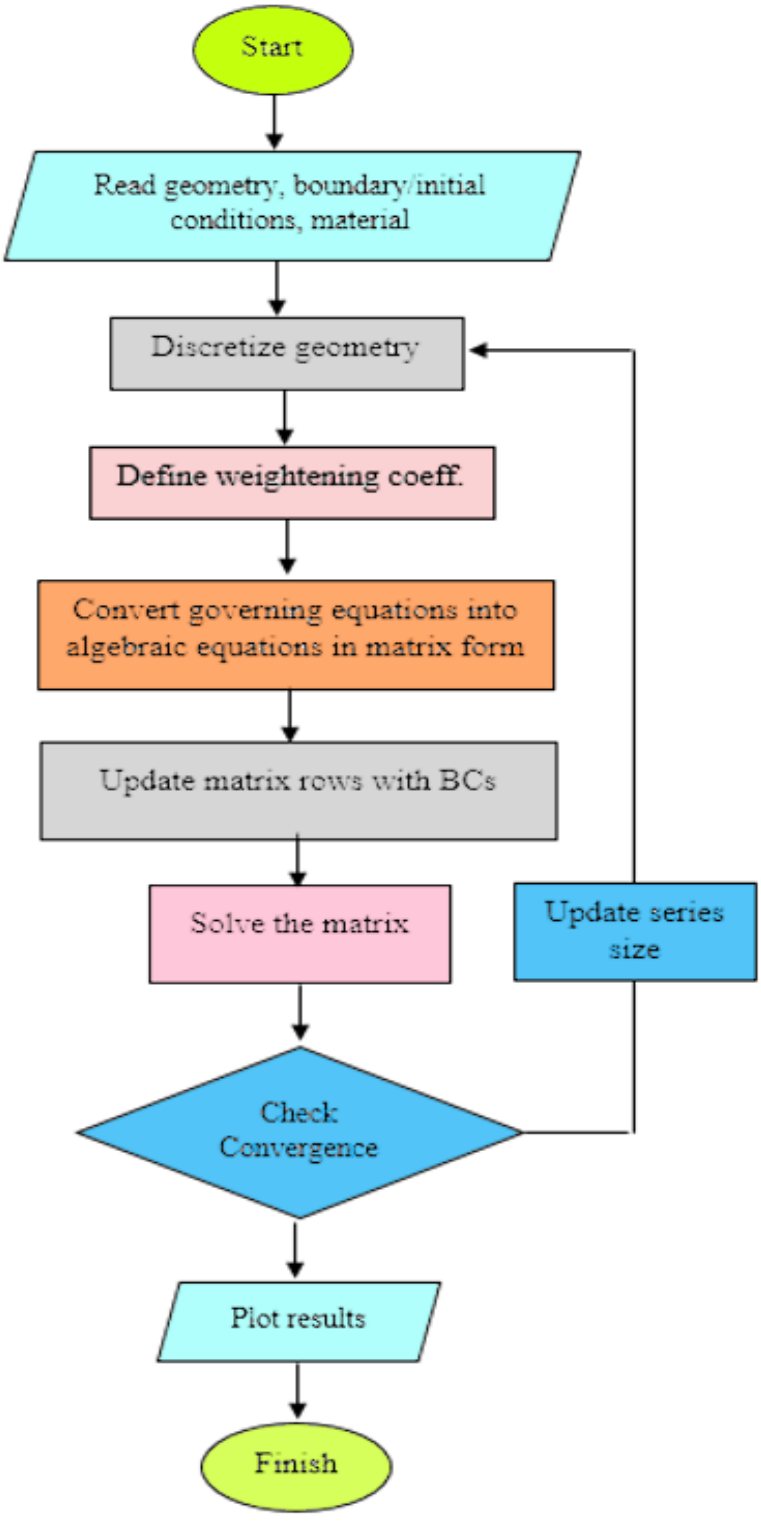

Figure 4.9 : Algorithm flowchart of the Differential Quadrature Method.

4.2.1 Application of differential quadrature method to beam element

As discussed, the Differential Quadrature Method (DQM) is one of the numerical solution techniques based on discretization of differential equations. Its ability in solving partial differential equations makes it well-suited for the numerical solution of various engineering problems. In this context, the DQM discretizes the equation of motion (EOM) using either uniform or non-uniform (CGL) grid distribution when applied to the free vibration analysis of the Euler-Bernoulli beam. Then, the equation of motion supplied in Equation (4.4) transforms into a combination of approximated functional values at grid points given in Equation (4.46) as:

$$w^{(4)}(x_i) - \Omega^2 w(x_i) = 0 \tag{4.46}$$

Employing the differential quadrature method, the discretized EOM can be represented as follow:

$$\sum_{j=1}^{N} c_{ij}^{(4)} . w(x_j) - \Omega^2 w(x_i) = 0 \tag{4.47}$$

By computing the approximated functional values at the grid points, the DQM enables the determination of the beam's natural frequencies and mode shapes, which are essential in understanding its dynamic behavior during free vibration. In matrix form, the discretized form of the Equation (4.47) can be rewritten as follows:

$$\left[c_{ij}^{(4)} - \Omega^2 I \right]_{N\times N} \left[w(x_j) \right]_{N\times 1} = 0, \qquad i, j = 1, 2, \ldots, N \tag{4.48}$$

where $c_{ij}^{(k)}$ terms are the weighting coefficients of k^{th} derivative of transverse displacement function, and defined as:

$$C = \begin{bmatrix} c_{1,1}^k & c_{1,2}^k & \cdots & c_{1,N-1}^k & c_{1,N}^k \\ c_{2,1}^k & c_{2,2}^k & \cdots & c_{2,N-1}^k & c_{2,N}^k \\ \vdots & \vdots & \cdots & \vdots & \vdots \\ \vdots & \vdots & \cdots & \vdots & \vdots \\ \vdots & \vdots & \cdots & \vdots & \vdots \\ c_{N-1,1}^k & c_{N-1,2}^k & \cdots & c_{N-1,N-1}^k & c_{N-1,N}^k \\ c_{N,1}^k & c_{N,2}^k & \cdots & c_{N,N-1}^k & c_{N,N}^k \end{bmatrix}$$

For the one-dimensional case, the grid distribution is demonstrated in Figure 4.10. As discussed in the previous section, the distribution of grids significantly affects the convergence of the numerical solution to the exact analytical solution and the overall accuracy. In other words, it is required to have more frequent mesh points around the geometric boundary regions at $x = 0$ and $x = 1$.

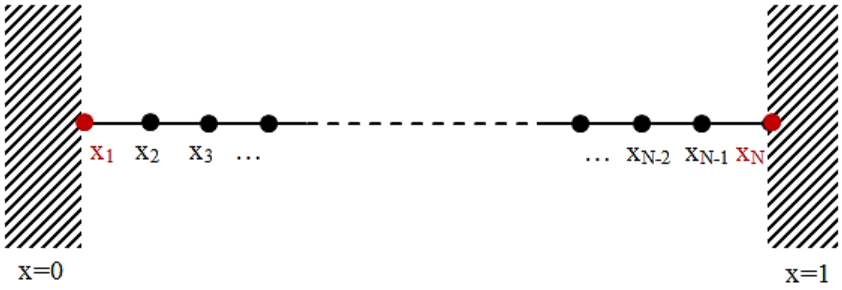

Figure 4.10 : Discretization process of the Euler-Bernoulli beam.

Meanwhile, the discretized boundary conditions of the beam are presented in Table 4.8. To implement these boundary conditions on the discretized EOM in Equation (4.48), the direct substitution of the boundary conditions into Equation (4.48) is performed.

Implementation of boundary conditions (BCs) is realized by updating the concerning rows or columns of the matrix represented in Equation (4.48). In Equations (4.49) and (4.50), the implementation steps are expressed for a beam with clamped-clamped and clamped-simply supported boundary conditions.

Table 4.8 : Discretized boundary conditions for Euler-Bernoulli beam.

Boundary Conditions	$x = 0$	$x = 1$
Clamped	$w_1 = 0, \quad \frac{dw_1}{dx} = \sum_{j=1}^{N} c_{1j}^{(1)}.w(x_j) = 0$	$w_N = 0, \quad \frac{dw_N}{dx} = \sum_{j=1}^{N} c_{Nj}^{(1)}.w(x_j) = 0$
Simply-supported	$w_1 = 0, \quad \frac{d^2w_1}{dx^2} = \sum_{j=1}^{N} c_{1j}^{(2)}.w(x_j) = 0$	$w_N = 0, \quad \frac{d^2w_N}{dx^2} = \sum_{j=1}^{N} c_{Nj}^{(2)}.w(x_j) = 0$
Free	$\frac{d^2w_1}{dx^2} = \sum_{j=1}^{N} c_{1j}^{(2)}.w(x_j) = 0,$ $\frac{d^3w_1}{dx^3} = \sum_{j=1}^{N} c_{1j}^{(3)}.w(x_j) = 0$	$\frac{d^2w_N}{dx^2} = \sum_{j=1}^{N} c_{Nj}^{(2)}.w(x_j) = 0,$ $\frac{d^3w_N}{dx^2} = \sum_{j=1}^{N} c_{Nj}^{(3)}.w(x_j) = 0$

1.Beam with Clamped- Clamped Boundary Conditions:

To substitute the clamped-clamped BCs into the weighting coefficients matrix of the beam in Equation (4.48), the rows of the matrix are updated by matching the related rows defined in the matrix of the boundary. For instance, the two geometric BCs at the edge *x=0* are firstly implemented into the first two rows of the main matrix, and then, the other two geometric BCs at the edge *x=1* are implemented into the last two rows of the matrix. The order of selecting rows in the coefficients matrix during the substitution of BCs can be arbitrary which provides flexibility in the implementation process.

$$\begin{bmatrix} 1 & 0 & 0 & \dots & 0 & 0 & 0 \\ c_{11}^{(1)} & c_{12}^{(1)} & c_{13}^{(1)} & \dots & c_{1(N-2)}^{(1)} & c_{1(N-1)}^{(1)} & c_{1N}^{(1)} \\ c_{31}^{(4)} & c_{32}^{(4)} & c_{33}^{(4)}-\Omega^2 & \dots & c_{3(N-2)}^{(4)} & c_{3(N-1)}^{(4)} & c_{3N}^{(4)} \\ \vdots & \vdots & \vdots & \ddots & \vdots & \vdots & \vdots \\ c_{(N-2)1}^{(4)} & c_{(N-2)2}^{(4)} & c_{(N-2)3}^{(4)} & \dots & c_{(N-2)(N-2)}^{(4)}-\Omega^2 & c_{(N-2)(N-1)}^{(4)} & c_{(N-2)N}^{(4)} \\ c_{N1}^{(1)} & c_{N2}^{(1)} & c_{N3}^{(1)} & \dots & c_{N(N-2)}^{(1)} & c_{N(N-1)}^{(1)} & c_{NN}^{(1)} \\ 0 & 0 & 0 & \dots & 0 & 0 & 1 \end{bmatrix} \begin{Bmatrix} w_1 \\ w_2 \\ w_3 \\ \vdots \\ w_{N-2} \\ w_{N-1} \\ w_N \end{Bmatrix} \quad (4.49)$$

The natural frequencies (eigenvalues of the matrix) of the beam are obtained by setting the determinant of the coefficient matrix in Equation (4.49) equal to zero. From the found natural frequencies, the corresponding mode shapes (Eigen functions) of the beam can be obtained.

2.Beam with Clamped- Simply Supported Boundary Conditions:

For the clamped-simply supported (C-S) boundary conditions, the weighting coefficients matrix of the C-S beam can be given as follows:

$$\begin{bmatrix} 1 & 0 & 0 & \dots & 0 & 0 & 0 \\ c_{11}^{(1)} & c_{12}^{(1)} & c_{13}^{(1)} & \dots & c_{1(N-2)}^{(1)} & c_{1(N-1)}^{(1)} & c_{1N}^{(1)} \\ c_{31}^{(4)} & c_{32}^{(4)} & c_{33}^{(4)}-\Omega^2 & \dots & c_{3(N-2)}^{(4)} & c_{3(N-1)}^{(4)} & c_{3N}^{(4)} \\ \vdots & \vdots & \vdots & \ddots & \vdots & \vdots & \vdots \\ c_{(N-2)1}^{(4)} & c_{(N-2)2}^{(4)} & c_{(N-2)3}^{(4)} & \dots & c_{(N-2)(N-2)}^{(4)}-\Omega^2 & c_{(N-2)(N-1)}^{(4)} & c_{(N-2)N}^{(4)} \\ c_{N1}^{(2)} & c_{N2}^{(2)} & c_{N3}^{(2)} & \dots & c_{N(N-2)}^{(2)} & c_{N(N-1)}^{(2)} & c_{NN}^{(2)} \\ 0 & 0 & 0 & \dots & 0 & 0 & 1 \end{bmatrix} \quad (4.50)$$

Following similar steps, the natural frequencies and mode shapes of the beam can be found for other types of natural and geometric BCs defined at the edges. The mode

shapes provide valuable insights into the dynamic behavior and deformation patterns of the beam.

The numerical results for the first ten dimensionless natural frequencies of various BCs are presented in Table 4.8, and they are compared to the exact analytic results from the study of Blevins (1991). The findings indicate that higher grid numbers result in improved accuracy for chosen optimal series size. To determine the series size and ensure the convergence to the exact analytic results, the convergence characteristics of the 9^{th} mode of the beam are specifically examined for different boundary conditions. For the stability and reliability of the solution, the series size N and M can be chosen from the Figure 4.11 between 27 and 30 nodes.

In the example of free vibration analysis for Euler-Bernoulli beam, the numerical results show that DQM is a robust and efficient numerical approach for one dimensional problems in structural dynamics.

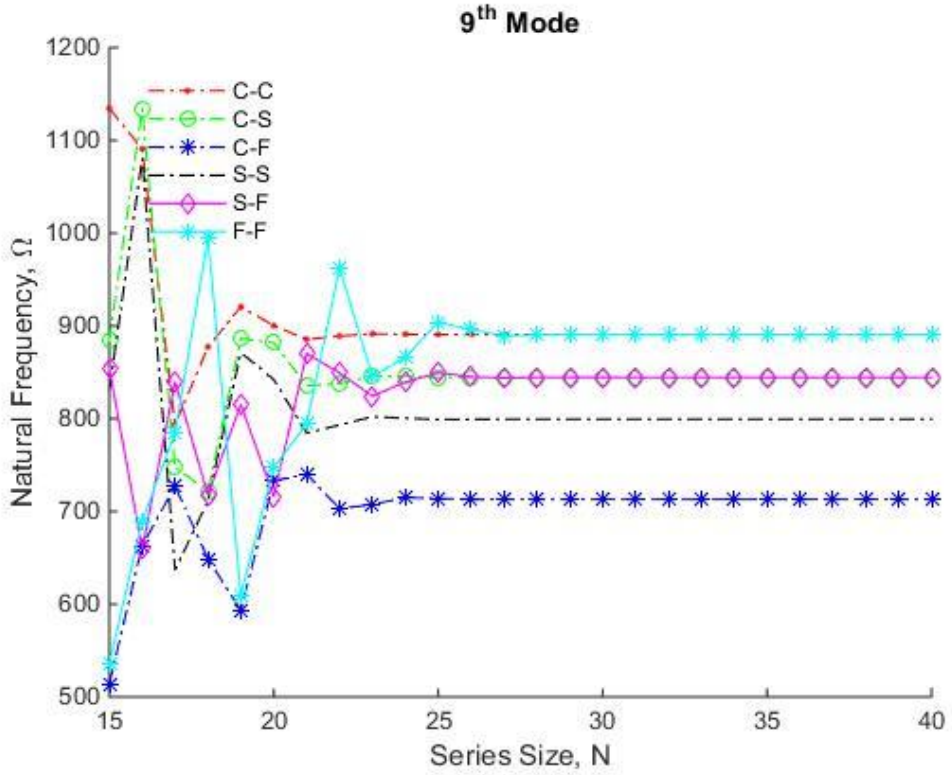

Figure 4.11 : Convergence analysis of the natural frequencies for CGL grid distribution.

Table 4.9 : The first ten dimensionless frequencies of Euler-Bernoulli beam.

Boundary Conditions		C-C	C-S	C-F	S-S	S-F	F-F
Mode							
1st	DQM a	22,3733	15,4180	3,5158	9,8696	15,4182	22,3733
	DQM b	22,3733	15,4182	3,5160	9,8696	15,4182	22,3733
	Exact	22,3733	15,4182	3,5160	9,8696	15,4182	22,3733
2nd	DQM a	61,6728	49,9649	22,0345	39,4784	49,9649	61,6776
	DQM b	61,6728	49,9649	22,0345	39,4784	49,9649	61,6728
	Exact	61,6728	49,9648	22,0345	39,4784	49,9649	61,6728
3rd	DQM a	120,9034	104,2477	61,6972	88,8264	104,2476	120,9028
	DQM b	120,9034	104,2477	61,6972	88,8264	104,2477	120,9034
	Exact	120,9034	104,2477	61,6972	88,8264	104,2477	120,9034
4th	DQM a	199,8607	178,2699	120,9016	157,9141	178,2605	199,8309
	DQM b	199,8594	178,2697	120,9019	157,9137	178,2697	199,8592
	Exact	199,8594	178,2697	120,9019	157,9137	178,2697	199,8594
5th	DQM a	298,3357	271,8292	199,8459	246,6215	272,3689	302,1213
	DQM b	298,5555	272,0307	199,8594	246,7399	272,0339	298,5756
	Exact	298,5555	272,0310	199,8595	246,7401	272,0310	298,5555
6th	DQM a	413,7238	383,7956	300,0946	353,2592	411,3388	427,4586
	DQM b	416,9894	385,5299	298,5655	355,3022	385,6189	417,2233
	Exact	416,9908	385,5314	298,5555	355,3058	385,5314	416,9908
7th	DQM a	557,6415	516,2124	429,3601	491,1128	411,3388	440,5495
	DQM b	555,1977	518,8931	417,1064	483,7155	518,1270	551,3529
	Exact	555,1652	518,7711	416,9908	483,6106	518,7711	555,1652
8th	DQM a	557,6415	516,2124	429,3601	491,1128	529,8806	440,5495
	DQM b	713,3467	672,2265	553,1932	632,5268	663,0258	692,6267
	Exact	713,0789	671,7499	555,1652	631,6547	671,7499	713,0789
9th	DQM a	628,9425	603,9060	591,1642	560,2755	529,8806	593,5509
	DQM b	889,0825	837,7557	702,9631	793,1577	849,2064	962,1214
	Exact	890,7318	844,4680	713,0789	799,4380	844,4680	890,7318
10th	DQM a	628,9425	603,9060	591,1642	560,2755	626,7816	593,5509
	DQM b	1077,2822	1018,5084	933,4812	955,8531	1039,1441	962,1214
	Exact	1088,1239	1036,9253	890,7318	986,9604	1036,9253	1088,1239

4.2.2 Application of differential quadrature method to plate element

To illustrate the application of DQM in the two-dimensional case, the free vibration analysis of a thin rectangular plate under Kirchhoff's assumptions is considered. Unlike the one-dimensional case, approximate derivative terms are expressed by u sing two different weighted coefficients. Along the x and y directions, approximate derivatives can be written as:

$$\left.\frac{\partial^r w}{\partial x^r}\right|_{x=x_i} = \sum_{k=1}^{N} A_{ik}^{(r)} w_{kj}, \quad \left.\frac{\partial^s w}{\partial y^s}\right|_{y=y_j} = \sum_{l=1}^{N} B_{jl}^{(s)} w_{il} \tag{4.51}$$

Using the differential quadrature method, the discretized equation of motion (EOM) in Equation (4.21) can be written as:

$$\sum_{k=1}^{N} A_{ik}^{(4)} W_{kj} + 2\beta^2 \sum_{l=1}^{M} B_{jl}^{(2)} \sum_{k=1}^{N} A_{ik}^{(2)} W_{kl} + \beta^4 \sum_{l=1}^{M} B_{jl}^{(4)} W_{il} = \Omega^2 W_{ij} \tag{4.52}$$

For two dimensional solution domain, the grid distribution can be depicted like in Figure 4.12. Similar to the one-dimensional case, the distribution of grid points has a significant impact on the accuracy of the solution. To ensure accuracy of the results, the Chebyshev-Gauss-Lobatto (CGL) grid distribution is preferred to a uniform grid distribution.

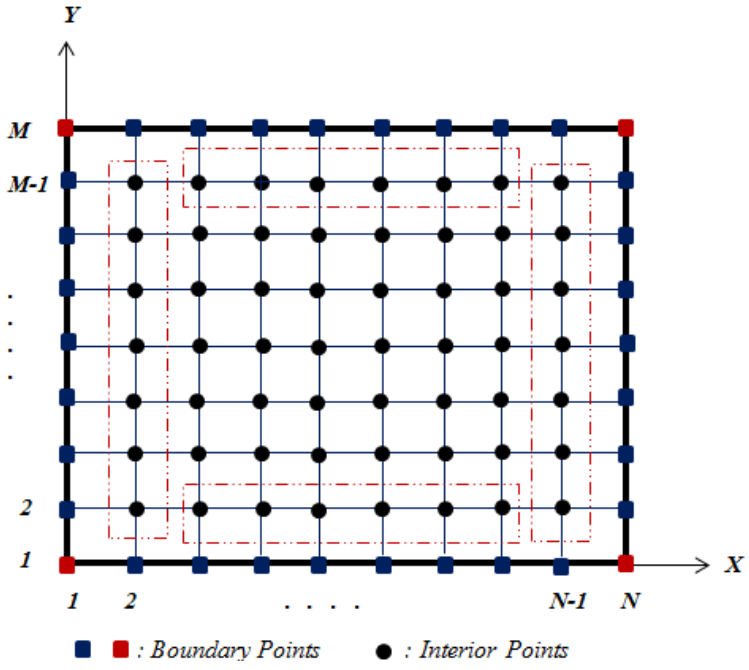

Figure 4.12 : Discretization of a rectangular plate using CGL grid distribution.

Table 4.10 : Boundary conditions at the edges of rectangular plate.

BCs	*Clamped*	*Simply-Supported*	*Free*
X=0	$W(0,Y)=0,$ $\frac{\partial W(0,Y)}{\partial X}=0$	$W(0,Y)=0,$ $\frac{\partial^2 W(0,Y)}{\partial X^2}=0$	$\frac{\partial^2 W(0,Y)}{\partial X^2}+\nu\lambda^2\frac{\partial^2 W(0,Y)}{\partial Y^2}=0,$ $\frac{\partial^3 W(0,Y)}{\partial X^3}+(2-\nu)\lambda^2\frac{\partial^3 W(0,Y)}{\partial X\partial Y^2}=0$
X=1	$W(1,Y)=0,$ $\frac{\partial W(1,Y)}{\partial X}=0$	$W(1,Y)=0,$ $\frac{\partial^2 W(1,Y)}{\partial X^2}=0$	$\frac{\partial^2 W(1,Y)}{\partial X^2}+\nu\lambda^2\frac{\partial^2 W(1,Y)}{\partial Y^2}=0,$ $\frac{\partial^3 W(1,Y)}{\partial X^3}+(2-\nu)\lambda^2\frac{\partial^3 W(1,Y)}{\partial X\partial Y^2}=0$
Y=0	$W(Y,0)=0,$ $\frac{\partial W(Y,0)}{\partial Y}=0$	$W(Y,0)=0,$ $\frac{\partial^2 W(Y,0)}{\partial Y^2}=0$	$\lambda^2\frac{\partial^2 W(Y,0)}{\partial Y^2}+\nu\frac{\partial^2 W(Y,0)}{\partial X^2}=0,$ $\lambda^2\frac{\partial^3 W(Y,0)}{\partial Y^3}+(2-\nu)\frac{\partial^3 W(Y,0)}{\partial X^2\partial Y}=0$
Y=1	$W(1,Y)=0,$ $\frac{\partial W(1,Y)}{\partial Y}=0$	$W(1,Y)=0,$ $\frac{\partial^2 W(1,Y)}{\partial Y^2}=0$	$\lambda^2\frac{\partial^2 W(Y,1)}{\partial Y^2}+\nu\frac{\partial^2 W(Y,1)}{\partial X^2}=0,$ $\lambda^2\frac{\partial^3 W(Y,1)}{\partial Y^3}+(2-\nu)\frac{\partial^3 W(Y,1)}{\partial X^2\partial Y}=0$

Table 4.11 : Transformed boundary conditions at the edges of rectangular plate.

BCs	*Clamped*	*Simply-Supported*	*Free*
X=0	$W_{1,j}=0,$ $\sum_{k=1}^{N}A_{1,k}^{(1)}W_{k,j}=0$	$W_{1,j}=0,$ $\sum_{k=1}^{N}A_{1,k}^{(2)}W_{k,j}=0$	$\sum_{k=1}^{N}A_{1k}^{(2)}W_{kj}+\nu\lambda^2\sum_{l=1}^{M}B_{jl}^{(2)}\sum_{k=1}^{N}A_{ik}^{(2)}W_{kl}=0,$ $\sum_{k=1}^{N}A_{1k}^{(3)}W_{kj}+(2-\nu)\lambda^2\sum_{l=1}^{M}B_{jl}^{(2)}\sum_{k=1}^{N}A_{1k}^{(1)}W_{kl}=0$
X=1	$W_{N,j}=0,$ $\sum_{k=1}^{N}A_{N,k}^{(1)}W_{k,j}=0$	$W_{N,j}=0,$ $\sum_{k=1}^{N}A_{N,k}^{(2)}W_{k,j}=0$	$\sum_{k=1}^{N}A_{N,k}^{(2)}W_{k,j}+\nu\lambda^2\sum_{k=1}^{N}A_{ik}^{(2)}W_{k1}=0,=0,$ $\sum_{k=1}^{N}A_{N,k}^{(3)}W_{k,j}+(2-\nu)\lambda^2\sum_{l=1}^{M}B_{jl}^{(2)}\sum_{k=1}^{N}A_{Nk}^{(1)}W_{kl}=0$
Y=0	$W_{i,1}=0,$ $\sum_{k=1}^{N}B_{1,k}^{(1)}W_{i,k}=0$	$W_{i,1}=0,$ $\sum_{k=1}^{N}B_{1,k}^{(2)}W_{i,k}=0$	$\lambda^2\sum_{k=1}^{N}B_{1k}^{(2)}W_{ik}+\nu\sum_{k=1}^{N}A_{ik}^{(2)}W_{k1}=0,$ $\lambda^2\sum_{k=1}^{N}B_{1k}^{(3)}W_{ik}+(2-\nu)\sum_{l=1}^{M}B_{jl}^{(1)}\sum_{k=1}^{N}A_{1k}^{(2)}W_{kl}=0$
Y=1	$W_{i,M}=0,$ $\sum_{k=1}^{N}B_{M,k}^{(1)}W_{i,k}=0$	$W_{i,M}=0,$ $\sum_{k=1}^{N}B_{M,k}^{(2)}W_{i,k}=0$	$\lambda^2\sum_{k=1}^{N}B_{M,k}^{(2)}W_{i,k}+\nu\sum_{k=1}^{N}A_{ik}^{(2)}W_{k1}=0,,$ $\lambda^2\sum_{k=1}^{N}B_{M,k}^{(3)}W_{i,k}+(2-\nu)\sum_{l=1}^{M}B_{jl}^{(1)}\sum_{k=1}^{N}A_{ik}^{(2)}W_{kl}=0$

Table 4.12 : The first nine dimensionless frequencies of Kirchoff-Love plate via DQM.

Boundary Conditions		S-S-S-S					S-S-S-F				
Aspect Ratio		a/b					a/b				
		2/5	2/3	1.0	3/2	5/2	2/5	2/3	1.0	3/2	5/2
Mode											
1st	Exact	11,4487	14,2561	19,7392	32,0762	71,5564	10,1259	10,6712	11,6845	13,7111	18,8009
	DQM	11,4487	14,2561	19,7392	32,0762	71,5546	10,0889	10,6083	11,5816	13,5359	18,4640
2nd	Exact	16,1862	27,4156	49,3480	61,6850	101,1634	13,0570	18,2995	27,7563	43,5723	50,5405
	DQM	16,1862	27,4156	49,3480	61,6850	101,1634	13,0087	18,1977	27,5917	43,2840	49,9897
3rd	Exact	24,0818	43,8649	49,3480	98,6960	150,5115	18,8390	33,6974	41,1967	47,8571	100,2321
	DQM	24,0818	43,8649	49,3480	98,6960	150,5115	18,7755	33,5854	41,0126	47,6284	99,4954
4th	Exact	35,1358	49,3480	78,9568	111,0330	219,5987	27,5580	40,1307	59,0655	81,4789	110,2259
	DQM	35,1358	49,3480	78,9568	111,0330	219,5987	27,4891	40,0055	58,7953	81,0037	109,9391
5th	Exact	41,0576	57,0244	98,6960	128,3049	256,6097	39,3377	48,4082	61,8606	92,6925	147,6317
	DQM	41,0576	57,0244	98,6960	128,3049	256,6097	39,2712	48,2611	61,7156	92,2784	146,8273
6th	Exact	45,7950	78,9568	98,6960	177,6529	286,2185	39,6118	57,5929	90,2941	124,5635	169,1026
	DQM	45,7950	78,9568	98,6960	177,6529	286,2185	39,5285	57,4931	90,0123	124,3978	168,1679
7th	Exact	49,3480	80,0535	128,3049	180,1203	308,4251	42,6964	64,7281	94,4837	132,8974	203,7304
	DQM	49,3485	80,0534	128,3049	180,1203	308,4283	42,6245	64,5319	94,1471	132,2895	202,5149
8th	Exact	53,6906	93,2129	128,3049	209,7291	335,5665	48,7745	89,1859	108,9185	158,9180	257,4791
	DQM	53,6906	93,2129	128,3049	209,7291	335,5665	48,6852	88,9607	108,5875	158,4272	256,3328
9th	Exact	66,7185	106,3724	167,7833	239,3379	416,9908	54,2497	89,2725	115,6857	161,4205	277,4280
	DQM	64,7446	106,3724	167,7832	239,3379	404,6538	54,1829	89,0697	115,5711	160,8636	275,9363

Table 4.12: The first nine dimensionless frequencies of Kirchoff-Love plate via DQM (Cont')

Boundary Conditions		S-C-S-S					S-C-S-C				
Aspect Ratio		a/b					a/b				
		2/5	2/3	1.0	3/2	5/2	2/5	2/3	1.0	3/2	5/2
Mode											
1st	Exact	11,7502	15,5783	23,6463	42,5278	103,9227	12,1347	17,3730	28,9509	56,3481	145,4839
	DQM	11,7502	15,5783	23,6463	42,5278	103,9227	12,1347	17,3730	28,9509	56,3481	145,4839
2nd	Exact	17,1872	31,0724	51,6743	69,0031	128,3382	18,3647	35,3445	54,7431	78,9836	164,7387
	DQM	17,1872	31,0724	51,6743	69,0031	128,3382	18,3647	35,3445	54,7431	78,9836	164,7387
3rd	Exact	25,9171	44,5644	58,6464	116,2671	172,3804	27,9657	45,4294	69,3270	123,1719	202,2271
	DQM	25,9171	44,5644	58,6464	116,2671	172,3804	27,9657	45,4294	69,3270	123,1719	202,2271
4th	Exact	37,8317	55,3926	86,1345	120,9956	237,2502	40,7500	62,0544	94,5853	146,2677	261,1053
	DQM	37,8317	55,3926	86,1345	120,9956	237,2502	40,7500	62,0544	94,5853	146,2677	261,1052
5th	Exact	41,2070	59,4627	100,2698	147,6353	320,7921	41,3782	62,3131	102,2162	170,1112	342,1442
	DQM	41,2070	59,4627	100,2698	147,6353	320,7921	41,3782	62,3131	102,2162	170,1112	342,1470
6th	Exact	46,3620	83,6060	113,2281	184,1006	322,9642	47,0009	88,8047	129,0955	189,1219	392,8746
	DQM	46,3620	83,6060	113,2281	184,1006	322,9672	47,0009	88,8047	129,0955	189,1219	392,8746
7th	Exact	52,9007	88,4384	133,7910	193,8025	346,7382	56,1782	94,2131	140,2045	212,8169	415,6906
	DQM	52,9014	88,4384	133,7910	193,8025	346,7382	56,1782	94,2131	140,2045	212,8169	415,6906
8th	Exact	54,8720	93,6758	140,8456	243,4964	391,0659	56,6756	97,4254	154,7757	276,0012	444,9682
	DQM	54,8720	93,6758	140,8456	243,4964	391,0659	56,6758	97,4254	154,7757	276,0047	445,0107
9th	Exact	66,6637	108,1069	168,9585	260,2020	429,2420	68,7486	101,0788	170,3465	276,0125	455,3054
	DQM	66,6637	108,1069	168,9585	260,2020	429,2860	68,7486	110,0788	170,3464	276,0125	455,3054

Table 4.12: The first nine dimensionless frequencies of Kirchoff-Love plate via DQM (Cont')

Boundary Conditions		S-C-S-F					S-F-S-F				
Aspect Ratio		a/b					a/b				
		2/5	2/3	1.0	3/2	5/2	2/5	2/3	1.0	3/2	5/2
Mode											
1st	Exact	10,1888	10,9752	12,6874	16,8225	30,6277	9,7600	9,6983	9,6314	9,5582	9,4841
	DQM	10,1485	10,9011	12,5569	16,6003	30,2740	9,7280	9,6507	9,5676	9,4777	9,3879
2nd	Exact	13,6036	20,3355	33,0651	45,3024	58,0804	11,0368	12,9813	16,1348	21,6192	33,6228
	DQM	13,5500	20,2229	32,8924	44,9543	57,3722	10,9589	12,8314	15,8799	21,2000	32,8788
3rd	Exact	20,0971	37,9552	41,7019	61,0178	105,5470	15,0626	22,9535	36,7256	38,7214	38,3629
	DQM	20,0296	37,8421	41,4952	60,7948	104,6398	14,9557	22,7458	36,4173	38,5132	38,0701
4th	Exact	29,6219	40,2717	63,0148	92,3073	149,4569	21,7064	39,1052	38,9450	54,8443	75,2037
	DQM	29,5515	40,1378	62,7128	91,7877	149,1969	21,5778	38,9939	38,7925	54,1434	73,8562
5th	Exact	39,6382	49,7317	72,3976	93,8293	173,1060	31,1771	40,3560	46,7381	65,7922	86,9684
	DQM	39,5521	49,5704	72,2579	93,3642	172,0157	31,0433	40,1448	46,3264	65,3906	86,4624
6th	Exact	42,2425	64,1889	90,6114	141,7834	182,8110	39,2387	42,6847	70,7401	87,6262	130,3576
	DQM	42,1763	64,0914	90,3100	141,1038	182,0009	39,1623	42,4333	70,1583	87,2832	128,5459
7th	Exact	42,9993	67,8993	103,1617	149,6055	235,0155	40,5035	54,2400	75,2834	103,9665	155,3211
	DQM	42,9233	67,6895	102,8104	149,4512	233,7042	40,3561	53,9117	75,0180	103,0219	154,5960
8th	Exact	49,5740	89,3571	111,8964	162,2413	260,6371	43,6698	66,2301	87,9867	105,1608	156,1248
	DQM	49,4798	89,1464	111,5334	161,6387	259,3490	43,5425	66,0428	87,7363	104,2345	155,6431
9th	Exact	58,0019	94,5150	131,4287	181,1868	305,2218	44,9416	73,1982	96,0405	152,7784	199,8452
	DQM	57,9243	94,2819	131,3195	180,6983	303,5642	44,7843	72,7908	95,4750	152,4784	198,3966

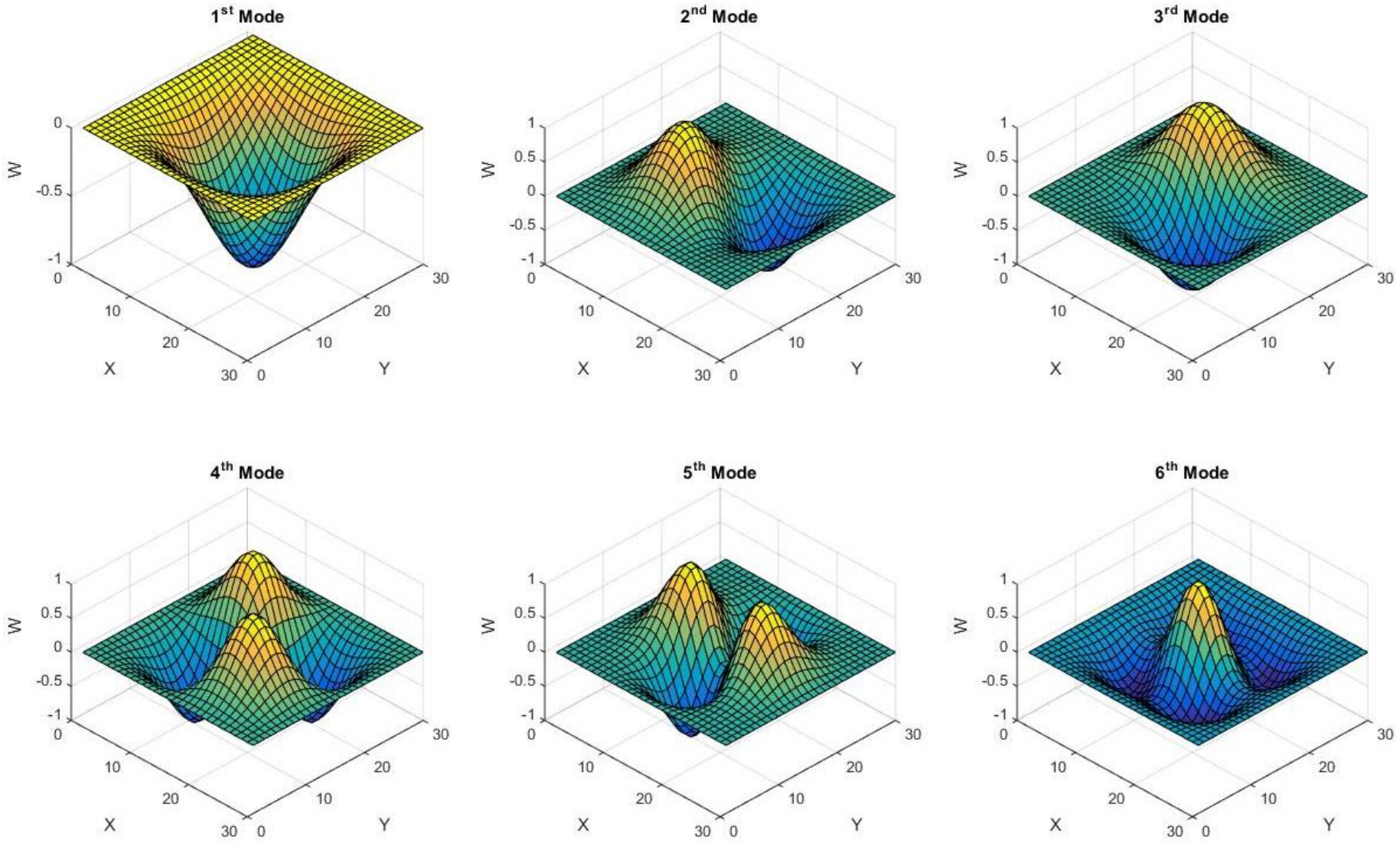

Figure 4.13 : Kirchhoff-Love plate mode shapes for SSSS BCs.

The numerical results for the first nine natural frequencies of the plate with various boundary types are presented in Table 4.11. The numerical results obtained via DQM are also compared to the exact analytic results from the study of Leissa (1971). In this comparison, it is observed that the boundary conditions defined at the edges of the plate have a significant effect on the natural frequencies and mode shapes. The influence of boundary conditions on the mode shapes can be seen in Figures 4.12 to 4.13. Other mode shapes are given in Appendix A.

Ease of implementing boundary conditions is one of the advantages of the Differential Quadrature Method (DQM) over other numerical methods. Employing DQM, the discretized equations are represented in matrix form, and the boundary conditions can be readily incorporated by updating the relevant rows or columns of the coefficient matrix. In contrast, other numerical methods may require complex treatments or additional steps to handle boundary conditions. For example, finite difference or finite element methods may necessitate the introduction of ghost points or special boundary conditions to enforce the constraints.

4.3 Finite Difference Method

In most cases, the analytical solution of partial differential equations (PDEs) are limited, and the solution process includes significant challenges. Traditional analytical methods used to solve PDEs such as separation of variables, Laplace transform, Fourier transform, perturbation methods and others can be applied to a limited range of engineering problems. Also, linearity of equation, a need for regular geometry, constant coefficients and other constraints limits solving PDEs, analytically [248]. In such a case, the utilization of numerical and semi-analytical solution methods is required to overcome these constraints and obtain approximate solutions.

The Finite Difference Method (FDM) offers a practical alternative solution to analytical and numerical solution techniques in computational mechanics, which is based on the calculus of finite differences [249-251]. Utilizing interconnected nodes within the computational domain, the PDEs or ODEs used to describe the governing equations of the system are transformed into a set of algebraic equations.

Straightforward implementation, applicability to linear and nonlinear problems, and compatibility with computer-based solutions are the prominent advantages of the FDM [248]. However, it does require some mathematical expertise, and handling complex geometries can be challenging.

The fundamentals of the Finite Difference Method (FDM) are based on the approximation of derivative terms expressing any physical phenomena. In one dimensional case, the first order derivative of a continuous function $y = f(x)$ with respect to x can be written in the terms of the finite difference expressions as:

$$f'(x_i)=\left(\frac{dy}{dx}\right)_i=\lim_{\Delta x\to 0}\frac{y_{i+1}-y_i}{\Delta x}\approx\frac{f(x_i+\Delta x)-f(x_i)}{\Delta x}=\frac{\Delta y_i}{h}\quad(\textit{forward difference})$$

or

$$f'(x_i)=\left(\frac{dy}{dx}\right)_i=\lim_{\Delta x\to 0}\frac{y_i-y_{i-1}}{\Delta x}\approx\frac{f(x_i)-f(x_i+\Delta x)}{\Delta x}=\frac{\nabla y_i}{h}\quad(\textit{backward difference}) \tag{4.53}$$

or

$$f'(x_i)=\left(\frac{dy}{dx}\right)_i=\lim_{\Delta x\to 0}\frac{y_{i+1}-y_{i-1}}{2\Delta x}\approx\frac{f(x_i+\Delta x)-f(x_i-\Delta x)}{2\Delta x}\quad(\textit{central difference})$$

where i denotes any arbitrary point on the curve depicted in Figure 4.14. Meanwhile, these approximate derivative derivatives are derived from the Taylor expansion as follows:

$$\begin{aligned}y_{i+1}&=y_i+\Delta x\frac{\partial y}{\partial x}+\frac{(\Delta x)^2}{2!}\frac{\partial^2 y}{\partial x^2}+\frac{(\Delta x)^3}{3!}\frac{\partial^3 y}{\partial x^3}+\frac{(\Delta x)^4}{4!}\frac{\partial^4 y}{\partial x^4}+\ldots\\ y_{i-1}&=y_i-\Delta x\frac{\partial y}{\partial x}+\frac{(\Delta x)^2}{2!}\frac{\partial^2 y}{\partial x^2}+\frac{(\Delta x)^3}{3!}\frac{\partial^3 y}{\partial x^3}-\frac{(\Delta x)^4}{4!}\frac{\partial^4 y}{\partial x^4}+\ldots\end{aligned} \tag{4.54}$$

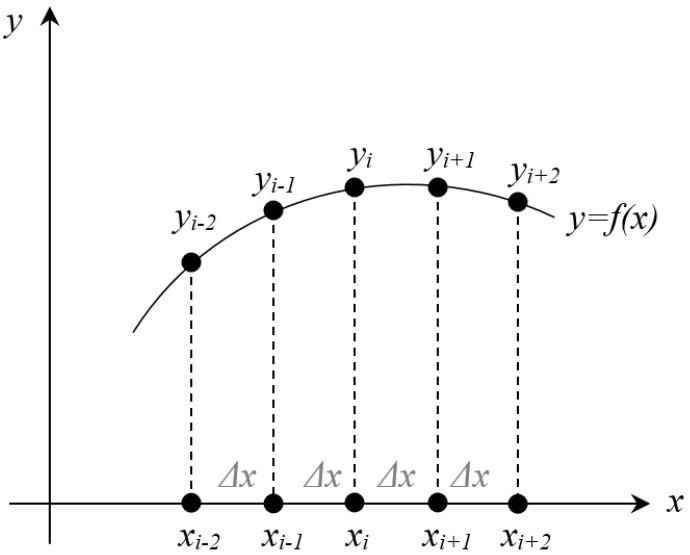

Figure 4.14 : Finite difference approximation.

Utilizing the expressions in Equation 4.53, the differential approximations for the second, third, fourth, and higher order derivatives for the function $f(x)$ can be derived.

Among these finite difference approaches, central differences give more accurate solution compared to forward and backward differences due to symmetrically positioned nodal points. The central difference approximations for the higher derivatives can be expressed as follows:

$$
\begin{aligned}
f_i'' &= \left(\frac{d^2y}{dx^2}\right)_i \approx \frac{y_{i+1} - 2y_i + y_{i-1}}{(\Delta x)^2} + O(\Delta x^2) \\
f_i''' &= \left(\frac{d^3y}{dx^3}\right)_i \approx \frac{y_{i+2} - 2y_{i+1} + 2y_{i-1} - y_{i-2}}{2(\Delta x)^3} + O(\Delta x^2) \\
f_i^{iv} &= \left(\frac{d^4y}{dx^4}\right)_i \approx \frac{y_{i+2} - 4y_{i+1} + 6y_i - 4y_{i-1} + y_{i-2}}{(\Delta x)^4} + O(\Delta x^2)
\end{aligned}
\tag{4.55}
$$

These expressions are utilized in solving one-dimensional governing equations represented by ODEs, such as the calculation of Euler beam's natural frequencies. Similarly, we can derive the expressions for the two-dimensional case of a function $w(x, y)$ with two variables as follows:

$$
\begin{aligned}
&\left(\frac{\partial w}{\partial x}\right)_{i,j} \approx \frac{w_{i+1,j} - w_{i-1,j}}{2.\Delta x} + O(\Delta x^2), \left(\frac{\partial w}{\partial y}\right)_{i,j} \approx \frac{w_{i,j+1} - w_{i,j-1}}{2.\Delta y} + O(\Delta y^2) \\
&\left(\frac{\partial^2 w}{\partial x \partial y}\right)_{i,j} \approx \frac{w_{i+1,j+1} - w_{i-1,j+1} - w_{i+1,j-1} + w_{i-1,j-1}}{4\Delta x \Delta y} + O\left((\Delta x + \Delta y)^2\right) \\
&\left(\frac{\partial^2 w}{\partial x^2}\right)_{i,j} \approx \frac{w_{i+1,j} - 2w_{i,j} + w_{i-1,j}}{(\Delta x)^2} + O(\Delta x^2), \left(\frac{\partial^2 w}{\partial y^2}\right)_{i,j} \approx \frac{w_{i,j+1} - 2w_{i,j} + w_{i,j-1}}{(\Delta y)^2} + O(\Delta y^2) \\
&\left(\frac{\partial^3 w}{\partial x^3}\right)_{i,j} \approx \frac{w_{i+2,j} - 2w_{i+1,j} + 2w_{i-1,j} - w_{i-2,j}}{2(\Delta x)^3} + O(\Delta x^2) \\
&\left(\frac{\partial^3 w}{\partial x^2 \partial y}\right)_{i,j} \approx \frac{w_{i+1,j+1} - 2w_{i,j+1} + w_{i-1,j+1} - w_{i+1,j-1} + 2w_{i,j-1} - w_{i-1,j-1}}{2(\Delta x)^2 \Delta y} + O\left((\Delta x + \Delta y)^2\right) \\
&\left(\frac{\partial^3 w}{\partial x \partial y^2}\right)_{i,j} \approx \frac{w_{i+1,j+1} - 2w_{i+1,j} + w_{i+1,j-1} - w_{i-1,j+1} + 2w_{i-1,j} - w_{i-1,j-1}}{2\Delta x(\Delta y)^2} + O\left((\Delta x + \Delta y)^2\right) \\
&\left(\frac{\partial^3 w}{\partial y^3}\right)_{i,j} \approx \frac{w_{i,j+2} - 2w_{i,j+1} + 2w_{i,j-1} - w_{i,j-2}}{2(\Delta y)^3} + O(\Delta y^2) \\
&\left(\frac{\partial^4 y}{\partial x^4}\right)_{i,j} \approx \frac{w_{i+2,j} - 4w_{i+1,j} + 6w_{i,j} - 4w_{i-1,j} + w_{i-2,j}}{(\Delta x)^4} + O(\Delta x^2) \\
&\left(\frac{\partial^4 w}{\partial y^4}\right)_{i,j} \approx \frac{w_{i,j+2} - 4w_{i,j+1} + 6w_{i,j} - 4w_{i,j-1} + w_{i,j-2}}{(\Delta y)^4} + O(\Delta y^2) \\
&\left(\frac{\partial^4 w}{\partial x^2 \partial y^2}\right)_{i,j} \approx \frac{w_{i+1,j+1} - 2w_{i,j+1} + w_{i-1,j+1} - 2w_{i+1,j} + 4w_{i,j} - 2w_{i-1,j} + w_{i+1,j-1} - 2w_{i,j-1} + w_{i-1,j-1}}{(\Delta x)^2 (\Delta y)^2} + O
\end{aligned}
\tag{4.56}
$$

These expressions are used to solve two-dimensional governing equations expressed by PDEs, specifically in calculating the natural frequencies of Kirchhoff plates. By approximating the various derivatives using finite differences, we can readily obtain the finite difference equivalent of derivative terms in the plate equation. Notably, certain finite difference operators are represented as coefficient patterns known as stencil points shown in Figure 4.15. It is important to emphasize that the center point of each stencil corresponds to the node around which the operator is defined.

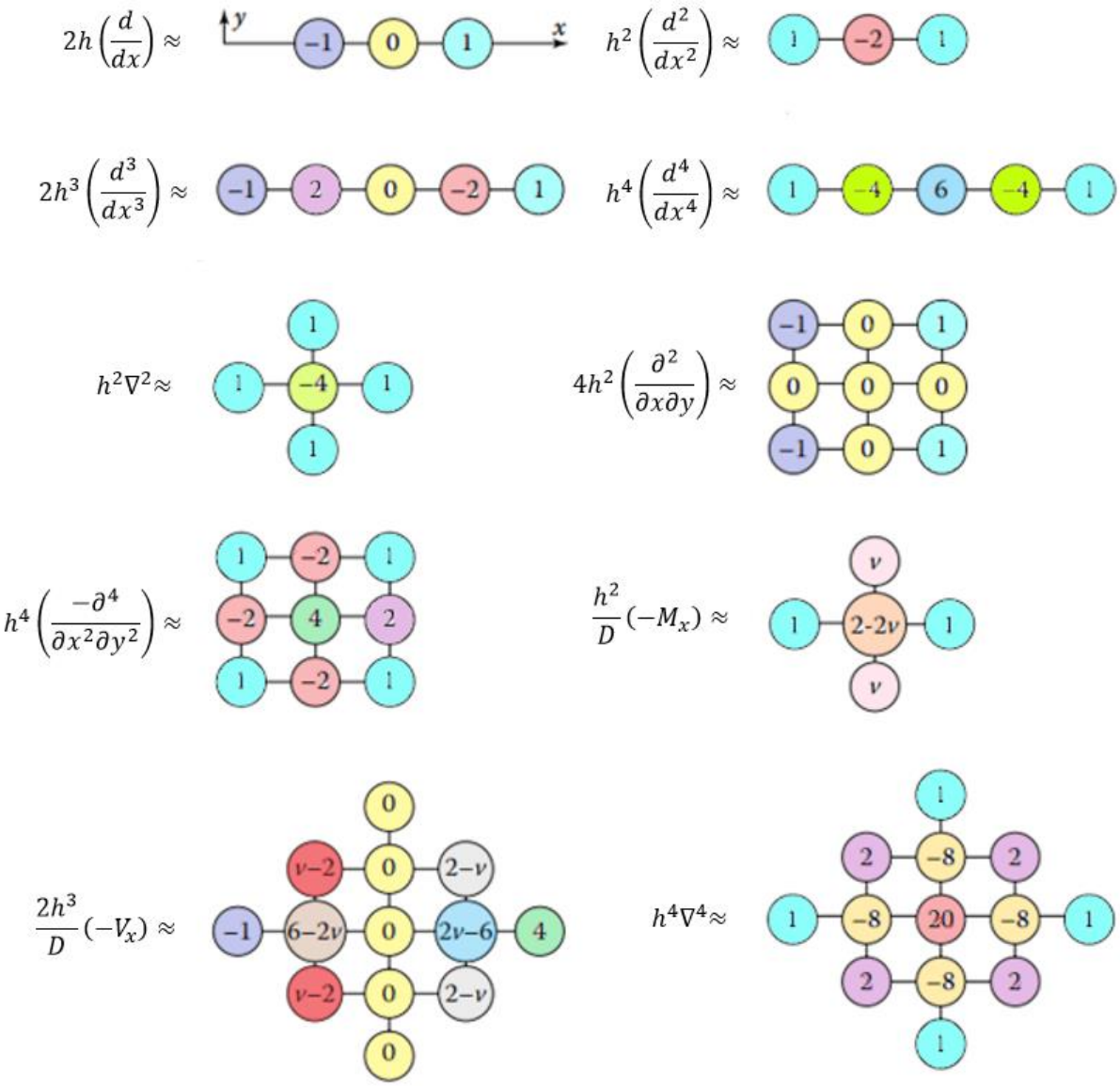

Figure 4.15 : Stencil points for some finite difference operators [252].

In order to demonstrate the application of the finite difference method (FDM) in structural problems, free vibration analysis of Euler-Bernoulli beam and a Kirchhoff-Love plate are considered similar to other discussed methods. If the steps in Figure 4.16 are followed, the governing equations of motion are discretized by applying finite difference approximations to

the derivatives, and then a system of algebraic equations for the dynamic behavior of the beam and plate is obtained. Solving this equation system allows us to determine the natural frequencies and mode shapes of the structures [253-256].

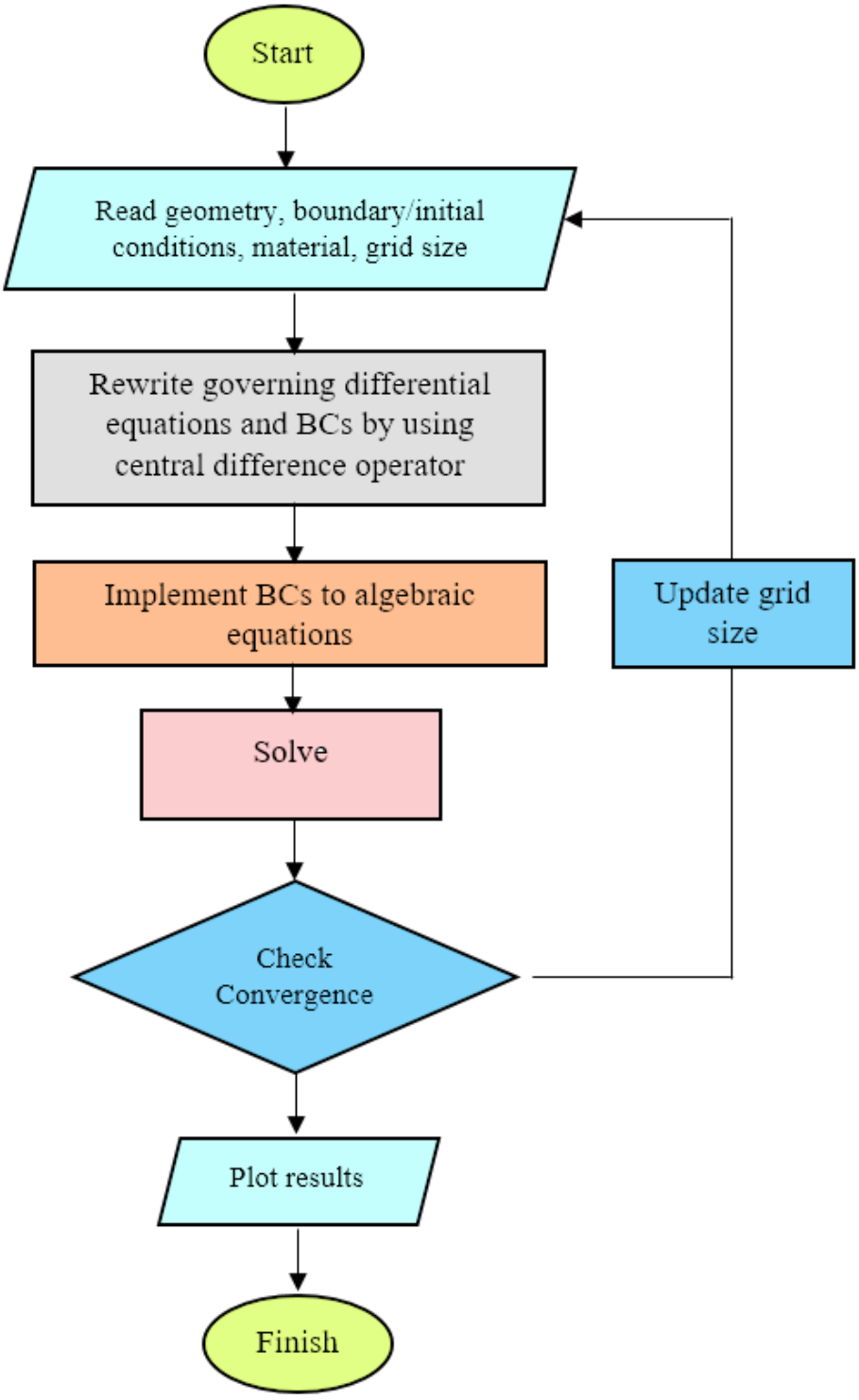

Figure 4.16 : FDM algorithm's flowchart.

4.3.1 Application of finite difference method to beam element

Like other numerical approaches mentioned before, the vibration of a Bernoulli-Euler beam may be used to illustrate the use of Finite Difference Method (FDM) in one-dimensional scenarios. The Bernoulli-Euler beam model is commonly employed in literature because to its simplicity and effective outcomes. Nevertheless, it is important to acknowledge that the Euler-Bernoulli model has a tendency to somewhat overstate the natural frequencies, especially for higher modes.

The vibration equation of the beam may be discretized by utilizing the finite difference approach as follows:

$$\frac{w_{i+2}-4w_{i+1}+6w_i-4w_{i-1}+w_{i-2}}{(\Delta x)^4}-\Omega^2 w_i=0 \tag{4.57}$$

where dimensionless frequency $\Omega=\sqrt{\rho AL^4\omega^2/EI}$.

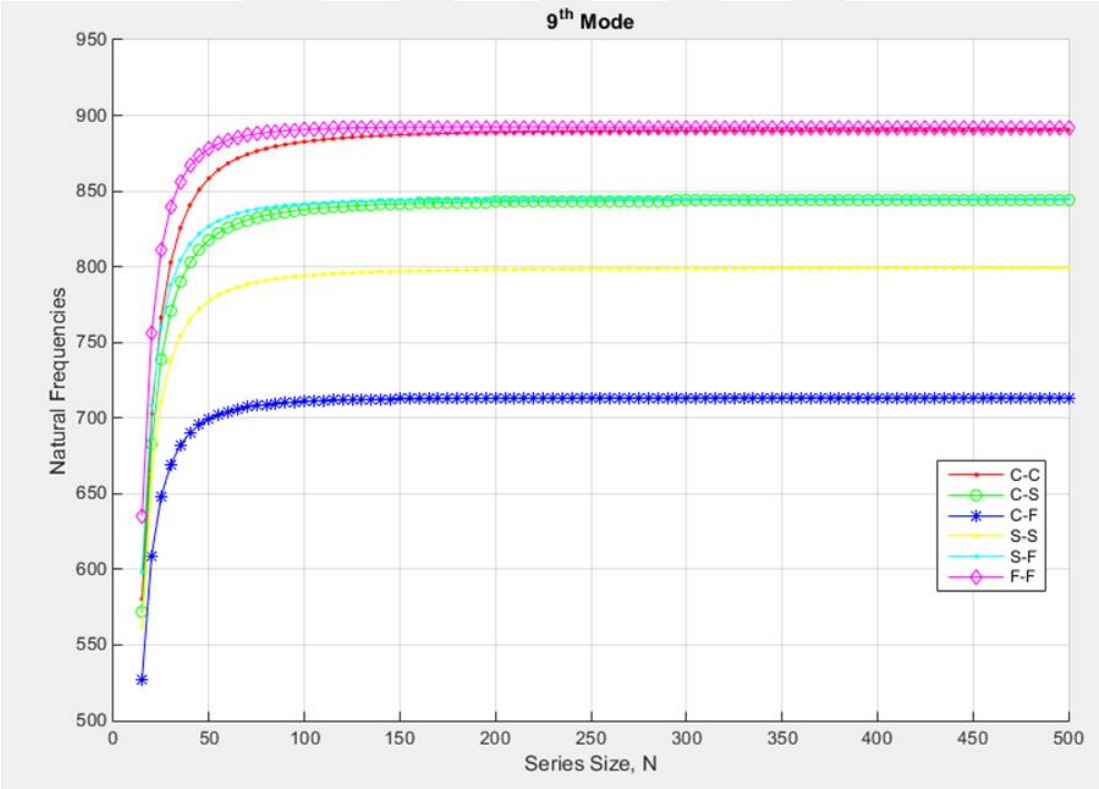

Figure 4.17 : Convergence analysis of the natural frequencies for the 9th mode.

Table 4.13 : The first ten dimensionless frequencies of Euler-Bernoulli beam.

Boundary Conditions		**C-C**	**C-S**	**C-F**	**S-S**	**S-F**	**F-F**
Mode							
1st	FDM	22,3733	15,4182	3,5172	9,8696	15,4233	22,3882
	Exact	22,3733	15,4182	3,5160	9,8696	15,4182	22,3733
2nd	FDM	61,6723	49,9646	22,0418	39,4783	49,9814	61,7138
	Exact	61,6728	49,9648	22,0345	39,4784	49,9649	61,6728
3rd	FDM	120,9015	104,2465	61,7174	88,8258	104,2817	120,9833
	Exact	120,9034	104,2477	61,6972	88,8264	104,2477	120,9034
4th	FDM	199,8547	178,2665	120,9409	157,9116	178,3269	199,9903
	Exact	199,8594	178,2697	120,9019	157,9137	178,2697	199,8594
5th	FDM	298,5455	272,0237	199,9226	246,7350	272,1162	298,7489
	Exact	298,5555	272,0310	199,8595	246,7401	272,0310	298,5555
6th	FDM	416,9720	385,5171	298,6472	355,2952	385,6487	417,2570
	Exact	416,9908	385,5314	298,5555	355,3058	385,5314	416,9908
7th	FDM	555,1330	518,7456	417,1145	483,5911	518,9234	555,5138
	Exact	555,1652	518,7711	416,9908	483,6106	518,7711	555,1652
8th	FDM	713,0269	671,7079	555,3233	631,6214	671,9389	713,5178
	Exact	713,0789	671,7499	555,1652	631,6547	671,7499	713,0789
9th	FDM	890,6522	844,4023	713,2723	799,3846	844,6937	891,2676
	Exact	890,7318	844,4680	713,0789	799,4380	844,4680	890,7318
10th	FDM	1088,0070	1036,8272	890,9598	986,8791	1037,1862	1088,7614
	Exact	1088,1239	1036,9253	890,7318	986,9604	1036,9253	1088,1239

By solving the discretized vibration equation given in Equation 4.5, the first ten natural frequencies of the beam in Table 4.12 can be obtained. These natural frequencies are necessary to understand the plate's dynamic characteristics. Similar to other employed numerical methods aforementioned, the results obtained from the FDM are compared to the analytical solutions given in the study of Blevins (2001). The numerical results confirm the accuracy and reliability of the Finite Difference Method (FDM) compared to analytical and numerical solutions. Meanwhile, a convergence analysis is performed to determine the optimal grid number ensuring the solution stability and accuracy. The finding of this analysis is presented in Figure 4.17.

4.3.2 Application of finite difference method to plate element

The application of FDM in the plate vibration is realized by replacing equivalent difference equations with derivatives in the governing differential equation and boundary conditions of the plate. Then, the non-dimensional transverse vibration equation for the thin isotropic rectangular plate can be written for each nodal point in Figure 4.18 as follow:

$$\frac{W_{i+2,j}-4W_{i+1,j}+6W_{i,j}-4W_{i-1,j}+W_{i-2,j}}{(\Delta X)^4}+2\lambda^2\frac{W_{i+1,j+1}-2W_{i,j+1}+W_{i-1,j+1}-2W_{i+1,j}}{(\Delta X)^2(\Delta Y)^2}$$
$$+2\lambda^2\frac{4W_{i,j}-2W_{i-1,j}+W_{i+1,j-1}-2W_{i,j-1}+W_{i-1,j-1}}{(\Delta X)^2(\Delta Y)^2}+\lambda^4\frac{W_{i,j+2}-4W_{i,j+1}+6W_{i,j}-4W_{i,j-1}+W_{i,j-2}}{(\Delta Y)^4} \quad (4.58)$$
$$-\Omega^2 W_{i,j}=0$$

where the non-dimensional coordinates are represented by X and Y, and the non-dimensional deflection is denoted by W while the dimensionless frequency of vibration is represented by Ω. Additionally, the length ratio is denoted by λ.

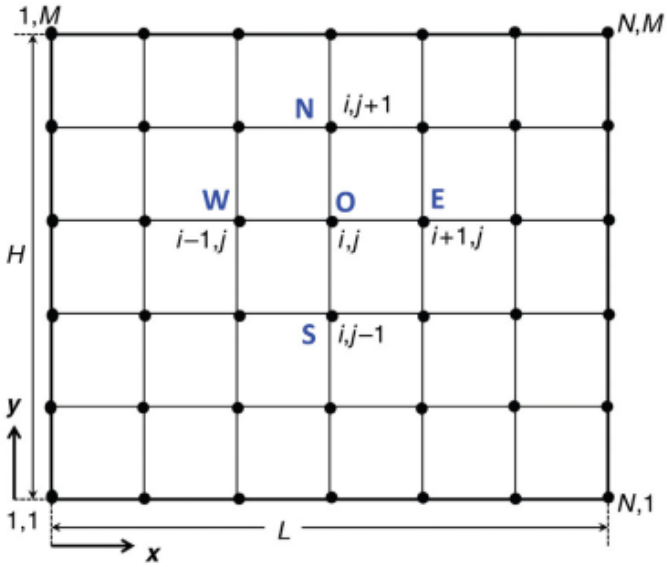

Figure 4.18 : A finite difference mesh and nodal points.

The obtained natural frequencies for the plate are tabulated in Table 4.14, and compared to the analytical solutions reported in the study of Leissa (1973) [234]. The numerical results are the good agreement with the analytical results and other numerical results obtained by the help of DTM and DQM. Therefore, it is still an attractive choice for a wide range of engineering applications due to its computational efficiency.

Table 4.14 : The first nine dimensionless frequencies of Kirchoff-Love plate via FDM.

Boundary Conditions		S-S-S-S					S-S-S-F				
Aspect Ratio		a/b					a/b				
Mode		2/5	2/3	1.0	3/2	5/2	2/5	2/3	1.0	3/2	5/2
1st	Exact	11,4487	14,2561	19,7392	32,0762	71,5564	10,1259	10,6712	11,6845	13,7111	18,8009
	FDM	11,4426	14,2484	19,7285	32,0589	71,5159	9,7277	10,0728	11,8270	23,9206	63,5380
2nd	Exact	16,1862	27,4156	49,3480	61,6850	101,1634	13,0570	18,2995	27,7563	43,5723	50,5405
	FDM	16,1672	27,3723	49,2574	61,5877	101,0448	12,0663	17,0357	28,1930	56,2547	92,0352
3rd	Exact	24,0818	43,8649	49,3480	98,6960	150,5115	18,8390	33,6974	41,1967	47,8571	100,2321
	FDM	24,0075	43,7772	49,2574	98,4987	150,0467	17,4793	32,3386	41,6736	79,3076	124,4366
4th	Exact	35,1358	49,3480	78,9568	111,0330	219,5987	27,5580	40,1307	59,0655	81,4789	110,2259
	FDM	34,9126	49,1509	78,7862	110,5896	218,2038	26,0747	38,9956	59,8569	107,4724	132,8902
5th	Exact	41,0576	57,0244	98,6960	128,3049	256,6097	39,3377	48,4082	61,8606	92,6925	147,6317
	FDM	40,9714	56,9011	98,2593	128,0276	256,0712	37,7263	46,7280	62,8647	118,6069	174,0607
6th	Exact	45,7950	78,9568	98,6960	177,6529	286,2185	39,6118	57,5929	90,2941	124,5635	169,1026
	FDM	45,6960	78,6798	98,2593	177,0295	285,6000	38,5982	56,2897	91,2438	173,1190	207,0340
7th	Exact	49,3480	80,0535	128,3049	180,1203	308,4251	42,6964	64,7281	94,4837	132,8974	203,7304
	FDM	48,8119	79,4430	127,7881	178,7467	305,0742	41,5187	62,2175	95,9204	177,4279	240,7948
8th	Exact	53,6906	93,2129	128,3049	209,7291	335,5665	48,7745	89,1859	108,9185	158,9180	257,4791
	FDM	53,5363	92,7791	127,7881	208,7530	334,6019	46,8259	86,1713	110,1721	195,0900	283,7807
9th	Exact	66,7185	106,3724	167,7833	239,3379	416,9908	54,2497	89,2725	115,6857	161,4205	277,4280
	FDM	64,4414	105,9030	166,4164	238,2818	402,7590	52,3282	87,1324	117,4084	236,2535	325,0646

Table 4.14: The First Nine Dimensionless Frequencies of Kirchoff-Love Plate via FDM (Cont ').

Boundary Conditions		S-C-S-S					S-C-S-C				
Aspect Ratio		a/b					a/b				
Mode		2/5	2/3	1.0	3/2	5/2	2/5	2/3	1.0	3/2	5/2
1st	Exact	11,7502	15,5783	23,6463	42,5278	103,9227	12,1347	17,3730	28,9509	56,3481	145,4839
	FDM	11,7502	15,5783	23,6463	42,5278	103,9227	12,1347	17,3730	28,9509	56,3481	145,4839
2nd	Exact	17,1872	31,0724	51,6743	69,0031	128,3382	18,3647	35,3445	54,7431	78,9836	164,7387
	FDM	17,1872	31,0724	51,6743	69,0031	128,3382	18,3647	35,3445	54,7431	78,9836	164,7387
3rd	Exact	25,9171	44,5644	58,6464	116,2671	172,3804	27,9657	45,4294	69,3270	123,1719	202,2271
	FDM	25,9171	44,5644	58,6464	116,2671	172,3804	27,9657	45,4294	69,3270	123,1719	202,2271
4th	Exact	37,8317	55,3926	86,1345	120,9956	237,2502	40,7500	62,0544	94,5853	146,2677	261,1053
	FDM	37,8317	55,3926	86,1345	120,9956	237,2502	40,7500	62,0544	94,5853	146,2677	261,1053
5th	Exact	41,2070	59,4627	100,2698	147,6353	320,7921	41,3782	62,3131	102,2162	170,1112	342,1442
	FDM	41,2070	59,4627	100,2698	147,6353	320,7921	41,3782	62,3131	102,2162	170,1112	342,1456
6th	Exact	46,3620	83,6060	113,2281	184,1006	322,9642	47,0009	88,8047	129,0955	189,1219	392,8746
	FDM	46,3620	83,6060	113,2281	184,1006	322,9657	47,0009	88,8047	129,0955	189,1219	392,8746
7th	Exact	52,9007	88,4384	133,7910	193,8025	346,7382	56,1782	94,2131	140,2045	212,8169	415,6906
	FDM	52,9010	88,4384	133,7910	193,8025	346,7382	56,1782	94,2131	140,2045	212,8169	415,6906
8th	Exact	54,8720	93,6758	140,8456	243,4964	391,0659	56,6756	97,4254	154,7757	276,0012	444,9682
	FDM	54,8720	93,6758	140,8456	243,4964	391,0659	56,6757	97,4254	154,7757	276,0030	444,9894
9th	Exact	66,6637	108,1069	168,9585	260,2020	429,2420	68,7486	101,0788	170,3465	276,0125	455,3054
	FDM	66,6637	108,1069	168,9585	260,2020	429,2640	68,7487	110,0788	170,3464	276,0125	455,3054

Table 4.14: The First Nine Dimensionless Frequencies of Kirchoff-Love Plate via FDM (Cont').

Boundary Conditions		S-C-S-F					S-F-S-F				
Aspect Ratio		a/b					a/b				
Mode		2/5	2/3	1.0	3/2	5/2	2/5	2/3	1.0	3/2	5/2
1st	Exact	10,1888	10,9752	12,6874	16,8225	30,6277	9,7600	9,6983	9,6314	9,5582	9,4841
	FDM	10,1686	10,9381	12,6221	16,7114	30,4508	9,8829	9,9988	10,2012	10,4804	10,1883
2nd	Exact	13,6036	20,3355	33,0651	45,3024	58,0804	11,0368	12,9813	16,1348	21,6192	33,6228
	FDM	13,5768	20,2792	32,9788	45,1284	57,7263	10,7866	12,4334	15,2098	20,3168	32,6301
3rd	Exact	20,0971	37,9552	41,7019	61,0178	105,5470	15,0626	22,9535	36,7256	38,7214	38,3629
	FDM	20,0634	37,8987	41,5986	60,9063	105,0934	15,1461	23,1100	36,9313	40,1830	41,4213
4th	Exact	29,6219	40,2717	63,0148	92,3073	149,4569	21,7064	39,1052	38,9450	54,8443	75,2037
	FDM	29,5867	40,2047	62,8638	92,0475	149,3269	21,5319	39,4607	39,6754	52,2596	70,5994
5th	Exact	39,6382	49,7317	72,3976	93,8293	173,1060	31,1771	40,3560	46,7381	65,7922	86,9684
	FDM	39,5952	49,6511	72,3278	93,5968	172,5608	31,1908	40,0804	45,3157	65,9847	90,8630
6th	Exact	42,2425	64,1889	90,6114	141,7834	182,8110	39,2387	42,6847	70,7401	87,6262	130,3576
	FDM	42,2094	64,1402	90,4607	141,4436	182,4059	39,3938	41,9350	71,1953	89,2697	123,6711
7th	Exact	42,9993	67,8993	103,1617	149,6055	235,0155	40,5035	54,2400	75,2834	103,9665	155,3211
	FDM	42,9613	67,7944	102,9860	149,5284	234,3599	40,1528	54,4897	74,9561	101,3541	155,5274
8th	Exact	49,5740	89,3571	111,8964	162,2413	260,6371	43,6698	66,2301	87,9867	105,1608	156,1248
	FDM	49,5269	89,2518	111,7149	161,9400	259,9930	43,5460	66,2422	88,7866	105,2666	160,1529
9th	Exact	58,0019	94,5150	131,4287	181,1868	305,2218	44,9416	73,1982	96,0405	152,7784	199,8452
	FDM	57,9631	94,3984	131,3741	180,9425	304,3930	45,0341	72,6419	94,3539	152,4481	193,3998

4.4 Closing Remarks

In the last few decades, many numerical methods have been developed and employed to solve various types of linear and nonlinear equations due to challenges in the aspect of the implementation of governing equations and boundary conditions, computation time, algorithm complexity, accuracy, convergence, stability of the solution and so on. Of the numerical methods in the open literature, differential quadrature (DQM), differential transform (DTM), and finite difference (FDM) methods are expressed briefly with their algorithms and compared to each other for the modal analysis of beam and plate elements in this chapter. For simplicity, shear strain effects are neglected for the chosen structural elements, and the plate element is reduced to a one-dimensional case up to the chosen simply-supported boundary condition due to the limitations of DTM in a two-dimensional case. Under these assumptions, computed non-dimensional natural frequencies by applying the concerned methods are tabulated, and mode shapes are plotted. To understand the strength and accuracy of employed methods, the numerical results in the high vibration modes are investigated, and it is seen that DTM gives faster and more accurate solutions while the results of DQM depend on chosen grid distribution and are less accurate than DTM. However, the ease of implementation and accurate results for multi-dimensional cases are pros properties of the DQM. Additionally, FDM is still a popular numerical method due to its simplicity in practical engineering problems.

5. VIBRATION ANALYSIS OF ROTATING BEAMS

Rotating beam structures are a common engineering component found in a variety of applications, such as aerospace systems, industrial machinery, wind turbines, turbofan engines, and automobile drivetrains. Understanding the vibrational characteristics of such rotating systems is critical to ensuring their safety and structural performance enhancement. Therefore, this chapter focuses on the free vibration analysis of rotating beam structures. Employing this eigenvalue analysis, the dynamic behavior of a system can be investigated in the case of variations in rotating speed, external forces, and thermal effects. With this aim, the dynamic behavior of rotating double-tapered and twisted beams is investigated in the first part of this chapter to understand the effects of geometrical parameters, structural boundary conditions, and rotation speed on natural frequencies and mode shapes. Then, the effects of elevated temperatures and material properties can be explored to grasp the interaction between rotation, thermal effects, and the vibrational behavior of beam structures.

5.1 Structural Dynamics of Double Tapered Rotating Beams

In recent years, there has been increasing interest in rotating aerospace structures such as gas turbine blades, helicopter rotary wings, wind turbine blades, tilt-rotor propellers, flexible appendages of space vehicles, etc. shown in Figure 5.1 due to various problems up to the chosen material type, boundary conditions, rotational speed, geometric properties, and environmental effects. To prevent possible failure cases, various structural analyses such as vibration, buckling, static structural, fatigue, and thermal are performed via engineering analysis software, user-written scripts based on numerical and semi-analytical methods, or specific test equipment. Then, the structure can be improved by changing design parameters or operating conditions at the beginning of the design process if any unwanted cases occur. In specific design problems, user-written scripts are generally preferred to engineering analysis tools, which guarantee to obtain more accurate and precise results than commercial software in a short time.

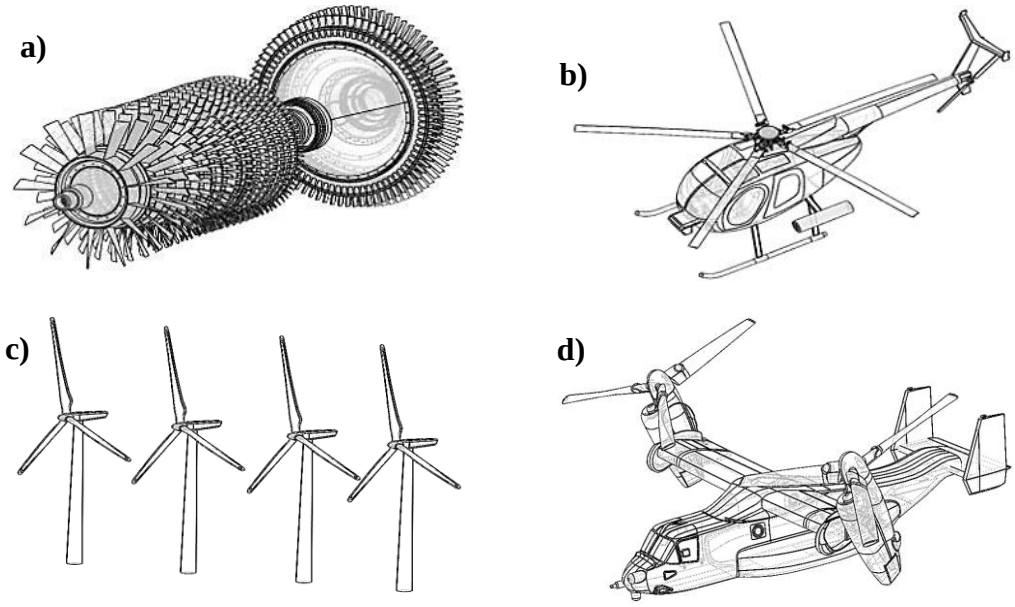

Figure 5.1 : Rotating structures: a) Turbine blades, b) Helicopter rotary wings, c) Wind turbine blades, d) Tilt-rotor propellers [74].

5.1.1 Equation of motion for beam vibration

In this section, the governing differential equation expressing flapwise motion or bending vibration of a double tapered Euler-Bernoulli beam in Figure 5.2 is derived by using the Hamiltonian principle step by step. Here, the beam attached at point O to a rotating rigid hub with flexible or rigid roots is considered made of both isotropic and homogenous material. To prevent coupling effects between bending and torsional vibrations, a doubly symmetric cross-section by two principal axes is preferred, which makes the shear center and the centroid axis of the cross-section coincident. In the governing equation, the effect of the rotary inertia term is taken into account; however, Coriolis effects are neglected by assuming constant axial displacement. Also, shear deformations are canceled to the chosen beam theory. Meanwhile, the advantage of using tapered geometry is to provide a high rigidity-mass ratio by optimizing the mass distribution of structures.

The beam's vibrational motion is elucidated through the displacement depicted in Figure 5.3, which has been adapted from the studies of Huang (2010) [29]. To express deformations accurately, it is necessary to consider the positions of any arbitrary point P on both the undeformed and deformed beams.

The expressions for the position vector of any point P, both before deformation as delineated in Equation 5.1 and after deformation as detailed in Equation 5.2, can be precisely formulated as follows:

$$\vec{r}_b = (R+x)\vec{i} + y\vec{j} + z\vec{k} \tag{5.1}$$

$$\vec{r}_a = \{R+x+u(x)-z.\sin(\theta(x,t))\}\vec{i} + y\vec{j} + \{w(x,t)+z.\cos(\theta(x,t))\}\vec{k} \tag{5.2}$$

In Equation 5.2, t represents time, θ denotes the rotation angle resulting from bending, x signifies the spanwise distance from the reference point O, y represents the transverse distance from the rotation axis, z indicates the vertical distance from the middle plane, and $u(x)$ and $w(x,t)$ stand for the displacements of point Q attributable to the centrifugal force and bending effects. In Figure 5.2, these distances are given with x_1, x_2, and x_3, respectively. These equations are harnessed to establish the position vector for any arbitrary point P within the deformed configuration of the beam depicted in Figure 5.3.

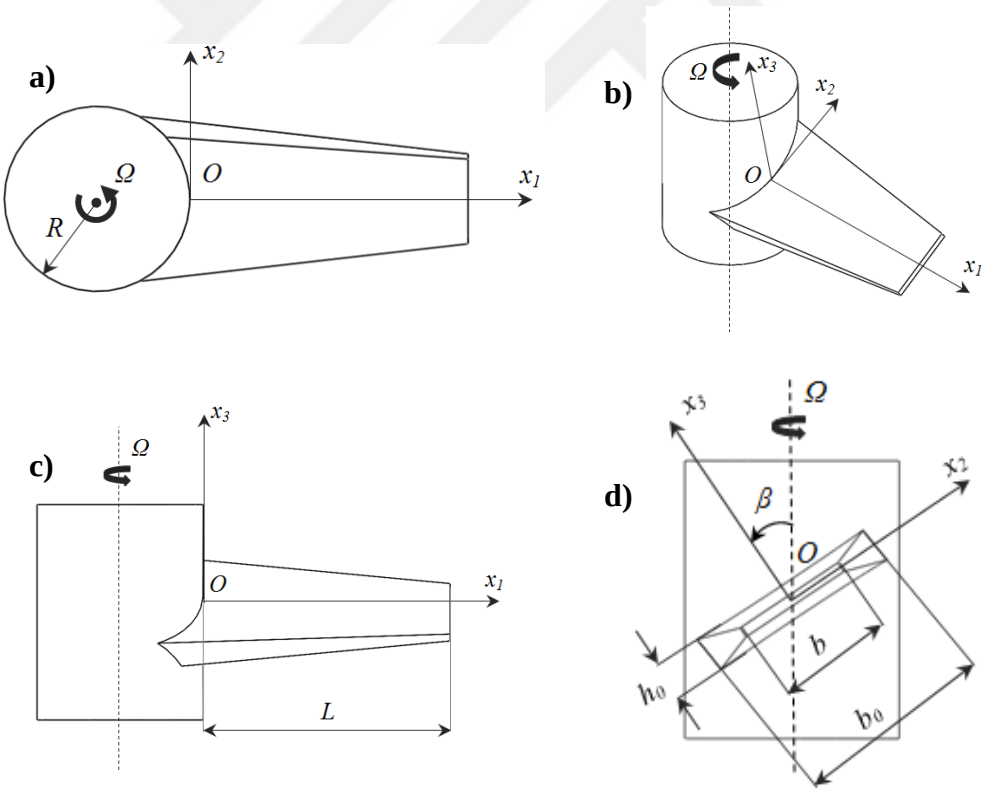

Figure 5.2 : Dimensions and axis system of the rotating double tapered beam with flexible root and setting angle: a) Top view, b) Front view, c) Isometric view, d) Side view [74].

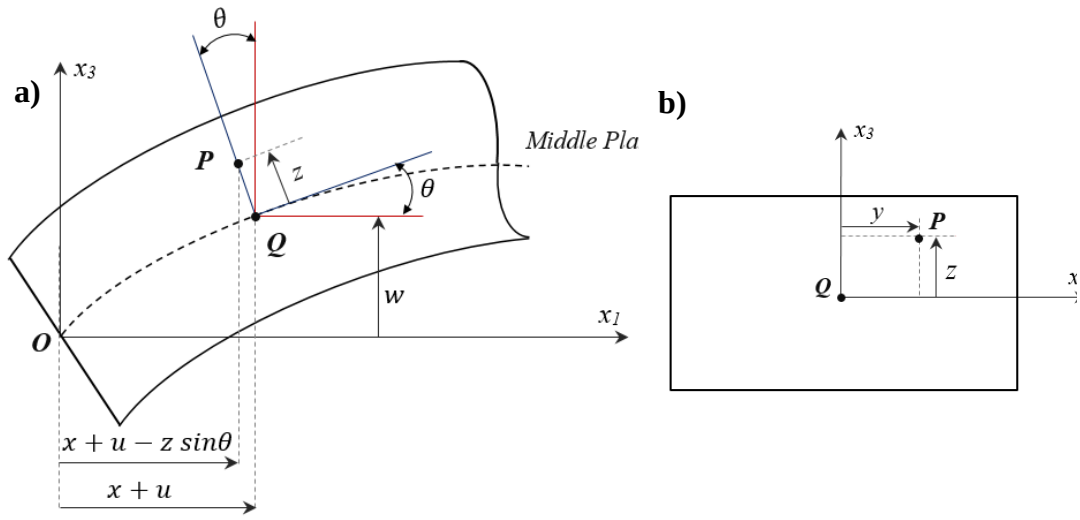

Figure 5.3 : Defined displacements for the deformed rotating euler-bernoulli beam: a) Longitudinal view, b) Cross-sectional view [74].

The expression for the centrifugal force acting on the beam can be written as follows:

$$F_{cent} = \int_{x}^{L} \rho A \Omega^2 \left(R + x\right) dx \tag{5.3}$$

where A represents the cross-sectional area, and ρ denotes the material density. The rotational speed vector in the beam axis system, concerning the setting angle, can be expressed as follows:

$$\vec{\Omega} = \Omega \sin\beta \ \vec{j} + \ \Omega \cos\beta \ \vec{k} \tag{5.4}$$

Under the assumption of small strain, where $sin\ \theta$ is approximated as θ and $cos\ \theta$ is approximated as 1, the reduced components of strain for the Euler-Bernoulli beam can be expressed as follows, as described in reference [70]:

$$\varepsilon_{xx} = u_{,x} - z w_{,xx} + \frac{1}{2} w_{,x}^2 = \frac{F_{cent}}{EA} - z\theta_{,x} + \frac{1}{2}\theta^2 \tag{5.5}$$

By employing the Hamiltonian approach, the equations of motion for a material characterized as homogeneous, isotropic, and linearly elastic can be formulated as follows:

$$\int_{t_1}^{t_2} \left(\delta \Im - \delta U\right) dt = 0 \tag{5.6}$$

In Equation 5.6, $\delta\Im$ represents the variation of kinetic energy due to the rotation of the beam, and δU denotes the variation of potential energy or strain energy due to bending. The terms for potential and kinetic energy are expressed as follows:

$$U = \frac{1}{2}\int_V E\varepsilon_{xx}^2 dV \qquad \Im = \frac{1}{2}\int_A\int_0^L \rho V_i^2 dA dx, \qquad i = 1,2,3. \tag{5.7}$$

where the components of the velocity vector in Equation 5.7 can be determined using the following expression:

$$\vec{V} = \frac{\partial \vec{r}}{\partial t} + \vec{\Omega} \times \vec{r} \tag{5.8}$$

By substituting Equations 5.1 through 5.5 into Equations 5.7 and 5.8, the energy expressions can be rewritten in an explicit form as follows:

$$U = \frac{1}{2}\int_0^L \left(EIw_{,xx}^2 + F_c w_{,x}^2 \right) dx \tag{5.9}$$

$$\Im = \frac{1}{2}\int_0^L \left(\rho A\left\{ \dot{w}^2 + w^2\Omega^2 \sin^2\beta \right\} + \rho I\left\{ \dot{w}_{,x}^2 + \Omega^2 w_{,x}^2 \right\} \right) dx \tag{5.10}$$

By substituting the energy relations in Equations 5.10 and 5.11 into the Hamiltonian expression in Equation 5.6, the governing differential equation for flapwise motion can be obtained as follows:

$$\rho A\frac{\partial^2 w}{\partial t^2} - \rho A\Omega^2 w \sin^2\beta + \frac{\partial^2}{\partial x^2}\left(E I \frac{\partial^2 w}{\partial x^2} \right) + \frac{\partial}{\partial x}\left(\rho I \Omega^2 \frac{\partial w}{\partial x} - F_c \frac{\partial w}{\partial x} - \rho I \frac{\partial}{\partial x}\frac{\partial^2 w}{\partial t^2} \right) = 0 \tag{5.11}$$

where the expressions for the cross-sectional area *A(x)* and the second moment of area *I(x)* for linear changes in taper ratios are provided in reference [42, 43] as follows:

$$A(x) = b_0 h_0 \left(1 - c_b \frac{x}{L} \right)\left(1 - c_h \frac{x}{L} \right) \tag{5.12}$$

$$I(x) = \frac{b_0 h_0^3}{12}\left(1 - c_b \frac{x}{L} \right)\left(1 - c_h \frac{x}{L} \right)^3 \tag{5.13}$$

To determine the vibration frequency of the beam, free vibration motion is analyzed assuming a sinusoidal displacement function given in Equation 5.14 with ω representing the circular frequency.

$$w(x,t) = \bar{w}(x)\ e^{i\omega t} \tag{5.14}$$

Then, the equation of flapwise motion is expressed as follows:

$$\begin{aligned} -\rho A \bar{w}\left\{\omega^2 + \Omega^2 \sin^2\beta\right\} + \frac{d^2}{dx^2}\left(E I \frac{d^2\bar{w}}{dx^2}\right) \\ + \frac{d}{dx}\left(\rho I \Omega^2 \frac{d\bar{w}}{dx} - F_c \frac{d\bar{w}}{dx} + \rho I \omega^2 \frac{d\bar{w}}{dx}\right) = 0 \end{aligned} \tag{5.15}$$

The expression defining the equation of flapwise motion in Equation 5.15 should be rewritten in a dimensionless form for easier comparisons with other techniques and to simplify the expression. Therefore, this expression is reformulated in terms of defined dimensionless parameters. The dimensionless equation of motion is derived as follows:

$$\begin{aligned} &-\left(\alpha^2 + \psi^2\right)\left(1 - c_b X\right)\left(1 - c_h X\right)W + \frac{d^2}{dX^2}\left(\left(1 - c_b X\right)\left(1 - c_h X\right)^3 \frac{d^2 W}{dX^2}\right) \\ &-\lambda^2 \frac{d}{dX}\left(\left\{\xi\left(1 - X\right) + \frac{1}{2}\left(1 - c_b\xi - c_h\xi\right)\left(1 - X^2\right) + \frac{1}{3}\left(c_b c_h \xi - c_h - c_b\right)\left(1 - X^3\right)\right. \right. \\ &\left.\left. + \frac{1}{4} c_b c_h \left(1 - X^4\right)\right\}\frac{dW}{dX}\right) + \left(\mu^2 + \eta^2\right)\frac{d}{dX}\left(\left(1 - c_b X\right)\left(1 - c_h X\right)^3 \frac{dW}{dX}\right) = 0 \end{aligned} \tag{5.16}$$

where the dimensionless parameters can be defined as:

$$\begin{aligned} &\alpha^2 = \frac{\rho A_0 \Omega^2 L^4 \sin^2\beta}{E I_0}, \quad \lambda^2 = \frac{\rho A_0 \Omega^2 L^4}{E I_0}, \quad W = \frac{\bar{w}}{L}, \quad X = \frac{x}{L}, \\ &\psi^2 = \frac{\rho A_0 \omega^2 L^4}{E I_0}, \quad \mu^2 = \frac{\rho \omega^2 L^2}{E}, \quad \eta^2 = \frac{\rho \Omega^2 L^2}{E}, \quad \xi = \frac{R}{L} \end{aligned} \tag{5.17}$$

In Equation 5.17, E represents Young's modulus, W stands for the displacement parameter, A_0 corresponds to the cross-sectional area of the root, I_0 represents the second moment of area of the root, α denotes the setting angle parameter, X stands for the length parameter, λ corresponds to the rotational speed parameter, ξ represents the hub radius parameter and ψ is the frequency parameter, μ and η serve as rotary inertia

parameters concerning frequency and rotation speed. These dimensionless parameters facilitate a standardized and comparative analysis with other techniques while simplifying the mathematical expressions. The dimensionless equation of motion (EOM) for the beam in Equation 5.16 can be explicitly expressed as a fourth-order linear ordinary differential equation with parametric coefficients, as follows:

$$P(X)\frac{d^4W}{dX^4} + Q(X)\frac{d^3W}{dX^3} + R(X)\frac{d^2W}{dX^2} + T(X)\frac{dW}{dX} - \gamma^2 W = 0 \qquad (5.18)$$

Finally, the essential boundary conditions of the beam are investigated, considering both non-classical ends (elastically clamped, elastically pinned, elastically clamped, and pinned) and classical ends (clamped, simply supported, free), as illustrated in Figure 5.4. These boundary conditions are summarized in Table 5.1. The specific choice of boundary conditions depends on the engineering requirements and the structural behavior of the rotating beam. These conditions play a crucial role in determining the mode shapes, natural frequencies, and overall dynamic behavior of the beam.

Table 5.1 : Equations for classical and non-classical supports.

Boundary Type	Essential Boundary Condition Equations
Clamped end	$W = \frac{dW}{dX} = 0$
Simply supported end	$W = \frac{d^2W}{dX^2} = 0$
Elastically Clamped End	$W = -K_R\frac{dW}{dX} + EI\frac{d^2W}{dX^2} = 0$
Elastically Pinned End	$\frac{d^2W}{dX^2} = K_T W + EI\frac{d^3W}{dX^3} = 0$
Elastically Clamped and Pinned End	$-K_R\frac{dW}{dX} + EI\frac{d^2W}{dX^2} = K_T W + EI\frac{d^3W}{dX^3} = 0$
Free End	$\frac{d^2W}{dX^2} = \frac{d^3W}{dX^3} = 0$

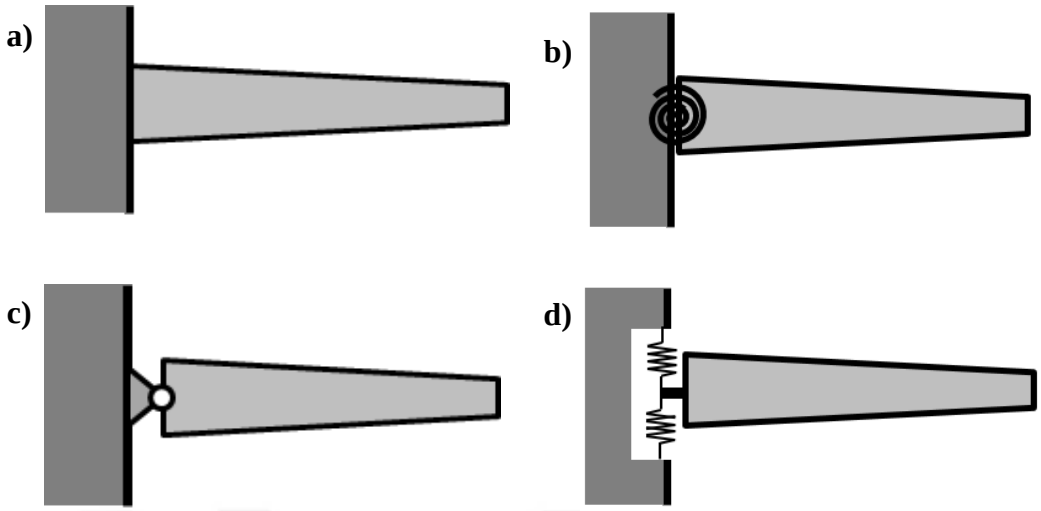

Figure 5.4 : The boundary conditions for the rotating tapered beam: a) Clamped, b) Elastically clamped, c) Simply-supported, d) Elastically pinned-free [74].

5.1.2 Numerical solution by generalized differential quadrature method

In this part of the study, the application of the Differential Quadrature Method (DQM) to a one-dimensional structural element is demonstrated for various boundary conditions as outlined in Table 5.1. As remembered from the previous chapter, the DQM involves discretizing the spatial domain using a grid of points and approximating the derivatives in the differential equations with weighted sums at these grid points.

By employing it, the beam in Figure 5.5 is initially discretized into *N* elements according to a Chebyshev-Gauss-Lobatto (CGL) grid distribution, where *i* ranges from *1* to *N*. Hence, the equation of motion (EOM) for the beam in Equation 5.19 can be reformulated as the following expression:

$$P(X_i)\sum_{k=1}^{N} A_{ik}^{(4)} W(X_k) + Q(X_i)\sum_{k=1}^{N} A_{ik}^{(3)} W(X_k) + R(X_i)\sum_{k=1}^{N} A_{ik}^{(2)} W(X_k) + T(X_i)\sum_{k=1}^{N} A_{ik}^{(1)} W(X_k) - \gamma^2 W(X_i) = 0 \tag{5.19}$$

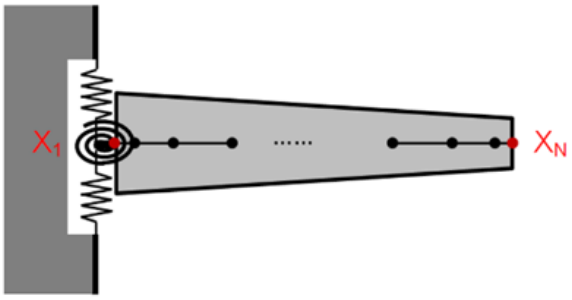

Figure 5.5 : CGL grid distribution on the beam with elastically clamped and pinned–free boundaries [74].

This expression leads to the explicit formulation of Equation 5.20. Subsequently, the following set of algebraic equations is derived for *i = 1, 2, …, N*:

$$\begin{aligned}
&P_1\left\{A^{(4)}_{11}W_1+\ldots+A^{(4)}_{1N}W_N\right\}+Q_1\left\{A^{(3)}_{11}W_1+\ldots+A^{(3)}_{1N}W_N\right\}+\ \ \ldots\ -\gamma^2 W_1=0\\
&P_2\left\{A^{(4)}_{21}W_1+\ldots+A^{(4)}_{2N}W_N\right\}+\ldots+R_2\left\{A^{(2)}_{21}W_1+\ldots+A^{(2)}_{2N}W_N\right\}+\ldots-\gamma^2 W_2=0\\
&P_3\left\{A^{(4)}_{31}W_1+\ldots+A^{(4)}_{3N}W_N\right\}+\ldots+R_3\left\{A^{(2)}_{31}W_1+\ldots+A^{(2)}_{3N}W_N\right\}+\ldots-\gamma^2 W_3=0\\
&\qquad\qquad\qquad\qquad .\\
&\qquad\qquad\qquad\qquad .\\
&\qquad\qquad\qquad\qquad .\\
&P_N\left\{A^{(4)}_{N1}W_1+\ldots+A^{(4)}_{NN}W_N\right\}+\ldots+T_N\left\{A^{(1)}_{N1}W_1+\ldots+A^{(1)}_{NN}W_N\right\}-\gamma^2 W_N=0
\end{aligned} \tag{5.20}$$

Here, the displacement function and parametric variables can be expressed as $W(X_i) = W_i$, $P(X_i) = P_i$, $Q(X_i) = Q_i$, $R(X_i) = R_i$, and $T(X_i) = T_i$. As seen, the computation of dynamic characteristics, or the free vibration analysis problem, transforms into an eigenvalue problem when the governing equation is presented in matrix form. The algebraic equation set given in Equation 5.21 can be expressed in matrix form as follows:

$$\begin{bmatrix}
\bar{A}_{11}-\gamma^2 & \bar{A}_{12} & \ldots & \bar{A}_{1N}\\
\bar{A}_{21} & \bar{A}_{22}-\gamma^2 & \ldots & \bar{A}_{2N}\\
. & & & \\
. & & & \\
. & & & \\
\bar{A}_{N1} & \bar{A}_{N2} & \ldots & \bar{A}_{NN}-\gamma^2
\end{bmatrix}
\begin{bmatrix} W_1\\ W_2\\ .\\ .\\ .\\ W_N \end{bmatrix}=0 \tag{5.21}$$

In matrix representation, the size of the coefficient matrix is $N\times N$, the size of the unknown vector is $N\times 1$, γ represents the dimensionless vibration frequency, and the elements of the coefficient matrix are defined as follows:

$$\begin{aligned}
\bar{A}_{11} &= P_1 A_{11}^{(4)} + Q_1 A_{11}^{(3)} + R_1 A_{11}^{(2)} + T_1 A_{11}^{(1)} \\
\bar{A}_{12} &= P_1 A_{12}^{(4)} + Q_1 A_{12}^{(3)} + R_1 A_{12}^{(2)} + T_1 A_{12}^{(1)} \\
\bar{A}_{1N} &= P_1 A_{1N}^{(4)} + Q_1 A_{1N}^{(3)} + R_1 A_{1N}^{(2)} + T_1 A_{1N}^{(1)} \\
&\vdots \\
\bar{A}_{N1} &= P_N A_{N1}^{(4)} + Q_N A_{N1}^{(3)} + R_N A_{N1}^{(2)} + T_N A_{N1}^{(1)} \\
\bar{A}_{N2} &= P_N A_{N2}^{(4)} + Q_N A_{N2}^{(3)} + R_N A_{N2}^{(2)} + T_N A_{N2}^{(1)} \\
\bar{A}_{NN} &= P_N A_{NN}^{(4)} + Q_N A_{NN}^{(3)} + R_N A_{NN}^{(2)} + T_N A_{NN}^{(1)}
\end{aligned} \tag{5.22}$$

Likewise, four boundary matrices are defined for the discretized boundary conditions outlined in Table 5.2. To incorporate these conditions, the rows of the system matrix in Equation 5.23 are updated by modifying the corresponding boundary rows of the boundary matrices. For instance, the implementation of clamped-free boundaries is detailed as follows:

$$\begin{bmatrix}
1 & 0 & 0 & \cdots & 0 \\
A_{11}^{(1)} & A_{12}^{(1)} & A_{13}^{(1)} & \cdots & A_{1N}^{(1)} \\
\bar{A}_{31} & \bar{A}_{32} & \bar{A}_{33}-\gamma^2 & \cdots & \bar{A}_{3N} \\
 & & \vdots & & \\
\bar{A}_{(N-2)1} & \bar{A}_{(N-2)2} & \bar{A}_{(N-2)3} & \cdots & \bar{A}_{(N-2)N} \\
A_{N1}^{(2)} & A_{N2}^{(2)} & A_{N3}^{(2)} & \cdots & A_{NN}^{(2)} \\
A_{N1}^{(3)} & A_{N2}^{(3)} & A_{N3}^{(3)} & \cdots & A_{NN}^{(3)}
\end{bmatrix} \tag{5.23}$$

In this context, $A_{ij}(k)$ represents the weighted coefficient of the k^{th} derivative in the X direction. Notably, boundaries are initially defined for both the first and the last elements of the beam. Consequently, the first and last two rows of the system matrix are updated by replacing them with the corresponding rows from the four boundary matrices.

Table 5.2 : Equations of discretized boundary conditions

BCs	**Essential Boundary Condition Equations**
Clamped End @ $X=X_1$	$W\big\|_{X=X_1} = W_1 = 0$ $\left.\frac{dW}{dX}\right\|_{X=X_1} = \sum_{k=1}^{N} A_{1k}^{(1)} W_k = 0$
Simply supported End @ $X=X_1$	$W\big\|_{X=X_1} = W_1 = 0$ $\left.\frac{d^2W}{dX^2}\right\|_{X=X_1} = \sum_{k=1}^{N} A_{1k}^{(2)} W_k = 0$
Elastically Clamped End @ $X=X_1$	$W\big\|_{X=X_1} = W_1 = 0$ $-K_R \sum_{k=1}^{N} A_{1k}^{(1)} W_k + EI \sum_{k=1}^{N} A_{1k}^{(2)} W_k = 0$
Elastically Pinned End @ $X=X_1$	$\left.\frac{d^2W}{dX^2}\right\|_{X=X_1} = \sum_{k=1}^{N} A_{1k}^{(2)} W_k = 0$ $K_T W_1 + EI \sum_{k=1}^{N} A_{1k}^{(3)} W_k = 0$
Elastically Clamped and Pinned End @ $X=X_1$	$-K_R \sum_{k=1}^{N} A_{1k}^{(1)} W_k + EI \sum_{k=1}^{N} A_{1k}^{(2)} W_k = 0$ $K_T W_1 + EI \sum_{k=1}^{N} A_{1k}^{(3)} W_k = 0$
Free End @ $X=X_N$	$\left.\frac{d^2W}{dX^2}\right\|_{X=X_N} = \sum_{k=1}^{N} A_{Nk}^{(2)} W_k = 0$ $\left.\frac{d^3W}{dX^3}\right\|_{X=X_N} = \sum_{k=1}^{N} A_{Nk}^{(3)} W_k = 0$

In computational mechanics, convergence analysis in Figure 5.6 is performed to ensure satisfactorily precise results with the minimum series terms for different modes of vibration. In this analysis, the natural frequency plot against varying series sizes is utilized to determine the point at which results stabilize. The smallest number of series sizes, or grid points is an optimal balance between computational efficiency and result accuracy. In this context, the series size for the system matrix is refined, and a choice is made to set it to $N = 23$ for the Chebyshev-Gauss-Lobatto (CGL) grid distribution.

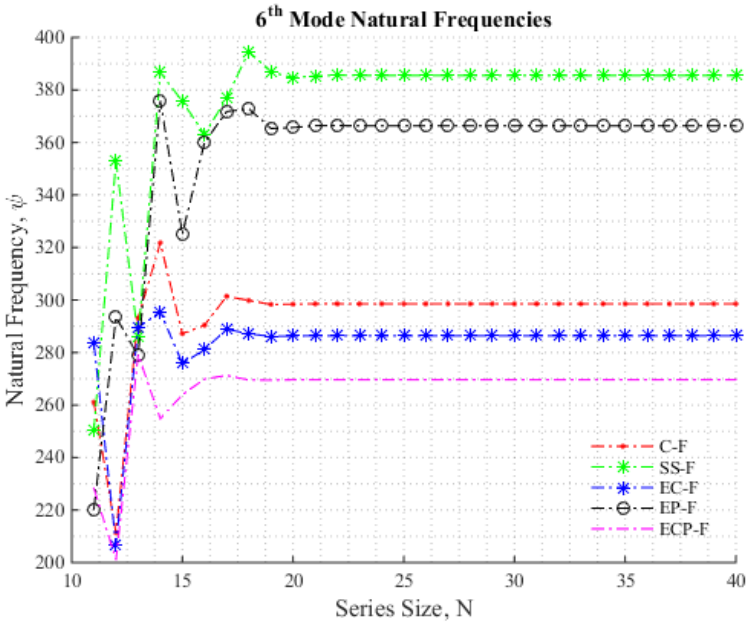

Figure 5.6 : Convergence analysis for clamped-free (C-F), simply supported-free (S-F), elastically clamped-free (EC-F), elastically pinned-free, elastically clamped and pinned-free (ECP-f) boundary conditions ($\lambda=0$, $c_b=c_h=0$, $\alpha=0$, $EI/K_{rot}=0.035$, $EI/K_{tran}=0.0001$).

5.1.3 Numerical results and discussion

To demonstrate the accuracy of the employed numerical method, the computer code is developed in Matlab R2019b, and the dynamic characteristics i.e. mode shapes and natural frequencies computed by the DQM for the various parameters are compared to the non-dimensional natural frequencies (NNF) published in the literature. Of the design and operating parameters, the effect of the rotational speed parameter on NNF can be seen in Figures 5.7-5.9, and Tables 5.3 and 5.5, which increases the natural frequencies by creating stiffening stresses along the beam axis due to centrifugal forces. Another design parameter is the setting angle or twist angle, which are used due to various reasons such as changing the direction of force, compressing the fluid, etc. in the rotating engineering structures. As shown in Figure 5.7, the increment in the setting angle decreases the NNF due to a decrease in rotational speed to the orientation of the velocity vector, which is similarly stated in the study of Navazi et al (2017) [257]. Meanwhile, the reason of difference between the results of FEM and DQM is due to used element numbers and computational errors while the results of DTM and DQM are consistent like in Figure 5.8. On the other hand, the increment in the hub radius increases the NNFs as a result of centrifugal force. As stated in Equation 5.3,

the centrifugal force is proportional to the hub radius, which is the distance between the rotation axis and the root of the structure.

The variation of the first four NNFs to hub radius and rotational speed is given in Figure 7-8, and Tables 5.3 and 5.4 validate this fact.

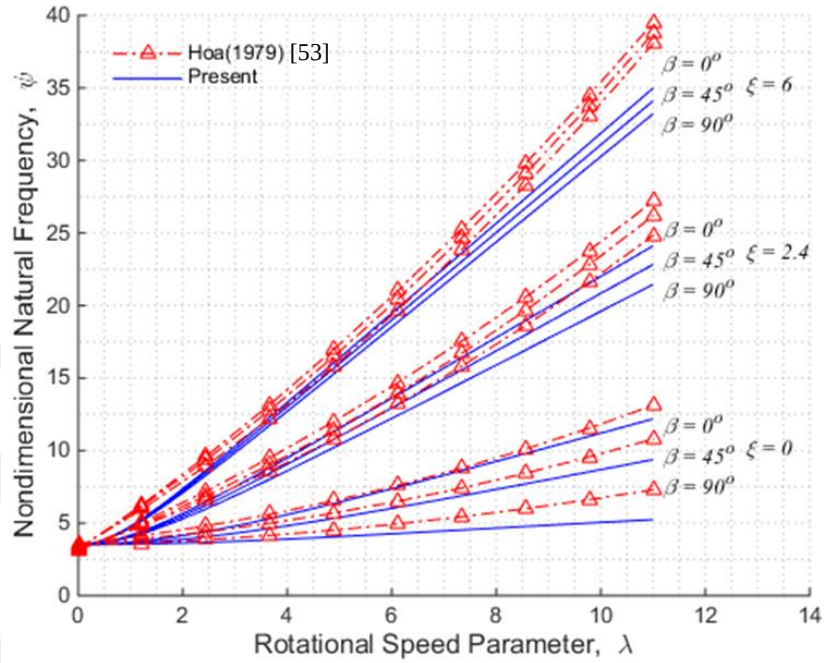

Figure 5.7 : Variation of the first natural frequency to the setting angle, hub radius, and the rotational speed for clamped-free boundaries ($c_b=c_h=0$, $K_{rot}=K_{tran}=0$).

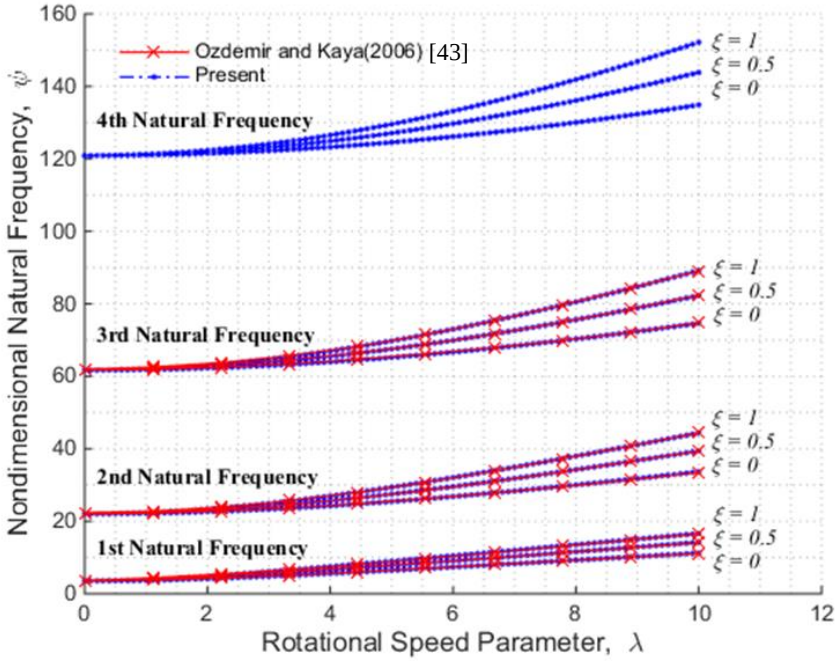

Figure 5.8 : Variation of the first natural frequency to the setting angle, hub radius, and the rotational speed for clamped-free boundaries ($c_b=c_h=0$, $K_{rot}=K_{tran}=0$).

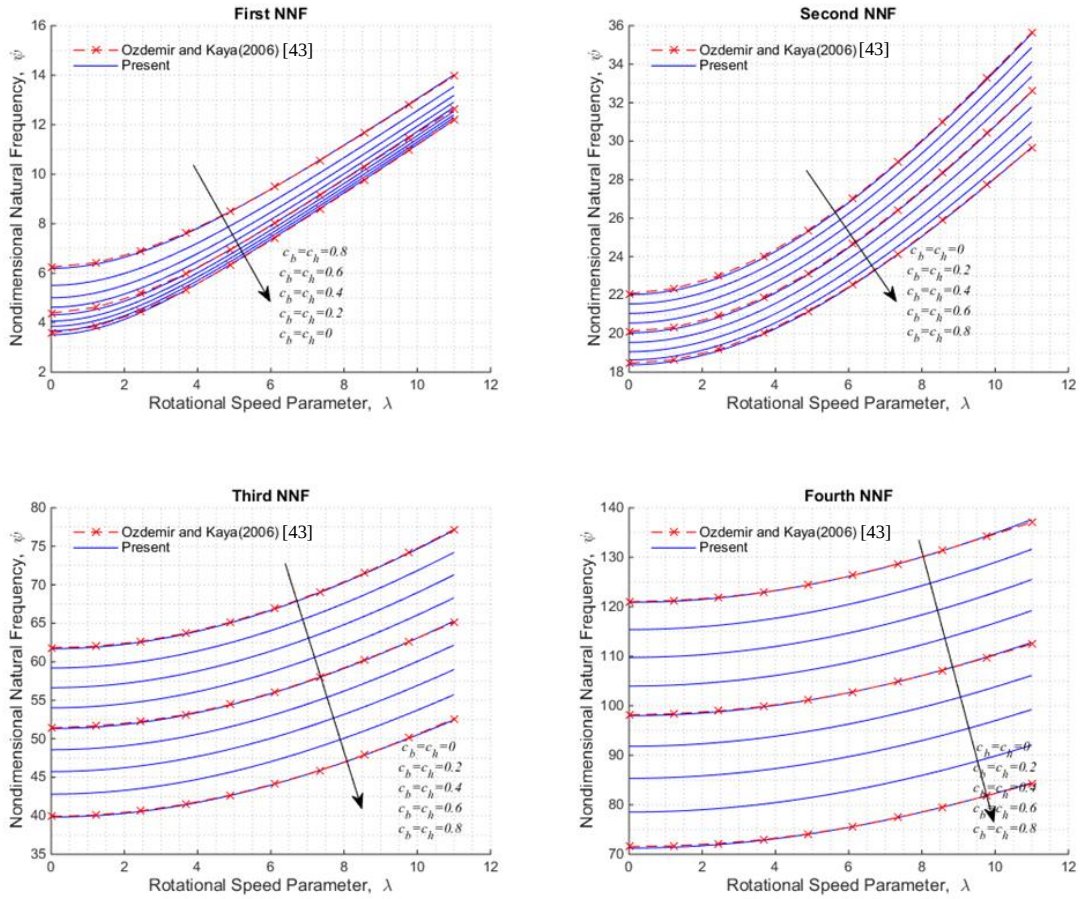

Figure 5.9 : Variation of the first four natural frequencies to rotational speed and taper ratios for clamped-free boundaries ($\xi=0$, $\alpha=0$, $K_{rot}=K_{tran}=0$).

The effect of the rotational speed parameter on various design parameters can be seen in Figures 5.7-5.8 and 5.9, and Tables 5.3 and 5.5, which increase the natural frequencies by creating stiffening stresses along the beam axis due to centrifugal forces. Another crucial design parameter design parameter is the setting angle or twist angle, which is used for various reasons such as changing the direction of force, compressing the fluid, etc. in the rotating engineering structures. As depicted in Figure 5.7, an increase in the setting angle leads to a decrease in nondimensional natural frequencies (NNF). This phenomenon is a result of decreased rotational speed aligning the orientation of the velocity vector, which a compatible with the findings in the study by Navazi et al. (2017) [257]. Furthermore, the increment in the hub radius contributes to an increase in NNFs due to centrifugal force. This observation aligns with Equation 5.3, indicating that centrifugal force is proportional to the hub radius, and rotation speed. The variation of the first four NNFs concerning hub radius and rotational speed is presented in Figures 5.7 and 5.8, and Tables 5.3 and 5.4 support the validity of this association.

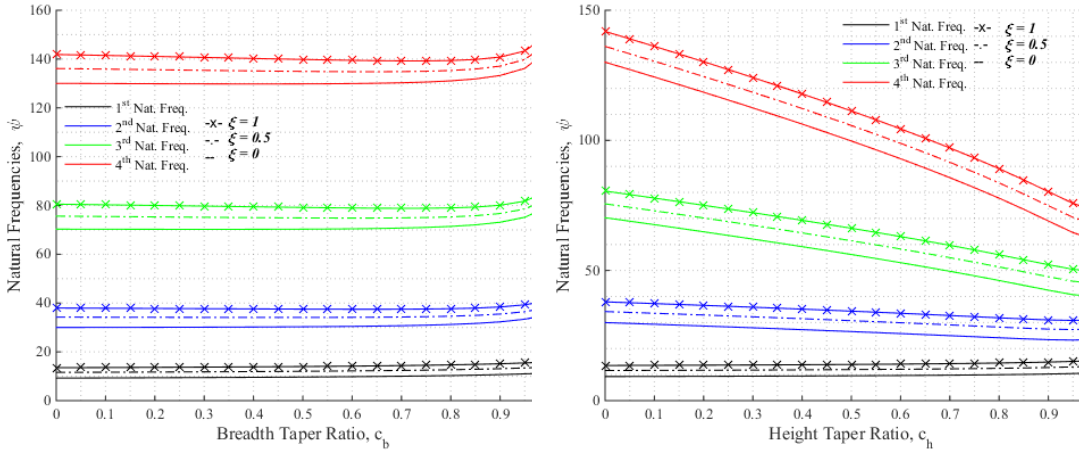

Figure 5.10 : Variation of the first four natural frequencies to breadth and height taper ratio for clamped-free boundaries ($\alpha = 0, \lambda=8, K_{rot}=K_{tran}=0$)

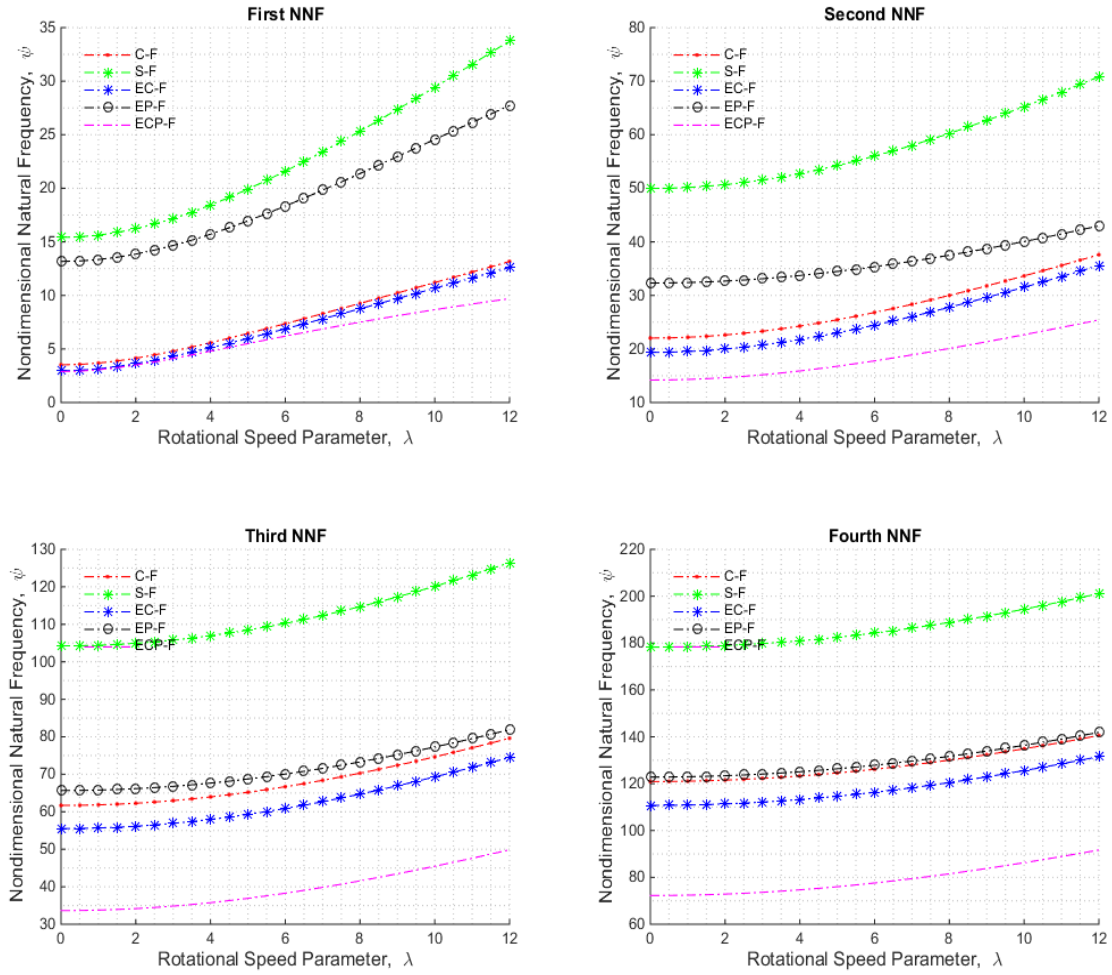

Figure 5.11 : Variation of the first four natural frequencies to rotational speed and taper ratios for clamped-free boundaries ($c_b=c_h=0, \mu=\eta=2, \xi=0, \alpha=0, K_{rot}=K_{tran}=0$).

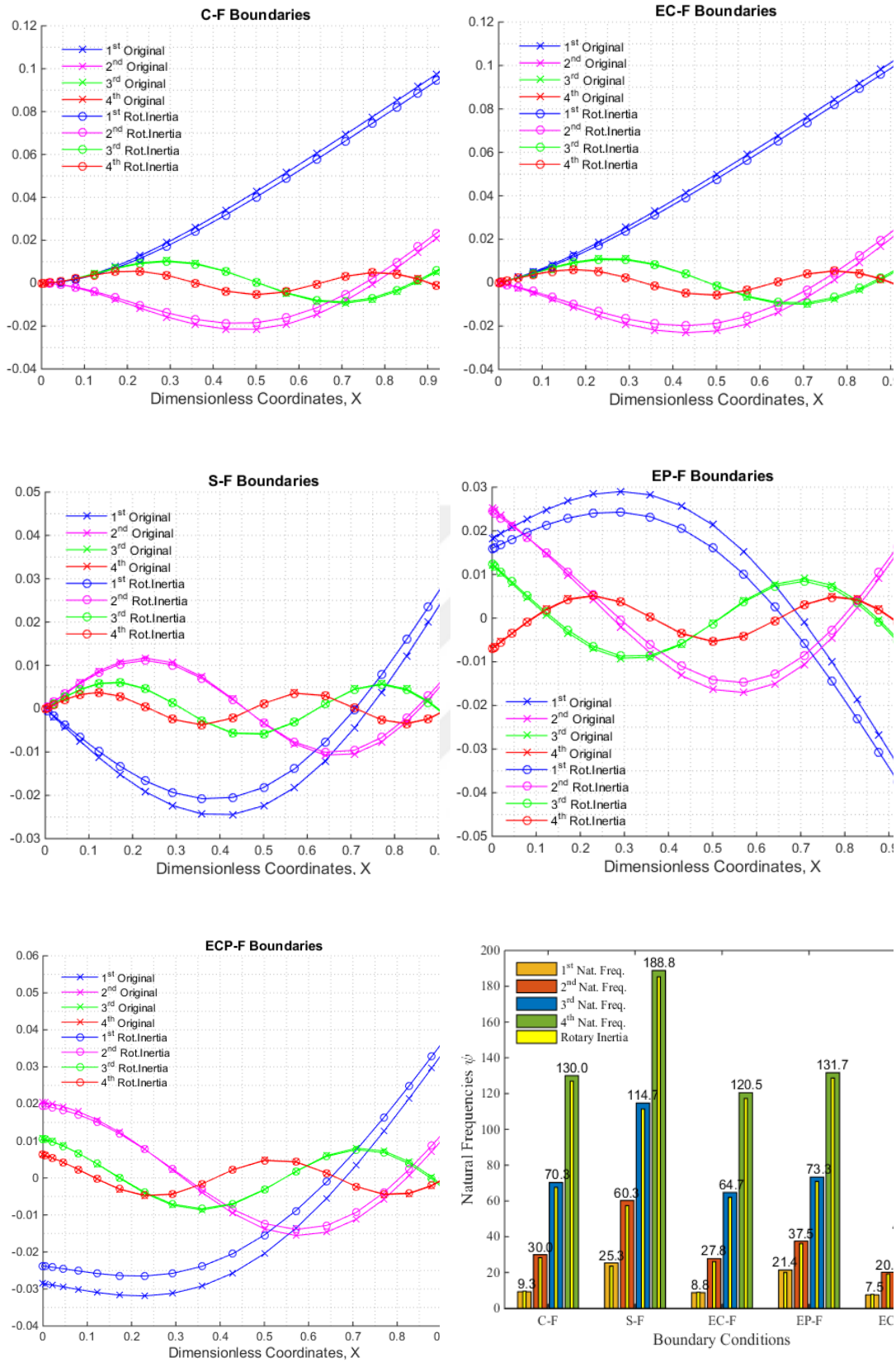

Figure 5.12 : Variation of the first four natural frequencies to dimensionless length for C-F ($K_{rot}=K_{tran}=0$), EC-F ($EI/K_{rot}=0.1$), S-F($K_{rot}=K_{tran}=0$), EP-F ($EI/K_{tran}=0.0092$), ECP-F ($EI/K_{rot}=0.1$, $EI/K_{tran}=0.0092$) boundaries ($c=0$, $\mu=2$, $\lambda=8$).

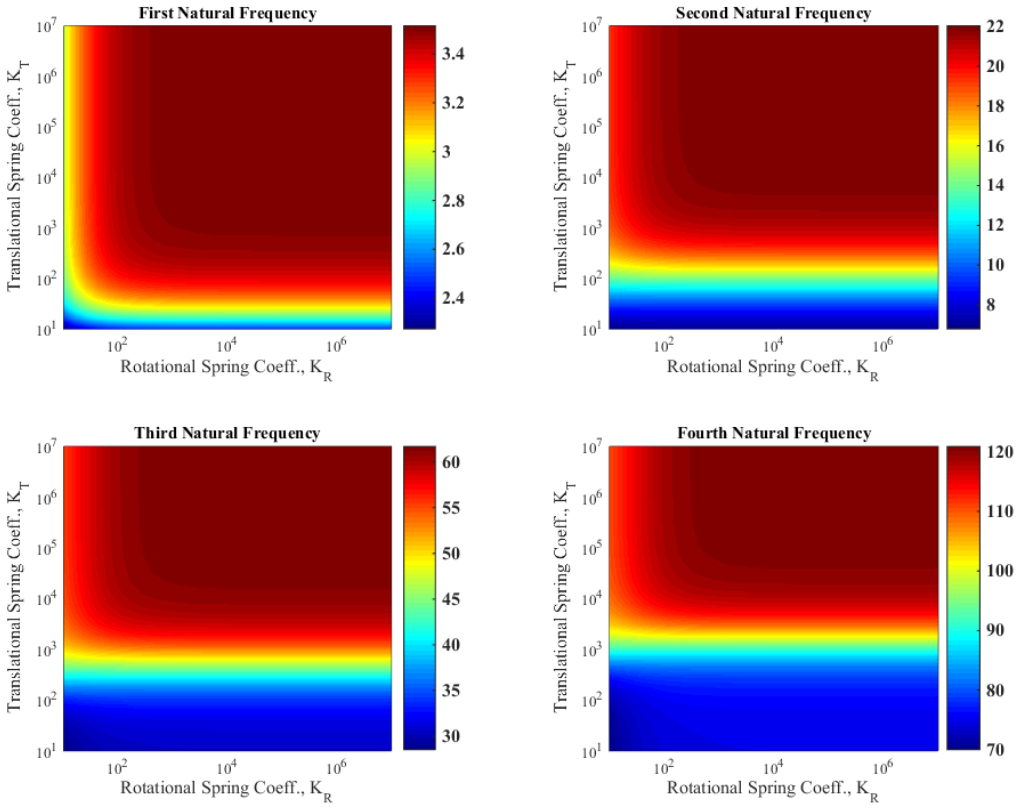

Figure 5.13 : Variation of the first four natural frequencies to spring coefficients for elastically clamped and pinned-free boundaries ($c_b=c_h=0$, $\mu=\eta=0$, $\xi=\alpha=0$, $\lambda = 0$)

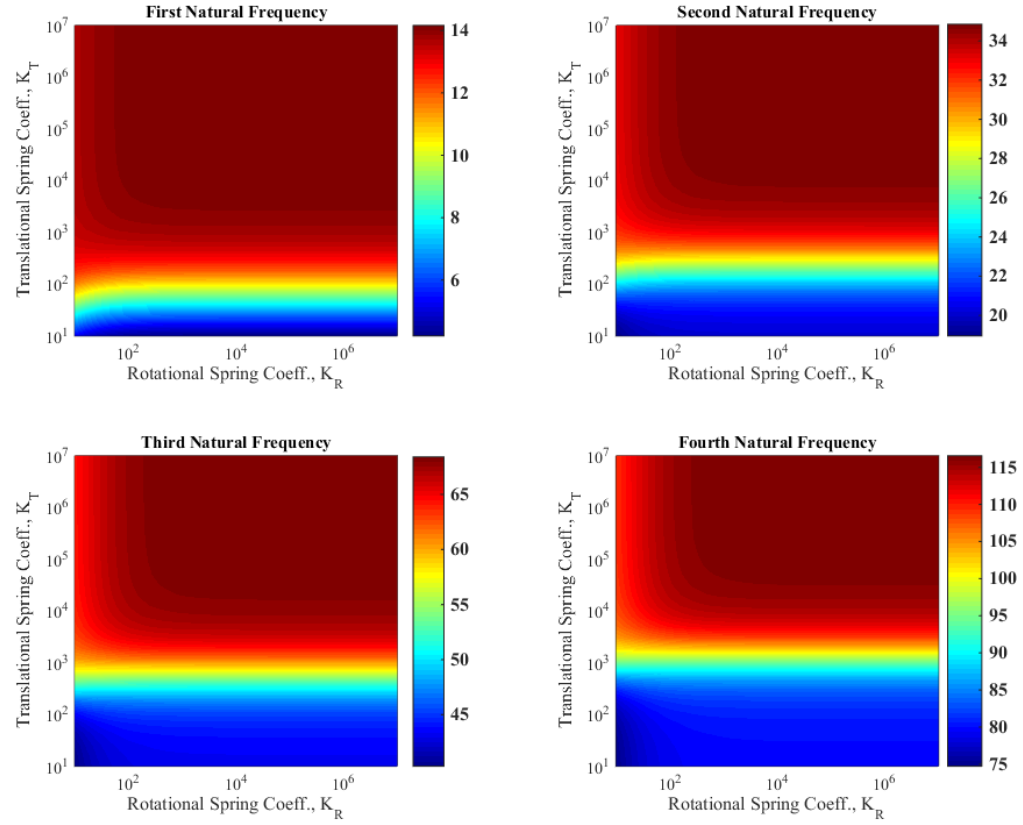

Figure 5.14 : Variation of the first four natural frequencies to spring coefficients for elastically clamped and pinned-free boundaries ($c_b=c_h=0.4$, $\mu=0$, $\xi=1$, $\alpha=0$, $\lambda =8$).

As previously stated, the structure is tapered to provide a high stiffness mass ratio and optimize the mass distribution. The effects of varying taper ratios are depicted in Figure 5.9 and Table 5.4, where uniform increments in taper ratios result in decreasing NNFs across all but the first NNF. In other words, Figures 5.9 and 5.10 show the height taper has a decreasing effect on the natural frequency except for the first one while the breadth taper ratio has approximately no effect. This is the result of the variation of the second moment of inertia in Equation 5.13 changing with the third-order power of the height taper ratio.

Of these design parameters, the boundary conditions of the root and tip of the beam are also important parameters to be considered. Practically, classical boundary conditions are defined to model the beam structures' end conditions, which causes the difference between the measured and computed natural frequencies. Modeling the root or tip of the beam with elastic boundary conditions is a more realistic engineering approach to determine the frequencies, accurately. For chosen rotational and translational spring coefficients, the variations of the natural frequencies to the rotational speed for the various boundary conditions are shown in Figure 5.11. Also, the mode shapes are presented with the case of rotary inertia term included in the governing differential equations. As seen in Figure 5.12(f), the rotary inertia terms have a negligible influence on the frequencies. Lastly, the variations in spring coefficients are investigated. Figure 5.13 illustrates the translational spring coefficient has more influence on the natural frequencies than the rotational spring coefficient. Moreover, increasing design parameters and rotational speed in Figure 5.14 make the spring coefficient more sensitive to the variations of the natural frequencies as reported by Chen and Du (2019) [51]. In summary, this section presents the numerical solution of a rotating double-tapered beam with a flexible root, step by step. While all analyses are carried out, deriving governing equations, applications of boundary conditions, assumptions, and their physical reasons behind and the solution technique are explicitly given. The results obtained by DQM are compared with previous studies in the literature to show the power of approaches developed and demonstrate acceptable accuracy with minimal computational work, supported by the graphical representations and tabulated values of natural frequencies, revealing the hidden mechanical interactions of geometrical properties, boundary conditions, and the rotational speed.

Table 5.3 : Variations of the first four natural frequencies of the rotating beam structure to hub radius, rotational speed, and boundary conditions ($c_b=c_h=0$, $\mu=\eta=0$, $\alpha=0$, $EI/K_{rot}=0.1$, $EI/K_{tran}=0.0092$).

	C-F		EC-F		EP-F		ECP-F		S-F	
	First Dimensionless Natural Frequency									
ξ	0	1	0	1	0	1	0	1	0	1
λ										
0	3,5160	3,5160	2,9678	2,9678	13,1804	13,1804	2,8900	2,8900	15,4182	15,4182
2	4,1373	4,8337	3,6305	4,3702	13,8653	14,8116	3,5014	4,1721	16,2261	17,3179
4	5,5850	7,4750	5,1125	7,0464	15,7245	18,8835	4,7980	6,3820	18,4313	21,9897
6	7,3604	10,4439	6,8824	10,0015	18,3554	24,1561	6,2006	8,4363	21,5944	27,9770
8	9,2568	13,5074	8,7539	13,0403	21,3948	29,8297	7,5072	10,1837	25,3436	34,5373
10	11,2023	16,6064	10,6686	16,1145	24,5849	35,3188	8,6736	11,6663	29,4439	41,3720
	Second Dimensionless Natural Frequency									
ξ	0	1	0	1	0	1	0	1	0	1
λ										
0	22,0345	22,0345	19,3558	19,3558	32,3432	32,3432	14,2080	14,2080	49,9649	49,9649
2	22,6149	23,3660	19,9864	20,8200	32,7033	33,0770	14,6550	15,2265	50,6760	51,7069
4	24,2733	26,9573	21,7698	24,6818	33,7491	35,0681	15,9141	17,8817	52,7463	56,5662
6	26,8091	32,0272	24,4547	29,9959	35,3938	37,8796	17,7956	21,4798	56,0099	63,7221
8	29,9954	37,9538	27,7771	36,0943	37,5369	41,1758	20,1016	25,5628	60,2513	72,3664
10	33,6404	44,3682	31,5307	42,6204	40,0953	44,9172	22,6824	29,9074	65,2554	81,9224
	Third Dimensionless Natural Frequency									
ξ	0	1	0	1	0	1	0	1	0	1
λ										
0	61,6972	61,6972	55,5182	55,5182	65,6816	65,6816	33,6512	33,6512	104,2477	104,2477
2	62,2732	63,0675	56,1421	57,0251	66,1823	66,7942	34,1934	34,9152	104,9358	105,9511
4	63,9668	66,9868	57,9694	61,2932	67,6643	70,0333	35,7793	38,4913	106,9708	110,8810
6	66,6839	72,9863	60,8817	67,7287	70,0705	75,1385	38,2973	43,8513	110,2695	118,5685
8	70,2930	80,5295	64,7180	75,6949	73,3151	81,7672	41,5914	50,4146	114,7094	128,4200
10	74,6493	89,1563	69,3082	84,6853	77,2948	89,5706	45,4959	57,7312	120,1464	139,8677
	Fourth Dimensionless Natural Frequency									
ξ	0	1	0	1	0	1	0	1	0	1
λ										
0	120,9019	120,9019	110,7080	110,7080	122,8148	122,8148	72,2632	72,2632	178,2697	178,2697
2	121,4967	122,3395	111,3462	112,2732	123,3883	124,1627	72,8799	73,7380	178,9490	179,9581
4	123,2615	126,5373	113,2367	116,8219	125,0917	128,1113	74,6973	77,9786	180,9698	184,9170
6	126,1405	133,1875	116,3107	123,9688	127,8763	134,4014	77,6250	84,5249	184,2830	192,8536
8	130,0490	141,8780	120,4658	133,2153	131,6671	142,6761	81,5334	92,8279	188,8124	203,3541
10	132,3576	146,8540	122,9109	138,4696	133,9112	147,4378	83,8099	97,4798	191,5036	209,4225

Table 5.4 : Variations of the first four natural frequencies of the rotating beam structure to hub radius, taper ratios, and boundary conditions (λ=8, μ=η=0, α=0, EI/K_{rot}=0.1, EI/K_{tran}=0.0092).

	C-F		EC-F		EP-F		ECP-F		S-F	
	First Dimensionless Natural Frequency									
ξ	0	1	0	1	0	1	0	1	0	1
c										
0.0	9,2568	13,5074	8,7539	13,0403	21,3948	29,8297	7,5072	10,1837	25,3436	34,5373
0.2	9,4802	13,7773	8,9446	13,2787	20,8431	29,2275	7,9777	10,8818	23,9469	32,8660
0.4	9,8005	14,1631	9,2251	13,6265	20,1612	28,5069	8,5479	11,7288	22,5000	31,0953
0.6	10,2986	14,7592	9,6687	14,1711	19,4185	27,6743	9,2838	12,8018	21,1011	29,3059
0.8	11,1765	15,7951	10,4495	15,1150	18,9618	26,9588	10,3561	14,2795	20,1553	27,8937
	Second Dimensionless Natural Frequency									
ξ	0	1	0	1	0	1	0	1	0	1
c										
0.0	29,9954	37,9538	27,7771	36,0943	37,5369	41,1758	20,1016	25,5628	60,2513	72,3664
0.2	28,7354	36,4463	26,5974	34,6071	35,9457	39,3794	20,0353	25,1556	55,1428	66,5968
0.4	27,4160	34,8442	25,3820	33,0448	34,3648	37,5717	20,0620	24,8412	49,9360	60,6933
0.6	26,0878	33,1934	24,1956	31,4694	32,7788	35,8162	20,2539	24,7256	44,6435	54,6606
0.8	25,0516	31,8095	23,3563	30,2207	31,2213	34,2604	20,8447	25,1011	39,4555	48,6595
	Third Dimensionless Natural Frequency									
ξ	0	1	0	1	0	1	0	1	0	1
c										
0.0	70,2930	80,5295	64,7180	75,6949	73,3151	81,7672	41,5914	50,4146	114,7094	128,4200
0.2	64,8280	74,5909	59,6807	70,0515	67,1258	75,1607	38,8153	47,1446	103,9237	116,7022
0.4	59,1402	68,4086	54,4920	64,2370	60,8529	68,3660	36,0674	43,8328	92,7270	104,5716
0.6	53,1704	61,9197	49,1182	58,2160	54,5040	61,3638	33,4097	40,5100	80,9517	91,8681
0.8	46,9467	55,1402	43,6384	52,0562	48,2820	54,3487	31,0468	37,3684	68,3472	78,3336
	Fourth Dimensionless Natural Frequency									
ξ	0	1	0	1	0	1	0	1	0	1
c										
0.0	130,0490	141,8780	120,4658	133,2153	131,6671	142,6761	81,5334	92,8279	188,8124	203,3541
0.2	118,3746	129,5187	109,6318	121,5255	119,0571	129,4717	74,1645	84,8189	170,3759	183,8451
0.4	106,1022	116,5530	98,3159	109,3551	105,9773	115,7431	66,6114	76,5931	151,0337	163,4493
0.6	92,9716	102,7256	86,3029	96,4957	92,2291	101,2892	58,8272	68,1010	130,3390	141,7317
0.8	78,5117	87,5678	73,2221	82,5771	77,2905	85,5800	50,9290	59,4466	107,3406	117,7477

Table 5.5 : Comparison of the first three dimensionless natural frequencies of the rotating beam [26,27,30,31,38,41,42,51,52].

		Lee (2018)	Lee (2020)	Adair (2018)	Adair (2018)	Banerjee (2006)	Wang (2004)	Ozdemir (2006)	Chen (2019)	Hodges (1981)	Present
λ	ψ										
0	1	3,8238	4,6252	3,8222	3,8238	3,8238	3,8238	3,8238	3,8238	3,8239	3,8238
	2	18,3173	19,5476	18,3171	18,3173	18,3173	18,3173	18,3173	18,3173	18,3254	18,3173
	3	47,2648	48,5789	47,2621	47,2648	47,2648	47,2648	47,2648	47,2648	47,4032	47,2648
1	1	3,9866	4,7641	3,9854	3,9867	3,9866	3,9866	3,9866	3,9866	3,9867	3,9866
	2	18,4740	19,6803	18,4698	18,4735	18,4740	18,4740	-	18,4740	18,4820	18,4740
	3	47,4173	48,7073	47,3441	47,4230	47,4173	47,4173	-	47,4173	47,5548	47,4173
2	1	4,4368	4,7641	4,4332	4,4351	4,4368	4,4368	4,4368	4,4368	4,4368	4,4368
	2	18,9366	19,6803	18,8914	18,9356	18,9366	18,9366	-	18,9366	18,9442	18,9366
	3	47,8716	48,7073	47,7691	47,8774	47,8717	47,8716	-	47,8716	48,0068	47,8716
3	1	5,0927	5,7458	5,0900	5,0919	5,0927	5,0927	5,0927	5,0927	5,0927	5,0927
	2	19,6839	20,7121	19,5330	19,6798	19,6839	19,6839	-	19,6839	19,6907	19,6839
	3	48,6190	49,7226	48,4372	48,5111	48,6190	48,6190	-	48,6190	48,7504	48,6190
4	1	5,8788	6,4726	5,8469	5,8501	5,8788	5,8788	5,8788	5,8788	5,8788	5,8788
	2	20,6852	21,5749	20,1343	20,6712	20,6851	20,6852	-	20,6852	20,6912	20,6852
	3	49,6456	50,5939	48,9895	49,5396	49,6456	49,6456	-	49,6456	49,7722	49,6456
5	1	6,7434	7,2901	6,7324	6,7379	6,7434	6,7434	-	6,7434	6,7434	6,7434
	2	21,9053	22,6360	21,6389	21,8813	21,9053	21,9053	-	21,9053	21,9105	21,9053
	3	50,9338	51,6918	50,4521	50,4987	50,9338	50,9338	-	50,9338	51,0548	50,9338
6	1	7,6551	8,1663	7,6411	7,6379	7,6551	7,6551	-	7,6551	7,6552	7,6551
	2	23,3093	23,8684	23,1111	23,2790	23,3093	23,3093	-	23,3093	23,3138	23,3093
	3	52,4633	53,0019	51,7892	51,8456	52,4632	52,4633	-	52,4633	52,5782	52,4633
7	1	8,5956	9,0804	8,5672	8,5411	8,5956	8,5956	-	8,5956	8,5957	8,5956
	2	24,8647	25,2461	23,8451	24,0245	24,8647	24,8647	-	24,8647	24,8686	24,8647
	3	54,2124	54,5081	53,6821	53,6771	54,2124	54,2124	-	54,2124	54,3213	54,2124
8	1	9,5540	10,0193	9,5234	9,5110	9,5540	9,5540	-	9,5540	9,5542	9,5540
	2	26,5437	26,7454	25,0677	25,3628	26,5437	26,5437	-	26,5437	26,5472	26,5437
	3	56,1595	56,1941	55,8329	55,4532	56,1595	56,1595	-	56,1595	56,2626	56,1595
9	1	10,5239	10,9747	10,4330	10,3920	10,5239	10,5239	-	10,5239	10,5244	10,5239
	2	28,3227	28,3459	27,3898	27,4089	28,3227	28,3227	-	28,3227	28,3261	28,3227
	3	58,2833	58,0433	57,7432	57,2333	58,2833	58,2833	-	58,2833	58,3813	58,2833
10	1	11,5015	11,9415	11,4010	11,3010	11,5015	11,5015	-	11,5015	11,5023	11,5015
	2	30,1827	30,0299	28,4492	28,4523	30,1827	30,1827	-	30,1827	30,1864	30,1827
	3	60,5639	60,0399	59,9782	59,0100	60,5639	60,5639	-	60,5639	60,6576	60,5639

5.2 Thermal Influences on Dynamic Characteristics

Functionally graded materials (FGMs) have garnered significant interest in various engineering applications due to their gradual variation in material properties, high thermal resistance, and so on. In the use of rotating beam structures such as turbofan engine components, it reduces thermal stresses while preventing the formation of thermal cracks or other probable failures without degradation in material properties. To understand their utilities and determine the best material combination, this section presents a free vibration analysis of FGM beam structures in thermal environments. In addition to previous section, the effects of material gradation and high temperatures on the structural dynamics are investigated.

Figure 5.15 illustrates the material gradation of a FGM beam. As seen, the outer layers of the beam are composed of ceramic material to exploit their high thermal resistance and insulation properties, which is especially beneficial in aerospace applications where surfaces are subjected to extreme temperatures. Moving into the inside of the structure, the shift from ceramic to metal provides greater structural strength and toughness.

Figure 5.15 : Material gradation through cross section of the beam made of FGM.

Meanwhile, the material properties of an FGM beam can be expressed by the power Law formula [258], which mathematically represents the gradation of properties from one material to another along thickness of the beam as:

$$P(z) = (P_c - P_m)\left|\frac{2z}{h}\right|^k + P_m \tag{5.24}$$

In Equation 5.24, engineers can tailor the spatial variation in material composition to optimize the beam's performance under specific loading and environmental conditions by adjusting the volume fraction index *k*. Meanwhile, the temperature-dependent material properties of an FGM beam can be described by utilizing a nonlinear function with coefficients P_i [259] as follows:

$$P(T) = P_0\left(P_{-1}T^{-1} + 1 + P_1T + P_2T^2 + P_3T^3\right) \tag{5.25}$$

Table 5.6 : Temperature-dependent coefficients of material properties for functionally graded material constituents [260-263].

Materials	Properties	P_0	P_{-1}	P_1	P_2	P_3
Al_2O_3 (Alumina)	*E (Pa)*	3,4955E+11	0	-3,853E-04	4,027E-07	-1,673E-10
	α (1/K)	6,8269E-06	0	1,838E-04	0	0
	k (W/mK)	14,087	1,123E-06	6,227E-03	0	0
	ν	0,26	0	0	0	0
	ρ (kg/m3)	3800	0	0	0	0
Si_3N_4 (Silicon Nitride)	*E (Pa)*	3,4843E+11	0	-3,070E-04	2,160E-07	-8,946E-11
	α (1/K)	5,8723E-06	0	9,095E-04	0	0
	k (W/mK)	13,723	0	-1,032E-03	5,466E-07	-7,876E-11
	ν	0,24	0	0	0	0
	ρ (kg/m3)	2370	0	0	0	0
ZrO_2 (Zirconia)	*E (Pa)*	2,4427E+11	0	-1,371E-03	1,214E-06	-3,681E-10
	α (1/K)	1,3300E-05	0	-1,421E-03	9,549E-07	0
	k (W/mK)	1,7	0	1,276E-04	6,648E-08	0
	ν	0,2882	0	1,133E-04	0	0
	ρ (kg/m3)	5680	0	0	0	0
CMSX-4 (Superalloy)	*E (Pa)*	1,7283E+11	-2,742E+01	-8,417E-04	8,064E-07	-3,635E-10
	α (1/K)	1,4593E-05	2,492E+02	4,500E-03	-4,446E-06	1,834E-09
	k (W/mK)	92,6	1,418E+02	2,700E-03	-2,238E-06	6,474E-10
	ν	0,1956	1,3458E+02	2,400E-03	-2,420E-06	8,564E-10
	ρ (kg/m3)	8914,8	-1,5197	-7,297E-05	4,444E-08	-2,107E-11
SUS304 (Stainless Steel)	*E (Pa)*	2,0100E+11	0	3,080E-04	-6,534E-07	0
	α (1/K)	1,2330E-05	0	8,086E-04	0	0
	k (W/mK)	15,379	0	-1,264E-03	2,092E-06	-7,223E-10
	ν	0,3262	0	-2,002E-04	3,797E-07	0
	ρ (kg/m3)	8166	0	0	0	0
Ti-6Al-4V (Titanium Alloy)	*E (Pa)*	1,2256E+11	0	-4,586E-04	0	0
	α (1/K)	7,5788E-06	0	6,638E-04	-3,147E-06	0
	k (W/mK)	1	0	1,704E-02	0	0
	ν	0,2884	0	1,121E-04	0	0
	ρ (kg/m3)	4429	0	0	0	0

By applying these formulations in Equations 5.24 and 5.25, the behavior of materials under various thermal conditions can be accurately characterized, providing an useful information for the structural analysis of components operating in severe thermal environments. Meanwhile, the temperature-dependent coefficients are given in Table

5.6, where each coefficient corresponds to a term in the polynomial expression in Equation 5.25 that defines how a specific material property varies with temperature. In the effect of temperature and volume fraction, the material properties in the thickness direction of the FGM beam can be presented in the concerning figures between Figure 5.16 and Figure 5.23.

These figures make clear the relationship between Young's modulus, the thermal expansion coefficient, Poisson's Ratio, and density against the volume fraction of the constituents over a range of temperatures. Each graph provides a visual interpretation of how these material properties vary under thermal influences and compositional changes, emphasizing the flexibility of FGMs to meet specific engineering demands. For instance, increasing the volume fraction index leads to a gradational shift in the material properties of the structure made of functionally graded material, such as a decrease in density, young modulus, and an increase in thermal expansion and Poisson ratio. In other words, this shift indicates a substantial change in the composite material's mechanical and thermal attributes. Simultaneously, increasing the operating temperature generally results in a decrease in young modulus and density and an increase in thermal expansion and Poisson ratio.

Among various FGM constituents of ceramics and metals in Table 5.7, the combination of Nickel Alloys and Zirconia is more appropriate for rotating beam structures exposed to elevated temperatures due to the low thermal conductivity and thermal expansion coefficient of Zirconia, which makes it an ideal coating material that can provide thermal barrier protection, while Nickel Alloys offer the necessary structural integrity at high operating temperatures typically encountered in high-pressure environment of turbofan engines. Such a combination would be particularly effective in applications requiring high-temperature resistance and structural stability that minimizes the development of thermal stresses due to small differential expansion difference when subjected to temperature changes.

Additionally, the temperature dependency of the material properties of FGM constituents for Zirconia and a Ni-based superalloy can be shown such as in Figure 5.24.

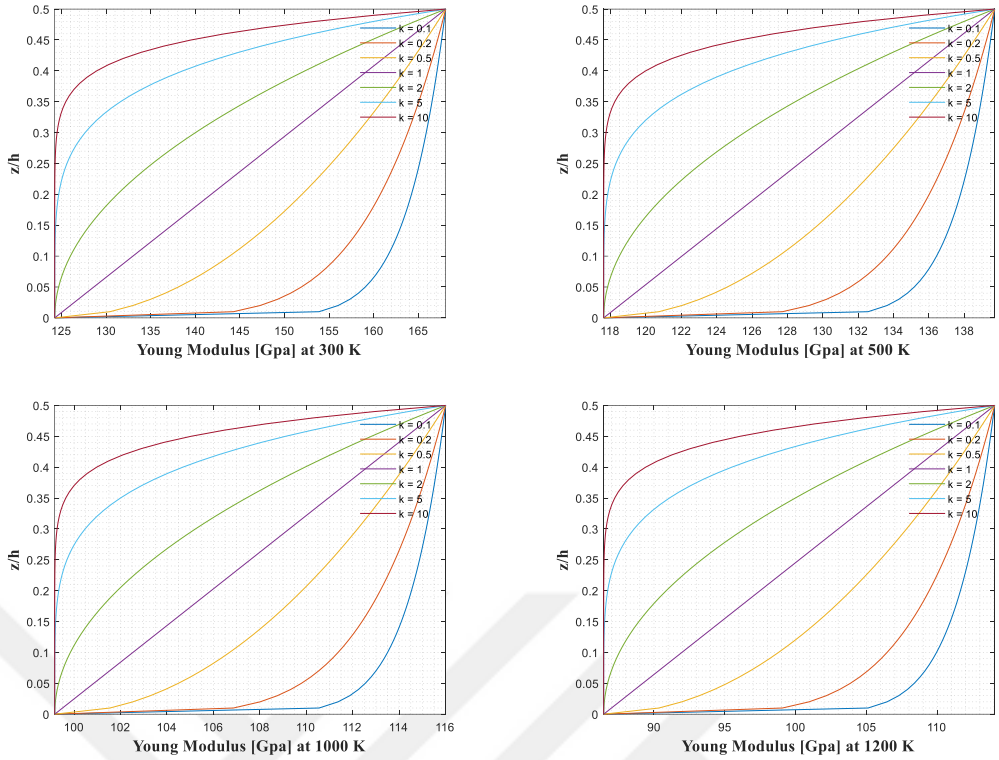

Figure 5.16 : Influence of temperature and volume fraction index on the Young's modulus in the thickness direction (CMSX-4 and Zirconia)

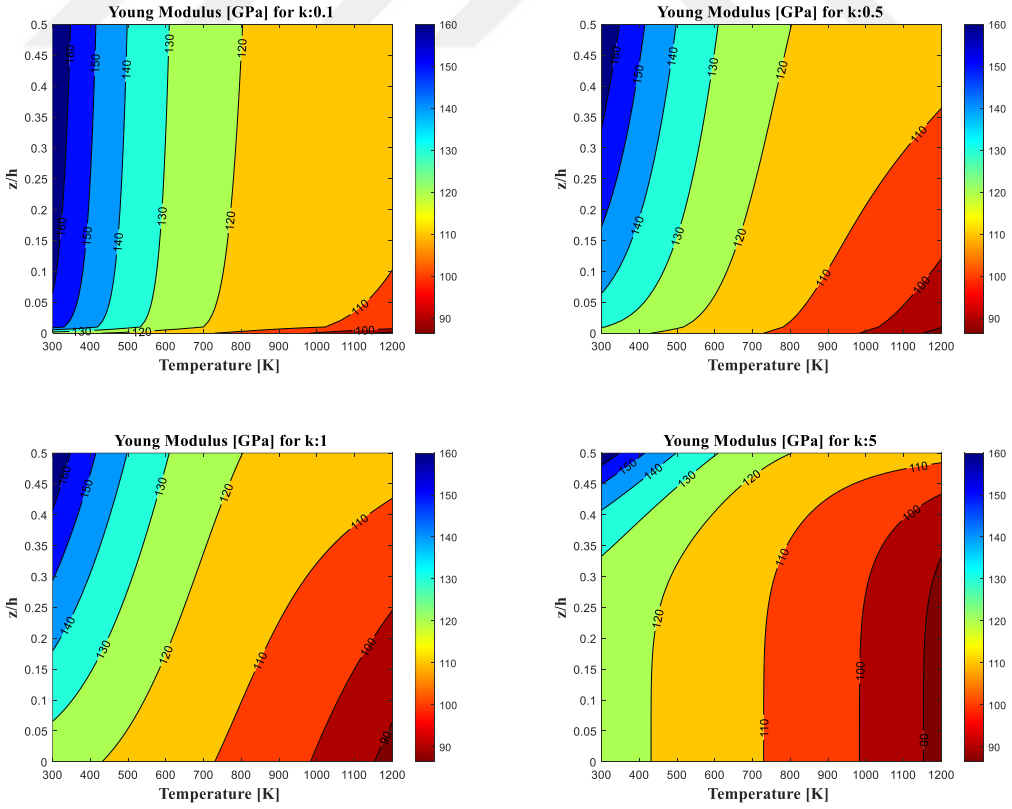

Figure 5.17 : Influence of temperature and volume fraction index on the Young modulus in the thickness direction (CMSX-4 and Zirconia)

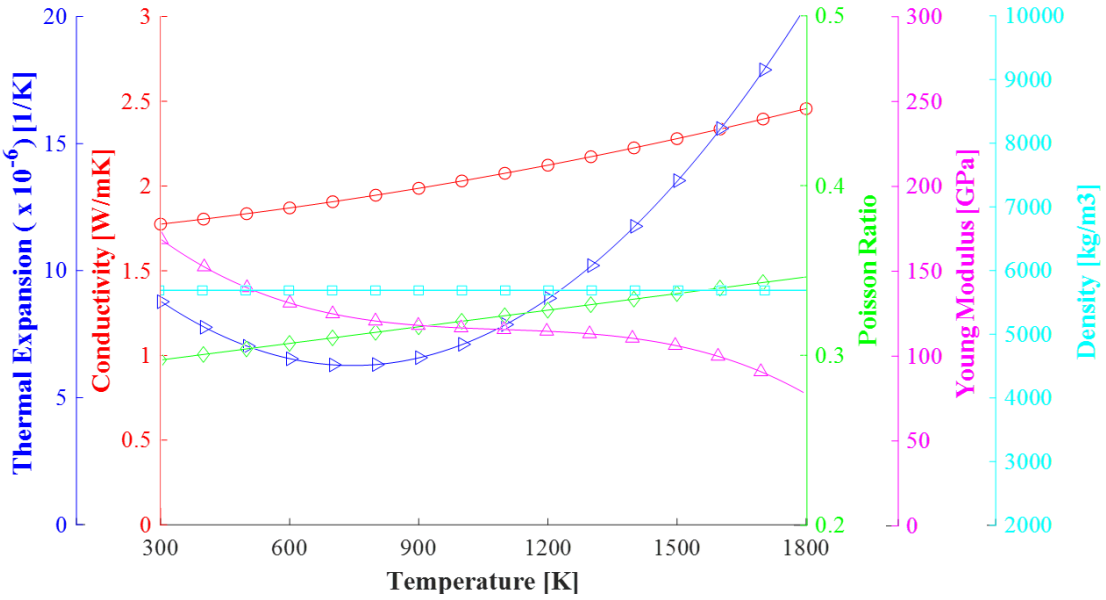

(a) Zirconia (ZrO_2)

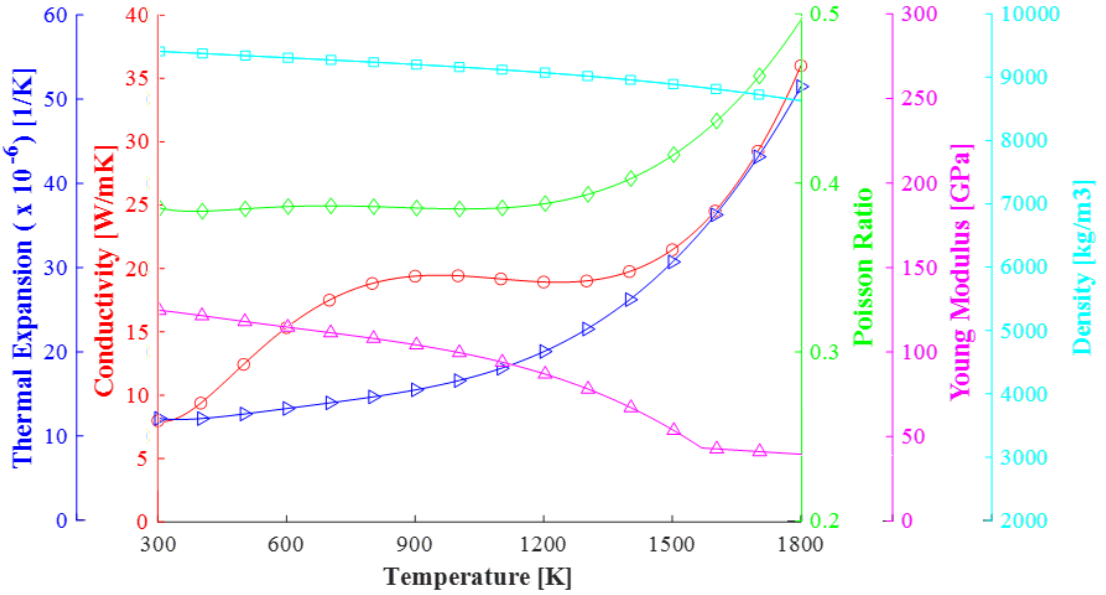

(b) Ni-Based Superalloy (CMSX4)

Figure 5.18 : Effect of temperature on material properties of functionally graded material constituents [262-264].

Table 5.7 : Thermophysical properties of ceramic and metal constituent of functionally graded materials [265].

	FGM Constituent	*Young Modulus [GPa]*	*Thermal Conductivity [W/mK]*	*Thermal Expansion Coefficient [1/K × 10^{-6}]*	*Density [kg/m^3]*
Ceramics	Zirconia	100–250	2.3–12.2	1.7–2.7	5000–6150
	Alumina	215–413	12–38.5	4.5–10.9	3500–3980
	Aluminum nitride	302–348	4.3–5.6	60–177	2920–3330
	Boron carbide	362–472	3.2–9.4	17–42	2350–2550
	Silicon	140–180	84–100	7–8	2280–2380
	Silicon carbide	90–137	7.9–11	3.8–20.7	4360–4840
	Silicon nitride	166–297	1.4–3.7	10–43	2370–3250
	Tungsten carbide	600–686	4.5–7.1	28–88	15250–15880
Metals	Cast Irons	80–150	40–72	11–13	6900–7350
	Stainless steels	189–203	12–25	16–18	7850–8100
	Aluminum alloys	68–82	76–240	21–24	2500–2900
	Copper alloys	112–148	160–390	16.2–21.6	8930–8940
	Lead alloys	12.5–15	23–44	19–29.3	10000–11400
	Magnesium alloys	42–47	50–160	25.2–27.1	1740–1950
	Nickel alloys	150–245	65–90	9–16	7750–8650
	Titanium alloys	90–120	7–15	8.4–9.36	4400–4800
	Zinc alloys	68–95	100–140	23–28	4950–7000

5.2.1 Equation of motion for fgm beam vibration thermal environment

Of the thermal structural problems discussed in Chapter 2, the exploration of the dynamic behavior of turbine blades in a high-temperature environment is important. The overall performance and safety of the blade structures in the high-pressure section is particularly more critical due to their direct exposure to extreme temperatures and high pressures. To understand their structural dynamics, the mathematical model of a rotating beam made of FGM is utilized for free vibration analysis of the blade in a thermal environment.

From the inlet fan to the exhaust nozzle, the material and temperature distribution at various sections of the turbofan engine can be seen in Figure 5.25. The inlet fan and LP & HP compressor stages are made predominantly of ferritic/austenitic steel and Ti-based alloys due to high-temperature strength properties and thermal fatigue resistance, which are exposed to temperatures ranging from 150-500°C. In the combustor and turbine sections, Ni-based superalloys such as CMSX-4 with thermal barrier coatings such as yttria-stabilized zirconia are preferred due to high-temperature strength and creep at elevated temperatures in the range of 500-1500°C.

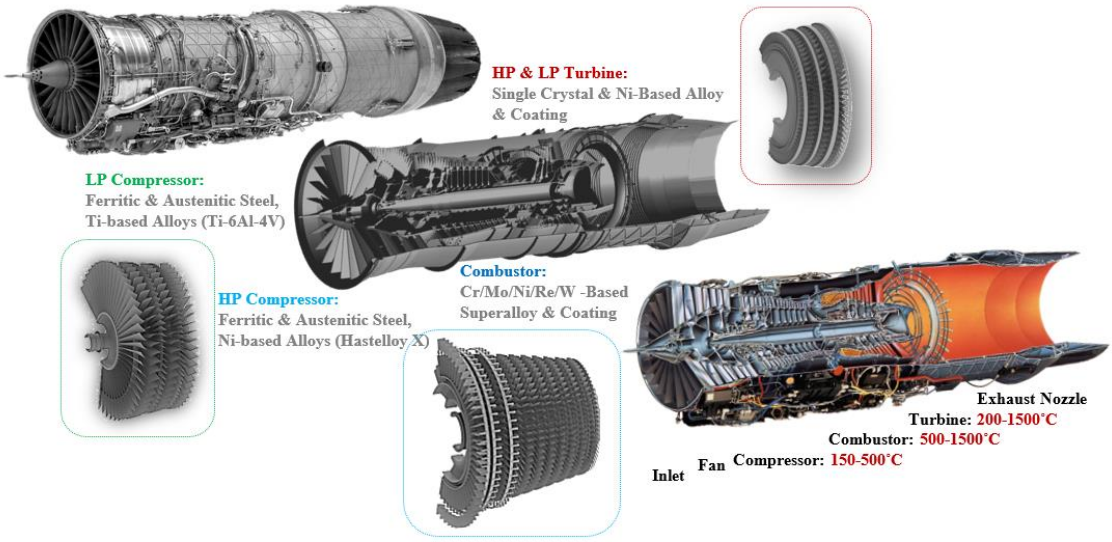

Figure 5.19 : Material and temperature distribution on the turbofan engine [266-269].

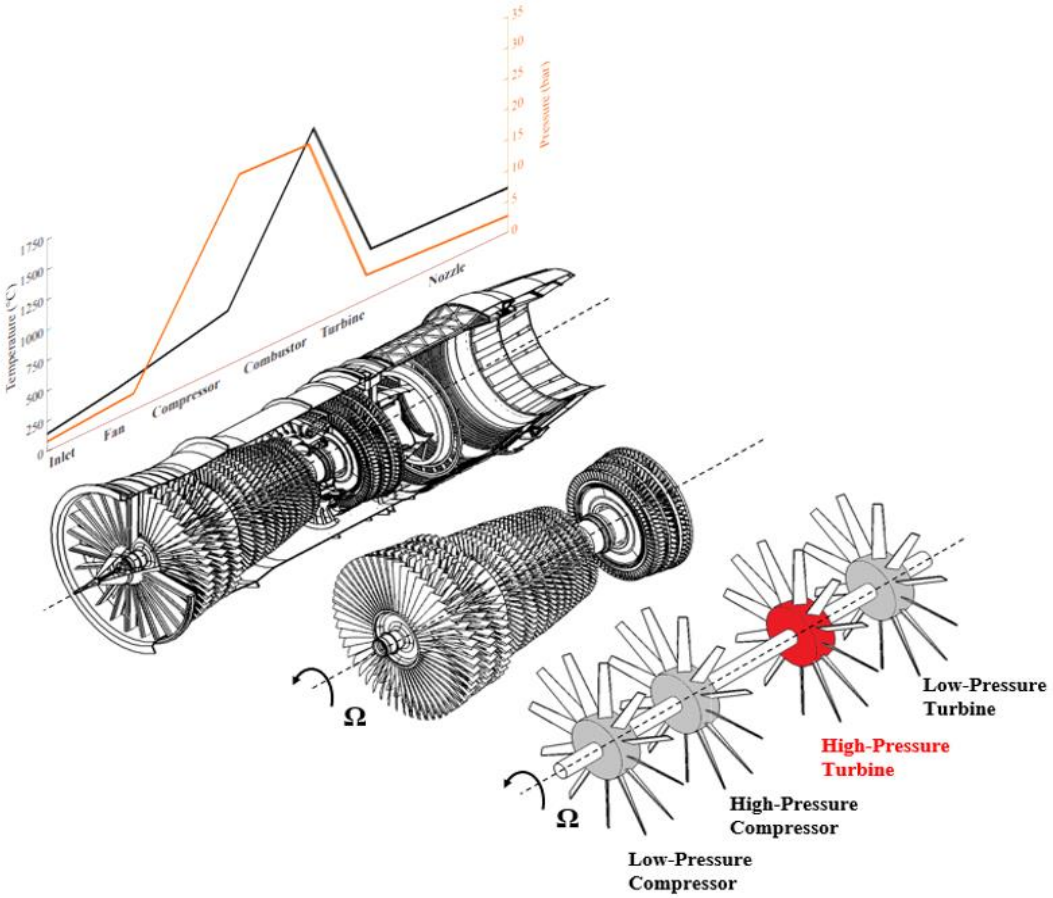

Figure 5.20 : Simplified View of a Rotating Blade in a Turbofan Engine [266-269].

Beam and shell theories are often used to model systems like those seen in Figure 5.25 because they are efficient at approximating complex geometries. Furthermore, the system's structural behaviors can be expressed using simpler analytical or numerical models, allowing engineers to predict the performance, stress distribution, and vibrational characteristics of such components with reasonable accuracy while keeping computational costs manageable. While beam theories offer simplicity and efficiency for slender blades primarily undergoing bending vibrations, shell theories provide a more detailed and accurate framework capable of capturing the complex vibrational behavior of thin blades, especially those with significant width or complex geometries. The choice between beam and shell theories for modeling vibrations in thin blades depends on the specific requirements for accuracy, computational resources, and the blade's geometric and material characteristics. For precise engineering applications, especially in aerospace and energy sectors, selecting the appropriate theoretical approach is critical for the design, analysis, and optimization of the blade structures exposed to elevated temperatures.

Higher-order shear beam theories used to reduce the rotating structure in Figure 5.26 can be preferred to shell theories while conducting vibration analysis of the blade due to computational efficiency, ease of implementation, adequate accuracy in predicting natural frequencies, and their ability to incorporate the effects of transverse shear and rotary inertia. A representation of the simplified blade's geometry, including its twist and the functional gradation of materials can be illustrated with a rotating pre-twisted beam structure such as in Figure 5.26. In addition to the previous model in Figure 5.2, the pretwist angle β along the spanwise axis of the beam is included to provide a more realistic assessment of the blade's vibrational characteristics. Also, a double symmetric cross-section is utilized to prevent the coupling of bending and torsional vibrations, by aligning the shear center directly with the cross-section's centroid axis which simplifies the vibration analysis. Simultaneously, the tapered design of the structure enhances the overall dynamic performance and stability by shifting the natural frequencies away from the operational frequency to avoid resonance and reduce the magnitude of vibrations at the free end of the blade. Using this idealized model, the preliminary design of the blades in each section can be performed quickly for various design parameters such as geometrical dimensions, temperature, rotation speed, and material distribution to achieve the desired vibrational characteristics.

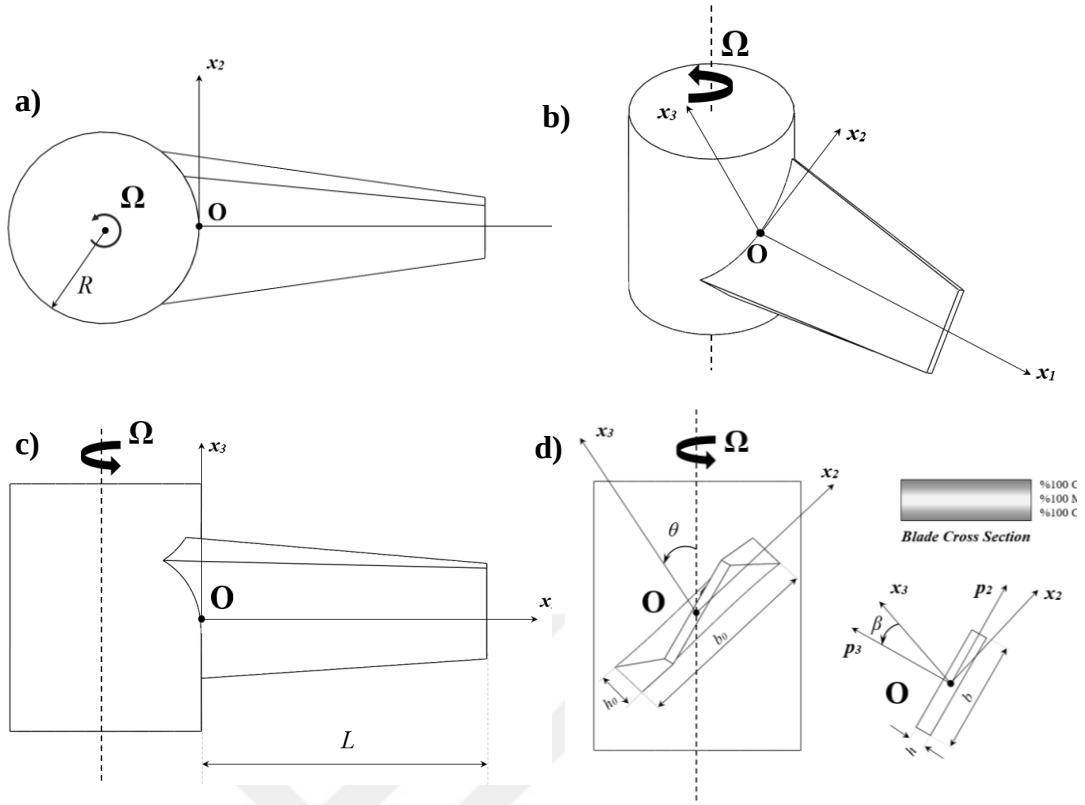

Figure 5.21 : Dimensions and axis system of the rotating pre-twisted functionally graded beam structure: a) Top view, b) Front view, c) Isometric view, d) Side view.

Each shear deformation beam theory provides a set of assumptions and mathematical formulations representing the transverse shear strain and stress through the thickness of the beam structure. These formulations are essential for predicting deflection, vibration characteristics, and stress distribution where classical theories may not be adequate. Shear deformations in higher-order beam theories are expressed by utilizing the following shape functions [270-272]:

$$
\begin{aligned}
&\text{CBT} && : \quad \Psi(z) = 0 \\
&\text{FSDBT} && : \quad \Psi(z) = z \\
&\text{PSDBT} && : \quad \Psi(z) = z\left(1 - \frac{4z^2}{3h^2}\right) \\
&\text{ESDBT} && : \quad \Psi(z) = z\, e^{-2(z/h)^2} \\
&\text{HSDBT} && : \quad \Psi(z) = h\sinh\left(\frac{z}{h}\right) - z\cosh\left(\frac{1}{2}\right) \\
&\text{TSDBT} && : \quad \Psi(z) = \frac{h}{\pi}\sin\left(\pi\frac{z}{h}\right)
\end{aligned}
\tag{5.26}
$$

These shape functions are derived to satisfy the governing differential equations of motion and boundary conditions, taking into account continuity requirements and the physical constraints of the material, which reflect the non-linear distribution of shear across the cross-section of the beam. Among these shape functions, functions given for CBT and FSDBT are used to derive the equation of motion.

The kinematics of the deformation concerning beam theories can be expressed by choosing the proper shape functions given in Equation 5.26. As seen in Figure 5.28, the total rotation of the beam cross-section is equal to the sum of shear distortion and bending rotation. In contrast to the CBT, in which plane cross sections remain plane after deformation, a cross-section of a beam in FSBDT is allowed to undergo additional deformation modes, such as warping and distortion, providing a more accurate representation of the actual behavior of beams under various loading conditions so that the need for a shear correction factor can be eliminated [273].

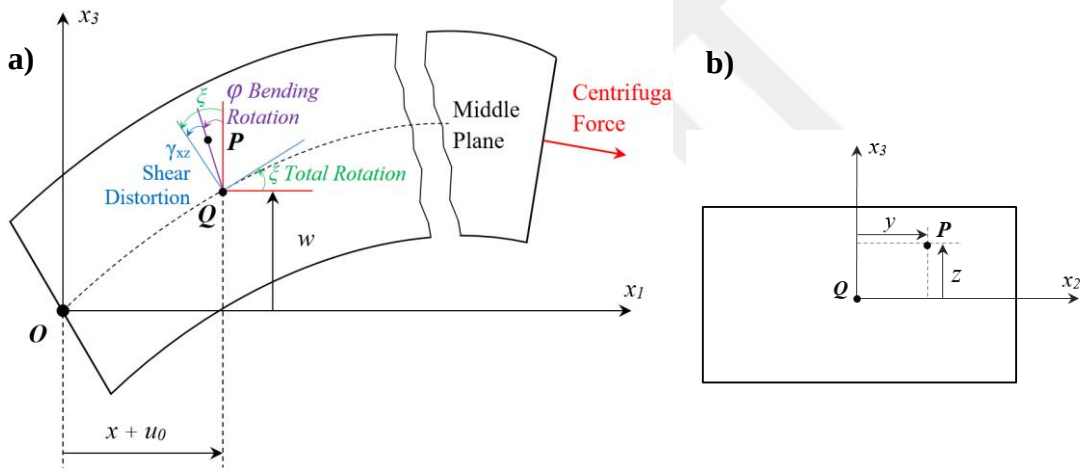

Figure 5.22 : Kinematics of the deformed rotating beam structures: a) Longitudinal view, b) Cross-sectional view [29,70].

Here, the infinitesimal axial and transverse displacement of the point Q along the x_1 and x_3 directions are represented by u_0 and w_0 for the steady state deformations while the displacement components along the x_1, x_2, and x_3 directions are demonstrated by u, v, and w, respectively. Based on the beam theories, the displacement of the considered rotating beam in Figure 5.28 can be expressed as the axial displacement and the transverse displacement at arbitrary point P and the point Q on the centroid axis on the cross-section.

To derive the kinematic relations and governing equations for rotating FGM beam structures in a thermal environment, we must make a few assumptions. To begin, we

assume that the beam encounters tiny deformations, allowing us to apply linear elasticity theory (Generalized Hooke's Law) to displacements substantially smaller than the beam's length in the x_1-x_3 plane. Secondly, the beam is considered to be slender, implying that the length is much greater than the other dimensions and that the deformation is primarily in the plane perpendicular to the beam's longitudinal axis. This approach allows for a simplified beam model to represent a rotating blade structure like in Figure 5.26, avoiding the need for shell models. Third, we want a doubly symmetric cross-section with two principal axes to avoid coupling between bending and torsional vibrations. This structural design ensures that the cross-section's shear center and centroid axis coincide, which simplifies the beam's behavior under combined stress circumstances.

Furthermore, adopting a doubly symmetric cross-section allows for a more accurate description of the beam's reaction to torsional loads, making it an appropriate choice for rotating beam structures rather than shell structures in a spinning blade. In addition, we use a tapered design to improve the beam's mass distribution, resulting in a high rigidity mass ratio. We change the mass distribution throughout the beam's length to increase stiffness, improve dynamic efficiency, and reduce overall mass. Fourth, we assume that the shaft carrying the blade is rigid, so we may neglect bending and torsional vibration. This assumption simplifies the model by focusing simply on the dynamics of the rotating blade, ignoring the interactions between the blade and a flexible shaft. In addition to these assumptions, it is further assumed that the isotropic material properties of the FGM beam are temperature dependent expressed as a nonlinear function in Equation 5.24, and vary continuously through its thickness to power law in Equation 5.25. Finally, the thermal effects are included, assuming that the temperature distribution across the thickness and along the longitudinal axis of the beam is uniform. This assumption simplifies the governing equations describing the dynamic behavior of the beam.

To perform the vibration analysis under the aforementioned assumptions, the thermoelastic constitutive equation for an isotropic FGM beam can be expressed by using the generalized Hooke's law as follows :

$$\begin{Bmatrix} \sigma_{xx} \\ \tau_{xz} \end{Bmatrix} = \begin{bmatrix} Q_{11} & 0 \\ 0 & Q_{55} \end{bmatrix} \begin{Bmatrix} \varepsilon_{xx} \\ \gamma_{xz} \end{Bmatrix} - \begin{bmatrix} \hat{\alpha}(z,T)\Delta T(x,z) \\ 0 \end{bmatrix} \tag{5.27}$$

where uniform temperature difference along the axis of the beam and through the thickness is equal to $\Delta T(x,z) = T(x,z) - T_0$, the transformed stiffness constants in the beam's local coordinate system and the modified thermal expansion coefficient can be given as:

$$Q_{11} = \frac{E(z,T)}{1-\upsilon^2(z,T)}, \qquad Q_{55} = \frac{E(z,T)}{2\left(1+\upsilon(z,T)\right)}, \qquad \hat{\alpha} = \frac{E(z,T)}{1-\upsilon(z,T)}\alpha(z,T)$$

Here, E and v denote the temperature-dependent and composition-dependent Elasticity modulus and Poisson's ratio, respectively. Meanwhile, the axial and shear strain terms in the constitutive equation are directly related to the displacement field, which describes the deformation of the rotating pre-twisted beam made of FGM under a uniform temperature distribution. To express strain terms, the following relations [70] are employed for CBT and FSDBT, respectively:

$$\begin{aligned} \varepsilon_{xx} &= \frac{du_0}{dx} - z\frac{\partial^2 w}{\partial x^2} + \frac{1}{2}\left(\frac{\partial w}{\partial x}\right)^2, \gamma_{xz} = 0 \\ \varepsilon_{xx} &= \frac{du_0}{dx} - z\frac{\partial \varphi}{\partial x} + \frac{1}{2}\left(\frac{\partial w}{\partial x}\right)^2, \gamma_{xz} = \frac{\partial w}{\partial x} - \varphi \end{aligned} \tag{5.28}$$

In these kinematic relations, the uniform strain ε_0 term due to centrifugal force in a rotating beam can be calculated based on the beam's geometry, material properties, and constant rotational speed, neglecting Coriolis effects.

The uniform strain ε_0 associated with the steady-state axial displacement u_0 of a rotating beam can be expressed as:

$$\varepsilon_0 = \frac{du_0}{dx} = \frac{F_{cent}(x)}{\int_A E(z,T)\,dA} = \hat{F}_{cent} \tag{5.29}$$

Here, the centrifugal force acting on the beam, considering the varying material properties across the thickness, may be expressed as follows:

$$F_{cent}(x) = \int_A \int_x^L \rho(z,T)\,\Omega^2(R+x)\,dx\,dA \tag{5.30}$$

where *dA* represents a differential cross-sectional area, and ρ denotes the material density. The rotational speed vector $\vec{\Omega}$ in the beam axis system to the setting angle θ and pre-twist angle β can be expressed as follows:

$$\vec{\Omega} = \Omega \sin(\theta + \frac{x}{L}\beta)\vec{j} + \Omega \cos(\theta + \frac{x}{L}\beta)\vec{k} \tag{5.31}$$

Here, *j* and *k* are unit vectors in the direction of x_2 and x_3 axes, respectively. Substituting these expressions into axial strain terms, the strain energy can be written in terms of rotation speed, centrifugal force, displacement, and shear distortion. Then, the governing equations can be derived by means of The Hamiltonian approach in Equation 5.32.

$$\int_{t_1}^{t_2} \left(\delta \Im - \delta U\right) dt = 0 \tag{5.32}$$

where δ denotes the variation, $\boldsymbol{\Im}$ is the kinetic energy of the beam due to rotational and translational motions, and $\boldsymbol{U}$ is the total potential energy due to mechanical strain and thermal effects. These energy terms can be written as follows:

$$\Im = \frac{1}{2}\int_0^L \int_A \rho(z;T)\left(V_x^2 + V_y^2 + V_z^2\right) dA dx \tag{5.33}$$

$$U = \frac{1}{2}\int_0^L \int_A \left(\sigma_{xx}\varepsilon_{xx} + \tau_{xz}\gamma_{xz}\right) dA dx \tag{5.34}$$

In the kinetic energy expression given in Equation 5.33, the components of the velocity vector in the local coordinates can be derived from the following total velocity vector expression with respect to position and rotation vectors:

$$\vec{V} = \frac{\partial \vec{r}}{\partial t} + \overrightarrow{\Omega} \times \vec{r} = V_x\vec{i} + V_y\vec{j} + V_z\vec{k} \tag{5.35}$$

where $\vec{r}$ denotes the position vector after deformation and is given as:

$$\begin{aligned} \vec{r}^{\,E} &= \left\{R + x + u_0(x) - z\frac{\partial w(x;t)}{\partial x}\right\}\vec{i} + y\vec{j} + \left\{w(x;t) + z\right\}\vec{k} \\ \vec{r}^{\,T} &= \left\{R + x + u_0(x) - z\,\varphi(x;t)\right\}\vec{i} + y\vec{j} + \left\{w(x;t) + z\right\}\vec{k} \end{aligned} \tag{5.36}$$

By substituting the derivative of the position vector with respect to time and the cross product of the rotational speed and position vectors into the total velocity vector in Equation 5.35, the velocity components of the deformed rotating beam for CBT (Classical Beam Theory or Euler-Bernoulli Beam Theory) and FSDBT (First Order Shear Deformation Beam Theory or Timoshenko Beam Theory) can be obtained as follows:

$$
\begin{aligned}
V_x^E &= \Omega\sin(\mu)\{w(x;t)+z\}-\Omega\cos(\mu)\,y-z\frac{\partial^2 w(x;t)}{\partial x\partial t}\\
V_y^E &= \Omega\cos(\mu)\left\{R+x+u_0(x)-z\frac{\partial w(x;t)}{\partial x}\right\}\\
V_z^E &= -\Omega\sin(\mu)\left\{R+x+u_0(x)-z\frac{\partial w(x;t)}{\partial x}\right\}+\frac{\partial w(x;t)}{\partial t}\\
V_x^T &= \Omega\sin(\mu)\{w(x;t)+z\}-\Omega\cos(\mu)\,y-z\frac{\partial \varphi(x;t)}{\partial t}\\
V_y^T &= \Omega\cos(\mu)\{R+x+u_0(x)-z\,\varphi(x;t)\}\\
V_z^T &= -\Omega\sin(\mu)\{R+x+u_0(x)-z\,\varphi(x;t)\}+\frac{\partial w(x;t)}{\partial t}
\end{aligned}
\tag{5.37}
$$

In these velocity components, any term in the velocity expression that does not depend on time is neglected in kinetic energy expression in Equation 5.38, because it does not represent a change in motion and does not contribute to kinetic energy. Moreover, Hodges's ordering scheme [274] is used to eliminate the higher order and nonlinear terms overcomplicating the kinetic energy expression. Then, the kinetic energy expressions resulting from both rotational and flapwise translational motion of the beam can be reformulated by using Equation 5.37 and canceling negligible small terms as:

$$
\begin{aligned}
\Im^E = \frac{1}{2}\int_0^L \Big\{ & I_0\left\{\Omega^2\sin^2(\mu)\,w^2+\dot{w}^2-2\Omega\sin(\mu)\{R+x+u_0\}\,\dot{w}\right\}\\
& +I_1\left\{2\Omega\sin(\mu)\,w_{,x}\dot{w}+2\Omega^2\sin^2(\mu)\,w-2\Omega^2\{R+x+u_0\}\,w_{,x}\right.\\
& \left.-2\Omega\sin(\mu)\,w\,\dot{w}_{,x}\right\}+I_2\left\{\dot{w}_{,x}^2-2\,\Omega\sin(\mu)\,\dot{w}_{,x}+\Omega^2 w_{,x}^2\right\}\Big\}\,dx+E_1
\end{aligned}
\tag{5.38}
$$

$$\mathfrak{I}^T = \frac{1}{2}\int_0^L \int_A \rho(z;T)\left\{\Omega^2 \sin^2(\mu) w^2 + z^2\dot{\varphi}^2 + 2\Omega^2 \sin^2(\mu) w z + \Omega^2 z^2 \varphi^2 \right.$$
$$+ \dot{w}^2 - 2\Omega \sin(\mu) w z\dot{\varphi} - 2\Omega \sin(\mu) z^2\dot{\varphi} - 2\Omega^2 \{R + x + u_0\} z\varphi$$
$$\left. -2\Omega \sin(\mu)\{R + x + u_0\}\dot{w} + 2\Omega \sin(\mu) z\varphi\dot{w}\right\} dAdx + T_1$$

where $\zeta = \theta + \frac{x}{L}\beta$, and superscript *dot* and subscript *x* means differentiation with respect time and spanwise motion, respectively.

The kinetic energy $\mathfrak{I}$ of the rotating beam at any instant time in the local cartesian coordinates can also be expressed by using the inertial coefficients as:

$$\mathfrak{I}^E = \frac{1}{2}\int_0^L \left\{ I_0 \left\{\Omega^2 \sin^2(\mu) w^2 + \dot{w}^2 - 2\Omega \sin(\mu)\{R + x + u_0\}\dot{w}\right\}\right.$$
$$+ I_1\left\{2\Omega \sin(\mu) w_{,x}\dot{w} + 2\Omega^2 \sin^2(\mu) w - 2\Omega^2\{R + x + u_0\} w_{,x}\right.$$
$$\left.\left. - 2\Omega \sin(\mu) w\dot{w}_{,x}\right\} + I_2\left\{\dot{w}_{,x}^2 - 2\Omega \sin(\mu)\dot{w}_{,x} + \Omega^2 w_{,x}^2\right\}\right\} dx + E_1$$
$$\mathfrak{I}^T = \frac{1}{2}\int_0^L \left\{ I_0 \left\{\Omega^2 \sin^2(\mu) w^2 - 2\Omega \sin(\mu)\{R + x + u_0\}\dot{w} + \dot{w}^2\right\}\right. \quad (5.39)$$
$$+ I_1\left\{2\Omega^2 \sin^2(\mu) w - 2\Omega \sin(\mu) w\dot{\varphi} - 2\Omega^2\{R + x + u_0\}\varphi\right.$$
$$\left.\left. + 2\Omega \sin(\mu)\varphi\dot{w}\right\} + I_2\left\{\dot{\varphi}^2 + \Omega^2\varphi^2 - 2\Omega \sin(\mu)\dot{\varphi}\right\}\right\} dx + T_1$$

The inertial coefficients or the mass moment of inertias in Equation (5.39) are defined for structures made of functionally graded materials as follows:

$$\left[I_0, I_1, I_2\right] = \int_{-b/2}^{b/2}\int_{-h/2}^{h/2} \rho(z,T)\left[1, z, z^2\right] dz\, dy \quad (5.40)$$

where the breadth and height of the beam can be written in terms of taper ratios c_b and c_h as:

$$b = b(x) = b_0\left(1 - c_b\frac{x}{L}\right),\ h = h(x) = h_0\left(1 - c_h\frac{x}{L}\right)$$

The potential energy expression given in Equation 5.34 can be rewritten in terms of extensional, coupling, and bending rigidities by substituting the axial and shear stresses provided in Equation 5.27 and strain expressions in Equation 5.28 as follows:

$$U^E = \frac{1}{2}\int_0^L \left\{ -2\frac{A_{12}}{A_{11}} F_{cent} w_{,xx} + F_{cent} w_{,x}^2 + A_{13}\, w_{,xx}^2 - A_{12}\, w_{,xx} w_{,x}^2 + \frac{1}{4} A_{11} w_{,x}^4 \right.$$
$$\left. + B_{12} w_{,xx} - \frac{1}{2} B_{11} w_{,x}^2 \right\} dx + E_2$$

$$U^T = \frac{1}{2}\int_0^L \left\{ -2\frac{A_{12}}{A_{11}} F_{cent}\, \varphi_{,x} + F_{cent} w_{,x}^2 + A_{13}\varphi_{,x}^2 - A_{12}\varphi_{,x} w_{,x}^2 + \frac{1}{4} A_{11} w_{,x}^4 + B_{12}\varphi_{,x} \right.$$
$$\left. - \frac{1}{2} B_{11} w_{,x}^2 + C_{11} w_x^2 - 2C_{11} w_x \varphi + C_{11}\varphi^2 \right\} dx + T_2 \tag{5.41}$$

In potential energy expression, the rigidities are defined as follows:

$$\left[A_{11}, A_{12}, A_{13}\right] = \int_{-b/2}^{b/2}\int_{-h/2}^{h/2} \left[Q_{11}, Q_{11} z, Q_{11} z^2\right] dz\, dy,$$
$$\left[B_{11}, B_{12}, B_{13}\right] = \int_{-b/2}^{b/2}\int_{-h/2}^{h/2} \left[\hat{\alpha}, \hat{\alpha}\, z, \hat{\alpha} z^2\right] \Delta T dz\, dy, \tag{5.42}$$
$$\left[C_{11}, C_{12}, C_{13}\right] = \int_{-b/2}^{b/2}\int_{-h/2}^{h/2} \left[Q_{55}, Q_{55} z, Q_{55} z^2\right] dz\, dy,$$

If these expressions are substituted into Hamilton's principle expression in Equation (5.32), the governing differential equations for rotating Euler and Timoshenko beams undergoing flapwise bending vibration can be given as:

$$I_0 \ddot{w} - I_0 \Omega^2 \sin^2(\mu) w + 2I_1 \Omega \sin(\mu) \dot{w}_{,x} + \frac{\partial}{\partial x}\left(2I_1 \Omega \sin(\mu) \dot{w} + I_2 \Omega^2 w_{,x}\right.$$
$$\left. - F_{cent} w_{,x} - I_2 \ddot{w}_{,x} + \frac{1}{2} B_{11} w_{,x}\right) + \frac{\partial^2}{\partial x^2}\left(A_{13}\, w_{,xx}\right) = 0 \tag{5.43}$$

$$I_0 \Omega^2 \sin^2(\mu) w - \Omega I_1 \sin(\mu) \dot{\varphi} - I_0 \ddot{w} - I_1 \Omega \sin(\mu) \dot{\varphi}$$
$$+ \frac{\partial}{\partial x}\left(F_{cent} w_x - \frac{1}{2} B_{11} w_x + C_{11} w_x - C_{11}\varphi\right) = 0$$
$$2I_1 \Omega \sin(\mu) \dot{w} + I_2 \Omega^2 \varphi + C_{11} w_{,x} - C_{11}\varphi - I_2 \ddot{\varphi} + \frac{\partial}{\partial x}\left(A_{13}\varphi_{,x}\right) = 0 \tag{5.44}$$

Employing Hamiltonian principle, the equations for the boundary conditions at $x = 0$ and $x = L$ can also be derived. As is known, these conditions ensure that the derived equations of motion are physically meaningful and accurately describe the behavior of

the beam under the given constraints. Obtaining nondimensional equations and discretized governing equations is similar to the processes discussed in the previous section. Therefore, they are skipped in this part of the study, and the approximate results of the numerical solution will be given in relation to tables and figures.

5.2.2 Numerical results and discussion

The effect of hub radius, twist angle, rotation speed, taper ratios, and flexible constraints on the structural dynamics of rotating beam structures have been investigated in the previous section. Therefore, similar results are shared again. Differently from these design parameters, the effect of shear deformation, slenderness ratio, temperature-dependent material properties, elevated temperatures, material distribution, and rotation speed on the vibration characteristics of rotating FGM beam structures is studied in this section. For the following nondimensional frequency and rotation speed parameters in Equation (5.45), the numerical results obtained by employing DQM are tabulated and plotted in the concerning Figures and Tables to understand the effects of these design parameters on the structural dynamics of rotating structures exposed to high temperatures.

$$\psi = \frac{\omega L^2}{h}\sqrt{\frac{\rho_m}{E_m}} \text{ and } \lambda = \Omega L^2\sqrt{\frac{I_0}{A_{13}}} \tag{5.45}$$

The effect of gradiation index, rotation speed, and shear deformation on the fundamental frequencies are demonstrated in Table 5.8-5 and Appendix C for different slenderness ratios and uniform temperatures. Then, the effect of slenderness ratio on NNFs is explored for constant rotation speed and temperatures in Figures 5.23-5.24, and Appendix D. Moreover, comparison of natural frequencies to chosen beam theory is depicted for increasing gradiation index in Figures 5.25- 5.26, and Appendix E. Ultimately, the relation between rotation speed and NNFs, and the variation of NNFs to increasing temperatures are are shown in Figures 5.27-5.28, and Figures 5.29-5.30, respectively. Other data illustrating the relation between rotation speed, temperature, and shear deformation are given in Appendices F and G.

Table 5.8 : Variations of the fundamental frequencies of rotating FGM beams to rotation speed, and material distribution ($L/h=5$, $c_b=c_h=0$, $\mu=0$, $\zeta=0$, $T=300^oK$)

Fundamental Natural Freqeuncies

First Dimensionless Natural Frequency

	CBT	FSDBT	CBT	FSDBT	CBT	FSDBT	CBT	FSDBT	CBT	FSDBT
λ	*k = 0*	*k = 0*	*k = 1*	*k = 1*	*k = 10*	*k = 10*	*k = 100*	*k = 100*	*Metal*	*Metal*
0	1,5310	1,0660	1,3252	1,0660	1,1520	1,0660	1,1065	1,0660	1,1003	1,0660
2	1,8021	1,2570	1,5599	1,2570	1,3560	1,2570	1,3024	1,2570	1,2952	1,2570
4	2,4334	1,6986	2,1062	1,6986	1,8310	1,6986	1,7587	1,6986	1,7489	1,6986
6	3,2072	2,2360	2,7759	2,2360	2,4132	2,2360	2,3179	2,2360	2,3050	2,2360
8	4,0333	2,8075	3,4910	2,8075	3,0349	2,8075	2,9150	2,8075	2,8987	2,8075
10	4,8806	3,3930	4,2245	3,3930	3,6724	3,3930	3,5274	3,3930	3,5077	3,3930

Second Dimensionless Natural Frequency

	CBT	FSDBT	CBT	FSDBT	CBT	FSDBT	CBT	FSDBT	CBT	FSDBT
λ	*k = 0*	*k = 0*	*k = 1*	*k = 1*	*k = 10*	*k = 10*	*k = 100*	*k = 100*	*Metal*	*Metal*
0	9,5946	5,7174	8,3051	5,7174	7,2196	5,7174	6,9343	5,7174	6,8955	5,7174
2	9,8456	5,9096	8,5226	5,9096	7,4086	5,9096	7,1157	5,9096	7,0759	5,9096
4	10,5632	6,4505	9,1441	6,4505	7,9488	6,4505	7,6344	6,4505	7,5917	6,4505
6	11,6612	7,2586	10,0952	7,2586	8,7752	7,2586	8,4280	7,2586	8,3808	7,2586
8	13,0420	8,2506	11,2909	8,2506	9,8144	8,2506	9,4259	8,2506	9,3731	8,2506
10	14,6224	9,3630	12,6596	9,3630	11,0039	9,3630	10,5682	9,3630	10,5090	9,3630

Third Dimensionless Natural Frequency

	CBT	FSDBT	CBT	FSDBT	CBT	FSDBT	CBT	FSDBT	CBT	FSDBT
λ	*k = 0*	*k = 0*	*k = 1*	*k = 1*	*k = 10*	*k = 10*	*k = 100*	*k = 100*	*Metal*	*Metal*
0	26,8650	13,5672	23,2545	13,5672	20,2152	13,5672	19,4161	13,5672	19,3076	13,5672
2	27,1137	13,7912	23,4700	13,7912	20,4024	13,7912	19,5958	13,7912	19,4863	13,7912
4	27,8449	14,4367	24,1035	14,4367	20,9529	14,4367	20,1244	14,4367	20,0119	14,4367
6	29,0185	15,4371	25,1202	15,4371	21,8363	15,4371	20,9725	15,4371	20,8553	15,4371
8	30,5777	16,7109	26,4710	16,7109	23,0100	16,7109	22,0995	16,7109	21,9759	16,7109
10	32,4605	18,1832	28,1020	18,1832	24,4273	18,1832	23,4603	18,1832	23,3290	18,1832

Fourth Dimensionless Natural Frequency

	CBT	FSDBT	CBT	FSDBT	CBT	FSDBT	CBT	FSDBT	CBT	FSDBT
λ	*k = 0*	*k = 0*	*k = 1*	*k = 1*	*k = 10*	*k = 10*	*k = 100*	*k = 100*	*Metal*	*Metal*
0	52,6448	22,4708	45,5696	22,4708	39,6137	22,4708	38,0479	22,4708	37,8353	22,4708
2	52,9014	22,7452	45,7920	22,7452	39,8069	22,7452	38,2333	22,7452	38,0197	22,7452
4	53,6629	23,5413	46,4517	23,5413	40,3802	23,5413	38,7837	23,5413	38,5669	23,5413
6	54,9053	24,7881	47,5282	24,7881	41,3155	24,7881	39,6817	24,7881	39,4599	24,7881
8	56,5924	26,3941	48,9899	26,3941	42,5855	26,3941	40,9011	26,3941	40,6724	26,3941
10	58,6799	28,2680	50,7985	28,2680	44,1570	28,2680	42,4099	28,2680	42,1727	28,2680

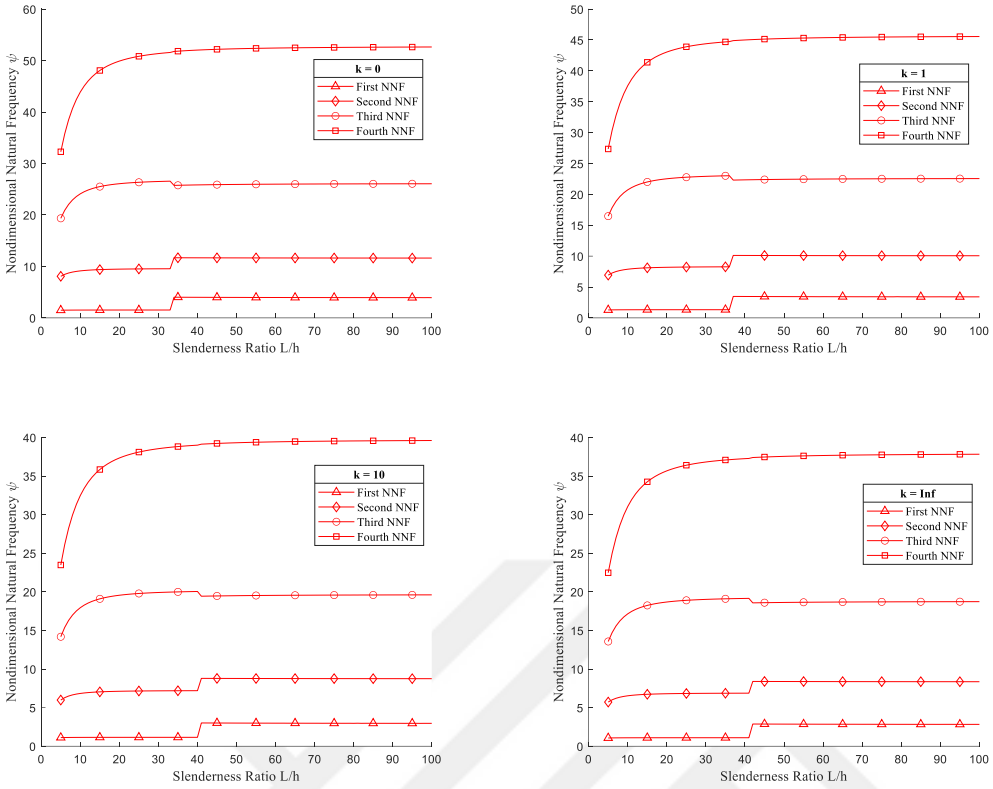

Figure 5.23 : Variation of first four NNF of Timoshenko beam with slenderness ratio *L/h* ($\lambda = 0$, $c_b=c_h=0$, $\mu=0$, $\xi=0$, $T=300^oK$).

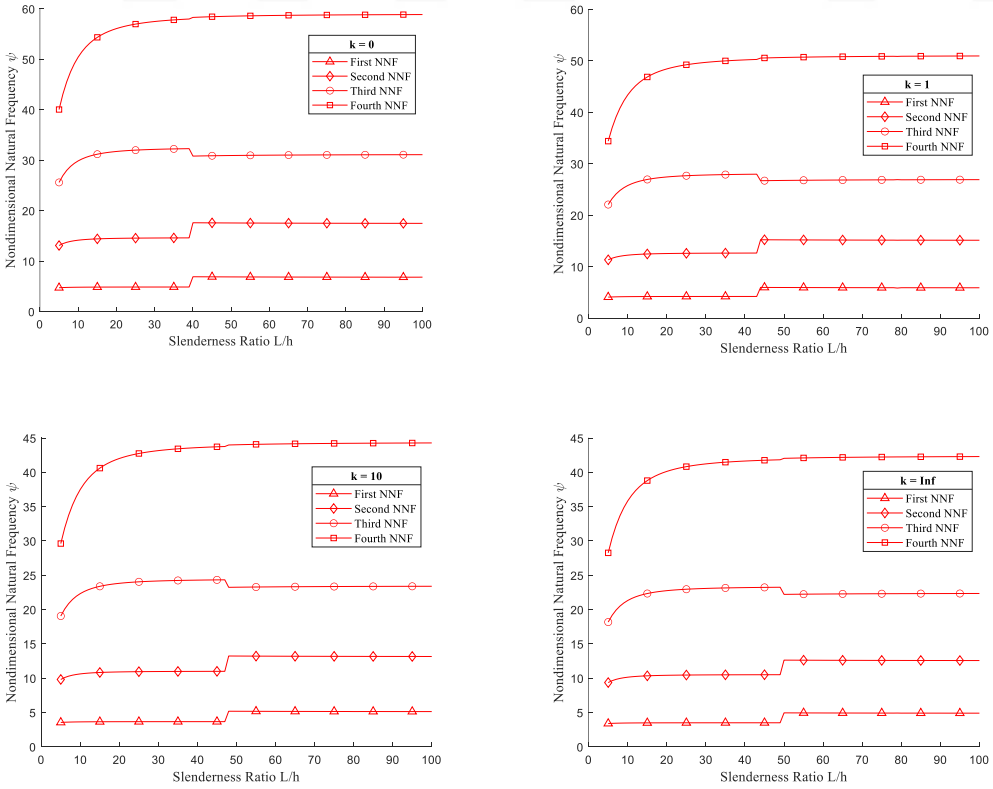

Figure 5.24 : Variation of first four NNF of Timoshenko beam with slenderness ratio *L/h* ($\lambda = 10$, $c_b=c_h=0$, $\mu=0$, $\xi=0$, $T=300^oK$).

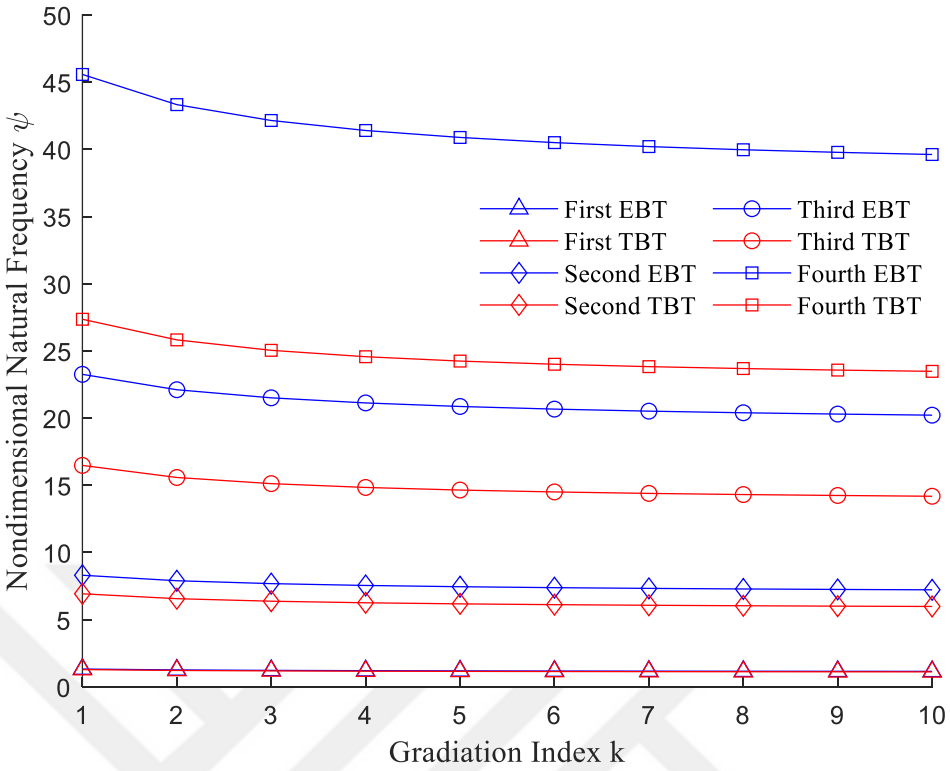

Figure 5.25 : Variation of first four nondimensional natural frequency with gradiation index k ($L/h = 5$, $\lambda = 0$, $c_b=c_h=0$, $\mu=0$, $\xi=0$, $T=300^oK$)

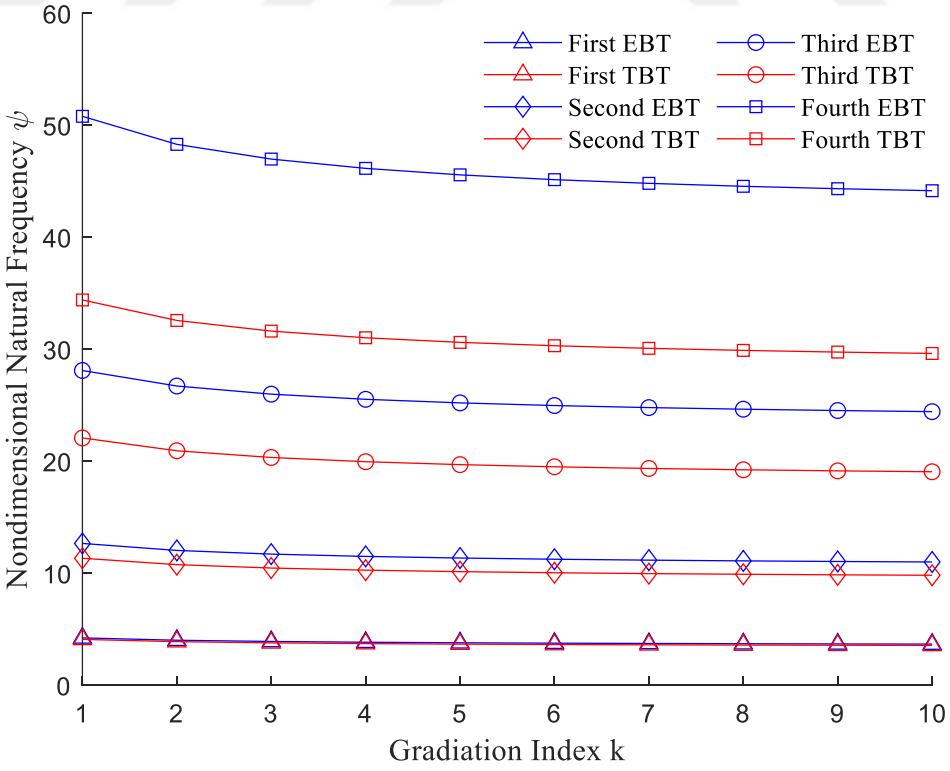

Figure 5.26 : Variation of first four nondimensional natural frequency with gradiation index k ($L/h = 5$, $\lambda = 10$, $c_b=c_h=0$, $\mu=0$, $\xi=0$, $T=300^oK$)

The relevant figures and tables present the effects of high temperature, shear deformation, and material distribution, in addition to the design parameters examined in Section 5.1. Among various design parameters, the influences of rotation speed, shear deformation, and gradiation index have been investigated first for various uniform temperatures and constant slenderness ratios. As expected, the fundamental natural frequencies based on first order shear deformations beam theory are lower than the results based on classical beam theory due to shear deformation, which reflect a more realistic results for slender structures such as turbine blades. Meanwhile, increasing gradiation index causes the decrease in the natural frequenices due to softening effect of it. In other words, the overall stiffness to mass ratio reduces with respect to material distribution through thickness, which leads to lower natural frequencies as shown in Tables 5.8 and Tables in Appendix C. From these tables, it is clear that increasing rotation speed increases the frequencies due to the effect of centrifugal force.

The effect of the slenderness ratio on the fundamental natural frequencies is depicted in Figures 5.23-5.24, and Figures given in Appendix D, which tends to make the frequencies increase until a specific point. On the other hand, it can be negligible for the long beams ($L/h \geq 20$), as seen from these figures. In Figures 5.25-5.26, and Figures in Appendix E, the effect of the gradiation index on the fundamental frequencies is re-highlighted. As known, the natural frequency depends on both Young's modulus and mass distribution. In the case of an increment in the gradiation index, the balance between Young's modulus and mass is disrupted, which decreases the frequencies for both beam theories at each frequency.

The effect of rotation speed on the fundamental frequencies is illustrated for the beam theories, uniform temperatures, and gradiation index in Figures 5.27-5.28, and Figures in Appendix F. Due to the centrifugal stiffening influence of the rotation speed, the frequencies increase with increasing rotation speed.

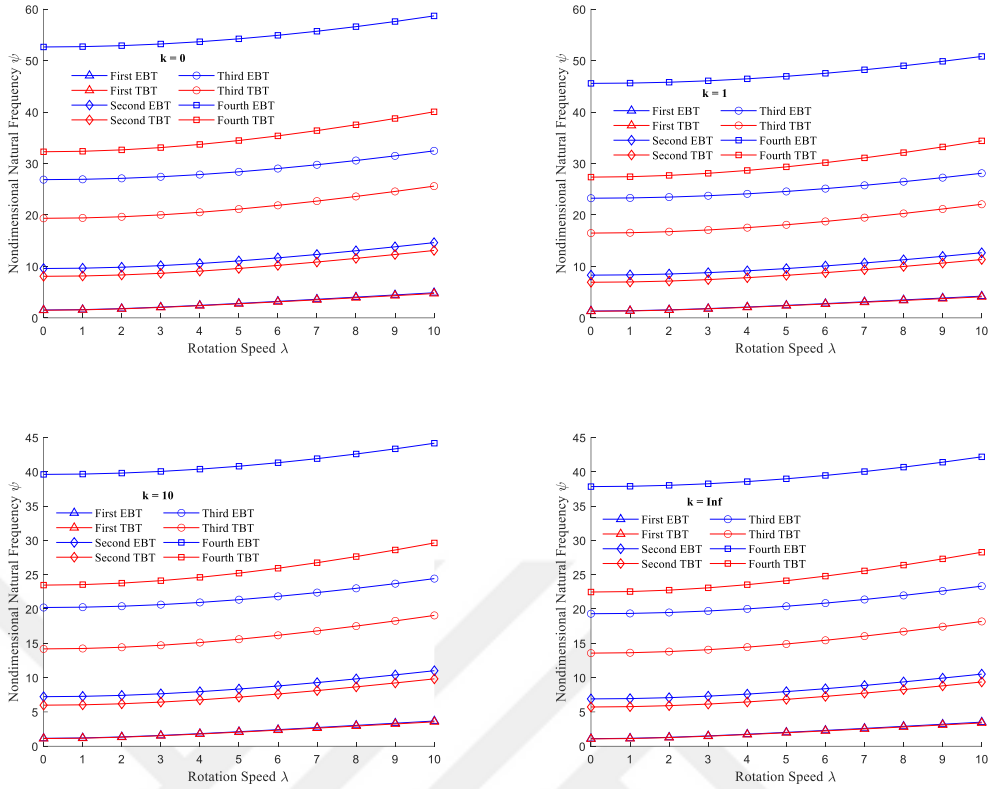

Figure 5.27 : Variation of first four nondimensional natural frequencies of FGM beam with rotation speed λ (L/h = 5, c_b=c_h=0, μ=0, ξ=0, T=300°K)

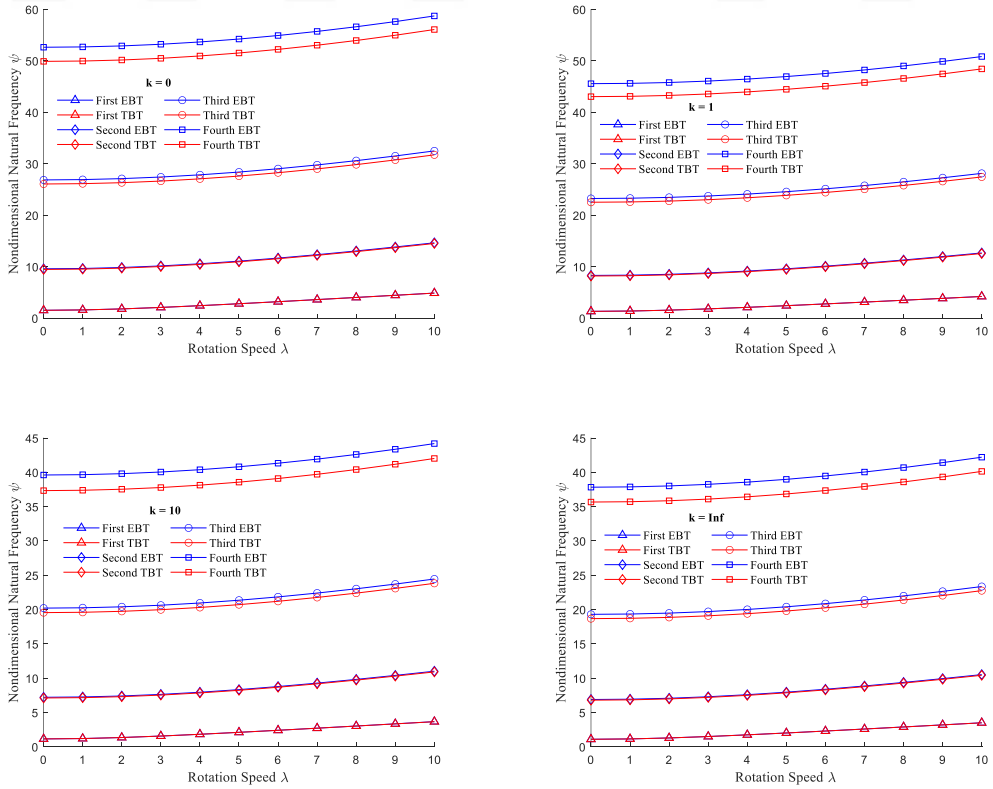

Figure 5.28 : Variation of first four nondimensional natural frequencies of FGM beam with rotation speed λ (L/h = 20, c_b=c_h=0, μ=0, ξ=0, T=300°K)

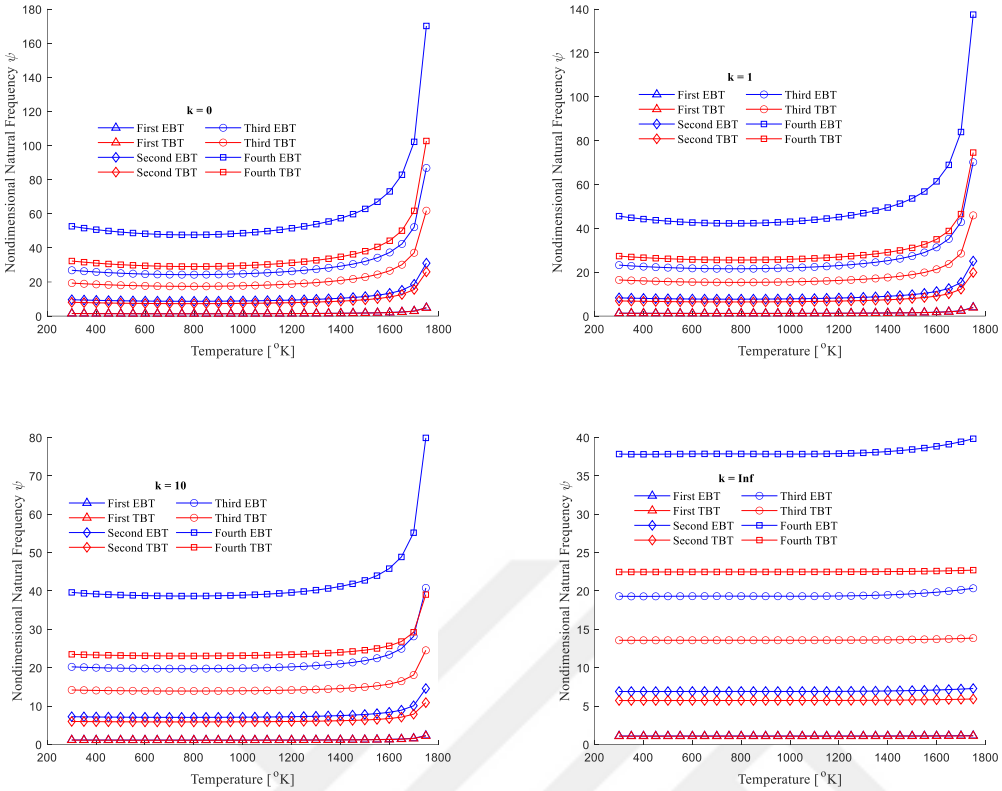

Figure 5.29 : Variation of first four nondimensional natural frequencies of FGM beam with temperature ($\lambda = 0$, $L/h = 5$, $c_b=c_h=0$, $\mu=0$, $\xi=0$)

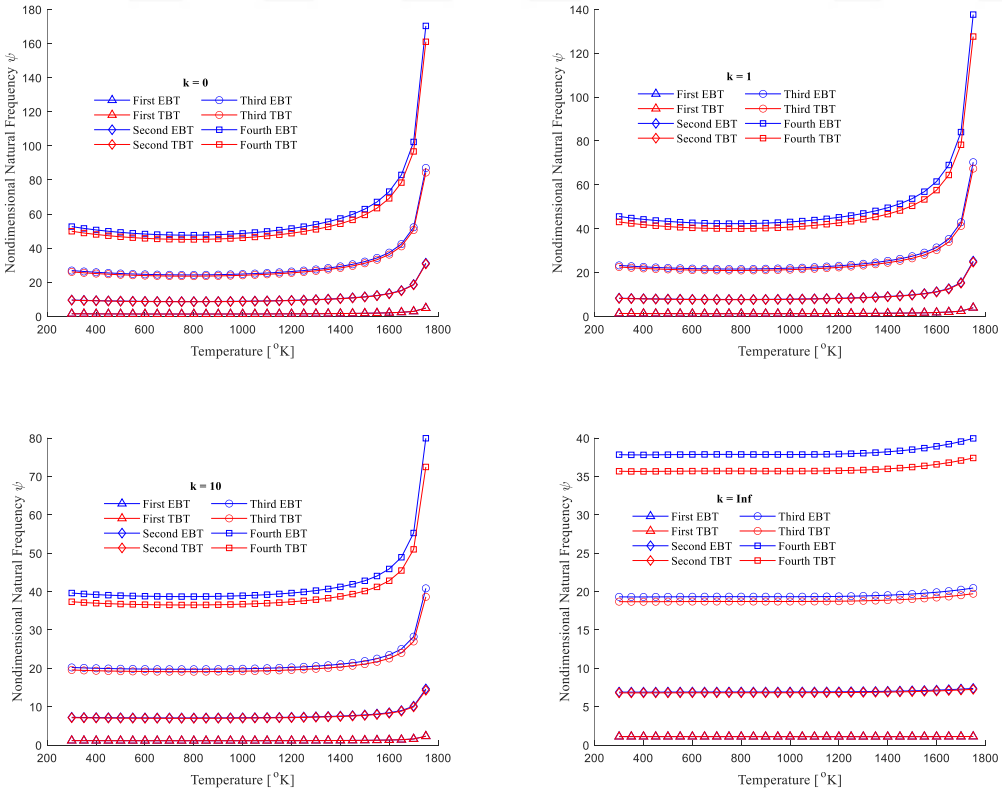

Figure 5.30 : Variation of first four nondimensional natural frequencies of FGM beam with temperature ($\lambda = 0$, $L/h = 20$, $c_b=c_h=0$, $\mu=0$, $\xi=0$)

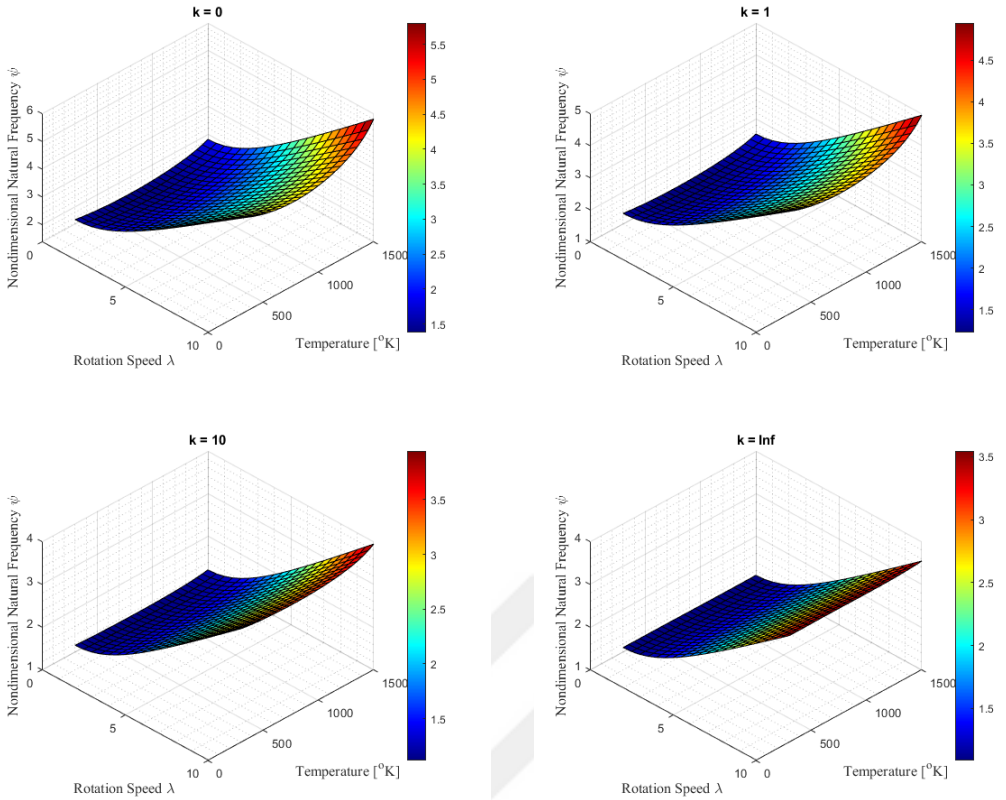

Figure 5.31 : Variation of first nondimensional natural frequency of FGM beam with respect to temperature and rotation speed (L/h = 20, c_b=c_h=0, μ=0, ξ=0)

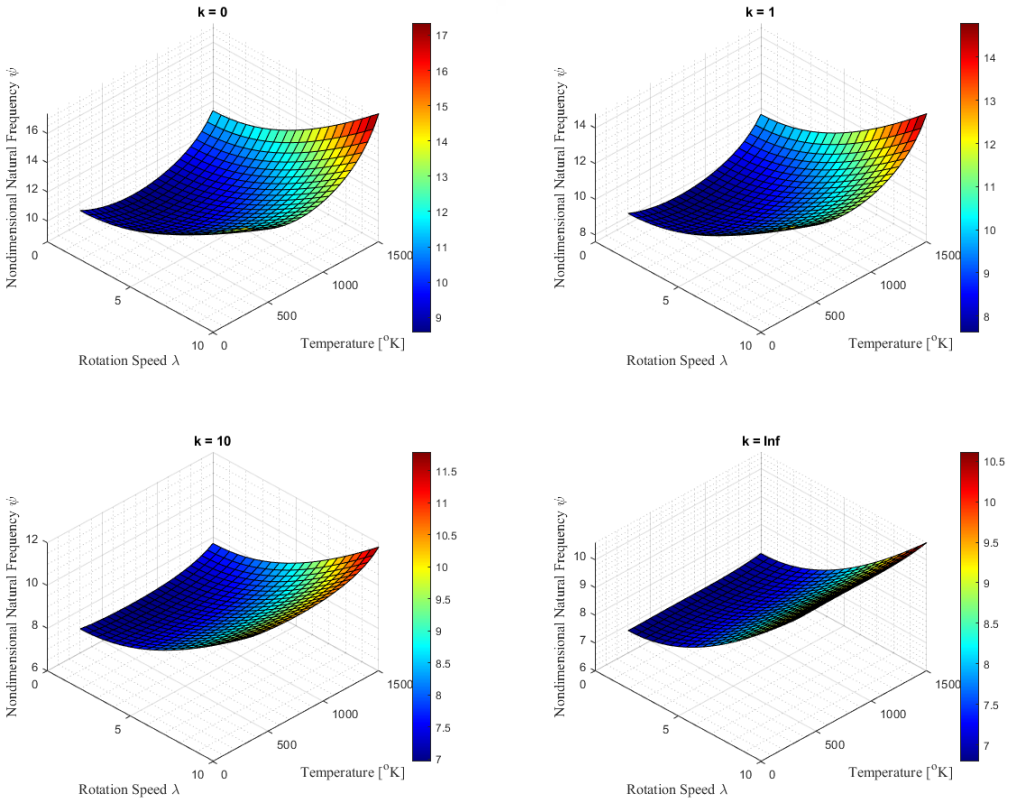

Figure 5.32 : Variation of second nondimensional natural frequency of FGM beam with respect to temperature and rotation speed *(L/h = 20, c_b=c_h=0, μ=0, ξ=0)*

In Figures 5.29-5.30, and Appendix G, the effect of temperatures on the frequencies can be seen. Increasing temperatures decrese the frequencies until reaching a specific temperature, and then the frequencies begin to increase with increasing temperatures. In other words, the softening effect due to a decrement in the material properties is predominant at lower temperatures, which causes a decrease in the natural frequencies as the temperature rises. However, the stiffening effect is observed at higher temperature values, which increases the frequencies due to temperature-dependent material properties.

Both the effects of rotation speed and temperature on the fundamental frequencies of rotating Timoshenko beams made of FGM are shown in Figures 5.31-5.32, and Figures in Appendix H for various slenderness ratios. When both temperature and rotation speed increase simultaneously, the natural frequencies of a rotating FGM beam initially decrease due to the thermal softening effect at lower temperatures. However, increasing values of these parameters lead to increasing the natural frequencies at higher temperatures due to temperature-dependent material properties, as depicted in Figure 5.18.

5.3 Closing Remarks

This chapter presents thermoelastic modeling and vibration analysis of rotating beam structures. Up to various design considerations, vibration characteristics are investigated for the effects of flexible boundary conditions, rotation speed, shear deformation, material distribution, and thermal environment. In this context, turbine blades exposed to high temperatures are modeled with rotating beam elements to demonstrate the effects of these parameters. By employing numerical simulation via GDQM, the obtained numerical results provide invaluable insights for the development of more efficient, and reliable rotating systems, capable of operating under challenging conditions of high angular velocity and temperatures.

6. CONCLUSION

This thesis presents a thorough investigation into the dynamic behavior of rotating beam structures, with a special focus on Functionally Graded Material (FGM) beams in thermal environments. The foundational chapters established a solid base, beginning with a literature review and examining FGM application in aircraft structures. The study then progressed to address the complex thermal structural problems in aviation. To prevent these problems, understanding issues related to thermal stress in high-performance aircraft structures is required. Therefore, the fundamentals of thermoelasticity and heat transfer in aircraft structures are discussed in the coming chapter. Following the discussion on thermoelasticity, some numerical methods used in solving these problems are expressed with illustrative examples. Based on this foundation, the focus of the thesis shifts to free vibration analysis in a thermal environment, which is one of the significant assessments for aircraft structures operating at elevated temperatures.

One of the critical parts exposed to high temperatures in aircraft structures is the turbofan blades in a high-pressure section of a turbofan engine, which can be modeled with rotating beam structures to understand its dynamic characteristics. Therefore, free vibration analysis of the beam structures was performed first before investigating the complex interplay of material properties and elevated temperatures. The key findings of this vibration analysis can be drawn as:

- The Differential Quadrature Method (DQM) offers high accuracy with minimal computational work while computing the natural frequencies and mode shapes of the rotating structures.
- The effect of rotary inertia, flexible root, setting angle, twist angle, and linear variations in taper ratios must be included in the governing equations, which enable a detailed assessment of dynamic characteristics.
- Increments in the breadth taper ratio, hub radius, and rotational speed increase the natural frequencies while increments in the height taper ratio except for the first natural frequency, setting angle, and rotary inertia decrease.

- Introducing elastic boundary conditions provides a more realistic representation of the beam's dynamic behavior. In practical applications, the perfectly clamped condition is rarely observed.

After investigating the contributions of structural variables, the vibration analysis of a rotating beam can be expanded, including the effects of varying material properties through the thickness direction and the influence of high temperatures on the mode shapes and natural frequencies.

For these effects, the following conclusions are found for a beam made of FGM exposed to elevated temperatures:

- The gradational composition of FGMs enables the customization of material properties to mitigate the detrimental effects of thermal stress, presenting a technique for improving structural resilience.
- The natural frequencies of the beam decrease due to the detrimental effect of temperatures at lower temperatures than 900ºC and increase due to the stiffening effect of high temperatures as a result of temperature-dependent material properties.
- The gradation index changes the natural frequencies and mode shapes of beam structures due to variations in stiffness and mass distribution through the thickness of the beam.
- The effect of the slenderness ratio can be negligible for long beam structures.
- Shear deformation provides more accurate results for slender rotating beam structures exposed to elevated temperatures.

To sum up, a comprehensive study of the vibration analysis of rotating beam structures made of FGM in a thermal environment has been presented through the thesis. Understanding the structural dynamics of thermal structures like a rotating thermoelastic beam is vital for sectors such as aerospace, energy, and manufacturing. As a result, the findings of this work must be validated by further research, such as aerothermoelastic analysis of thin-walled rotating structures, buckling analysis of FGM beams with a non-uniform temperature distribution, or comparisons with rotating shell structures.

REFERENCES

[1] **Madier, D.** (2020). *Practical Finite Element Analysis for Mechanical Engineers.* FEA Academy.

[2] **Megson, T. H. G.** (2010). *Introduction to Aircraft Structural Analysis.* Elsevier.

[3] **Donaldson, B. K.** (2008). *Analysis of Aircraft Structures: An Introduction* .Cambridge Aerospace Series.

[4] **Meirovitch, L.** (2010). *Fundamentals of Vibrations*. Waveland Press.

[5] **Couture, S.** (2023). *Becoming an Aircraft Stress Engineer*. Aircraft Stress Publishing.

[6] **Wright, J. R., and Cooper, J. E.** (2014). *Introduction to Aircraft Aeroelasticity and Loads*. Wiley.

[7] **Bent, L. J.** (2010). *Practical Airframe Fatigue and Damage Tolerance*. Sigma K Ltd. Publications.

[8] **Duprat, D.** (2019). *Practical Fatigue and Damage Tolerance for Aircraft*. Sigma K Ltd. Publications.

[9] **Cooley, W. G.** (2005). *Application of Functionally Graded Materials in Aircraft Structures* (Master Thesis). Air Force Institute of Technology, Air University.

[10] **Birman, V., and Byrd, L. W.** (2007). Modeling and Analysis of Functionally Graded Materials and Structures. *Applied Mechanics Reviews*, 60(5), 195–216.

[11] **Noda, N.** (1999). Thermal Stresses in Functionally Graded Materials. *Journal of Thermal Stresses*, 22(4-5), 477-512.

[12] **Lee, W. Y., Stinton, D. P., Berndt, C. C., Erdogan, F., Lee, Y.-D., and Mutasim, Z.** (1996). Concept of Functionally Graded Materials for Advanced Thermal Barrier Coating Applications. *Journal of the American Ceramic Society*, 79(11), 3003-3012.

[13] **Udupa, G., Rao, S. S., and Gangadharan, K.** (2014). Functionally Graded Composite Materials: An Overview. *Procedia Materials Science*, 5, 1291-1299.

[14] **Stere, A., and Librescu, L.** (2000). Nonlinear thermoaeroelastic modeling of advanced aircraft wings made of functionally graded materials. *41st Structures, Structural Dynamics, and Materials Conference and Exhibit.* Atlanta, GA, U.S.A.

[15] **Saleh, B., Jiang, J., Fathi, R., Al-hababi, T., Xu, Q., Wang, L., Song, D., and Ma, A.** (2020). 30 Years of functionally graded materials: An overview of manufacturing methods, applications, and future challenges. *Composites Part B: Engineering*, 201, 108376.

[16] ***Advanced Materials for Gas Turbine Engines Fan Blades.*** *(2021). Retrieved August 30, 2021, from https://www.azom.com/ article. aspx? ArticleID=110*

[17] ***Tiltrotor.****(2021). Retrieved October 29, 2021, from https://en.wikipedia.org/ wiki/Tiltrotor*

[18] ***What happens to end-of-life wind turbine blades.*** *(2021). Retrieved April 23, 2021, from https://ny1.com/nyc/all-boroughs/weather/ 2022/ 08/15/what-happens-to-end-of-life-windmill-blades*

[19] ***First Certification Flight of Turkish Helicopter Gokbey.*** *(2021). Retrieved March 18, 2021, from https://www.aa.com.tr/tr/bilim-teknoloji /gokbey-helikopteri-ilk-sertifikasyon-ucusunu-yapti/ 1519149*

[20] **Space shuttle** (2023). Encyclopaedia Britannica. Retrieved May 19, 2023 from https://www.britannica.com/technology/space-shuttle

[21] ***Ceramic coatings for jet engine turbine blades.*** *(2023). Retrieved May 19, 2023, from https://cord.cranfield.ac. uk/articles/dataset /Carbon_Brainprint_quantifying_the_impact_of_universities _on_carbon_footprint_reduction /7655579*

[22] ***A Typhoon F2 fighter ignites its afterburners whilst taking off from RAF Conings*** *(2023). Retrieved May 19, 2023, https://tr.m.wikiped ia.org/wiki/Dosya:A_Typhoon_F2fighter_ignites_its_afterbur ners_whilst_taking_off_from_AF_Coningsby_MOD_4514795 7.jpg*

[23] **Spacecraft propulsion** (2023). Wikipedia. Retrieved May 19, 2023, from https://en.wikipedia.org/wiki/Spacecraft_propulsion

[24] **Rolls-Royce Turbofan Engine** (2023). Wikimedia. Retrieved May 19, 2023, from https://commons.wikimedia.org/wiki/File:Combustor_of _sectioned_Rolls-oyce_Turbom%C3%A9ca_Adour_turbofan

[25] ***Anatomy of Aircraft & Spacecraft*** *(2023). Retrieved May 19, 2023 from https://eaglepubs.erau.edu/introductiontoaerospaceflightvehic les/chapter/anatomy-of-aircraft-and-spacecraft/*

[26] **Lee, J. W., and Lee, J. Y.** (2018). An exact transfer matrix expression for bending vibration analysis of a rotating tapered beam. *Applied Mathematical Modelling*, 53, 167-188.

[27] **Lee, J. W., and Lee, J. Y.** (2020). Free vibration analysis of a rotating double-tapered beam using the transfer matrix method. *Journal of Mechanical Science and Technology*, 34(7), 2731–2744.

[28] **Rui, X., Abbas, L. K., Yang, F., Wang, G., Yu, H., and Wang, Y.** (2018). Flapwise vibration computations of coupled helicopter rotor/fuselage: Application of multibody system dynamics. *AIAA Journal*, 56(2), 818–835.

[29] **Huang, C. L., Lin, W. Y., and Hsiao, K.** (2010). Free vibration analysis of rotating Euler beams at a high angular velocity. *Computers & Structures*, 88(17-18), 991-1001.

[30] **Adair, D., and Jaeger, M.** (2018). A power series solution for rotating nonuniform Euler–Bernoulli cantilever beams. *Journal of Vibration and Control*, 24(27), 3855-3864.

[31] **Adair, D., and Jaeger, M.** (2018). Vibration analysis of uniform pre-twisted rotating Euler–Bernoulli beam using the modified Adomian decomposition method. *Mathematics and Mechanics of Solids*, 23(9), 1345-1363.

[32] **Mao, Q.** (2014). Free vibrations of spinning beams under nonclassical boundary conditions using Adomian modified decomposition method. *International Journal of Structural Stability and Dynamics*, 14(7), 1-14.

[33] **Aksencer, T., and Aydogdu, M.** (2018). Vibration of a rotating composite beam with an attached point mass. *Composite Structures*, 190, 1-9.

[34] **Ramesh, M. N. V., and Rao, N. M.** (2014). Free vibration analysis of rotating functionally-graded cantilever beams. *International Journal of Acoustics and Vibration*, 19(1), 31-41.

[35] **Oh, Y., and Yoo, H.** (2016). Vibration analysis of rotating cantilever beams orienting inward. *Journal of Mechanical Science and Technology*, 30(9), 4177-4184.

[36] **Roy, P. A., and Meguid, S.** (2018). Analytical modeling of the coupled free vibration response of a rotating blade in a gas turbine engine. *Acta Mechanica*, 229(8), 3355-3373.

[37] **Panchore, V., Ganguli, R., and Omkar, S. N.** (2018). Meshfree Galerkin method for a rotating Euler-Bernoulli beam. International *Journal for Computational Methods in Engineering Science and Mechanics*, 19(1), 11-21.

[38] **Banerjee, J. R.** (2000). Free vibration of centrifugally stiffened uniform and tapered beams using the dynamic stiffness method. *Journal of Sound and Vibration*, 233(5), 857-875.

[39] **Banerjee, J. R., Su, H., and Jackson, D. R.** (2006). Free vibration of rotating tapered beams using the dynamic stiffness method. *Journal of Sound and Vibration*, 298, 1034–1054.

[40] **Banerjee, J. R., and Kennedy, D.** (2014). Dynamic stiffness method for in-plane free vibration of rotating beams including Coriolis effects. *Journal of Sound and Vibration*, 333, 7299-7312.

[41] **Wang, G., and Werely, N. M.** (2004). Free vibration analysis of rotating blades with uniform tapers. *AIAA Journal*, 42(12), 2429-2437.

[42] **Ozdemir, O., and Kaya, M. O.** (2006). Flapwise bending vibration analysis of double tapered rotating Euler–Bernoulli beam by using the differential transform method. *Meccanica*, 41, 661-670.

[43] **Ozdemir, O., and Kaya, M. O.** (2006). Flapwise bending vibration analysis of a rotating tapered cantilever Bernoulli–Euler beam by differential transform method. *Journal of Sound and Vibration*, 289, 413–420.

[44] **Mei, C.** (2008). Application of differential transformation technique to free vibration analysis of a centrifugally stiffened beam. *Computer and Structures*, 86(11-12), 1280-1284.

[45] **Nourifar, M., Keyhani, A., and Sani, A.** (2018). Free vibration analysis of rotating Euler–Bernoulli beam with exponentially varying cross-section by differential transform method. International *Journal of Structural Stability and Dynamics*, 18(2), 1-27.

[46] **Kumar, P. R., Rao, K. M., and Rao, N. M.** (2019). Effect of taper on free vibration of functionally graded rotating beam by Mori-Tanaka method. *Journal of The Institution of Engineers (India): Series C*, 100, 729-736.

[47] **Choi, S. T., Wu, J. D., and Chou, Y.** (1999). Dynamic analysis of a spinning Timoshenko beam by the differential quadrature method. *AIAA Journal,* 38(5), 851-856.

[48] **Bambill, D. V., Felix, D. H., and Rossi, R. E.** (2010). Vibration analysis of rotating Timoshenko beams by means of the differential quadrature method. *Journal of Structural Engineering and Mechanics,* 34(2), 231-245.

[49] **Rajasekaran, S.** (2013). Differential transformation and differential quadrature methods for centrifugally stiffened axially functionally graded tapered beams. *International Journal of Mechanical Sciences*, 74, 15–31.

[50] **Chen, Y., Zhang, J., and& Zhang, H.** (2016). Flapwise bending vibration of rotating tapered beams using variational iteration method. *Journal of Vibration and Control*, 22(15), 3384-3395.

[51] **Chen, Q., and Du, J.** (2019). A Fourier series solution for the transverse vibration of rotating beams with elastic boundary supports. *Applied Acoustics*, 155, 1-15.

[52] **Hodges, D. H., and Rutkowski, M. J.** (1981). Free-vibration analysis of rotating beams by a variable-order finite-element method. *AIAA Journal,* 19(11), 1459-1466.

[53] **Hoa, S. V.** (1979). Vibration of a rotating beam with tip mass. *Journal of Sound and Vibration,* 67(3), 369-381.

[54] **Abbas, B. A. H.** (1986). Dynamic stability of a rotating Timoshenko beam with a flexible root. *Journal of Sound and Vibration*, 108(1), 25-32.

[55] **Chung, J., and Yoo, H. H.** (2002). Dynamic analysis of a rotating cantilever beam by using the finite element method. *Journal of Sound and Vibration,* 249(1), 147-164.

[56] **van Nimwegen, R. R.** (1961). Transient Temperatures and Thermal Stress Problems in Small Gas Turbines. *ASME 1961 Gas Turbine Power Conference and Exhibit*, Washington, DC, USA, March 5–9.

[57] **Men, X., Pan, Y., Jiang, Z., Zhang, T., Zhao, H., and Fu, X.** (2022). Study on Linear and Nonlinear Thermal Buckling Mode and Instability Characteristics for Engine Rotating Thin-Walled Blade. *Applied Sciences*, 12(5), 2437.

[58] **Padture, N. P.** (2019). Environmental degradation of high-temperature protective coatings for ceramic-matrix composites in gas-turbine engines. *Materials Degradation*, 3(11).

[59] **Guo, X., Zheng, W., Xiao, C., Li, L., Antonov, S., Zheng, Y., and Feng, Q.** (2019). Evaluation of microstructural degradation in a failed gas turbine blade due to overheating. *Engineering Failure Analysis,* 103, 308-318.

[60] **Blachnio, J., Spychała, J., and Zasada, D.** (2021). Analysis of structural changes in a gas turbine blade as a result of high temperature and stress. *Engineering Failure Analysis*, 127, 105554.

[61] **Szczepankowski, A., and Przya, R.** (2022). Thermal degradation of turbine components in a military turbofan. *Engineering Failure Analysis*, 134, 106088.

[62] **Reddy, A. V.** (2004). *Investigation of Aeronautical and Engineering Component Failures* (1st ed.). CRC Press.

[63] **Sharma, K., Aditya, A., and Srinias, G.** (2020). Material failure analysis and engine combustion instabilities of both air and non-air breathing engines. *Materials Today: Proceedings,* 27(Part 1), 231-237.

[64] **Wang, L., Yin, Y., Wang, A., Heng, X., and Jin, M.** (2021). Dynamic Modeling and Vibration Characteristics for a High-Speed Aero-Engine Rotor with Blade Off. *Applied Sciences*, 11(20), 9674.

[65] **Mourad, A. I., Almomani, A., Sheikh, I. A., and Elsheikh, A. H.** (2023). Failure analysis of gas and wind turbine blades: A review. *Engineering Failure Analysis*, 146, 107107.

[66] **Sankar, B. V., and Tzeng, J. T.** (2002). Thermal Stresses in Functionally Graded Beams. *AIAA Journal*, 40(6), 1228-1232.

[67] **Huda, Z., and Edi, P.** (2013). Materials selection in design of structures and engines of supersonic aircrafts: A review. *Materials & Design* (1980-2015), 46, 552-560.

[68] **Hu, Z.-C., Liu, B., Wang, L., Cui, Y.-H., Wang, Y.-W., Ma, Y.-D., Sun, W.-W., and Yang, Y.** (2020). Research Progress of Failure Mechanism of Thermal Barrier Coatings at High Temperature via Finite Element Method. *Coatings*, 10, 732.

[69] **Hodges, D. H., and Rutkowski, M. J.** (1981). Free-Vibration Analysis of Rotating Beams by a Variable-Order Finite-Element Method. *AIAA Journal*, 19(11), 1459-1466.

[70] **Kaya, M. O.** (2006). Free vibration analysis of a rotating Timoshenko beam by differential transform method. *Aircraft Engineering and Aerospace Technology*, 78(3), 194-203.

[71] **Ozdemir Ozgumus, O., & Kaya, M. O.** (2010). Vibration analysis of a rotating tapered Timoshenko beam using DTM. *Meccanica*, 45(1), 33–42.

[72] **Banerjee, J. R., and Kennedy, D.** (2014). Dynamic stiffness method for inplane free vibration of rotating beams including Coriolis effects. *Journal of Sound and Vibration*, 333(26), 7299-7312.

[73] **Banerjee, J. R., Su, H., and Jackson, D. R.** (2006). Free vibration of rotating tapered beams using the dynamic stiffness method. *Journal of Sound and Vibration*, 298(4–5), 1034-1054.

[74] **Yavuz, M. T., and Ozkol, I.** (2021). Free vibration nalysis of a rotating tapered beam with flexible root via differential quadrature method. *Aircraft Engineering and Aerospace Technology*, 93(5), 900-914.

[75] **Yao, M. H., Chen, Y. P., and Zhang, W.** (2012). Nonlinear vibrations of the blade with varying rotating speed. *Nonlinear Dynamics*, 68, 487–504.

[76] **Roy, P. A., and Meguid, S. A.** (2018). Analytical modeling of the coupled nonlinear free vibration response of a rotating blade in a gas turbine engine. *Acta Mechanica*, 229, 3355–3373.

[77] **Kumar, P. R., Rao, K. M., and Rao, N. M.** (2017). Flapwise Vibration of Rotating Functionally Graded Beam. *Materials Today: Proceedings*, 4(2, Part A), 3736-3744.

[78] **Maganti, N. V. R., and Nalluri, M. R.** (2015). Flapwise bending vibration analysis of functionally graded rotating double-tapered beams. International *Journal of Mechanical, Materials, and Engineering*, 10, 21.

[79] **Oh, Y., and Yoo, H.** (2016). Vibration analysis of rotating pretwisted tapered blades made of functionally graded materials. International *Journal of Mechanical Sciences*, 119, 68-79.

[80] **Amoozgar, M., and Gelman, L.** (2022). Vibration analysis of rotating porous functionally graded material beams using exact formulation. *Journal of Vibration and Control*, 28(21-22), 3195-3206.

[81] **Rathore, S., Kar, V. R., and Sanjay.** (2022). Modal analysis of rotating pre-twisted functionally graded sandwich blade. *Materials Today: Proceedings*, 56 (Part 2), 896-901.

[82] **Ramesh, M. N. V., and Mohan Rao, N.** (2013). Free vibration analysis of pre-twisted rotating FGM beams. *International Journal of Mechanical and Materials Design*, 9, 367–383.

[83] **Li, L., Zhang, D. G., and Zhu, W. D.** (2014). Free vibration analysis of a rotating hub–functionally graded material beam system with the dynamic stiffening effect. *Journal of Sound and Vibration*, 333(5), 1526-1541.

[84] **Tian, J., Zhang, Z., and Hua, H.** (2019). Free vibration analysis of rotating functionally graded double-tapered beam including porosities. *International Journal of Mechanical Sciences*, 150, 526-538.

[85] **Oh, S.-Y., Librescu, L., and Song, O.** (2003). Thermoelastic Modeling and Vibration of Functionally Graded Thin-Walled Rotating Blades. *AIAA Journal*, 41(10), 2051-2061.

[86] **Oh, S. Y., Librescu, L., and Song, O.** (2003). Vibration of turbomachinery rotating blades made-up of functionally graded materials and operating in a high-temperature field. *Acta Mechanica*, 166, 69–87.

[87] **Librescu, L., Oh, S.-Y., and Song, O.** (2005). Thin-Walled Beams Made of Functionally Graded Materials and Operating in a High-Temperature Environment: Vibration and Stability. *Journal of Thermal Stresses*, 28(6-7), 649-712.

[88] **Librescu, L., Oh, S. Y., Song, O., et al.** (2008). Dynamics of advanced rotating blades made of functionally graded materials and operating in a high-temperature field. *Journal of Engineering Mathematics*, 61, 1–16.

[89] **Fazelzadeh, S. A., and Hosseini, M.** (2007). Aerothermoelastic behavior of supersonic rotating thin-walled beams made of functionally graded materials. *Journal of Fluids and Structures*, 23(8), 1251-1264.

[90] **Fazelzadeh, S. A., Malekzadeh, P., Zahedinejad, P., and Hosseini, M.** (2007). Vibration analysis of functionally graded thin-walled rotating blades under high-temperature supersonic flow using the differential quadrature method. *Journal of Sound and Vibration*, 306(1–2), 333-348.

[91] **Shenas, A., Ziaee, S., and Malekzadeh, P.** (2016). Vibrational behavior of rotating pre-twisted functionally graded microbeams in thermal environment. *Composite Structures*, 157, 222-235.

[92] **Inala, R., and Mohanty, S.** (2017). Flapwise bending vibration and dynamic stability of rotating functionally graded material plates in thermal environments. *Proceedings of the Institution of Mechanical Engineers, Part G: Journal of Aerospace Engineering*, 231(2), 203-217.

[93] **Pal, S., and Das, D.** (2018). Free vibration analysis of functionally graded double-tapered beam rotating in thermal environment considering geometric nonlinearity, shear deformability, and Coriolis effect. *Proceedings of the Institution of Mechanical Engineers, Part G: Journal of Aerospace Engineering*, 232(12), 2244-2262.

[94] **Shafiei, N., Ghadiri, M., and Mahinzare, M.** (2019). Flapwise bending vibration analysis of rotary tapered functionally graded nanobeam in thermal environment. *Mechanics of Advanced Materials and Structures*, 26(2), 139-155.

[95] **Chen, Y., Ye, T., Jin, G., Li, S., and Yang, C.** (2021). Vibration analysis of rotating pretwist FG sandwich blades operating in thermal environment. *International Journal of Mechanical Sciences*, 205, 106596.

[96] **Wang, Y., Yang, C., Zhang, Y., Dong, S., and Li, L.** (2021). Dynamics of a rotating hollow FGM beam in the temperature field. *Reviews on Advanced Materials Science*, 60(1), 643-662.

[97] **Xu, J., Yang, Z., Yang, J., and Li, Y.** (2021). Free vibration analysis of rotating FG-CNT reinforced composite beams in thermal environments with general boundary conditions. *Aerospace Science and Technology*, 118, 107030.

[98] **Arvin, H., Hosseini, S. M., and Kiani, Y.** (2021). Free vibration analysis of pre/post-buckled rotating functionally graded beams subjected to uniform temperature rise. *Thin-Walled Structures*, 158, 107187.

[99] **Assem, H., Hadjoui, A., and Saimi, A.** (2022). Numerical analysis on the dynamics behavior of FGM rotor in thermal environment using h-p finite element method. *Mechanics Based Design of Structures and Machines*, 50(11), 3925-3948.

[100] **Yavuz, M. T., and Uyulan, C.** (2022). Thermal Modal Analysis of Turbofan Blades Modeled as Rotating Thermoelastic Beams by Using Differential Transform Method, *19th Israeli Symposium on Jet Engines & Gas Turbines*, Technion-IIT, Haifa, Israel.

[101] **Dey, T., and Bandyopadhyay, T.** (2023). Free Vibration Response of Porous FGM Plates Using Finite Element Analysis in Thermal Environment. *Journal of Vibration Engineering and Technology*.

[102] **Crawford, C. A., and Simm, S. E.** (1999). Conceptual Design and Optimization of Modern Combat Aircraft, *RTO AVT Symposium on Aerodynamic Design and Optimization of Flight Vehicles in a Concurrent Multi-Disciplinary Environment*, Ottawa, Canada, October 18-21.

[103] **Huenecke, K.** (1987). *Modern Combat Aircraft Design*. Naval Institute Press.

[104] **Ananthasayanam, M., and Muralidharan, M.** (2005). Historical Evolution of the Military Fighter Airplanes Around the Twentieth Century, *43rd AIAA Aerospace Sciences Meeting and Exhibit*, January 10-13, 2005, Reno, Nevada.

[105] **Aronstein, D. C., Hirschberg, M. J., and Piccirillo, A. C.** (1998). *Advanced Tactical Fighter to F-22 Raptor: Origins of the 21st Century Air Dominance Fighter*. Reston: American Institute of Aeronautics and Astronautics, Inc.

[106] **Carlisle, H. J.** (2015). 5th Generation Fighters, *Air Force Association and Space Conference and Technology Exposition*, Washington, DC, December 15.

[107] **Thornborough, A.** (1995). *Modern Fighter Aircraft Technology and Tactics*. London: Patrick Stephens Ltd.

[108] **Wheeler, B. C.** (1985). *An Illustrated Guide to Modern American Fighters and Attack Aircraft*. London: Salamander Book Ltd.

[109] **Spick, M.** (1987). *An Illustrated Guide to Modern Fighter Combat*. London, New York: Salamander Books Ltd.

[110] **Gunston, B.** (1980). *An Illustrated Guide to Modern Fighters and Attack Aircraft.* London: Salamander Book Ltd.

[111] **Sizemore, D.** (2022). *Beyond the Speed of Sound*. Tennessee: United States Air Force's Arnold Engineering Development Center.

[112] **Whitford, R.** (1987). *Design for Air Combat*. New York: Jane's Publishing Company Ltd.

[113] **Whitford, R.** (1996). Designing for Stealth in Fighter Aircraft: Stealth from the Aircraft Designer's Viewpoint, *1996 World Aviation Congress.*

[114] **Raymer, D.** (1995). National design of an advanced strike fighter. *Aircraft Engineering, Technology, and Operations Congress*, September 19-21, 1995, Los Angeles, CA, U.S.A.

[115] **Tendeland, T., and Schlaff, B. A.** (1948). *Temperature Gradients in the Wing of a High-Speed Airplane During Dives from High Altitudes* (Technical Note). National Advisory Committee for Aeronautics.

[116] **O'Sullivan Jr., W. J.** (1951). Factors Governing Aerodynamic Heating. *NACA Conference on Aircraft Structures*, 1951, Structural Problems Associated with Aerodynamic Heating.

[117] **Parkes, E. W.** (1953). Transient Thermal Stresses in Wings: An Assessment of the Stresses in a Cellular Wing Structure Which Undergoes a Change of Temperature. *Aircraft Engineering and Aerospace Technology*, 25(12), 373-378.

[118] **Rendel, D.** (1954). Thermal Problems of High-Performance Flight: A Further Contribution to the Bristol Conference on Thermal Stress Organized by the Stress Analysis Group of the Institute of Physics. *Aircraft Engineering and Aerospace Technology*, 26(7), 220-223.

[119] **Loveless, E., and Boswell, A. C.** (1954). The Problem of Thermal Stresses in Aircraft Structures. *Aircraft Engineering and Aerospace Technology*, 26(4), 122-124.

[120] **Pohle, F. V., and Oliver, H.** (1954). Temperature Distribution and Thermal Stresses in a Model of a Supersonic Wing. *Journal of the Aeronautical Sciences*, 21(1), 8-16.

[121] **Walker, P.** (1955). The Structural Effects of Kinetic Heating in Supersonic Flight. *The Aeronautical Journal*, 59(537), 581-586.

[122] **Schuh, H.** (1955). Transient Temperature Distributions and Thermal Stresses in a Skin-Shear Web Configuration at High-Speed Flight for a Wide Range of Parameters. *Journal of the Aeronautical Sciences*, 22(12), 829-836.

[123] **Chauvin, L. T.** (1956). *Aerodynamic Heating of Aircraft Components* (Technical Note). National Advisory Committee for Aeronautics.

[124] **Mahlmeister, E., and Ambrosio, A.** (1955). *Studies on Thermal Stresses for Aircraft Structures Exposed to Transient External Heating* (Technical Report). Wright Air Development Center.

[125] **Hoff, N. J.** (1956). *Thermal problems in aircraft structures* (Technical Report). North Atlantic Treaty Organization, Advisory Group for Aeronautical Research and Development.

[126] **O'Sullivan, W. J.** (1957). *Theory of Aircraft Structural Models Subject to Aerodynamic Heating and External Loads* (Technical Note). National Advisory Committee for Aeronautics.

[127] **Brooks, W. A. Jr., Griffith, G. E., and Strass, H. K.** (1957). *Two Factors Influencing Temperature Distributions and Thermal Stresses in Structures* (Technical Note). National Advisory Committee for Aeronautics.

[128] **Vosteen, L. F., McWithey, R. R., and Thomson, R. G.** (1957). *Effect of transient heating on vibration frequencies of some simple wing structures* (Technical Note). National Advisory Committee for Aeronautics.

[129] **Hoff, N. J.** (1958). *High Temperature Effects in Aircraft Structures*. Pergamon Press.

[130] **Kitchenside, A. W.** (1958). The Effects of Kinetic Heating on Aircraft Structures. *The Aeronautical Journal*, 62(566), 105-117.

[131] **Kordes, E. E., Reed, R. D., and Dawdy, A. L.** (1961). Structural Heating Experiences of the X-15, *Research-Airplane-Committee Report on Conference*, National Aeronautics and Space Administration.

[132] **Capey, E. C.** (1965). *Alleviation of Thermal Stresses in Aircraft Structures.* (Technical Report). Ministry of Aviation, Aeronautical Research Council.

[133] **Gossard, M. L., and Roberts, W. M.** (1951). Thermal Buckling of Flat Plates, *NACA Conference on Aircraft Structures on Structural Problems Associated with Aerodynamic Heating*.

[134] **Heldenfels, R. R., and Roberts, W. M.** (1951). Theoretical and Experimental Determination of Thermal Stresses, *NACA Conference on Aircraft Structures on Structural Problems Associated with Aerodynamic Heating*.

[135] **Hoff, N. J.** (1956). Thermal Buckling of Supersonic Wing Panels. *Journal of the Aeronautical Sciences*, 23(11), 1019-1028.

[136] **Pride, R. A., Hall, J. B. Jr., and Anderson, M. S.** (1957). *Effects of Rapid Heating on Strength of Airframe Components* (Technical Note). National Advisory Committee for Aeronautics.

[137] **Mansfield, E. H.** (1960). *Leading-Edge Buckling due to Aerodynamic Heating* (Technical Note). Aeronautical Research Council.

[138] **Webber, J. P. H., and Houghton, D. S.** (1963). Spar Web Buckling of a Supersonic Aircraft: An Analysis of a Simply-Supported Rectangular Plate Under the Action of In-Plane Stresses Due to the Action of Aerodynamic and Inertia Forces and Kinetic Heating Effects. *Aircraft Engineering and Aerospace Technology*, 35(12), 364-368.

[139] **McKenzie, K. I.** (1962). *The Leading-Edge Buckling of a Thin Built-up Wing due to Aerodynamic Heating* (Technical Note). Aeronautical Research Council.

[140] **Budiansky, B., and Mayers, J.** (1956). Influence of Aerodynamic Heating on the Effective Torsional Stiffness of Thin Wings. *Journal of the Aeronautical Sciences*, 23(12).

[141] **Kochanski, S. L., and Argyris, J. H.** (1957). Some Effects of Kinetic Heating on the Stiffness of Thin Wings: A Preliminary Investigation of the Effects of Thermal Stresses on the Torsional and Flexural Stiffness of Thin Solid Wings. *Aircraft Engineering and Aerospace Technology*, 29(10), 310-318.

[142] **Biot, M. A.** (1957). Influence of Thermal Stresses on the Aeroelastic Stability of Supersonic Wings. *Journal of the Aeronautical Sciences*, 24(6), 418-420.

[143] **Houbolt, J. C.** (1958). *A Study of Several Aerothermoelastic Problems of Aircraft Structures in High-Speed Flight* (Doctoral thesis). ETH Zurich.

[144] **Heath-Smith, J. R., and Kiddle, F. E.** (1975). *Effects of Heat on Fatigue in Aircraft Structure* (Technical Note). Aeronautical Research Council.

[145] **Kroll, W. D.** (1959). *Aerodynamic Heating and Fatigue* (Technical Note: 6-4-59W). National Aeronautics and Space Administration.

[146] **Libove, C., and Heimerl, G. J.** (1951). Some Aircraft Structural Problems Resulting from Creep, *NACA Conference on Aircraft Structures on Structural Problems Associated with Aerodynamic Heating*.

[147] **Pope, G. G.** (1961). *Thermal Stresses near the Roots of Rectangular Wings* (Technical Note). Aeronautical Research Council.

[148] **Hoff, N. J.** (1956). *Thermal problems in aircraft structures* (Technical Report). North Atlantic Treaty Organization, Advisory Group for Aeronautical Research and Development.

[149] **Baker, A. A., and Scott, M. L.** (2016). *Composite Materials for Aircraft Structures*. AIAA American Institute of Aeronautics & Astronautics.

[150] **Kassapoglou, C.** (2013). *Design and Analysis of Composite Structures: With Applications to Aerospace Structures*. John Wiley & Sons Ltd.

[151] **Younossi, O., Kennedy, M., and Graser, J.** (2001). *Military Airframe Costs: The Effects of Advanced Materials and Manufacturing Processes.* RAND Publication Series.

[152] **Ashton, H.** (1996). Damage tolerance and durability testing for F/A-18 E/F composite materials structures. *37th Structure, Structural Dynamics and Materials Conference*, Salt Lake City, UT, U.S.A., April 17-19.

[153] **Resetar, S., Rogers, C., and Hess, R.** (1991). *Advanced Airframe Structural Materials: A Primer and Cost Estimating Methodology*. RAND Publication Series.

[154] **Nordin, P.** (2011). Saab experience with application of composites in aerospace structures. *ICAS Biennial Workshop 2011*, Stockholm.

[155] **Lewis, S. J.** (1994). The use of carbon fibre composites on military aircraft. *Composites Manufacturing*, 5(2), 95-103.

[156] **Huda, Z., and Edi, P.** (2013). Materials selection the design of structures and engines of supersonic aircraft: A review. *Materials & Design*, 46, 552-560.

[157] **Boyer, R. R., Cotton, J. D., Mohaghegh, M., and Schafrik, R. E.** (2015). Materials considerations for aerospace applications. *Materials Research Society Bulletin*, 40.

[158] **Flower, H., and Soutis, C.** (2003). Materials for airframes. *The Aeronautical Journal*, 107(1072), 331-341.

[159] **Marsh, G.** (2005). Composites fight for share of military applications. *Reinforced Plastics*, 49(5), 18-22.

[160] **Castanie, B., Bouvet, C., and Ginot, M.** (2020). Review of composite sandwich structure in aeronautic applications. *Composites Part C: Open Access*, 1, 100004.

[161] **Setlak, L., Kowalik, R., and Lusiak, T.** (2021). Practical use of composite materials used in military aircraft. *Materials*, 14(17), 4812.

[162] **Starke, E. A., and Staley, J. T.** (1996). Application of modern aluminum alloys to aircraft. *Progress in Aerospace Sciences*, 32(2–3), 131-172.

[163] **Dorward, R. C., and Pritchett, T. R.** (1988). Advanced aluminium alloys for aircraft and aerospace applications. *Materials & Design*, 9(2), 63-69.

[164] **Dursun, T., and Soutis, C.** (2014). Recent developments in advanced aircraft aluminium alloys. *Materials & Design*, 56, 862-871.

[165] **Cotton, J. D., Clark, L., and Phelps, H.** (2002). Titanium alloys on the F-22 fighter airframe. *Materials Science & Engineering: Advanced Materials & Processes*, 160(5), 25-28.

[166] **Malaznik, S.** (2011). Thermal Stress Analysis of a High-Speed Aircraft Wing Box. *MSC Software 2011 Users Conference*.

[167] **Xie, G., Wang, C., Ji, and Sunden, B.** (2016). Investigation on thermal and thermomechanical performances of actively cooled corrugated sandwich structures. *Applied Thermal Engineering*, 103, 660-669.

[168] **Sprague, G. H., and Huang, P. C.** (1958). Behavior of Aircraft Structures under Thermal Stress. *SAE Transactions*, 66, 457-465.

[169] **Przemieniecki, J. S.** (1965). Alleviation of Thermal Stresses in Bi-metallic Spar Webs. *Aircraft Engineering and Aerospace Technology*, 37(9), 267-272.

[170] **Wolfe, M. O. W.** (1964). Aspects of elevated temperature design and design criteria for supersonic aircraft structures. *High Temperature Structures and Materials*, 413-438.

[171] **Przemieniecki, J.** (1956). Transient Temperature Distributions and Thermal Stresses in Fuselage Shells with Bulkheads or Frames. *The Journal of the Royal Aeronautical Society*, 60, 799 - 804.

[172] **Collard, D.** (1991). Concorde Airframe Design and Development. *SAE Transactions*, 100, 2620–2641.

[173] **Parkes, E. W.** (1953). The Alleviation of Thermal Stresses: The Influence of Surface Insulation on the Stresses Set Up When an Aircraft Undergoes a Change of External Temperature. *Aircraft Engineering and Aerospace Technology*, 25(2), 51-53.

[174] **Harpur, N. F.** (1968). Concorde Structural Development. *Journal of Aircraft*, 5(2), 176-183.

[175] **Thornton, E. A.** (1996). Experimental Methods for High-Temperature Aerospace Structures. In R. B. Hetnarski (Ed.), Thermal Stresses IV (Mechanics and Mathematical Methods–Series of Handbooks). North-Holland.

[176] **Department of Defense.** (2008). MIL-STD-810G: Environmental engineering considerations and laboratory tests (31 October 2008).

[177] **Tendeland, T., and Schlaff, B. A.** (1948). *Temperature gradients in the wing of a high-speed airplane during dives from high altitudes* (Technical Note: 1675). NACA.

[178] **Madhusudana, C. V.** (2013). *Thermal Contact Conductance* (Mechanical Engineering Series). Springer.

[179] **Andersson, V.** (2018). *Thermal Contact Conductance in Aircraft Application* (Master Thesis). Luleå University of Technology, Department of Engineering Sciences and Mathematics.

[180] **Stark, A. E.** (2020). *Thermal Contact Resistance Measurement and Related Uncertainties* (Master's thesis). Old Dominion University.

[181] **Zhao, J., Yang, J., Wang, Z., Wang, Y., Jin, X., Li, P., Liu, P., Chen, K., Yang, L., and Fan, X.** (2023). Thermal Shock Resistance and Failure Mechanisms of High-Temperature Resistant Radar and Infrared Compatible Stealth Coatings. *Surface and Coatings Technology*, 465.

[182] **Zheng, L., Wu, D., and Zhou, A.** (2014). Experimental and Numerical Study on Heat Transfer Characteristics of Metallic Honeycomb Core Structure in Transient Thermal Shock Environments. *International Journal of Thermophysics*, 35, 1557-1576.

[183] **Wu, D. F., Zhou, A. F., Pan, B., Wang, Y. W., and Pu, Y.** (2014). Research on Thermal Protection Performances of Metallic Honeycomb Panel Subjected to High-Speed Thermal Shock. *Applied Mechanics and Materials*, 494, 519–524.

[184] **Guerrero, J., Sasikumar, A., Llobet, J., and Costa, J.** (2022). Testing and simulation of a composite-aluminium wingbox subcomponent subjected to thermal loading. *Composite Structures*, 296, 115887.

[185] **Norwood, D. S., Schneberger, B. M., Fuller, K. M., & Brown, K.** (2021). Prediction of Airframe Thermal Stresses for Hybrid Composite-Metallic Structure. *AIAA Paper 2021-0572. AIAA Scitech 2021 Forum*, January 2021.

[186] **Mueller, B., and Taylor, R. M.** (2008). Methodology for thermally induced loading in structural analysis on the F-35 Lightning II, *26th International Congress of the Aeronautical Sciences*, Anchorage, Alaska, USA, September 14-19.

[187] **Payne, A. O.** (1976). The fatigue of aircraft structures. *Engineering Fracture Mechanics*, 8(1), 157-203.

[188] **Freudenthal, A. M., and Weiner, J. H.** (1956). On the Thermal Aspect of Fatigue. *Journal of Applied Physics*, 27(1), 44–50.

[189] **Mueller, B., Hagenbeek, M., and Sinke, J.** (2016). Thermal cycling of (heated) fibre metal laminates. *Composite Structures*, 152, 106-116.

[190] **Abdo, Z., and Aglan, H.** (1997). Analysis of aircraft adhesive joints under combined thermal and mechanical cyclic loadings. *Journal of Adhesion Science and Technology*, 11(7), 941-956.

[191] **Gerard, G.** (1954). Life Expectancy of Aircraft Under Thermal Flight Conditions. *Journal of the Aeronautical Sciences*, 21(10), 675-680.

[192] **Mordfin, L., and Legate, A. C.** (1957). *Creep behavior of structural joints of aircraft materials under constant loads and temperatures* (Technical Report: 3842). National Advisory Committee for Aeronautics.

[193] ***Creep Testing Machine - IBcreep Series** (2023). Retrieved November 11, 2023, from https://www.ibertest.es/en/products/ creep -testing -machine-ibcreep-series/*

[194] **Gossard, M. L., Seide, P., and Roberts, W. M.** (1952). *Thermal buckling of plates* (Technical Note: 2771). National Advisory Committee for Aeronautics, Washington.

[195] **Bartlett, J., and Stratford, C.** (2001). Fire resistance certification of aircraft composite materials. *Practical Failure Analysis*, 1, 37–43.

[196] **Mouritz, A.P.** (2003). Fire resistance of aircraft composite laminates. *Journal of Materials Science Letters*, 22(21), 1507-1509.

[197] **Barron, R. F., and Barron, B. R.** (2012). *Design for Thermal Stress*. Hoboken, New Jersey: John Wiley & Sons, Inc.

[198] **Gatewood, B. E.** (1957). *Thermal Stresses with Applications to Airplanes, Missiles, Turbines, and Nuclear Reactors*. New York: McGraw-Hill Book Company, Inc.

[199] **Johns, D. J.** (1965). *Thermal Stresses Analyses*. Oxford: Pergamon Press.

[200] **Ellis, R. M., Gross, P., Yates, J., Casement, J. R., Chichester, R. H. and Nesmith, K.** (2018). F-35 Structural Design, Development, and Verification. *Aviation Technology, Integration, and Operations Conference.* Atlanta, Georgia: AIAA.

[201] **Nam, J., Chang, I., Lee, Y., Kim, J., and Cho, H.** (2020). Effect of Flight Altitude on Minimal Infrared Signature of Combat Aircraft. *Journal of the Computational Structural Engineering Institute of Korea*, 33. 375-382.

[202] **MSC Software Corporation.** (2004). MSC Nastran Thermal Analysis Tutorial.

[203] **Ugural, A. C., and Fenster, S. K.** (2019). *Advanced Mechanics of Materials and Applied Elasticity* (6 ed.). Pearson Pub.

[204] **Inan, M.** (2019). *Strength of Materials* (10 ed.). Istanbul: ITU Foundation Pub.

[205] **Yayla, P.** (2014). *Applied Elasticity Theory* (Turkish ed.). Ankara: Nobel Pub.

[206] **Doggett, R. V., Ricketts, R. H., Noll, T. E., and Malone, J. B.** (1991). *NASP Aeroservothermoelasticity Studies* (Technical Note: 104058). Hampton, Virginia: NASA.

[207] **McNamara, J., and Friedmann, P.** (2011). Aeroelastic and Aerothermelastic Analysis in Hypersonic Flow: Past, Present, and Future. *AIAA Journal*, 49(6), 1089-1122.

[208] **Garrick, I. E.** (1961). Problems and Developments in Aerothermoelasticity. Proceedings of Symposium on Aerothermoelasticity. Ohio: Aeronautical System Division of United States Air Force.

[209] **Sadd, M. H.** (2021). *Elasticity Theory, Applications, and Numerics* (4 ed.). London, San Diego, Cambridge, Oxford: Academic Press, Elsevier Inc.

[210] **Ahlers, M.** (2019). *An Introduction to Aircraft Thermal Management*. SAE International.

[211] **Arpaci, V. S., Selamet, A., and Kao, S.** (2000). *Introduction to Heat Transfer*. London, Sydney, Toronto, Mexico, New Delhi, Tokyo, Singapore, Rio de Janerio: Prentice-Hall, Inc.

[212] **Holman, J. P.** (2010). *Heat Transfer* (10 ed.). New York: McGraw-Hill Companies, Inc.

[213] **Lavine, A. S., Bergman, T. L., Incropera, F. P., and DeWitt, D.** (2011). *Fundamentals of Heat and Mass Transfer* (7 ed.). John Wiley & Sons Pub.

[214] **Schuh, H.** (1965). *Heat Transfer in Structures*. Oxford, London, Edinburgh, New York, Paris, Frankfurt: Pergamon Press Ltd.

[215] **Cha, J. H.** (2014). Variation of Supersonic Aircraft Skin Temperature under. *Journal of the KIMST*, 463-470.

[216] **Robbins, D., Boblik, J., and Plag, K.** (2018). F-35 Subsystems Design, Development and Verification. *Aviation Technology, Integration, and Operations Conference*. Atlanta, Georgia: AIAA.

[217] **Eslami, M. R., Hetnarski, R. B., Ignaczak, J., and Noda, N.** (2013). *Theory of Elasticity and Thermal Stresses: Explanations, Problems and Solutions*. Dordrecht, Heidelberg, New York, London: Springer Pub.

[218] **Norwood, S., Brown, K., Malaznik, S., Schneberger, B., and Fuller, K.** (2022). A Study of Airframe Thermal Stresses in Hybrid Composite-Metallic Structure. *AIAA Scitech 2022 Forum*. San Diego: AIAA, April 15-17.

[219] **Perrons, R.** (1997). *Make-Buy Decisions in the U.S. Aircraft Industry* (Master Thesis). Massachusetts Institute of Technology.

[220] **Sneddon, I. N.** (1974). *The Linear Theory of Thermoelasticity*. Wien, New York: Springer-Verlag Pub.

[221] **Nowacki, W.** (2013). *Thermoelasticity*. Warsaw: Pergamon Press.

[222] **Parkus, H.** (1976). *Thermoelasticity*. Wien, New York: Springer-Verlag.

[223] **Thornton, E.** (1996). *Thermal Structures for Aerospace Applications*. American Institute of Aeronautics and Astronautics, Inc.

[224] **Noda, N., Hetnarski, R. B., and Tanigawa, Y.** (2003). *Thermal Stresses*. New York, London: Taylor & Francis Group.

[225] **Ghaboussi, J., Pecknold, D. A., and Wu, X. S.** (2017). *Nonlinear Computational Solid Mechanics*. CRC Press.

[226] **Ghaboussi, J., and Wu, X. S.** (2016). *Numerical Methods in Computational Mechanics*. CRC Press.

[227] **Zhou, J. K.** (1986). *Differential Transformation and Its Application for Electrical Circuits*. Wuhan: Huazhong University Press.

[228] **Jang, M., Chen, C. L., and Liu, Y. C.** (2001). Two-dimensional differential transform for partial differential equations. *Applied Mathematics and Computation*, 123, 109-122.

[229] **Hatami, M., Ganji, D. D., and Sheikholesmani, M.** (2017). *Differential Transformation Method for Mechanical Engineering Problems*. Academic Press.

[230] **Yavuz, M. T., and Ozkol, I.** (2021). Solution Integro-Differential Difference equations via Differential Transform Method. *Cankaya University Journal of Science and Engineering*, 18(1), 33-46.

[231] **Malik, M., and Dang, H. H.** (1998). Vibration analysis of continuous systems by differential transformation. *Applied Mathematics and Computation*, 96, 17-26.

[232] **Blevins, R. D.** (2001). *Formulas for Natural Frequency and Mode Shape*. Krieger Publishing.

[233] **Malik, M., and Allali, M.** (2000). Characteristic equations of rectangular plates by differential transformation. *Journal of Sound and Vibration*, 233(2), 359-366.

[234] **Leissa, A. W.** (1973). The Free Vibration of Rectangular Plates. *Journal of Sound and Vibration*, 31(3), 257-293.

[235] **Bellman, R., Kashef, B. G., and Casti, J.** (1972). Differential quadrature: a technique for the rapid solution of nonlinear partial differential equations. *Journal of Computational Physics*, 10, 40-52.

[236] **Civan, F., and Sliepcevich, C. M.** (1984). Differential quadrature for multidimensional problems. *Journal of Mathematical Analysis and Applications*, 101, 423-443.

[237] **Wang, X., and Bert, W.** (1993). A new approach in applying differential quadrature to static and free vibrational analyses of beams and plates. *Journal of Sound and Vibration*, 162, 566-572.

[238] **Du, H., Lim, M. K., and Lin, R. M.** (1994). Application of generalized differential quadrature method to structural problems. *International Journal of Numerical Methods in Engineering*, 37, 1881-1896.

[239] **Malik, M., and Bert, C. W.** (1996). Implementing multiple boundary conditions in the DQ solution of higher-order PDEs: Application to free vibration of plates. *International Journal for Numerical Methods in Engineering*, 39, 1237-1258.

[240] **Bert, C. W., and Malik, M.** (1996). Semianalytical differential quadrature solution for free vibration analysis of rectangular plates. *AIAA Journal*, 34(3), 601-606.

[241] **Shu, C., and Du, H.** (1997). Implementation of clamped and simply supported boundary conditions in the GDQ free vibration analysis of beams and plates. *International Journal of Solids and Structures*, 34(7), 819-835.

[242] **Tornabene, F., Viola, E., and Inman, D.** (2009). 2-D differential quadrature solution for vibration analysis of functionally graded conical, cylindrical shell and annular plate structures. *Journal of Sound and Vibration*, 328(3), 259-290.

[243] **Tornabene, F., Fantuzzi, N., Bacciocchi, M., and Dimitri, R.** (2015). Free vibrations of composite oval and elliptic cylinders by the generalized differential quadrature method. *Thin-Walled Structures*, 97, 114-129.

[244] **Arikoglu, A., and Ozkol, I.** (2012). Vibratin Analysis Composite Sandwich Plates by the Generalized Differential Quadrature Method. *AIAA Journal*, 50(3), 620-630.

[245] **Yavuz, M. T., and Ozkol, I.** (2021). Comparison of Some Numerical Approaches for Determination of Dynamic Characteristics in Beam and Plate Elements. *European Journal of Science and Technology*, Special Issue 28, 1454-1468.

[246] **Baskaya, E.** (2018). *Heat transfer modes enhancement by using magnetic nanofluids* (Doctorate thesis). Istanbul Technical University, Science Engineering and Technology Institute, Istanbul.

[247] **Shu, C.** (2000). *Differential Quadrature and Its Application in Engineering*. Springer.

[248] **Mazumder, S.** (2016). *Numerical Methods for Partial Differential Equations: Finite Difference and Finite Volume Methods*. Academic Press.

[249] **Levy, H., and Lessman, F.** (1992). *Finite Difference Equations*. New York, NY: Dover Publications.

[250] **LeVeque, R. J.** (2007). *Finite Difference Methods for Ordinary and Partial Differential Equations: Steady-State and Time-dependent Problems*. Society for Industrial and Applied Mathematics.

[251] **Özişik, M. N., Orlande, H. R. B., Colaço, M. J., and Cotta, R. M.** (2017). *Finite Difference Methods in Heat Transfer*. CRC Press.

[252] **Barton, M. V.** (1948). *Finite Difference Equations for the Analysis of Thin Rectangular Plates with Combinations of Fixed and Free Edges* (Technical Report: 175). Defense Research Lab., University of Texas.

[253] **Barton, M. V.** (1948). *Finite Difference Equations for the Analysis of Thin Rectangular Plates with Combinations of Fixed and Free Edges* (Technical Report: 175). Defense Research Lab., University of Texas.

[254] **Numayr, K. S., Haddad, R. H., and Haddad, M.** (2004). Free vibration of composite plates using the finite difference method. *Thin-Walled Structures*, 42(3), 399-414.

[255] **Numayr, K. S., Haddad, M. A., and Ayoub, A.** (2006). Investigation of free vibrations of composite beams by using the finite-difference method. *Mechanics of Composite Materials*, 42, 231-242.

[256] **Mukhopadhyay, M.** (2021). *Structural Dynamics: Vibrations and Systems*. Springer.

[257] **Navazi, H. M., Bornassi, S., Haddadpour, H.**(2017).Vibration analysis of a rotating magnetorheological tapered sandwich beam, International *Journal of Mechanical Sciences*,122, 308-317.

[258] **Wakashima, K., Hirano, T., Niino, M.** (1990). Space Applications of Advanced Structural Materials.

[259] **Touloukian, Y. S.** (1967). *Thermophysical Properties of High Temperature Solid Materials* (Technical Report: AD0649950). Ohio: Wright-Patterson Air Force Base.

[260] **Reddy, J. N., and Chin C. D.** (1998). Thermomehaical analyis of functionally graded cylinders and plates, *Journal Thermal Stress*, 21, 593–626.

[261] **Paul, A., and Das, D.** (2016). Nonlinear Thermal Postbkling analysis of FGM Timoshenko Beam under Nonuniform Temperature Rise across Thickness. *Engineering Science and Technology*, 19 (2016), 1608-1625.

[262] **Epishin, A., and Lisovenko, D.** (2023). Comparison of Isotheal and Adiabatic Elasticity Characteristics of the Single Crystal Nickel-Based Superalloy CMSX-4 in the Temperature Range Between Room Temperature and 1300°C. *Mechanics of Solids*, 58, 1587-1598.

[263] **Abas, R., Hayashi, M., and Seetharaman, S.** (2007). Thermal Diffusivity Measurements of CMSX-4 Alloy by the Laser-Flash Method, *International Journal of Thermophysics*, 28, 109-122.

[264] **Noda, N.** (1993). Thermal Stresses in Materials with Temperature Dependent Properties. In: Schneider, G.A., Petzow, G. (eds) Thermal Shock and Thermal Fatigue Behavior of Advanced Ceramics. NATO ASI Series, vol 241. Springer, Dordrecht.

[265] **Swaminathan, K., and Sangeetha, D. M.** (2017). Thermal analysis of FGM plates – A critical review of various modeling techniques and solution methods. *Composite Structures*, 160, 43-60.

[266] ***Pratt and Whitney.*** *(n.d.). F100 Engines. Retrieved August 30, 2023, from https://www.prattwhitney.com/en/products/military-engines /f100*

[267] ***NASA Glenn Research Center.*** *(n.d.). Gas Turbine Parts. Retrieved October 29, 2023, from https://www.grc.nasa.gov/www/k-12/airplane /entb.html*

[268] ***Military Blog.*** *(n.d.). F100-PW-220 Turbofan Engine. Retrieved November 10, 2023, from https://military-blog.com/f100-pw-220-engine/*

[269] ***GrabCAD.*** *(n.d.). Low Bypass Turbofan Pratt & Whitney F100. Retrieved April 23, 2023, from https://grabcad.com/library/low-bypass-turbofan-pratt-whitney-f100*

[270] **Chakraverty, S., and Pradhan, K.** (2016). *Vibration of functionally graded beams and plates*, Academic Press.

[271] **Aydogdu, M., and Taskin, V.** (2007). Free vibration analysis of functionally graded beams with simply supported edges. *Materials & Design*, 28(5), 1651-1656.

[272] **Wang, C. M., Reddy, J. N., and Lee, K. H.** (2000). *Shear deformable beams and plates.* Elsevier Science Ltd.

[273] **Ochsner, A.** (2021). *Classical Beam Theories of Structural Mechanics*. Springer.

[274] **Hodges, D. H., and Dowell, E. H.** (1974). *Nonlinear equations of motion for the elastic bending and torsion of twisted nonuniform rotor blades* (Technical Note: A-5711). NASA Ames Research Center.

[275] **Shen, H**. (2009), *Functionally Graded Materials: Non-linear Analysis of Plates and Shells*, CRC Press, New York, NY, USA.

APPENDICES

APPENDIX A: Plate Mode Shapes

APPENDIX B: Influence of Temperature and Volume Fraction Index

APPENDIX C: Influence of Rotation Speed and Material Distribution

APPENDIX D: Influence of Slenderness Ratio

APPENDIX E: Influence of Gradiation Index

APPENDIX F: Influence of Rotation Speed and Shear Deformation

APPENDIX G: Influence of Temperature and Shear Deformation

APPENDIX H: Influence of Rotation Speed and Temperature

APPENDIX A

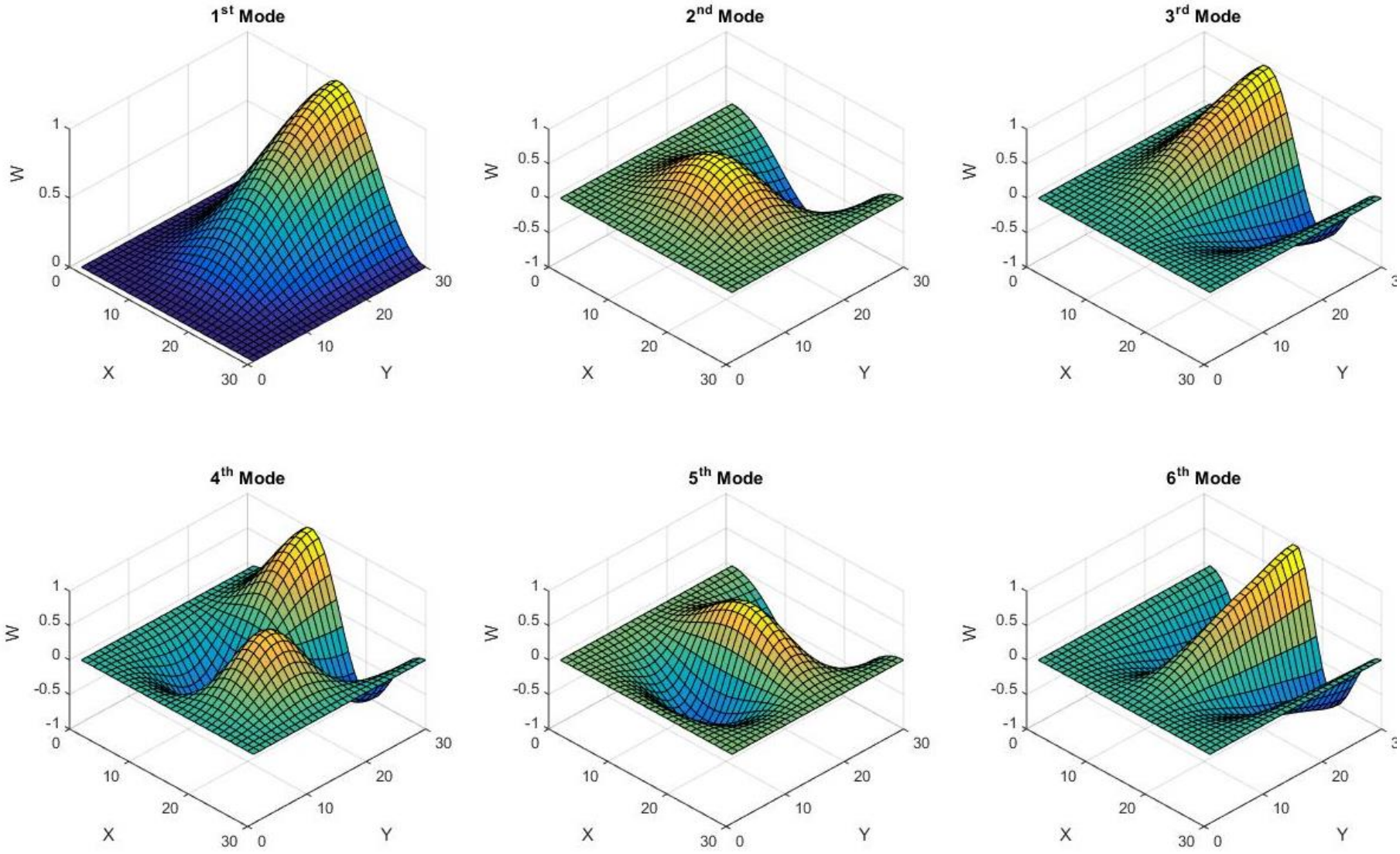

Figure A.1 : Kirchhoff-Love plate mode shapes for SSSF BCs.

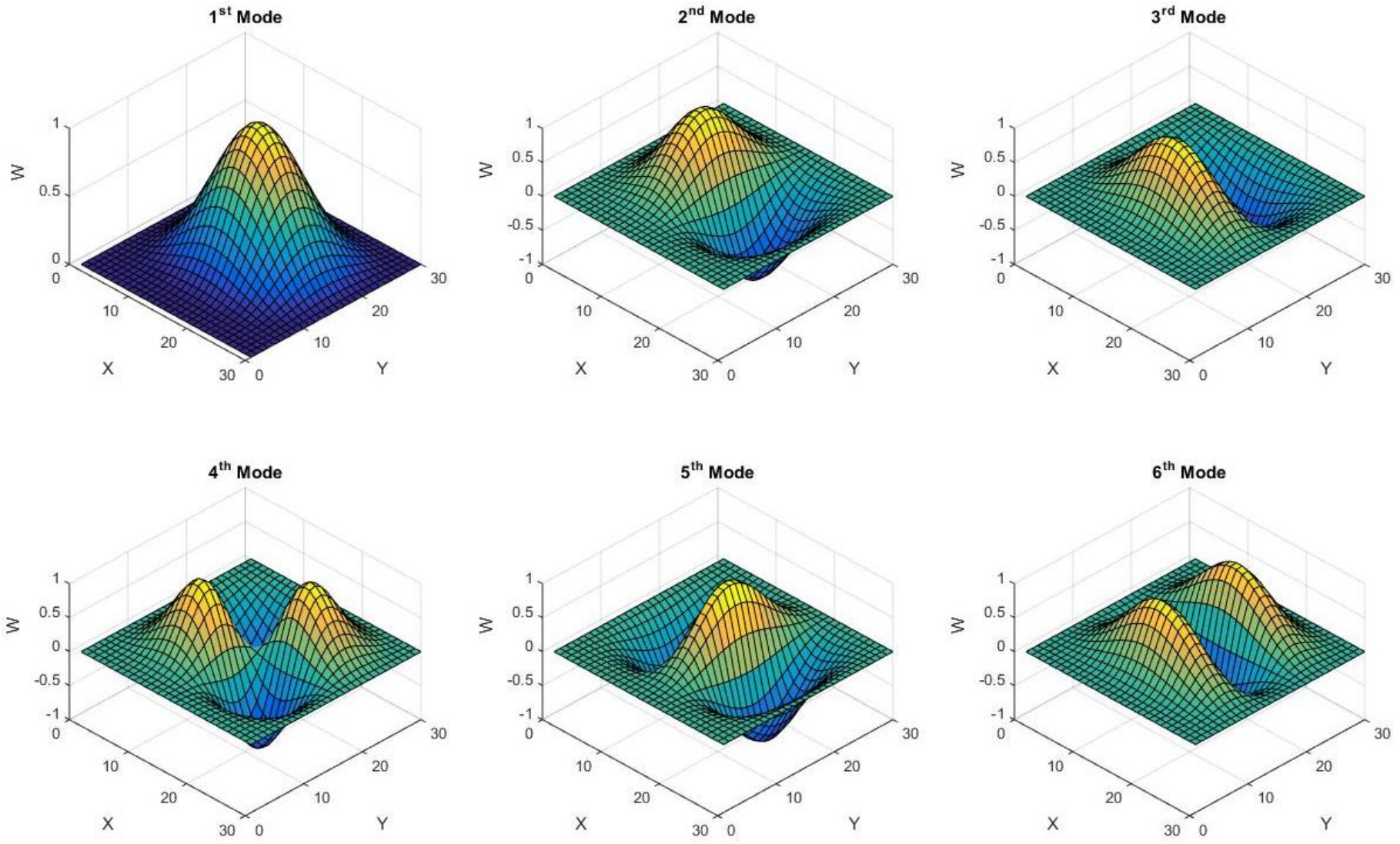

Figure A.2 : Kirchhoff-Love plate mode shapes for SCSS BCs.

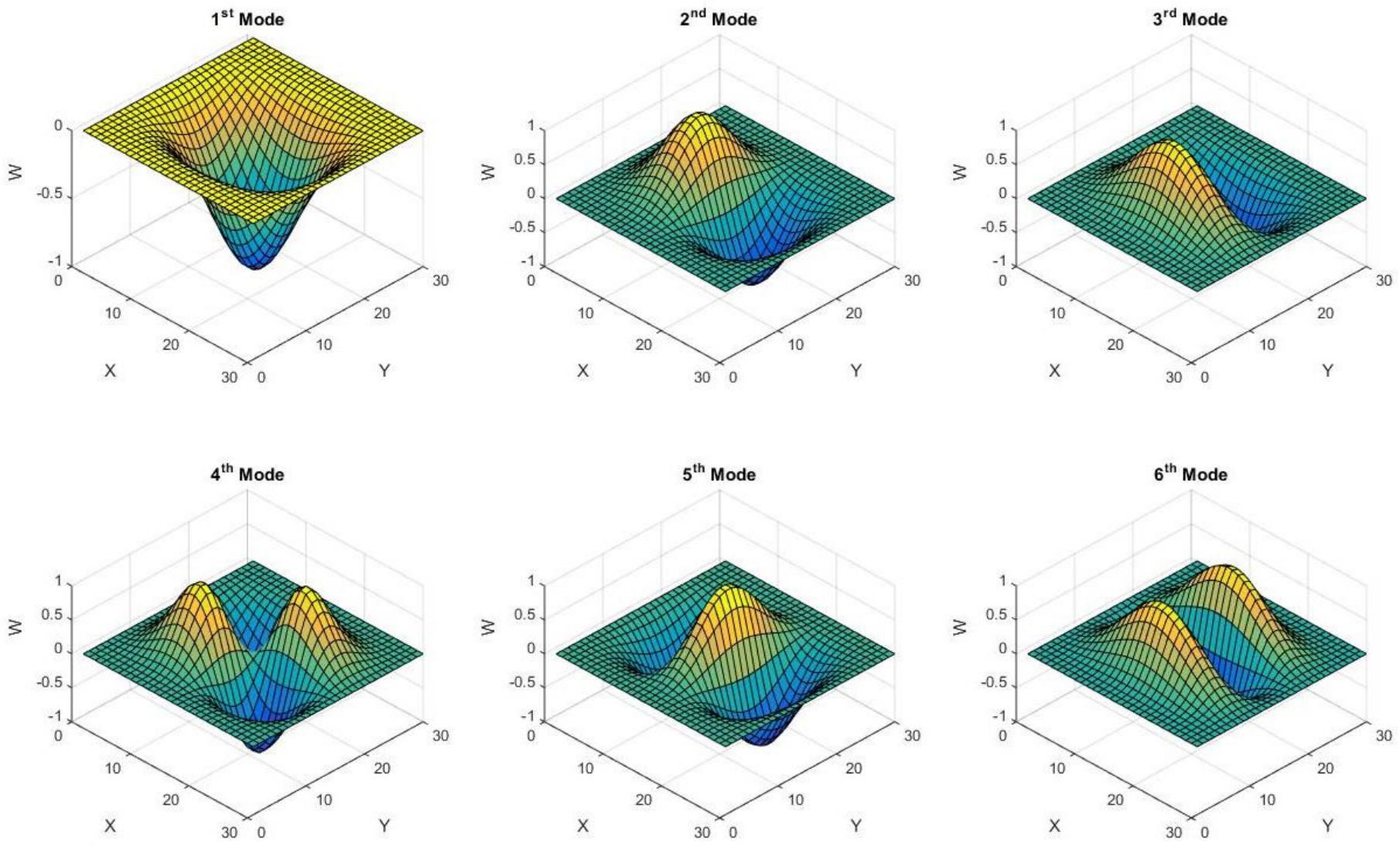

Figure A.3 : Kirchhoff –Love plate mode shapes for SCSC BCs.

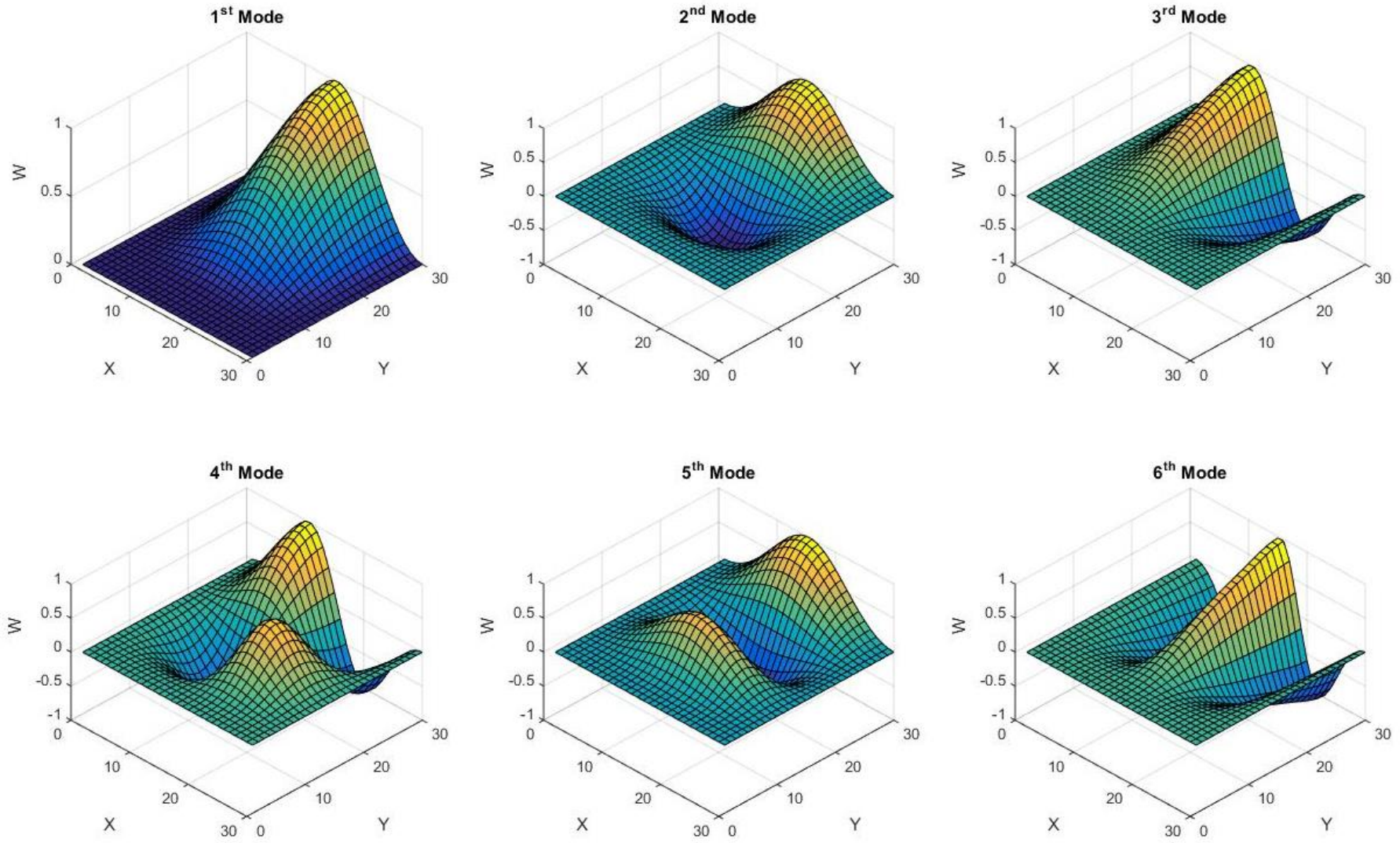

Figure A.4 : Kirchhoff –Love plate mode shapes for SCSF BCs.

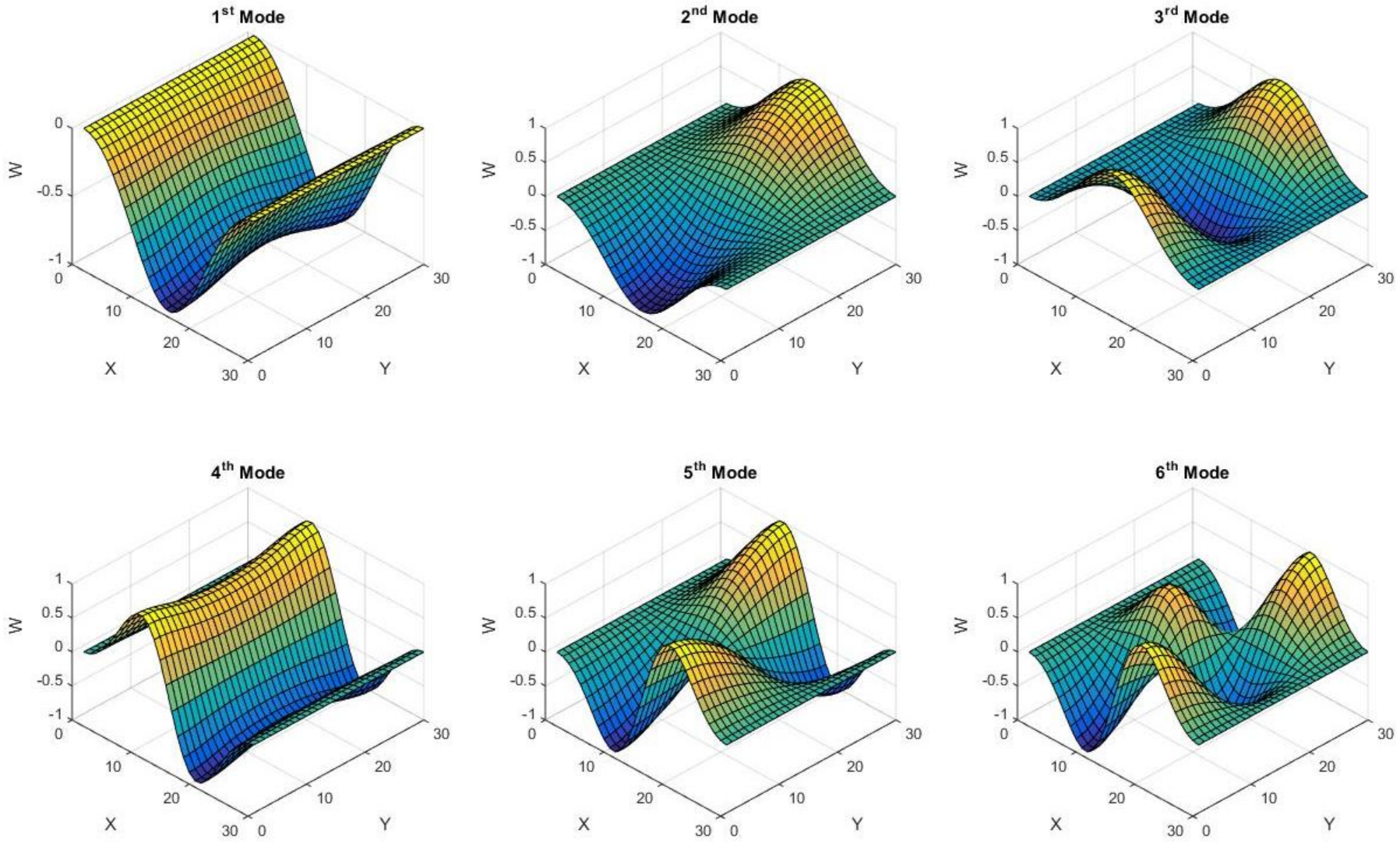

Figure A.5 : Kirchhoff-Love plate mode shapes for SFSF BCs.

APPENDIX B

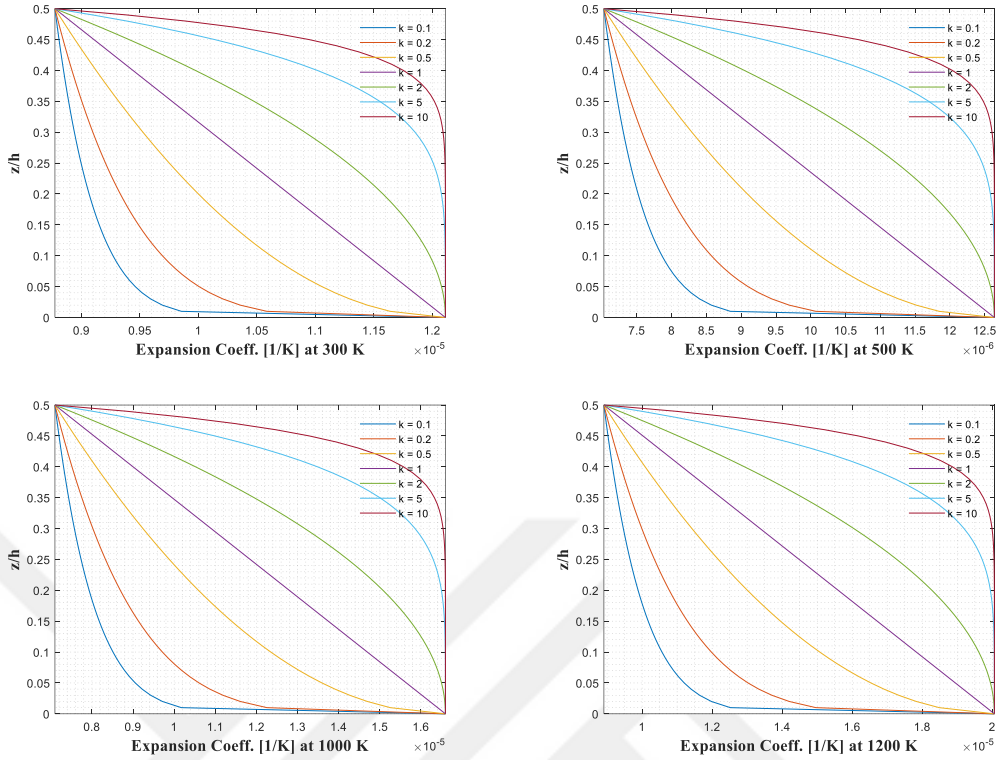

Figure B.6 : Influence of temperature and volume fraction index on the thermal expansion coefficient in the thickness direction (CMSX-4 and Zirconia)

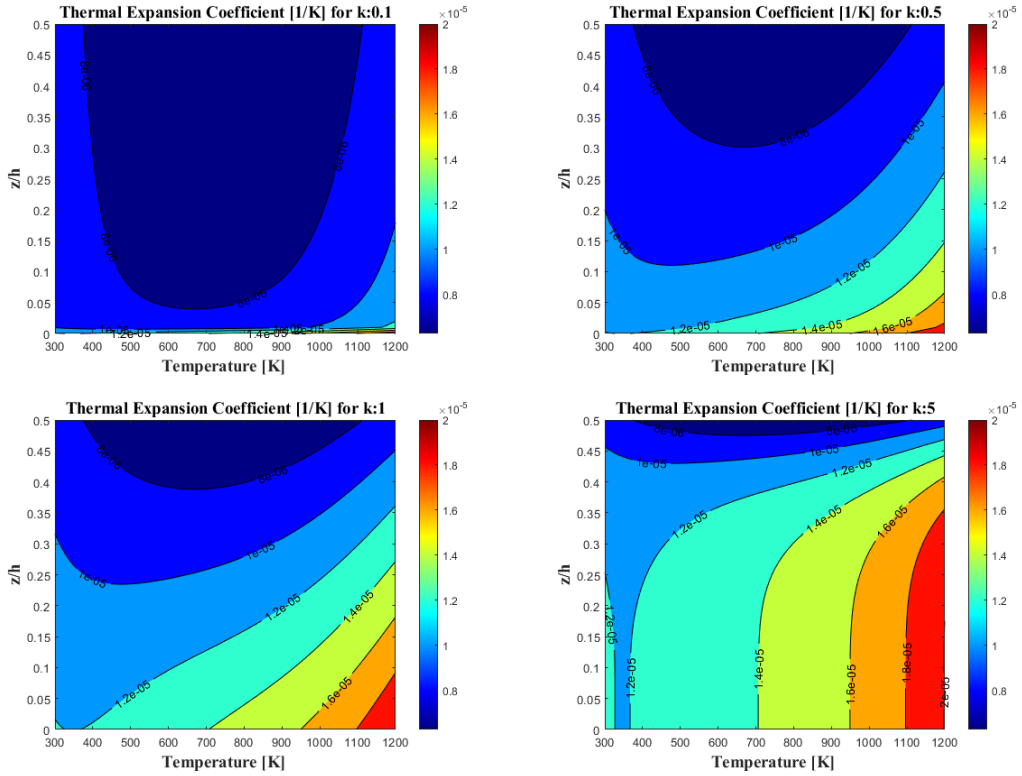

Figure B.7 : Influence of temperature and volume fraction index on the thermal expansion coefficient in the thickness direction (CMSX-4 and Zirconia)

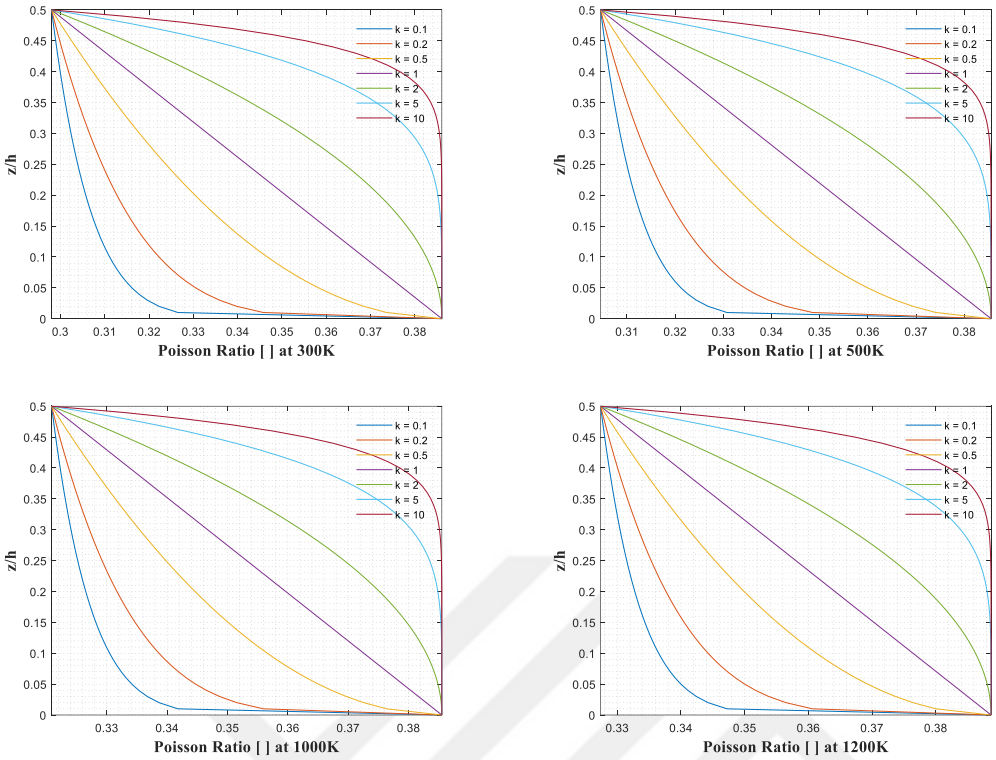

Figure B.8 : Influence of temperature and volume fraction index on the Poisson ratio in the thickness direction (CMSX-4 and Zirconia)

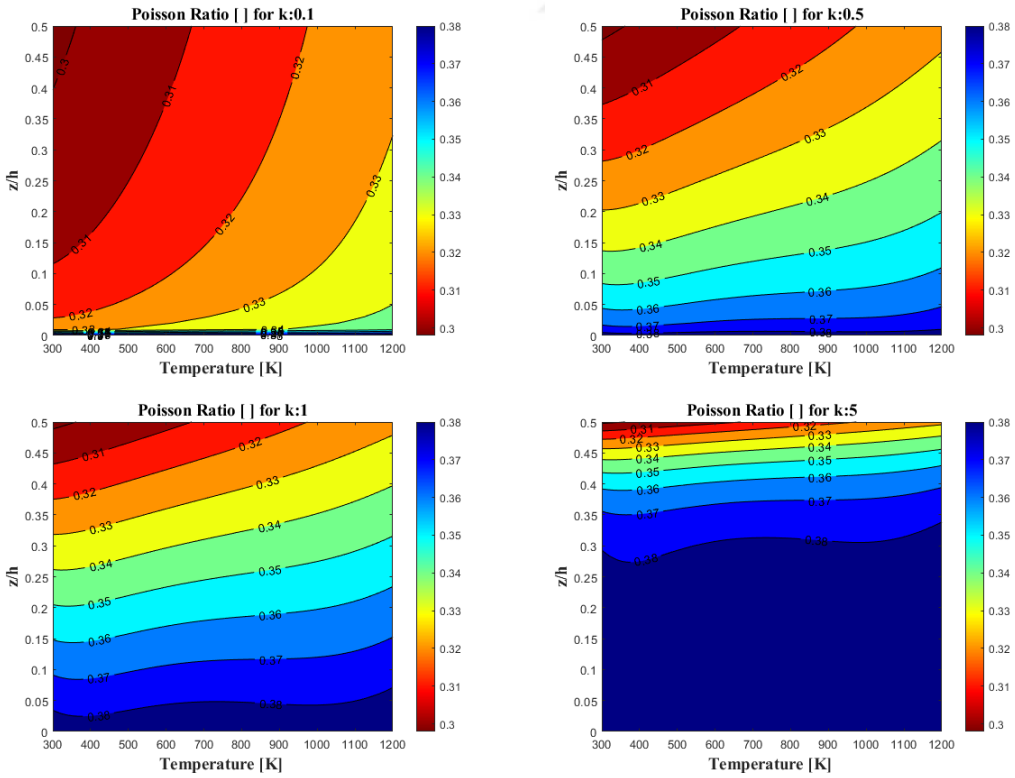

Figure B.9 : Influence of temperature and volume fraction index on the Poisson ratio in the thickness direction (CMSX-4 and Zirconia)

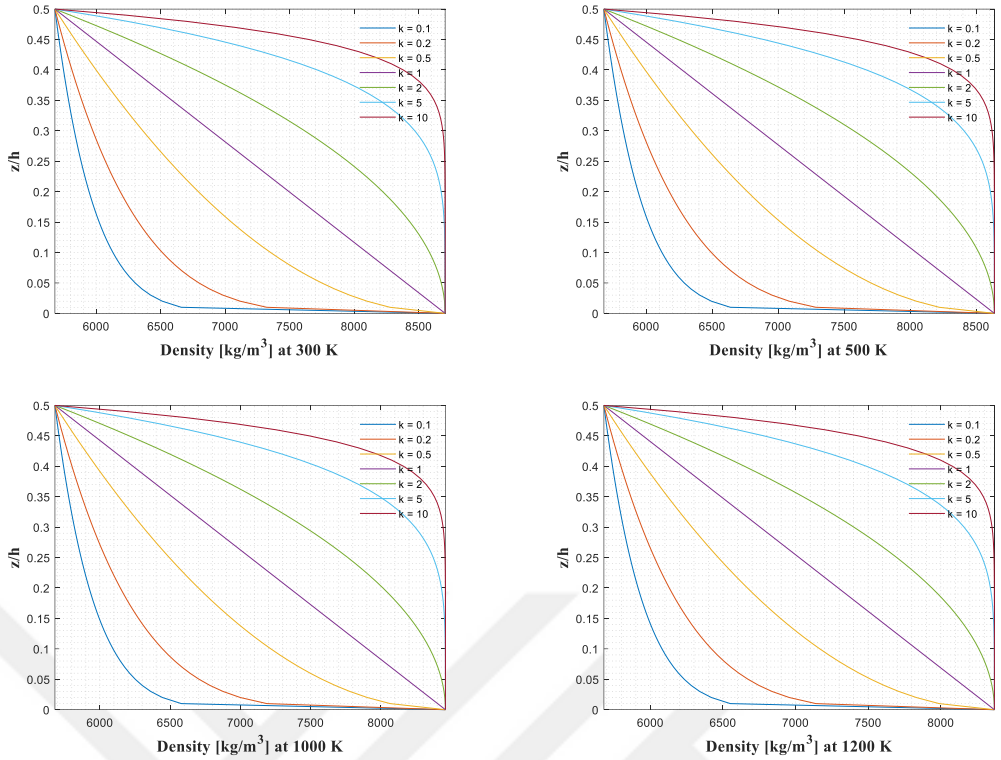

Figure B.10 : Influence of temperature and volume fraction index on the density in the thickness direction (CMSX-4 and Zirconia)

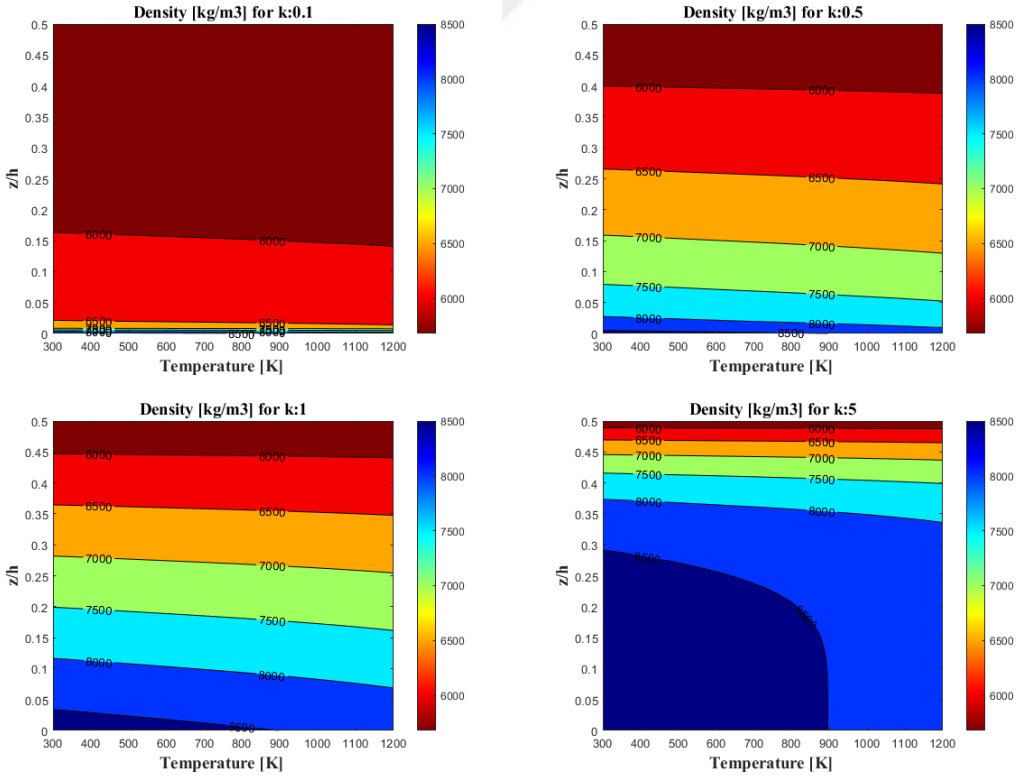

Figure B.11 : Influence of temperature and volume fraction index on the density in the thickness direction (CMSX-4 and Zirconia)

APPENDIX C

Table C.1 : Variations of the fundamental frequencies of rotating FGM beams to rotation speed, and material distribution (*L/h=5, c_b=c_h=0, μ=0, ξ=0, T=1500°K*)

Fundamental Natural Freqeuncies

First Dimensionless Natural Frequency

	CBT	FSDBT	CBT	FSDBT	CBT	FSDBT	CBT	FSDBT	CBT	FSDBT
λ	*k = 0*	*k = 0*	*k = 1*	*k = 1*	*k = 10*	*k = 10*	*k = 100*	*k = 100*	*Metal*	*Metal*
0	1,82343	1,07571	1,55392	1,07571	1,23696	1,07571	1,12706	1,07571	1,11101	1,07571
2	2,14782	1,27058	1,83095	1,27058	1,45801	1,27058	1,32881	1,27058	1,30995	1,27058
4	2,90257	1,72008	2,47526	1,72008	1,9719	1,72008	1,79768	1,72008	1,77225	1,72008
6	3,82697	2,26615	3,26419	2,26615	2,60092	2,26615	2,37144	2,26615	2,33795	2,26615
8	4,81366	2,84645	4,10616	2,84645	3,27208	2,84645	2,98356	2,84645	2,94146	2,84645
10	5,8254	3,44082	4,96944	3,44082	3,96016	3,44082	3,61106	3,44082	3,56012	3,44082

Second Dimensionless Natural Frequency

	CBT	FSDBT	CBT	FSDBT	CBT	FSDBT	CBT	FSDBT	CBT	FSDBT
λ	*k = 0*	*k = 0*	*k = 1*	*k = 1*	*k = 10*	*k = 10*	*k = 100*	*k = 100*	*Metal*	*Metal*
0	11,4633	5,7847	9,7843	5,7847	7,8008	5,7847	7,1155	5,7847	7,0155	5,7847
2	11,7626	5,9804	10,0397	5,9804	8,0042	5,9804	7,3008	5,9804	7,1982	5,9804
4	12,6184	6,5311	10,7699	6,5311	8,5857	6,5311	7,8307	6,5311	7,7206	6,5311
6	13,9281	7,3533	11,8873	7,3533	9,4756	7,3533	8,6418	7,3533	8,5202	7,3533
8	15,5752	8,3621	13,2928	8,3621	10,5950	8,3621	9,6621	8,3621	9,5260	8,3621
10	17,4609	9,4930	14,9018	9,4930	11,8767	9,4930	10,8305	9,4930	10,6778	9,4930

Third Dimensionless Natural Frequency

	CBT	FSDBT	CBT	FSDBT	CBT	FSDBT	CBT	FSDBT	CBT	FSDBT
λ	*k = 0*	*k = 0*	*k = 1*	*k = 1*	*k = 10*	*k = 10*	*k = 100*	*k = 100*	*Metal*	*Metal*
0	32,0815	13,6581	27,3759	13,6581	21,8209	13,6581	19,9003	13,6581	19,6201	13,6581
2	32,3782	13,8884	27,6291	13,8884	22,0226	13,8884	20,0842	13,8884	19,8014	13,8884
4	33,2508	14,5518	28,3740	14,5518	22,6158	14,5518	20,6249	14,5518	20,3344	14,5518
6	34,6511	15,5782	29,5694	15,5782	23,5679	15,5782	21,4927	15,5782	21,1899	15,5782
8	36,5118	16,8831	31,1577	16,8831	24,8330	16,8831	22,6458	16,8831	22,3267	16,8831
10	38,7587	18,3889	33,0756	18,3889	26,3607	18,3889	24,0383	18,3889	23,6994	18,3889

Fourth Dimensionless Natural Frequency

	CBT	FSDBT	CBT	FSDBT	CBT	FSDBT	CBT	FSDBT	CBT	FSDBT
λ	*k = 0*	*k = 0*	*k = 1*	*k = 1*	*k = 10*	*k = 10*	*k = 100*	*k = 100*	*Metal*	*Metal*
0	62,8563	22,5456	53,6320	22,5456	42,7455	22,5456	38,9810	22,5456	38,4317	22,5456
2	63,1625	22,8294	53,8935	22,8294	42,9538	22,8294	39,1708	22,8294	38,6189	22,8294
4	64,0713	23,6517	54,6693	23,6517	43,5718	23,6517	39,7341	23,6517	39,1741	23,6517
6	65,5540	24,9373	55,9353	24,9373	44,5801	24,9373	40,6532	24,9373	40,0802	24,9373
8	67,5675	26,5895	57,6543	26,5895	45,9493	26,5895	41,9012	26,5895	41,3105	26,5895
10	70,0590	28,5129	59,7813	28,5129	47,6436	28,5129	43,4456	28,5129	42,8330	28,5129

Table C.2 : Variations of the fundamental frequencies of rotating FGM beams to rotation speed, and material distribution ($L/h=20$, $c_b=c_h=0$, $\mu=0$, $\xi=0$, $T=300^oK$)

Fundamental Natural Freqeuncies

First Dimensionless Natural Frequency

	CBT	FSDBT	CBT	FSDBT	CBT	FSDBT	CBT	FSDBT	CBT	FSDBT
λ	*k = 0*	*k = 0*	*k = 1*	*k = 1*	*k = 10*	*k = 10*	*k = 100*	*k = 100*	*Metal*	*Metal*
0	1,5310	1,0980	1,3252	1,0980	1,1520	1,0980	1,1065	1,0980	1,1003	1,0980
2	1,8016	1,2922	1,5594	1,2922	1,3556	1,2922	1,3020	1,2922	1,2948	1,2922
4	2,4320	1,7444	2,1051	1,7444	1,8300	1,7444	1,7577	1,7444	1,7478	1,7444
6	3,2051	2,2986	2,7743	2,2986	2,4117	2,2986	2,3164	2,2986	2,3035	2,2986
8	4,0309	2,8901	3,4892	2,8901	3,0331	2,8901	2,9132	2,8901	2,8970	2,8901
10	4,8780	3,4965	4,2224	3,4965	3,6706	3,4965	3,5255	3,4965	3,5058	3,4965

Second Dimensionless Natural Frequency

	CBT	FSDBT	CBT	FSDBT	CBT	FSDBT	CBT	FSDBT	CBT	FSDBT
λ	*k = 0*	*k = 0*	*k = 1*	*k = 1*	*k = 10*	*k = 10*	*k = 100*	*k = 100*	*Metal*	*Metal*
0	9,5946	6,7986	8,3051	6,7986	7,2196	6,7986	6,9343	6,7986	6,8955	6,7986
2	9,8472	6,9806	8,5238	6,9806	7,4097	6,9806	7,1168	6,9806	7,0771	6,9806
4	10,5690	7,5001	9,1487	7,5001	7,9529	7,5001	7,6385	7,5001	7,5959	7,5001
6	11,6728	8,2931	10,1041	8,2931	8,7835	8,2931	8,4363	8,2931	8,3891	8,2931
8	13,0598	9,2878	11,3047	9,2878	9,8272	9,2878	9,4387	9,2878	9,3859	9,2878
10	14,6465	10,4237	12,6783	10,4237	11,0212	10,4237	10,5855	10,4237	10,5263	10,4237

Third Dimensionless Natural Frequency

	CBT	FSDBT	CBT	FSDBT	CBT	FSDBT	CBT	FSDBT	CBT	FSDBT
λ	*k = 0*	*k = 0*	*k = 1*	*k = 1*	*k = 10*	*k = 10*	*k = 100*	*k = 100*	*Metal*	*Metal*
0	26,8650	18,6822	23,2545	18,6822	20,2152	18,6822	19,4161	18,6822	19,3076	18,6822
2	27,1157	18,8646	23,4715	18,8646	20,4038	18,8646	19,5973	18,8646	19,4878	18,8646
4	27,8527	19,4002	24,1095	19,4002	20,9584	19,4002	20,1300	19,4002	20,0175	19,4002
6	29,0353	20,2575	25,1332	20,2575	21,8483	20,2575	20,9846	20,2575	20,8674	20,2575
8	30,6060	21,3930	26,4929	21,3930	23,0302	21,3930	22,1198	21,3930	21,9962	21,3930
10	32,5020	22,7592	28,1342	22,7592	24,4570	22,7592	23,4901	22,7592	23,3589	22,7592

Fourth Dimensionless Natural Frequency

	CBT	FSDBT	CBT	FSDBT	CBT	FSDBT	CBT	FSDBT	CBT	FSDBT
λ	*k = 0*	*k = 0*	*k = 1*	*k = 1*	*k = 10*	*k = 10*	*k = 100*	*k = 100*	*Metal*	*Metal*
0	52,6448	35,6721	45,5696	35,6721	39,6137	35,6721	38,0479	35,6721	37,8353	35,6721
2	52,9036	35,8634	45,7937	35,8634	39,8085	35,8634	38,2349	35,8634	38,0213	35,8634
4	53,6716	36,4304	46,4585	36,4304	40,3864	36,4304	38,7900	36,4304	38,5732	36,4304
6	54,9245	37,3530	47,5430	37,3530	41,3292	37,3530	39,6954	37,3530	39,4736	37,3530
8	56,6254	38,6013	49,0155	38,6013	42,6092	38,6013	40,9248	38,6013	40,6961	38,6013
10	58,7297	40,1393	50,8371	40,1393	44,1926	40,1393	42,4456	40,1393	42,2084	40,1393

Table C.3 : Variations of the fundamental frequencies of rotating FGM beams to rotation speed, and material distribution ($L/h=20$, $c_b=c_h=0$, $\mu=0$, $\xi=0$, $T=900^oK$)

Fundamental Natural Freqeuncies

First Dimensionless Natural Frequency

	CBT	FSDBT	CBT	FSDBT	CBT	FSDBT	CBT	FSDBT	CBT	FSDBT
λ	*k = 0*	*k = 0*	*k = 1*	*k = 1*	*k = 10*	*k = 10*	*k = 100*	*k = 100*	*Metal*	*Metal*
0	1,3906	1,0922	1,2313	1,0922	1,1205	1,0922	1,0973	1,0922	1,0944	1,0922
2	1,6374	1,2874	1,4509	1,2874	1,3207	1,2874	1,2934	1,2874	1,2899	1,2874
4	2,2121	1,7412	1,9616	1,7412	1,7862	1,7412	1,7493	1,7412	1,7446	1,7412
6	2,9164	2,2965	2,5872	2,2965	2,3561	2,2965	2,3076	2,2965	2,3014	2,2965
8	3,6684	2,8887	3,2549	2,8887	2,9644	2,8887	2,9033	2,8887	2,8956	2,8887
10	4,4398	3,4955	3,9396	3,4955	3,5881	3,4955	3,5142	3,4955	3,5048	3,4955

Second Dimensionless Natural Frequency

	CBT	FSDBT	CBT	FSDBT	CBT	FSDBT	CBT	FSDBT	CBT	FSDBT
λ	*k = 0*	*k = 0*	*k = 1*	*k = 1*	*k = 10*	*k = 10*	*k = 100*	*k = 100*	*Metal*	*Metal*
0	8,7409	6,8132	7,7638	6,8132	7,0739	6,8132	6,9285	6,8132	6,9099	6,8132
2	8,9706	6,9947	7,9675	6,9947	7,2593	6,9947	7,1100	6,9947	7,0910	6,9947
4	9,6271	7,5130	8,5495	7,5130	7,7893	7,5130	7,6290	7,5130	7,6086	7,5130
6	10,6310	8,3044	9,4398	8,3044	8,5998	8,3044	8,4229	8,3044	8,4003	8,3044
8	11,8927	9,2976	10,5588	9,2976	9,6188	9,2976	9,4209	9,2976	9,3956	9,2976
10	13,3364	10,4321	11,8394	10,4321	10,7849	10,4321	10,5629	10,4321	10,5346	10,4321

Third Dimensionless Natural Frequency

	CBT	FSDBT	CBT	FSDBT	CBT	FSDBT	CBT	FSDBT	CBT	FSDBT
λ	*k = 0*	*k = 0*	*k = 1*	*k = 1*	*k = 10*	*k = 10*	*k = 100*	*k = 100*	*Metal*	*Metal*
0	24,4630	18,7002	21,7179	18,7002	19,7842	18,7002	19,3771	18,7002	19,3252	18,7002
2	24,6911	18,8823	21,9203	18,8823	19,9685	18,8823	19,5575	18,8823	19,5051	18,8823
4	25,3618	19,4174	22,5152	19,4174	20,5103	19,4174	20,0881	19,4174	20,0343	19,4174
6	26,4378	20,2740	23,4699	20,2740	21,3796	20,2740	20,9396	20,2740	20,8835	20,2740
8	27,8671	21,4085	24,7379	21,4085	22,5344	21,4085	22,0705	21,4085	22,0114	21,4085
10	29,5924	22,7736	26,2687	22,7736	23,9285	22,7736	23,4359	22,7736	23,3731	22,7736

Fourth Dimensionless Natural Frequency

	CBT	FSDBT	CBT	FSDBT	CBT	FSDBT	CBT	FSDBT	CBT	FSDBT
λ	*k = 0*	*k = 0*	*k = 1*	*k = 1*	*k = 10*	*k = 10*	*k = 100*	*k = 100*	*Metal*	*Metal*
0	47,9299	35,6919	42,5443	35,6919	38,7536	35,6919	37,9558	35,6919	37,8542	35,6919
2	48,1655	35,8831	42,7533	35,8831	38,9440	35,8831	38,1423	35,8831	38,0401	35,8831
4	48,8644	36,4497	43,3735	36,4497	39,5087	36,4497	38,6954	36,4497	38,5917	36,4497
6	50,0046	37,3718	44,3851	37,3718	40,4301	37,3718	39,5977	37,3718	39,4916	37,3718
8	51,5526	38,6194	45,7587	38,6194	41,6810	38,6194	40,8229	38,6194	40,7135	38,6194
10	53,4676	40,1566	47,4580	40,1566	43,2286	40,1566	42,3386	40,1566	42,2251	40,1566

Table C.4 : Variations of the fundamental frequencies of rotating FGM beams to rotation speed, and material distribution (*L/h=20*, $c_b=c_h=0$, $\mu=0$, $\xi=0$, *T=1500°K*)

Fundamental Natural Freqeuncies

First Dimensionless Natural Frequency

	CBT	FSDBT	CBT	FSDBT	CBT	FSDBT	CBT	FSDBT	CBT	FSDBT
λ	*k = 0*	*k = 0*	*k = 1*	*k = 1*	*k = 10*	*k = 10*	*k = 100*	*k = 100*	*Metal*	*Metal*
0	1,8111	1,0910	1,5383	1,0910	1,2204	1,0910	1,1094	1,0910	1,0932	1,0910
2	2,1372	1,2926	1,8177	1,2926	1,4441	1,2926	1,3141	1,2926	1,2950	1,2926
4	2,8943	1,7581	2,4656	1,7581	1,9619	1,7581	1,7872	1,7581	1,7616	1,7581
6	3,8203	2,3252	3,2569	2,3252	2,5936	2,3252	2,3638	2,3252	2,3303	2,3252
8	4,8080	2,9284	4,1004	2,9284	3,2664	2,9284	2,9778	2,9284	2,9356	2,9284
10	5,8204	3,5456	4,9646	3,5456	3,9556	3,5456	3,6064	3,5456	3,5554	3,5456

Second Dimensionless Natural Frequency

	CBT	FSDBT	CBT	FSDBT	CBT	FSDBT	CBT	FSDBT	CBT	FSDBT
λ	*k = 0*	*k = 0*	*k = 1*	*k = 1*	*k = 10*	*k = 10*	*k = 100*	*k = 100*	*Metal*	*Metal*
0	11,4938	6,9584	9,8232	6,9584	7,8422	6,9584	7,1596	6,9584	7,0601	6,9584
2	11,7941	7,1414	10,0788	7,1414	8,0455	7,1414	7,3448	7,1414	7,2426	7,1414
4	12,6524	7,6640	10,8098	7,6640	8,6269	7,6640	7,8742	7,6640	7,7644	7,6640
6	13,9658	8,4630	11,9285	8,4630	9,5170	8,4630	8,6850	8,4630	8,5636	8,4630
8	15,6173	9,4666	13,3358	9,4666	10,6370	9,4666	9,7054	9,4666	9,5695	9,4666
10	17,5076	10,6143	14,9470	10,6143	11,9197	10,6143	10,8742	10,6143	10,7217	10,6143

Third Dimensionless Natural Frequency

	CBT	FSDBT	CBT	FSDBT	CBT	FSDBT	CBT	FSDBT	CBT	FSDBT
λ	*k = 0*	*k = 0*	*k = 1*	*k = 1*	*k = 10*	*k = 10*	*k = 100*	*k = 100*	*Metal*	*Metal*
0	32,1193	19,0172	27,4240	19,0172	21,8721	19,0172	19,9551	19,0172	19,6755	19,0172
2	32,4180	19,2018	27,6787	19,2018	22,0749	19,2018	20,1399	19,2018	19,8577	19,2018
4	33,2965	19,7440	28,4276	19,7440	22,6712	19,7440	20,6834	19,7440	20,3935	19,7440
6	34,7060	20,6121	29,6294	20,6121	23,6282	20,6121	21,5556	20,6121	21,2533	20,6121
8	36,5785	21,7620	31,2259	21,7620	24,8997	21,7620	22,7144	21,7620	22,3957	21,7620
10	38,8391	23,1458	33,1535	23,1458	26,4349	23,1458	24,1137	23,1458	23,7751	23,1458

Fourth Dimensionless Natural Frequency

	CBT	FSDBT	CBT	FSDBT	CBT	FSDBT	CBT	FSDBT	CBT	FSDBT
λ	*k = 0*	*k = 0*	*k = 1*	*k = 1*	*k = 10*	*k = 10*	*k = 100*	*k = 100*	*Metal*	*Metal*
0	62,8978	36,2170	53,6850	36,2170	42,8019	36,2170	39,0413	36,2170	38,4927	36,2170
2	63,2065	36,4112	53,9482	36,4112	43,0116	36,4112	39,2325	36,4112	38,6811	36,4112
4	64,1224	36,9868	54,7294	36,9868	43,6338	36,9868	39,7997	36,9868	39,2403	36,9868
6	65,6167	37,9233	56,0038	37,9233	44,6489	37,9233	40,7250	37,9233	40,1525	37,9233
8	67,6455	39,1904	57,7341	39,1904	46,0273	39,1904	41,9815	39,1904	41,3912	39,1904
10	70,1555	40,7515	59,8747	40,7515	47,7326	40,7515	43,5360	40,7515	42,9238	40,7515

Table C.5 : Variations of the fundamental frequencies of rotating FGM beams to rotation speed, and material distribution (*L/h=5, c_b=c_h=0, μ=0, ξ=0, T=900ºK*)

Fundamental Natural Freqeuncies

First Dimensionless Natural Frequency

	CBT	FSDBT	CBT	FSDBT	CBT	FSDBT	CBT	FSDBT	CBT	FSDBT
λ	*k = 0*	*k = 0*	*k = 1*	*k = 1*	*k = 10*	*k = 10*	*k = 100*	*k = 100*	*Metal*	*Metal*
0	1,3928	1,0647	1,2354	1,0647	1,1249	1,0647	1,1018	1,0647	1,0988	1,0647
2	1,6397	1,2560	1,4546	1,2560	1,3247	1,2560	1,2974	1,2560	1,2939	1,2560
4	2,2146	1,6979	1,9648	1,6979	1,7895	1,6979	1,7527	1,6979	1,7480	1,6979
6	2,9190	2,2355	2,5901	2,2355	2,3591	2,2355	2,3106	2,2355	2,3044	2,2355
8	3,6711	2,8071	3,2576	2,8071	2,9671	2,8071	2,9061	2,8071	2,8983	2,8071
10	4,4425	3,3927	3,9421	3,3927	3,5906	3,3927	3,5168	3,3927	3,5073	3,3927

Second Dimensionless Natural Frequency

	CBT	FSDBT	CBT	FSDBT	CBT	FSDBT	CBT	FSDBT	CBT	FSDBT
λ	*k = 0*	*k = 0*	*k = 1*	*k = 1*	*k = 10*	*k = 10*	*k = 100*	*k = 100*	*Metal*	*Metal*
0	8,7353	5,7216	7,7538	5,7216	7,0629	5,7216	6,9175	5,7216	6,8990	5,7216
2	8,9637	5,9136	7,9566	5,9136	7,2476	5,9136	7,0983	5,9136	7,0793	5,9136
4	9,6168	6,4541	8,5364	6,4541	7,7754	6,4541	7,6152	6,4541	7,5947	6,4541
6	10,6161	7,2616	9,4235	7,2616	8,5831	7,2616	8,4060	7,2616	8,3835	7,2616
8	11,8727	8,2530	10,5390	8,2530	9,5989	8,2530	9,4007	8,2530	9,3754	8,2530
10	13,3111	9,3650	11,8159	9,3650	10,7616	9,3650	10,5392	9,3650	10,5109	9,3650

Third Dimensionless Natural Frequency

	CBT	FSDBT	CBT	FSDBT	CBT	FSDBT	CBT	FSDBT	CBT	FSDBT
λ	*k = 0*	*k = 0*	*k = 1*	*k = 1*	*k = 10*	*k = 10*	*k = 100*	*k = 100*	*Metal*	*Metal*
0	24,4561	13,5730	21,7055	13,5730	19,7706	13,5730	19,3635	13,5730	19,3117	13,5730
2	24,6825	13,7969	21,9065	13,7969	19,9536	13,7969	19,5427	13,7969	19,4903	13,7969
4	25,3480	14,4421	22,4976	14,4421	20,4917	14,4421	20,0695	14,4421	20,0157	14,4421
6	26,4161	15,4420	23,4462	15,4420	21,3553	15,4420	20,9151	15,4420	20,8589	15,4420
8	27,8353	16,7153	24,7065	16,7153	22,5027	16,7153	22,0385	16,7153	21,9793	16,7153
10	29,5490	18,1871	26,2284	18,1871	23,8883	18,1871	23,3951	18,1871	23,3322	18,1871

Fourth Dimensionless Natural Frequency

	CBT	FSDBT	CBT	FSDBT	CBT	FSDBT	CBT	FSDBT	CBT	FSDBT
λ	*k = 0*	*k = 0*	*k = 1*	*k = 1*	*k = 10*	*k = 10*	*k = 100*	*k = 100*	*Metal*	*Metal*
0	47,9223	22,4782	42,5307	22,4782	38,7387	22,4782	37,9410	22,4782	37,8393	22,4782
2	48,1559	22,7525	42,7381	22,7525	38,9275	22,7525	38,1259	22,7525	38,0237	22,7525
4	48,8490	23,5483	43,3537	23,5483	39,4880	23,5483	38,6746	23,5483	38,5709	23,5483
6	49,9798	24,7946	44,3581	24,7946	40,4023	24,7946	39,5698	24,7946	39,4636	24,7946
8	51,5154	26,4000	45,7220	26,4000	41,6440	26,4000	40,7854	26,4000	40,6760	26,4000
10	53,4155	28,2734	47,4096	28,2734	43,1804	28,2734	42,2896	28,2734	42,1761	28,2734

APPENDIX D

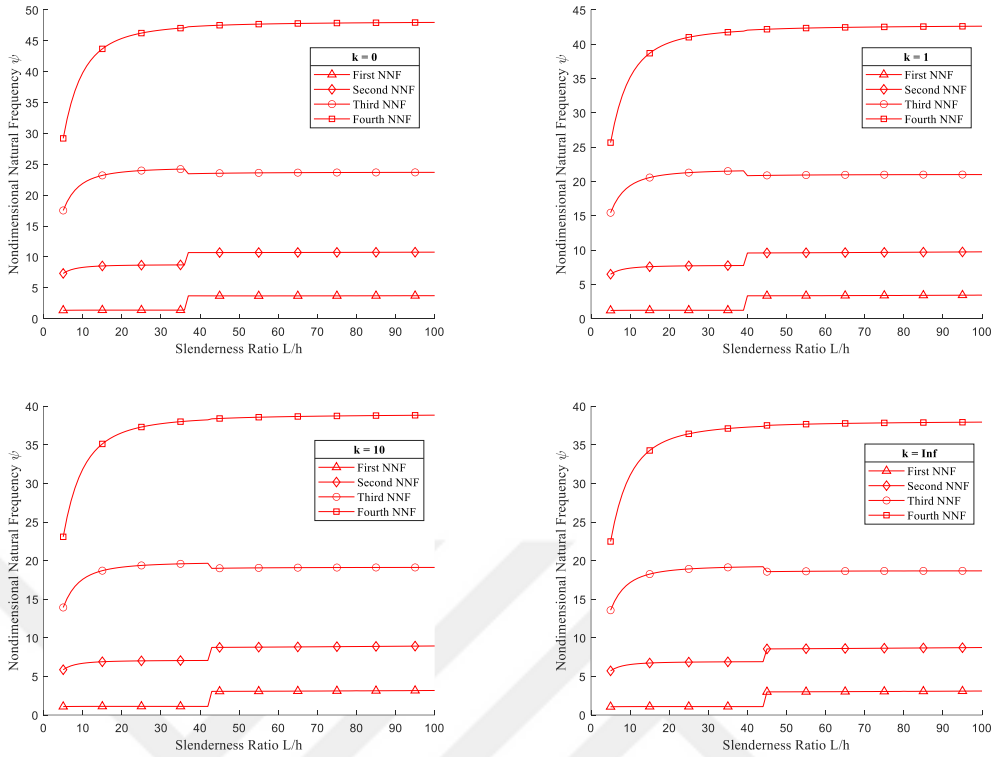

Figure D.12 : Variation of first four NNF of Timoshenko beam with slenderness ratio *L/h* ($\lambda = 0$, $c_b=c_h=0$, $\mu=0$, $\xi=0$, $T=900^oK$).

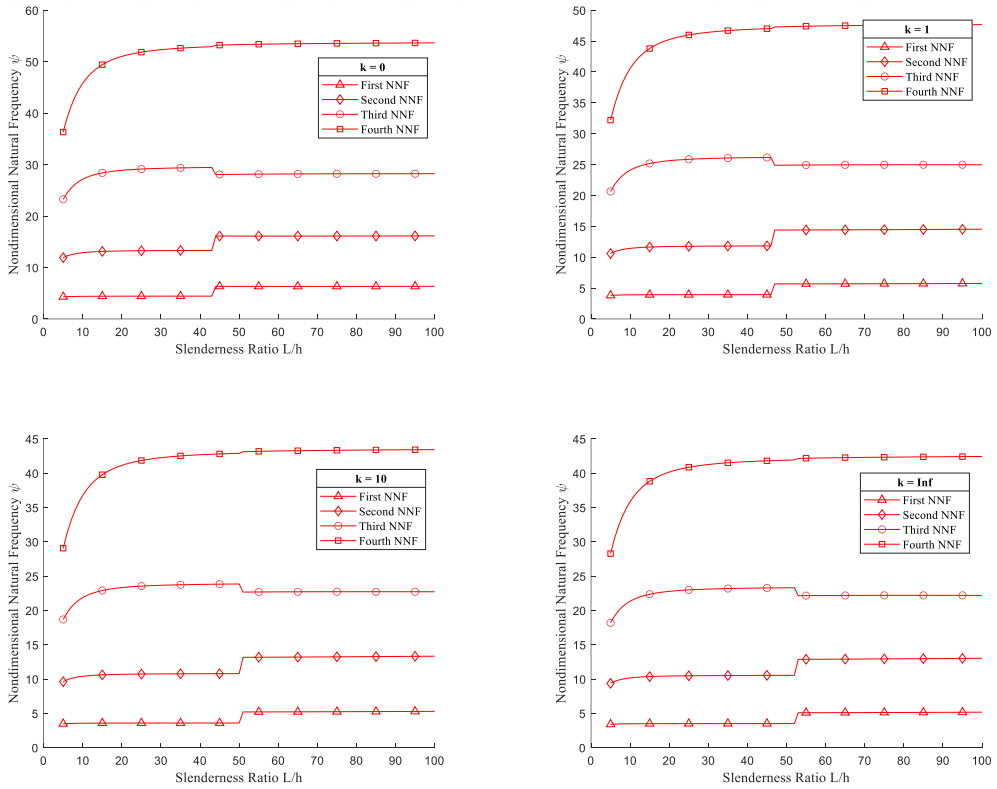

Figure D.13 : Variation of first four NNF of Timoshenko beam with slenderness ratio *L/h* ($\lambda = 10$, $c_b=c_h=0$, $\mu=0$, $\xi=0$, $T=900^oK$).

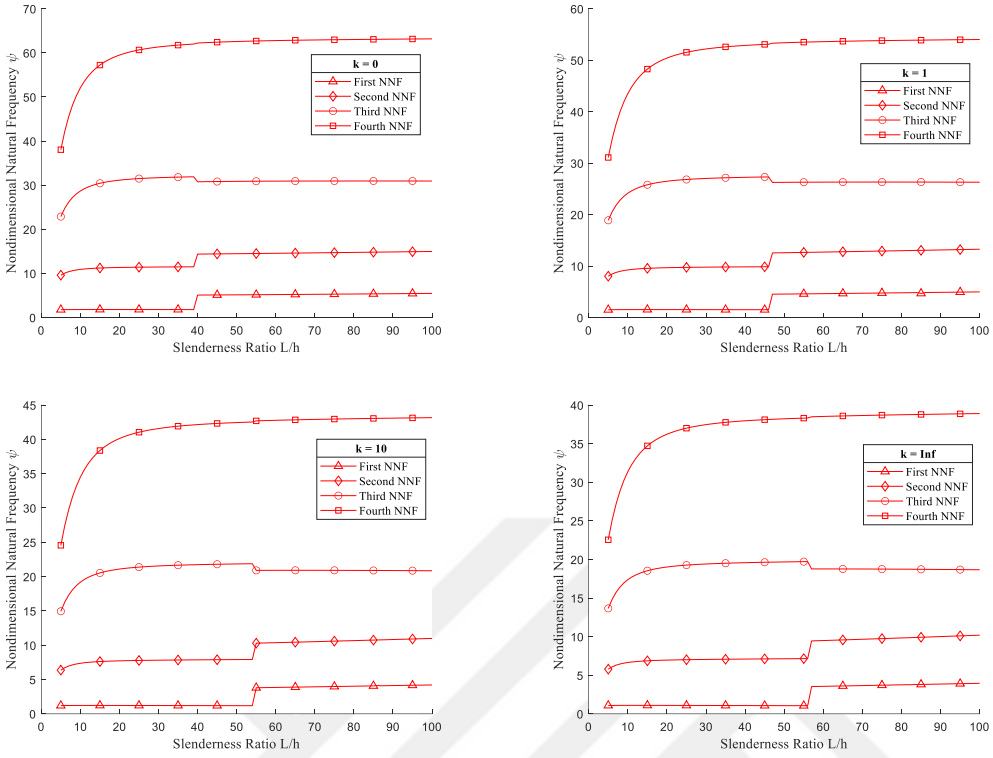

Figure D.14 : Variation of first four NNF of Timoshenko beam with slenderness ratio *L/h* ($\lambda = 0$, $c_b=c_h=0$, $\mu=0$, $\xi=0$, $T=1500^oK$).

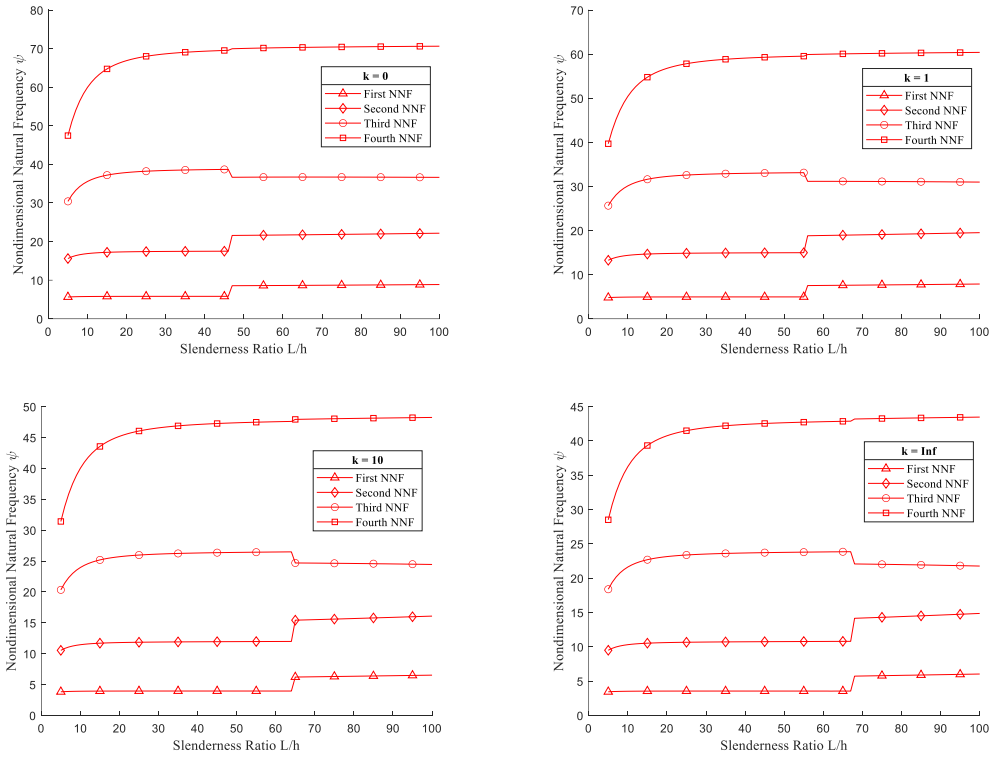

Figure D.15 : Variation of first four NNF of Timoshenko beam with slenderness ratio *L/h* ($\lambda = 10$, $c_b=c_h=0$, $\mu=0$, $\xi=0$, $T=1500^oK$).

APPENDIX E

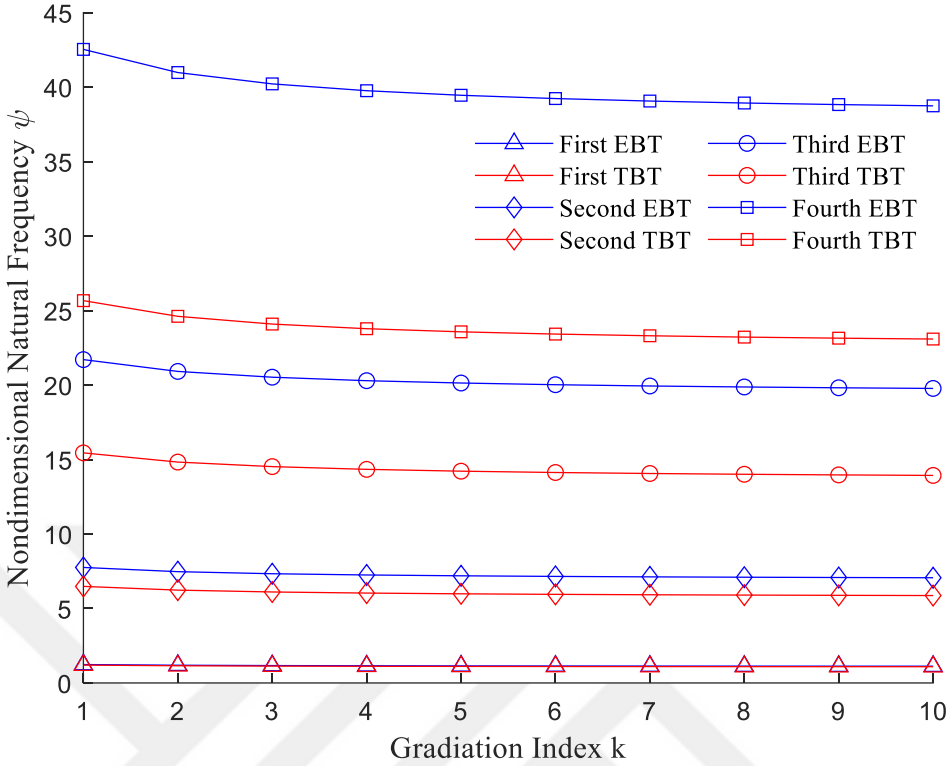

Figure E.16 : Variation of first four nondimensional natural frequency with gradiation index k ($L/h = 5$, $\lambda = 0$, $c_b=c_h=0$, $\mu=0$, $\xi=0$, $T=900^oK$)

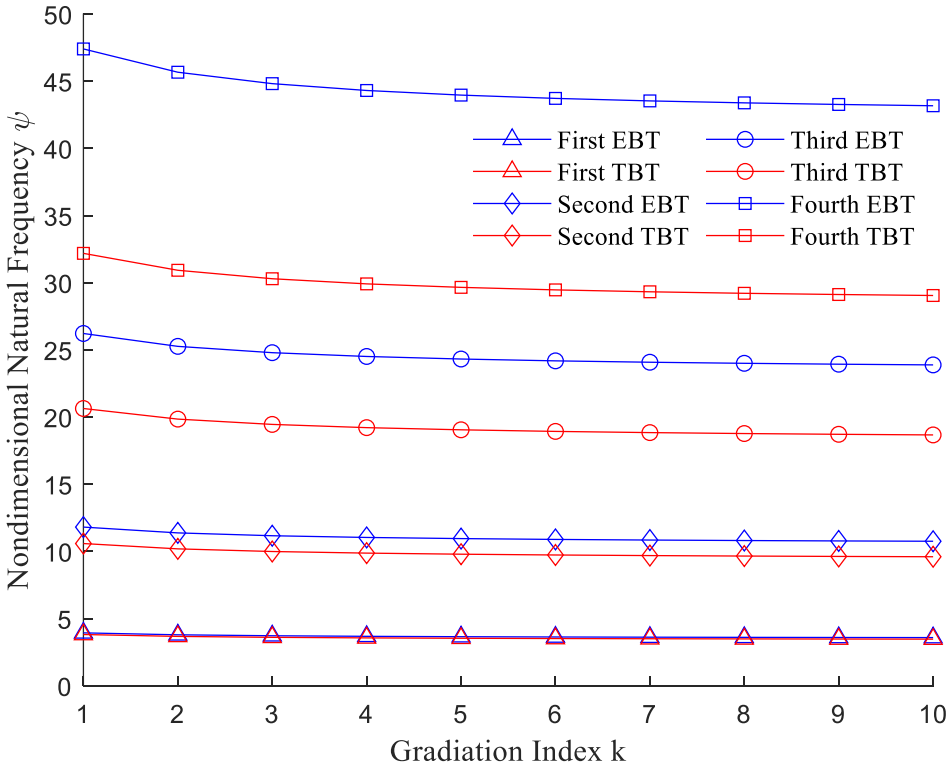

Figure E.17 : Variation of first four nondimensional natural frequency with gradiation index k ($L/h = 5$, $\lambda = 10$, $c_b=c_h=0$, $\mu=0$, $\xi=0$, $T=900^oK$)

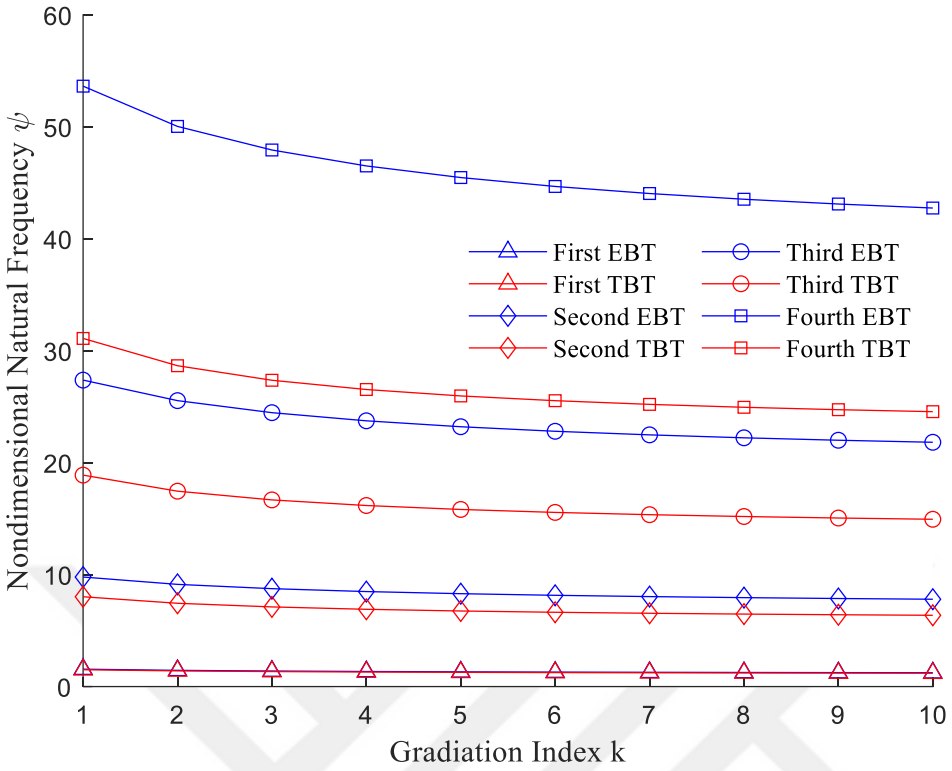

Figure E.18 : Variation of first four nondimensional natural frequency with gradiation index k ($L/h = 5$, $\lambda = 0$, $c_b=c_h=0$, $\mu=0$, $\xi=0$, $T=1500^oK$)

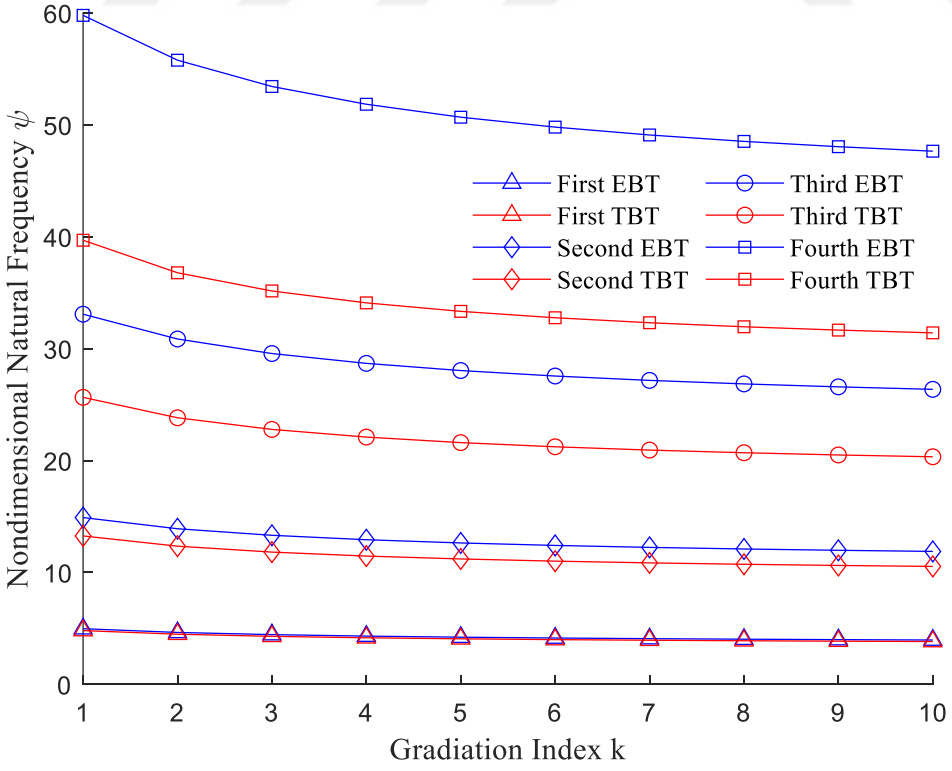

Figure E.19 : Variation of first four nondimensional natural frequency with gradiation index k ($L/h = 5$, $\lambda = 10$, $c_b=c_h=0$, $\mu=0$, $\xi=0$, $T=1500^oK$)

APPENDIX F

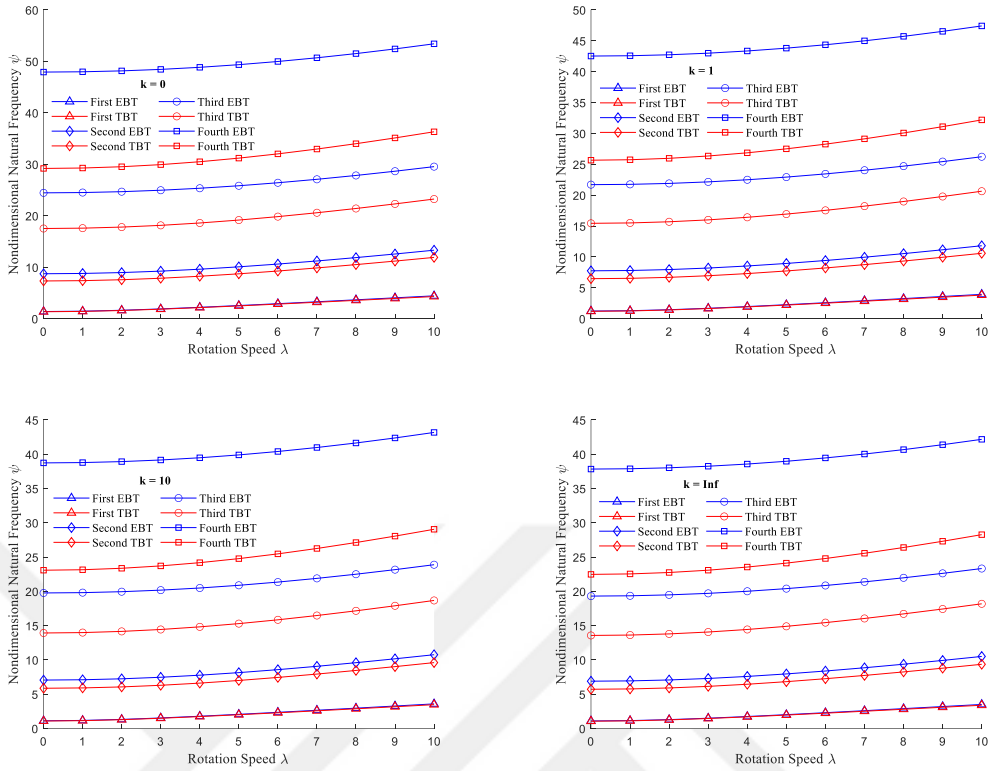

Figure F.20 : Variation of first four nondimensional natural frequencies of FGM beam with rotation speed λ (L/h = 5, c_b=c_h=0, μ=0, ξ=0, T=900°K)

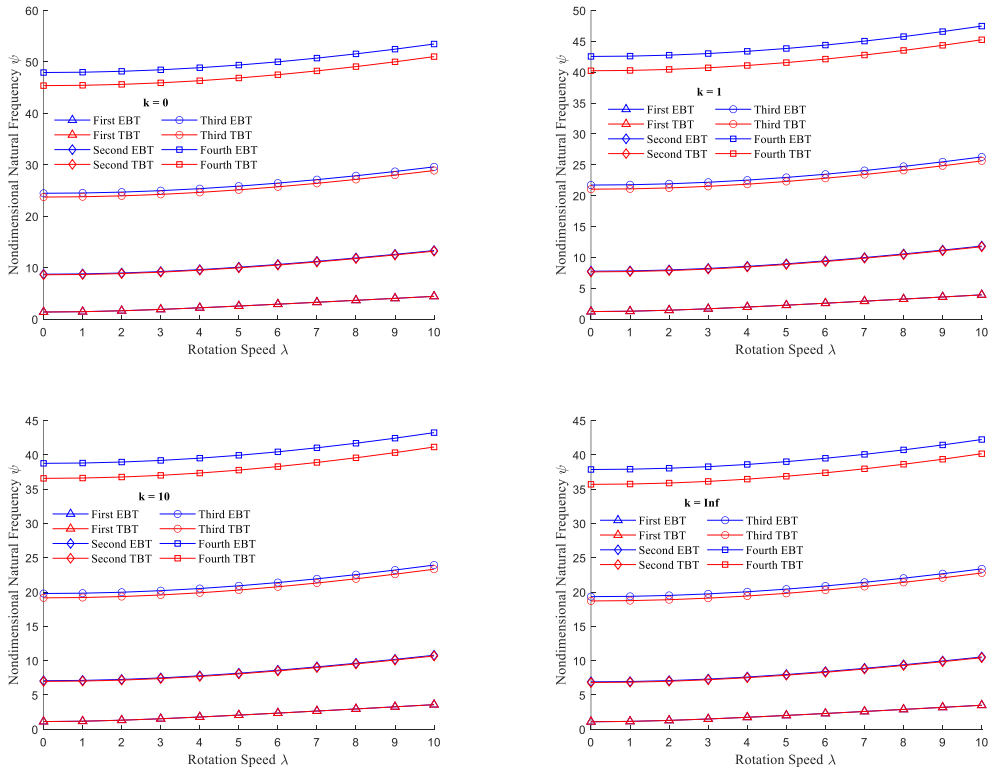

Figure F.21 : Variation of first four nondimensional natural frequencies of FGM beam with rotation speed λ (L/h = 20, c_b=c_h=0, μ=0, ξ=0, T=900°K)

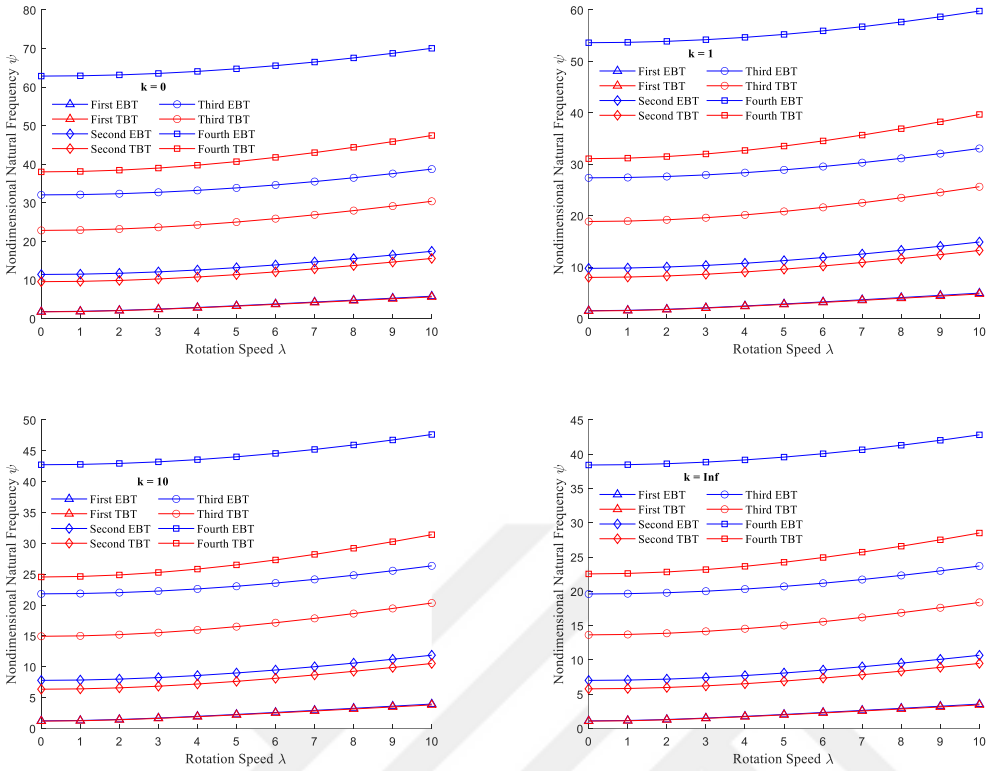

Figure F.22 : Variation of first four nondimensional natural frequencies of FGM beam with rotation speed λ (*L/h* = 5, c_b=c_h=0, μ=0, ξ=0, *T=1500ºK*)

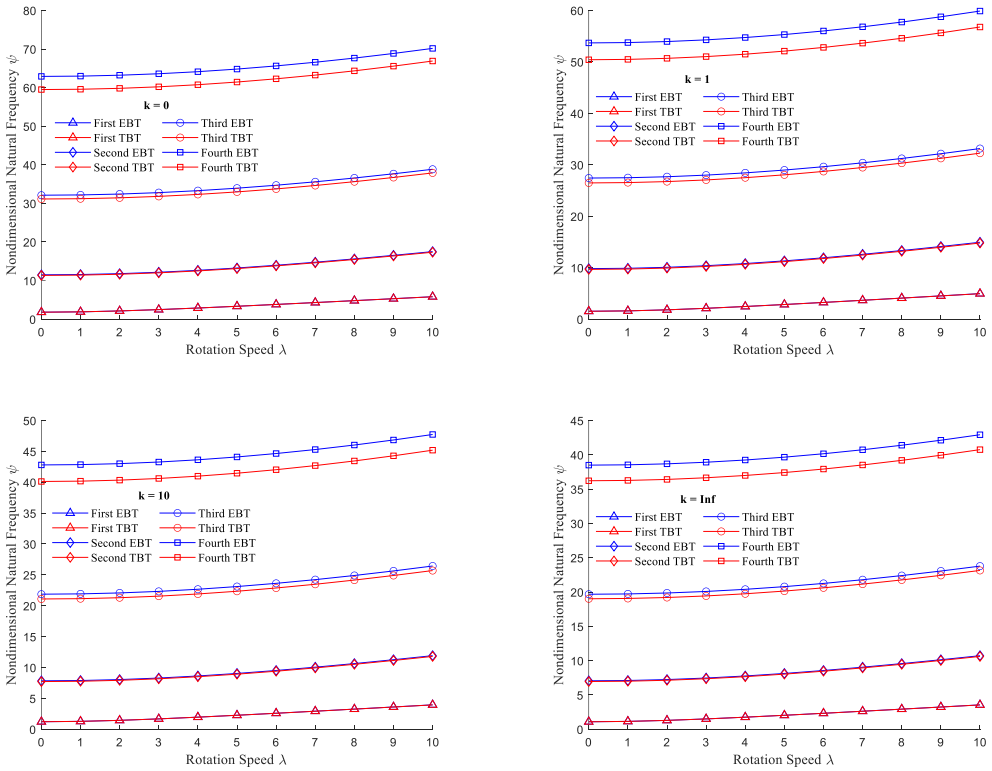

Figure F.23 : Variation of first four nondimensional natural frequencies of FGM beam with rotation speed λ (*L/h* = 20, c_b=c_h=0, μ=0, ξ=0, *T=1500ºK*)

APPENDIX G

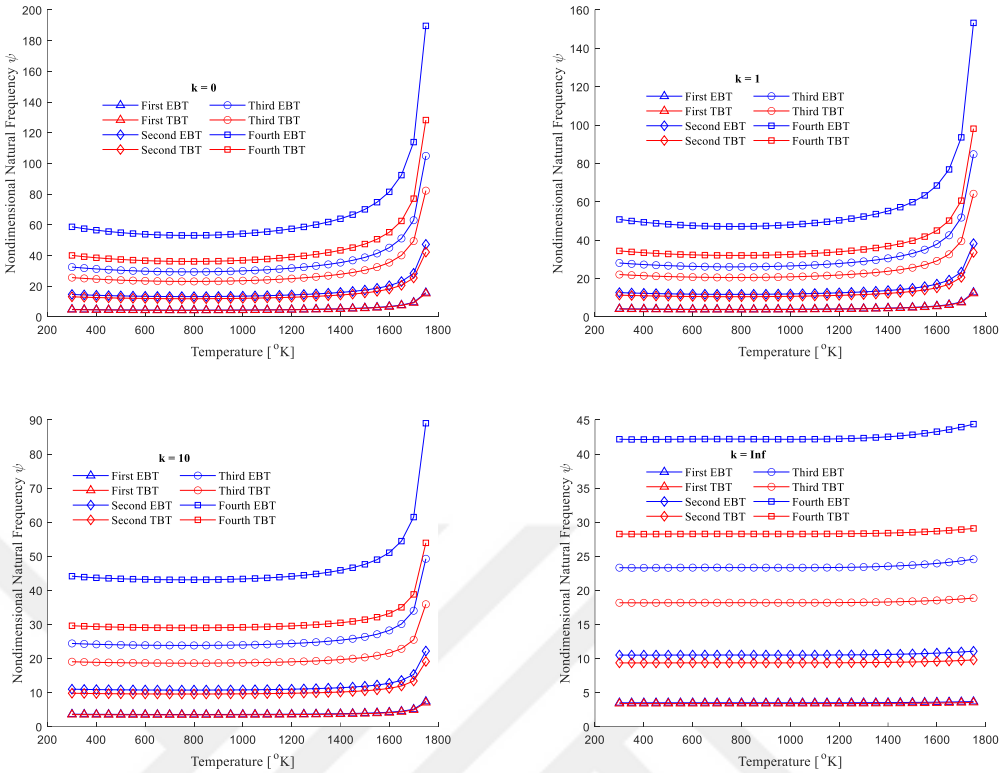

Figure G.24 : Variation of first four nondimensional natural frequencies of FGM beam with temperature ($\lambda = 10$, $L/h = 5$, $c_b=c_h=0$, $\mu=0$, $\xi=0$)

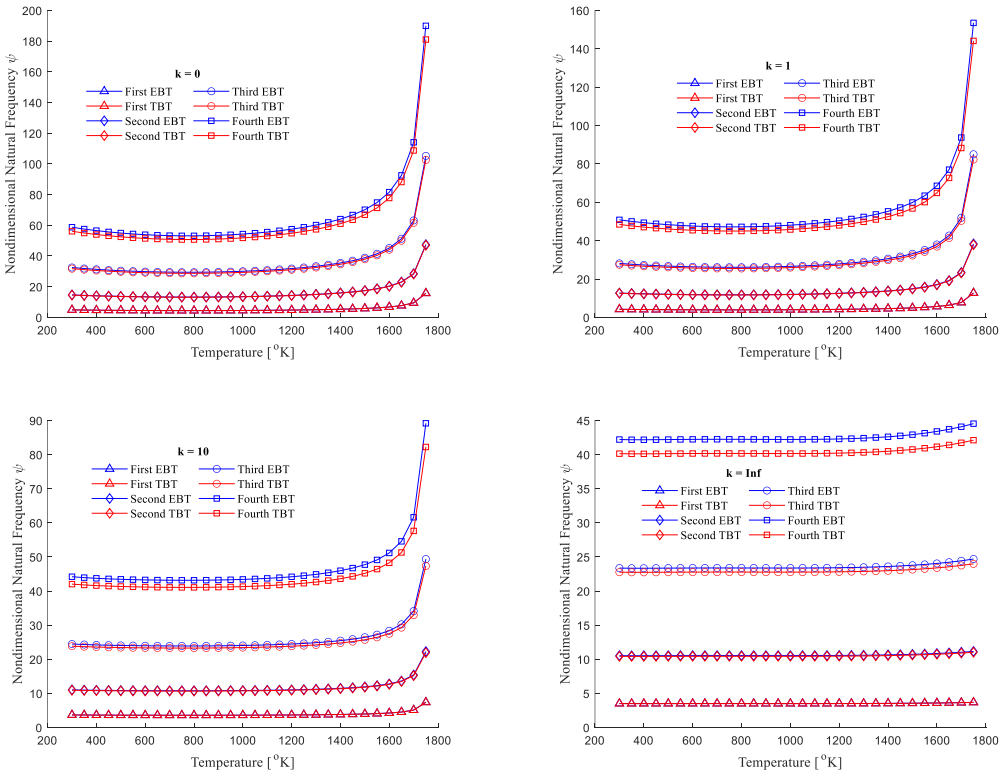

Figure G.25 : Variation of first four nondimensional natural frequencies of FGM beam with temperature ($\lambda = 10$, $L/h = 20$, $c_b=c_h=0$, $\mu=0$, $\xi=0$)

APPENDIX H

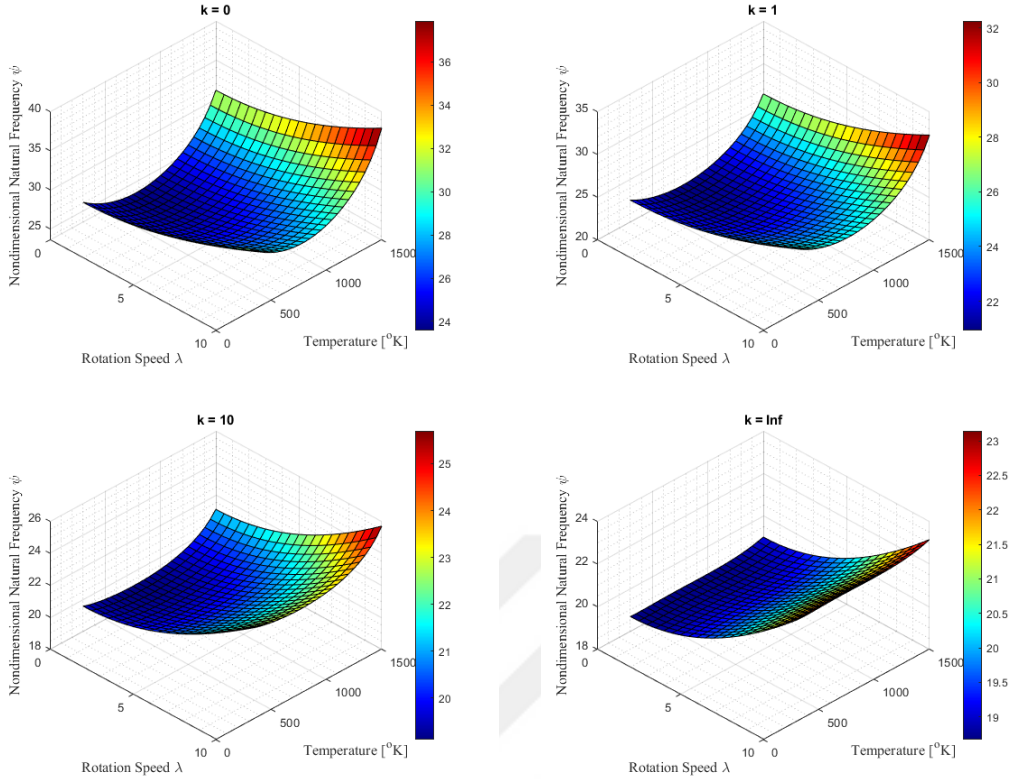

Figure H.26 : Variation of third nondimensional natural frequency of FGM beam with respect to temperature and rotation speed *(L/h = 20, c_b=c_h=0, μ=0, ξ=0)*

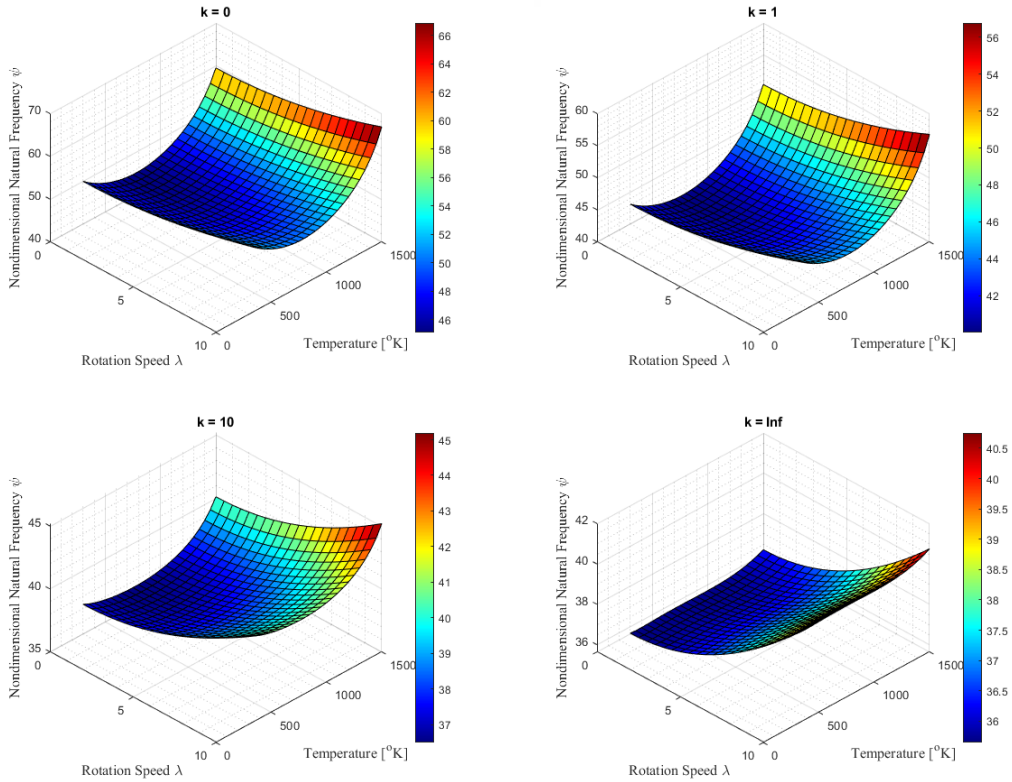

Figure H.27 : Variation of fourth nondimensional natural frequency of FGM beam with respect to temperature and rotation speed *(L/h = 20, c_b=c_h=0, μ=0, ξ=0)*

CURRICULUM VITAE

Name Surname **:** Mustafa Tolga YAVUZ

EDUCATION

- **B.Sc.** **:** 2011, Istanbul Technical University, Mechanical Engineering, Mechanical Engineering.
- **M.Sc.** **:** 2014, Istanbul Technical University, Mechatronics Engineering, Mechatronics Engineering.

PUBLICATIONS, PRESENTATIONS AND PATENTS ON THE THESIS

- **Yavuz, M. T.**, and Ozkol, I. 2021. Comparison of Some Numerical Approaches for Determination of Dynamic Characteristics in Beam and Plate Elements, *European Journal of Science and Technology*, Vol. 28, pp.1454-1468.
- **Yavuz, M. T.**, and Ozkol, I. 2021. Free Vibration Analysis of a Rotating Double Tapered Beam with Flexible Root via Differential Quadrature Method, *Aircraft Engineering and Aerospace Technology*, Vol. 93 no. 5, pp. 900-914.
- **Yavuz, M. T.**, and Ozkol, I. 2024.Thermal Structural Design Aspects of Military Aircraft, *Journal of Aeronautics and Space Technologies*, Vol. 17 no. 1, pp. 124-158.

OTHER PUBLICATIONS, PRESENTATIONS AND PATENTS

- Uyulan, C., and **Yavuz, M. T.** 2019. Robust $H\infty$ Control Applied on a Fixed Wing Unmanned Aerial Vehicle, *Advances in Aircraft and Spacecraft Science, Vol.*6 no.5, pp. 371-389.
- **Yavuz, M. T.**, and Ozkol, I. 2021. Solutions of Integro-Differential Difference Equations via Differential Transform Method, *Cankaya University Journal of Science and Engineering*, Vol. 18 no. 1, pp. 33-46.
- **Yavuz, M. T.**, and Uyulan, C. 2022. Modal Analysis of Turbofan Blades Modeled as Rotating Beam in Thermal Environment, *19th Annual Israeli Symposium for Jet Engines and Gas Turbines*, November 15-17, 2022 Haifa, Israel.
- Cetin, F., Yandim, C., Acar, M., Bagriyanik, M., Copur, E., and **Yavuz, M. T.**, 2023. Suppression of Flutter Using Active Control Algorithms in Two Degree of Freedom Simple Wing Structures, *The 24th National Meeting of Automatic Control*, September 14-16, 2023 Istanbul, Turkiye.

- Uyulan, C., **Yavuz, M. T.**, and Ozkol, I. 2023. Stabilizing Adaptive Feedback Controller Design for a Helicopter Gun Turret System, *10th International Conference on Recent Advances in Air and Space Technologies*, June 7-9, 2023 Istanbul, Turkiye.
- **Yavuz, M. T.**, Arikoglu, A., and Ozkol, I. 2023. Thermal Buckling Analysis of Rectangular Plate Structures by Differential Quadrature Method, *10th International Conference on Recent Advances in Air and Space Technologies*, June 7-9, 2023 Istanbul, Turkiye.
- Uyulan, C., **Yavuz, M. T.,** and Ozkol, I. 2023. Active Control of Store Separation Induced Flapwise Bending Vibrations on Simplified Wing Structures, *Aviation Technologies and Application Conference 2023*, October 20-21, 2023 Izmir, Turkiye.
- Acar, M., Cetin, F., Yandim, C., Bagriyanik, M., Copur, E., **Yavuz, M. T.** 2023. Flutter Analysis of 2 Degree of Freedom Wing Profile, *2nd National Aeronautical Engineering Students Symposium 2023*, May 15-17, 2023 Konya, Turkiye.
- **Yavuz, M. T.**, Uyulan, C., and Ozkol, I. 2024. Development of a Stabilizing Adaptive Feedback Control System for Helicopter Gun Turrets, *Journal of Aeronautics and Space Technologies*, Vol. 17 no. Special Issue, pp. 135-158.
- Ermis, O., Kaldirim, R., Yalcinkaya, F., Uyaner, M., and **Yavuz, M. T.** 2024. Thermal Buckling Analysis of Hybrid Composite Plates, *10th National Aviation and Space Conference*, September 18-20, 2024 Ankara, Turkiye.